Univeristy of Seville

Doctoral Thesis

Multibody modeling of railway vehicles and experimental validation

Author:
Javier Fernández Aceituno

Supervisor:
Dr. José L. Escalona Franco

A thesis submitted in fulfilment of the requirements for the degree of PhilosophiæDoctor (PhD)

University of Seville
Department of Mechanical and Manufacturing Engineering

January 2016

Abstract

The development of this thesis is focused on a comparison between efficient simulations of railroad vehicles in arbitrary tracks with irregularities and experimental results. Simulation of vehicles is a necessary tool to improve design and maintenance of vehicles and tracks. In addition, efficient simulations provide a useful mechanism to rapidly adjust model parameters in order to accurately reproduce its dynamic behavior. In this thesis, a dynamic formulation characterized by the definition of a moving frame of reference that follows the vehicle motion is presented. Also, different reference frames that allow the use of efficient assumptions, such as the use of contact lookup tables for the wheel-rail contact scenario, are proposed. Moreover, to check the validity of the proposed formulation, a scaled railroad vehicle is designed and tested in a 5-inch gauge railroad, whose geometry has also been measured. The procedure to accurately measure its irregularities is presented together with the parameter identification of the scaled vehicle. Finally, the numerical results stemming from the proposed method compared to the experimental results acquired by the scaled vehicle are presented and discussed at the end of the thesis.

Keywords: Multibody systems, railroad dynamics simulation, track frame formulation, wheel-rail contact lookup tables, vehicle design, track irregularities

Resumen

El desarrollo de esta tesis se centra en la comparación de simulaciones eficientes de vehículos ferroviarios en vías de geometría arbitraria e irregular frente a resultados experimentales. La simulación de vehículos es una herramienta necesaria para mejorar tanto su diseño como el mantemiento de las vías. Además, las simulaciones computacionalmente eficientes suponen una herramienta útil para poder ajustar rápidamente los parámetros numéricos y así poder reproducir fielmente el comportamiento dinámico de los vehículos. En esta tesis se presenta una formulación dinámica caracterizada por la definición de un sistema de referencia móvil que sigue el movimiento del vehículo. También se proponen diferentes sistemas de referencia que permiten el uso de simplificaciones, como el del uso de tablas precalculadas para el tratamiento del contacto rueda-carril. Igualmente, para comprobar la validez de la formulación propuesta, se ha diseñado un vehículo ferroviario a escala y se ha ensayado en una vía de 5 pulgadas de ancho de vía, cuya geometría también se ha medido. También se presenta el proceso para la medición precisa de sus irregularidades así como de la identificación paramétrica del vehículo a escala. Finalmente, los resultados numéricos de la formulación propuesta se han comparado con los experimentales adquiridos por el vehículo.

Palabras clave: Sistemas multicuerpo, simulación de la dinámica ferroviaria, sistema de referencia de la vía, tablas precalculadas de contacto rueda-carril, diseño de vehículos, irregularidades de vía

A mi familia

Acknowledgements

This research work was carried out between 2012 and 2015 in the School of Engineering (ESI) at the University of Seville. There are many factors that have contributed to the development of this thesis. First, I thank the Spanish government for the financial support I have received during the four-year FPI program, which has allowed me to focus on my research.

I am deeply grateful to Dr. José Luis Escalona, the supervisor of this thesis. His knowledge, guidance, explanations, encouragement and especially, his patience and time devoted to my training, have been crucial for the fulfillment of this thesis.

I am also thankful to Professor Ahmed Shabana for the oportunity to work in his research group at the University of Illinois at Chicago (UIC). His interest in my learning is cause for the greatest appreciation. Also I would like to thank Dr. Antonio Recuero for his advice and guidance during my stay at the UIC.

Likewise I thank my parents and sister for the support and encouragement they have given me during this work.

Finally, I dedicate this thesis to Ana. You have given me the strenght to complete this research.

Contents

List of Figures

List of Tables

Abbreviations

MSD	**M**ultibody **S**ystems **D**ynamic
MBS	**M**ultibody **S**ystem
FEM	**F**inite **E**lement **M**ethod
DOF	**D**egree **O**f **F**reedom
COG	**C**enter **O**f **G**ravity
GF	**G**lobal **F**rame
TF	**T**rack **F**rame
BF	**B**ody **F**rame
BTF	**B**ody **T**rack **F**rame
WF	**W**heelset **F**rame
WT	**W**heelset **T**rack frame
WIF	**W**heelset **I**ntermediate **F**rame
NE	**N**ewton-**E**uler
DAE	**D**ifferential **A**lgebraic **E**quation
ODE	**O**rdinary **D**ifferential **E**quation
HIL	**H**ardware **I**n the **L**oop
OOP	**O**bject **O**riented **P**rogramming
ORE	**O**ffice of **R**esearch and **E**xperiments
BBR	**B**ritish **R**ail **R**esearch
MMU	**M**anchester **M**etropolitan **U**niversity
RCF	**R**olling **C**ontact **F**atigue

PSD	**P**ower **S**pectral **D**ensity
IMU	**I**nertial **M**easurement **U**nit
DC	**D**irect **C**urrent
TCL	**T**rack **C**enter**L**ine
DAQ	**D**ata **A**cquisition software

Symbols

x	Longitudinal Cartesian coordinate
y	Lateral Cartesian coordinate
z	Vertical Cartesian coordinate
φ	Roll Euler angle
θ	Pitch Euler angle
ψ	Yaw Euler angle
$\mathbf{R}$	Position vector which origin coincides with the GF
$\mathbf{r}$	Position vector which origin coincides with the TF
$\mathbf{u}$	Position vector which origin coincides with the BF, WF and WIF
$\mathbf{w}$	Position vector which origin coincides with the BTF and WTF
$\mathbf{\Phi}$	Euler angles in vector form
$\mathbf{A}$	Transformation matrix
$\boldsymbol{\omega}$	Angular velocity vector
$\boldsymbol{\alpha}$	Angular acceleration vector
$\mathbf{q}$	6×1 vector of coordinates
$\mathbf{H}$	Partial derivative: $\partial\mathbf{R}/\partial\mathbf{q}$
$\mathbf{h}$	Partial derivative: $\partial\dot{\mathbf{R}}/\partial\mathbf{q}$
$\mathbf{G}$	Partial derivative: $\partial\boldsymbol{\omega}/\partial\dot{\mathbf{q}}$
$\mathbf{g}$	Partial derivative: $\partial\boldsymbol{\omega}/\partial\mathbf{q}$
$\mathbf{I}$	Inertia tensor

$\mathbf{F}$	Force vector
$\mathbf{T}$	Torque vector
$\mathbf{M}$	Mass matrix
$\mathbf{C}$	Damping matrix
$\mathbf{K}$	Stiffness matrix
$\mathbf{Q}$	Generalized force vector
$\mathbf{a}$	Vector of Cartesian and angular accelerations
$\mathbf{L}$	Jacobian matrix: $\begin{bmatrix} \mathbf{H} & \mathbf{G} \end{bmatrix}^T$
$\mathbf{l}$	Jacobian matrix: $\begin{bmatrix} \mathbf{h} & \mathbf{g} \end{bmatrix}^T$
k	Stiffness parameter
c	Damping parameter
l	Suspension element length
l_0	Suspension element initial length
$\dot{l}$	Suspension element deformation rate
f_s	Suspension element scalar force
U_s	Potencial energy
F_d	Rayleigh dissipation function
$\mathbf{B}_{susp}$	6×6 transformation matrix for suspension forces
$\mathbf{B}$	Matrix that relates independent with dependent coordinates
$\mathbf{D}$	Kalker linear coefficient matrix
$\boldsymbol{\varepsilon}$	Vector of creepages
F_f^T	Tangential flange contact scalar force
F_f^N	Normal flange contact scalar force
δ	Indentation
$\dot{\delta}$	Indentation rate
μ_f	Coulomb friction coefficient
s	Trajectory coordinate
$\mathbf{C}$	Vector of constraints

$\mathbf{C_q}$	Jacobian matrix of the constraints
$\dot{\mathbf{C}}_\mathbf{q}$	Time derivative of the Jacobian matrix
$\mathbf{C}_t$	First partial-time derivative of the vector of constraints
$\mathbf{C}_{tt}$	Second partial-time derivative of the vector of constraints
$\mathbf{s}^w$	Vector of wheel surface parameters
$\mathbf{s}^r$	Vector of rail surface parameters
$\mathbf{t}$	Tangent vector
$\mathbf{n}$	normal of constraints
$\boldsymbol{\lambda}$	Vector of Lagrange multipliers
u_z	Vertical track irregularity
u_y	Lateral track irregularity
d	Track gauge
d'	Irregular track gauge
$\mathbf{f}$	Function vector

Chapter 1

Introduction

Nowadays rail transport is one of the most significant indicators used at evaluating the economic development of countries. Since the industrial revolution in the second half of the 18th century, where it helped in the industrialization process by easy transportation of coal and raw-materials at a cheaper rate, rail transport has also allowed the possibility of shipping great amount of goods and passengers with many more advantages with respect to other land transports. The main feature of rail transport is that it is guided by the tracks on which the vehicles run, usually made by steel, that generally have a low frictional resistance with respect to the vehicles wheels, and consequently, allow them to roll with a minimum of friction.

Regarding its advantages, rail transit is a quick and regular form of transport that facilitates reliable long distance travels that are not easily transported through other motor vehicles and whose capacity can easily be increased by adding wagons. It is considered as the safest form of shipping. This reliability does not result from a lower number of traffic accidents, but also lesser losses incurred from these accidentes. Furthermore, due to the new technologies that have allowed the development of high-speed trains, rail transport is also competitive against air transport when mid-distances up to around 700 km are considered.

However, there are also some disadvantages of the rail transport that make it unsuitable for some situations. For instance, it is an inflexible way of transport because routes and timings cannot be adjusted to individual requirements and cannot provide door to door services. It is also uneconomical for short distances and small traffic of goods or passengers. In addition, it requires a large investment of capital for the construction and maintenance of the railroad network, where special care should be focused on the last one. Due to the complexity of wheel and rail surfaces in contact, railway tracks need regular maintenance to remain in good order.

In the broadest sense, track maintenance can be defined as a product of resources, judgments, experience, skills, tools, and policies that are exercised in a range of service environments and within every conceivable type of organizational structure. Its purpose is to keep below a certain level the geometric rail head deviations in order to avoid undesirable dynamic behaviours of railroad vehicles that go through the tracks. There is a large variety of different maintenance jobs, such as simple visual inspections, or highly cost preventing and correcting actions like switches adjustment, ballast tamping or rail and sleeper replacement. As track maintenance is an expensive task, in order to reduce its costs many research work has been done in the literature. They mainly focused on accurate detection of track irregularities so as preventing maintenance actions can be precisely carried out.

In order to study how important the quality of track geometry is and how it affects the dynamics of railroad vehicles, two different approaches or even a combination of both can be developed; experimental tests and simulation results. In the former, highly cost experiments with sensored railroad vehicles and tracks are carried out to measured the dynamic behaviour of different railroad vehicles when running on irregular tracks. It is the most reliable way of analysis whose main disadvantages are, as already stated, the economic cost and the time needed for the experiments achievement. On the contrary, computer simulations allow the development of mathematical models that can

reproduce accurately the dynamics of the railroad system. This requieres a strong background in the field of study in order to account for desired behaviours that are supposed to be checked. However one of the main disadvantages of computer simulations is the possiblity of obtaining inaccurate results that lead to an easy misunderstanding of the system. Therefore, they require at least, a minimum of experimental tests or analytical solutions, in order to validate the simulation model.

Regarding computer simulations, two important approaches can be followed: Finite Element Analysis (FEA) and Multibody System Dynamic analysis (MBD). The well-known FEA is the most commonly used analysis technique in which a big diversity of specializations in the mechanical engineering discipline such as railroad, automotive or aeronautical industries, uses. On the other hand, MBD is defined as the study of the dynamics of interconnected rigid or deformable bodies, that are subject to both small and large translational and rotational displacements. Generally, the MBD approach is employed at a higher scale than FEA. In the case of vehicle dynamics, MBD is first used in order to calculate the motion and reaction forces among the bodies in the system. Later, for an accurate and local computation of the stress distribution that these forces have in the bodies, FEA is employed.

This thesis intends to develop an efficient numerical method to be used in real-time simulations for model-based condition monitoring within the field of Multibody Systems Dynamics to accurately measure railroad vehicle dynamic responses when rolling on tracks with irregularities. To this end, experimental results obtained in a 5-inch scaled railroad vehicle tested in a measured track are compared to check the validity of the method. Furthermore, a brief summary of the structure of general tracks is presented together with a general characterization of track irregularities. Likewise in this introductory chapter, a review of the state of the art in the modeling of railroad vehicles is included to then, finish with an outline of the rest of the thesis as a closure.

1.1 Track structure

A railroad track can be defined as a permanent road having a line of rails fixed to ties and laid on a roadbed that hold and guide the railroad vehicles. It can be divided into three different sections; superstructure, substructure and special structures [42]. The superstructure is formed of rails, sleepers, railpads and fixing components or clips. The substructure is associated with a geotechnical system and can be divided into two different subsections; on the one hand, one can find the traditional substructure (see Fig. 1.2), which consists of the ballast, subballast, soils and drainage systems and on the other hand, one can find the slab tracks, a modern form of track construction that substitutes the ballast by a rigid concrete track slab, which improves stability and load transfer and is commonly used for tram systems, heavy rail and in some cases, for high speed trains. Both superstructure and substructure are mutually important in ensuring the safety and comfort of passengers and quality of the ride. Bridges, tunnels and retaining walls are known as special structures.

Rails are bar elements made of steel that are placed on the sleepers and whose main purpose is to guide the rolling stock. As they transfer the loads to the sleepers, their cross sectional shape is designed accordingly to the type of rail traffic they are intended to have. Nonetheless, they all have in common that their head is profiled to resist wear and to give a good ride while the foot is profiled to suit the fixing system. The railpads are viscoelastic materials which are installed directly under the foot of the rail and whose purpose is summarized below:

- Improve load distribution
- Minimize wear
- Reduce vibrations caused by rail traffic
- Provide electrical isolation for embedded rails

- Increase passengers comfort

The rail fastening system, or *fastenings*, includes every component that connects the rail to the sleeper in order to ensure a solid bond and prevent longitudinal or lateral relative movements (see Fig. 1.1). Fastenings clamp the rail gauge within acceptable tolerances and then absorb forces from the rails and transfer them to the railpads. The sleepers are rectangular supports for the rails that laid perpendicular to them. In the past they were made of wood but nowadays, it is more common to have pre-stressed or reinforced concrete sleepers. Their main functions are:

- Transmit loads to the ballast and subgrade
- Provide adequate mechanical strength both in the horizontal and in the vertical direction
- Provide an anchorage for the fastening system that holds the rails at their correct gauge and preserves inclination

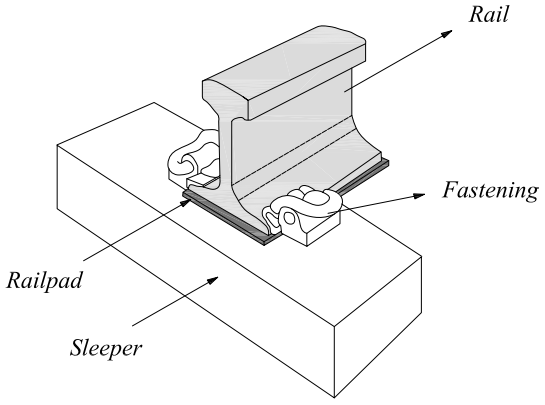

FIGURE 1.1: Rail fastening

The ballast forms the track bed upon which sleepers are laid. It is typically a layer of free draining coarse aggregate used as a tensionless elastic support for resting sleepers. This layer is usually made of crushed stone and crushed gravel such as granite and basalt. The main functions of the ballast are:

- Bear the load from the railroad fastenings
- Limit the sleepers movements longitudinally, laterally and vertically
- Facilitate drainage of water
- Allow optimal settlement
- Keep down vegetation that might interfere with the track structure
- Avoid damages caused by freezing and unfreezing
- Reduce noise caused by rail traffic
- Give resiliency and energy absorption to the sleeper
- Assist track maintenance in surfacing and lining operations by the ability to manipulate ballast with low energy tamping

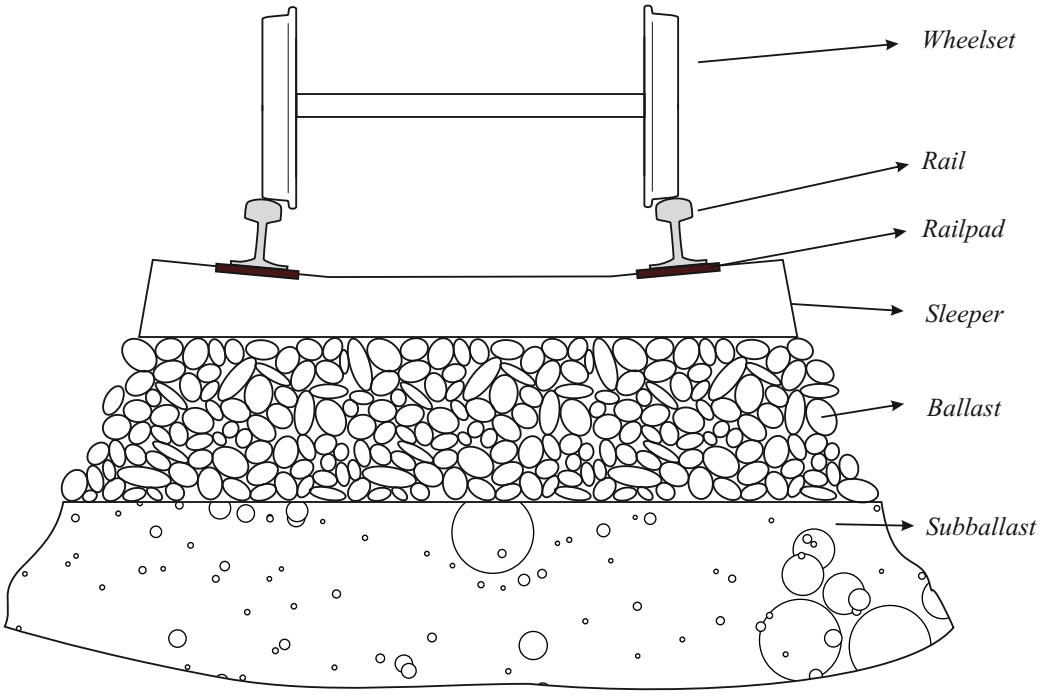

FIGURE 1.2: Wheelset and traditional railroad track structure

The subballast is located below the ballast and is a layer of granular material usually formed by sandy gravel. The main purposes of the subballast can be described as:

- Reduce the influence of unstable soils
- Prevent strange elements to become part of the ballast
- Slow down the growth of vegetation
- Improve the load distribution
- Drain the rainwater
- Act as a shedding layer to keep water away from subgrade

1.2 Track irregularities

The study of railroad vehicle dynamics is a difficult task. Due to the complex geometry of the wheel-rail surfaces in contact, contact forces in the wheel/rail scenario are highly non-linear and subject to large variations if the track geometry quality is low. This could lead to undesirable dynamic responses in the passing of a railroad vehicle, such as dynamic impact forces and vibrations, that in the worst cases, could cause it to derail. It is known that the size of track irregularities changes with wavelength, commonly the higher wavelength the longer amplitude. On the other hand, small wavelength irregularities may produce high wheel-rail contact dynamic forces regardless of their short amplitudes. It is then obvious that the study of irregularities is an important topic within railway engineering.

1.2.1 Track damage mechanisms

Track irregularities can be considered as geometrical deviations of the rail cross-sections from an ideal track alignment. They are caused by many damage mechanisms that can

appear on a regular pattern along the track i.e. corrugation, or as isolated defects such as dipped joints or lack of support at the sleeper-ballast interaction. Some of these damage mechanisms that influence in the appearance of track irregularities can be listed as:

- Corrugation
- Rail welds
- Dipped joints
- Lack of support
- Rail plastic bending
- Rail manufacturing
- Rolling contact fatigue
- Wear

Rail corrugation is one of the most serious problems in railway engineering. It is a constant-frequency phenomenona in which the rail head is wrinkled (see Fig.1.3), so it can heavily influence the vehicle motion and lead to safety concerns. This kind of defect can possess a wide range of wavelength (25-300 mm) and it is mainly caused by the dynamic contact forces that act in the wheel/rail interface [29]. However, it is a complex phenomena with many different capabilities that has not been fully explained yet. For a complete review, one can refer to [28, 34, 86]

Raild welding is the process of solding the ends of two consecutive rails in order to avoid shocks and damage to wheels when the vehicle passes. It is generally achieved by electrical resistance or flash-butt welding [72]. The former process is based on the exothermic reaction derived from the reduction of metals with the help of aluminium while the latter one is an approach of joining metals in which the heat generated is

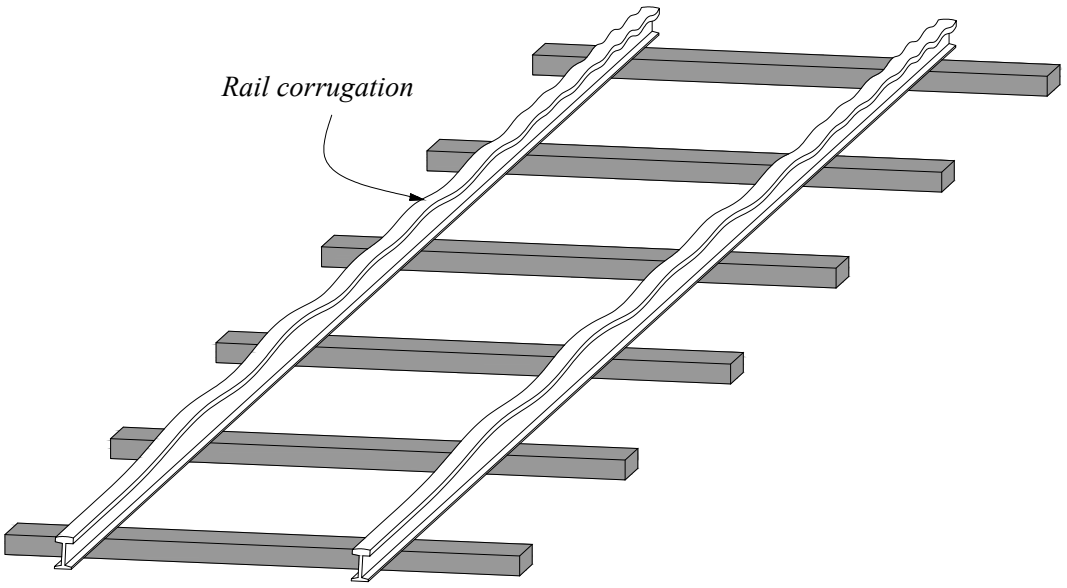

FIGURE 1.3: Corrugation on a tangent track

produced by the opposition of the rails to the transit of an electric current. In this flush-butt welding process, no additional material is needed to develop the weld.

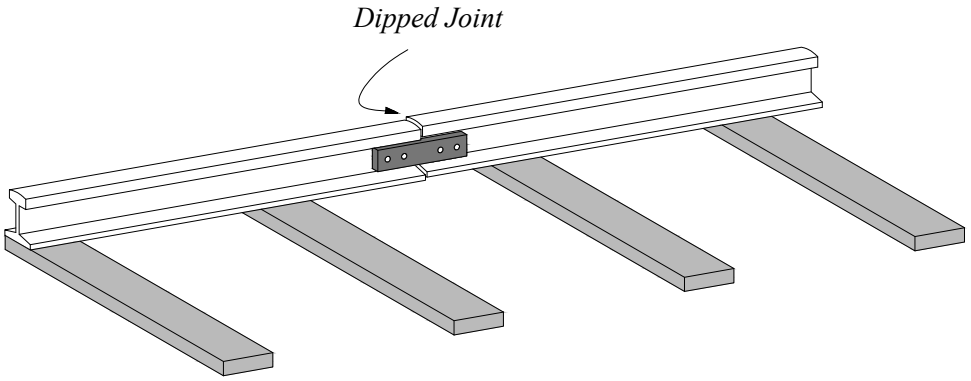

FIGURE 1.4: Dipped Joint

Depending on the quality of the process followed, rail welding can produce vertical and horizontal defects at a regular pattern that affect the dynamics of the railroad vehicle. Similarly, when rail ends are not welded but joined, there may be a small difference

in the level of the two cross-sections at the joint (dipped joints [37]) causing a large dynamic pressing force when the vehicle *climbs* over it (see Fig.1.4)

Lack of sleeper support is a common phenomena that happens when there is a loss of contact between the sleepers and the ballast, mainly due to a local sinkage of the latter that causes a gap. When this happens, the distance between two consecutive sleepers is augmented (see Fig.1.5) letting severe damage to occur, such as plastic bending of the rails at the passing of railroad vehicles. As it is an important event that compromise the vehicles stability, one can find in the literature different studies of the influence that the sleepers loose of contact has on the vehicle dynamics [62, 77].

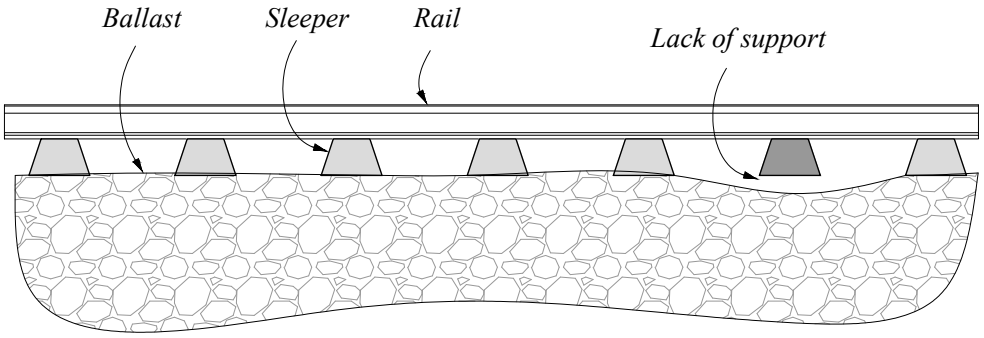

FIGURE 1.5: Lack of sleeper support

Other important wheel/track damage mechanisms are rolling contact fatigue (RCF) and wear. RCF is the damage produced by repeated cyclic loading and unloading together with contact creep forces that appear when the railroad vehicle runs over the track [6]. It leads to the formation and growth of surface cracks produced by a combination of shear and compressive stresses in the wheel/rail interface. It is a complex mechanism that is magnified by the effect of water and grease in the way that they can press against the crack tip producing high tensile stresses and speeding up the crack growth. Therefore, it is the responsible of more than the 40% of wheel damage cases and it is the major cause of replacements and maintenance of railroad track lines. On the other hand, wheel/rail wear is the loss of material produced by the friction between the surfaces in contact that modifies its cross sections (see Fig.1.6). Because these are the main damage

mechanisms, many investigations have been devoted to this important topic. In [103], there is a review of different publications on wear and RCF mechanisms and models that are influenced by the wheel material microstructure and how this microstructure is modified during loading. It also discusses the surface stress distribution in the wheel assuming the presence of fluid in the contact area. In addition, in [18], it is provided a literature review of the wheel/rail deterioration mechanisms accounting for the effect of the contact modeling, contact stresses, wear models, RCF and surface plasticity in the contact patch.

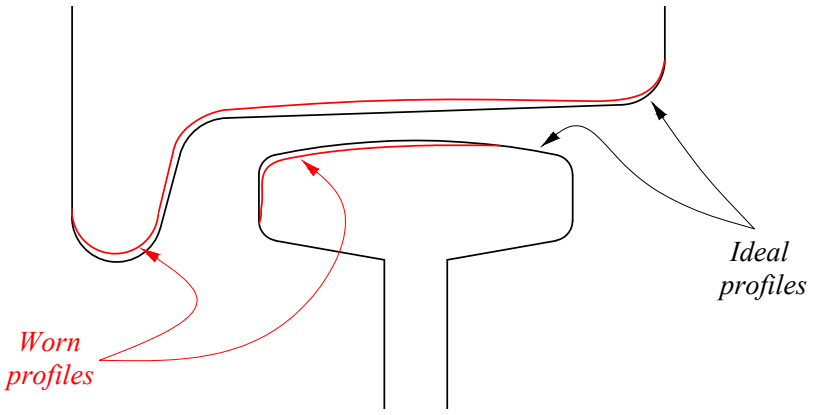

FIGURE 1.6: Wheel/rail worn profiles

1.2.2 Modeling track irregularities

In order to improve track quality, rail safety, passenger comfort and vehicle performance, an analytical description of track irregularities is of major importance for simulation purposes. As mentioned in section 1.2.1 as the main consequence of track damage mechanisms, they can be quantified as lateral and vertical displacements of the rail cross-sections with respect to a reference track geometry (see Fig. 1.7).

Therefore and as it can be found in the literature, to properly account for track irregularities it is first necessary to identify two different kinds of geometry variations: distributed track geometry variations and isolated track geometry variations [24, 31].

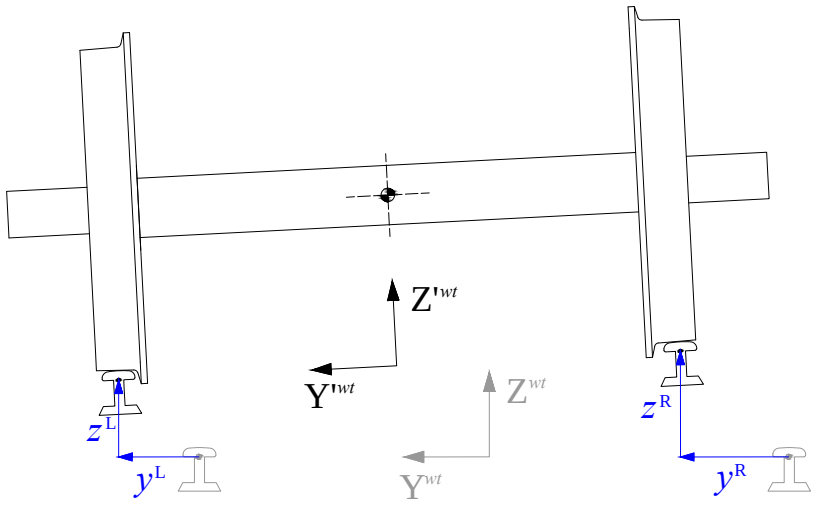

FIGURE 1.7: Track lateral and vertical deviations

1.2.2.1 Distributed track irregularities

Distributed track geometry variations can be defined as a combination of two processes: a stationary arbitrary one that considers the amplitude of the irregularities in the rail and a process linked with the wavelength in which the irregularity is observed. They can be described in terms of four magnitudes: alignment, gauge, cross level and vertical profile [24] (see Fig.1.9 and Fig.1.10).

The four magnitudes that describe track irregularities are referred with respect to the ideal or reference track geometry. This is, the initial geometry that the railroad track should have by construction drawings and without the presence of track defects. In Fig. 1.8 one can see both the reference and real geometry of a track where $\mathbf{r}_{left}$ and $\mathbf{r}_{right}$ refer to the position vectors of the left and right rail real geometry with respect to the reference one. Moreover, Eq. 1.1 shows the analytical definition of these magnitudes where x, y and z refer to the Cartesian components of vector $\mathbf{r}$.

Alignment is the lateral position of the two rails with respect to the reference railroad track, computed as the half of the sum of both lateral positions as in Eq.1.1. It is also named *track centerline* and it is the main cause of lateral vibrations in railroad

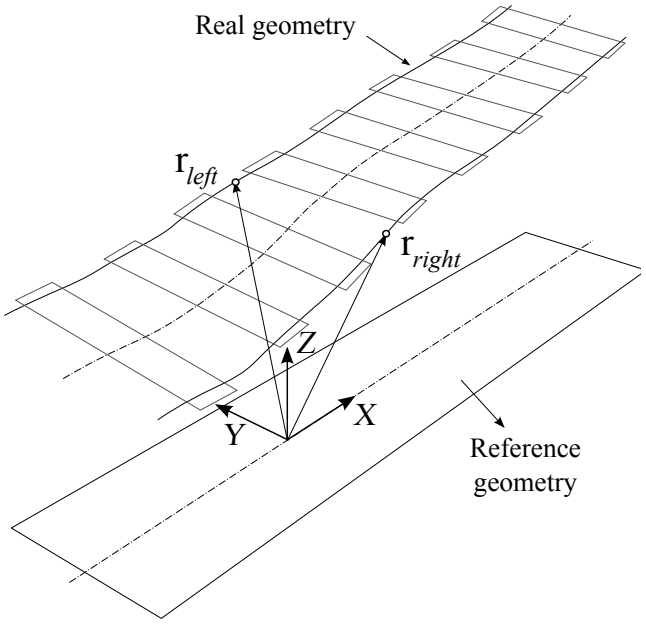

FIGURE 1.8: Real and reference railroad track geometry

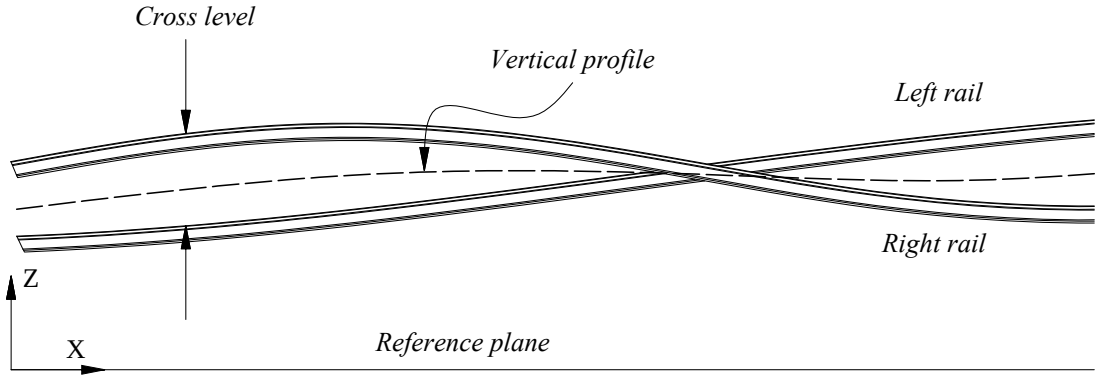

FIGURE 1.9: Cross level and vertical profile

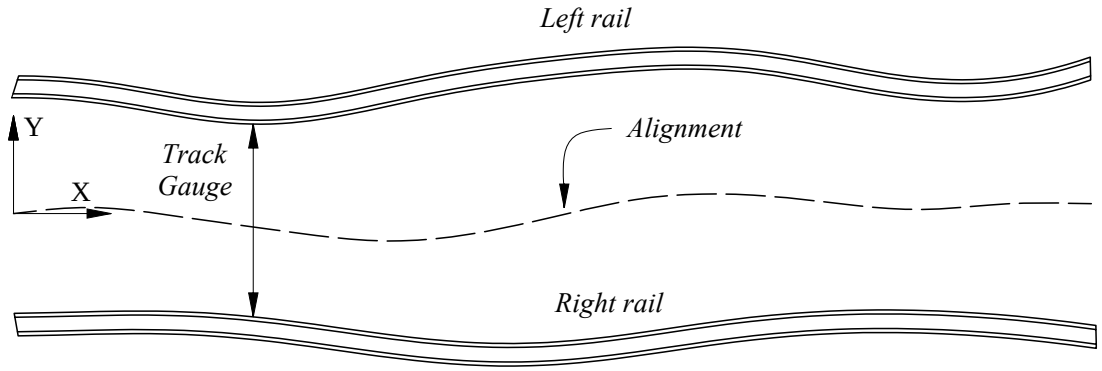

FIGURE 1.10: Track gauge and alignment

vehicles together with cross level, that can be defined as the relative distance between the vertical position of the two rails. Track gauge, which plays an major role in the vehicle lateral stability, is the lateral distance between the inner faces of the two rails and is measured in a plane that is 5/8 inches below the top of the rail heads while vertical profile is the average vertical position of the rails.

$$\begin{aligned} \text{Alignment} &= (y_{left} + y_{right})/2 \\ \text{Gauge} &= (y_{left} - y_{right})/2 \\ \text{Cross level} &= (z_{left} - z_{right})/2 \\ \text{Vertical profile} &= (z_{left} + z_{right})/2 \end{aligned} \tag{1.1}$$

This description of the typical track irregularities allows to quantify the geometry of the track through a trajectory coordinate. However, as infinite numbers of geometry variations can occur in the railroad track, features such as their amplitude and wavelength can only be characterized by a statistics process. The most used tool to analyse this random process is the power spectral density (PSD) [102], which provides a full analytic despcription of an arbitrary variable having a normal distribution in which statistical parameters are constant in time and independent of position. Some PSD functions for track irregularities can be found in the literature, as those developed in

[31] for wavelengths up to 300 m, where it can be noted that wavelengths between 1 m and 100 m are critical for railroad vehicle dynamics.

1.2.2.2 Isolated track irregularities

Isolated track defects, which are the main cause of unsafe responses, are exceptional cases which appear rarely but may have regular patterns. They are usually present at special track work, in poor drainage areas, and at road crossings, bridges or turnouts. Their frequency of happening depends on the track features, but their relevant influence on vehicles dynamics requires a special care when dealing with them.

A proper way to model isolated defects consists of analytical forms obtained by functions of two parameters; their amplitude A and duration-parameter k [24]. These forms are superposed in the center of a rail cross-section through the length of the k-parameter.

In general, there is a total of seven different kinds of analytical isotaled defects functions whose name and representation are listed as follows: Bump 1.11(a), cusp 1.11(b), plateau 1.12(a), jog 1.12(b), sinusoid 1.13(a), damped sinusoid 1.13(b) and trough 1.14(a).

1.2.3 Track quality regulations

Some general regulations about track quality standards and specifications about the safety related limits can be found in the literature. In Europe, there is the prEN 13848-5 [71] that classifies different limits of track irregularities according to their severity. These limits are stablished for different wavelengths and vehicles forward velocity. In case they are exceeded, some of the recommended actions may vary from closing the track, reducing the speed of operating of the track or applying corrective actions to fix its geometry.

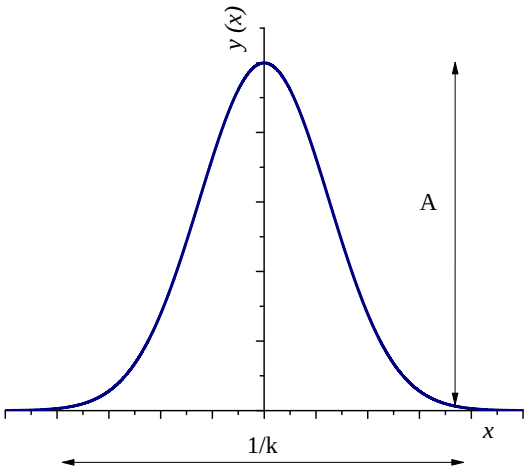

(a) Bump: $y = Ae^{-0.5(k|x|)^2}$

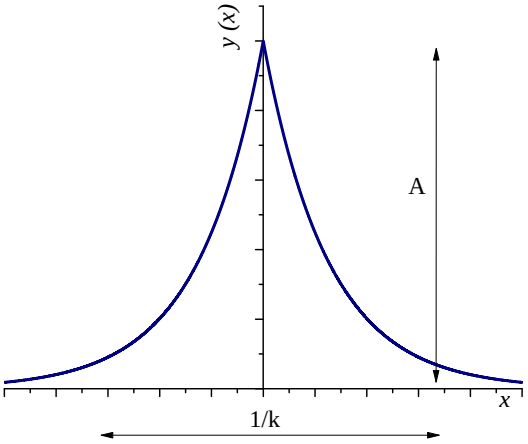

(b) Cusp: $y = Ae^{-k|x|}$

FIGURE 1.11: Isolated track defects I

In [71], there are three different ranges in the wavelength of track defects λ for the magnitudes of cross level and alignment that can be listed as:

- D1: $3 \text{ m} < \lambda < 25 \text{ m}$
  (some authors consider this D1 range as $1 \text{ m} < \lambda < 25 \text{ m}$)
- D2: $25 \text{ m} < \lambda < 70 \text{ m}$

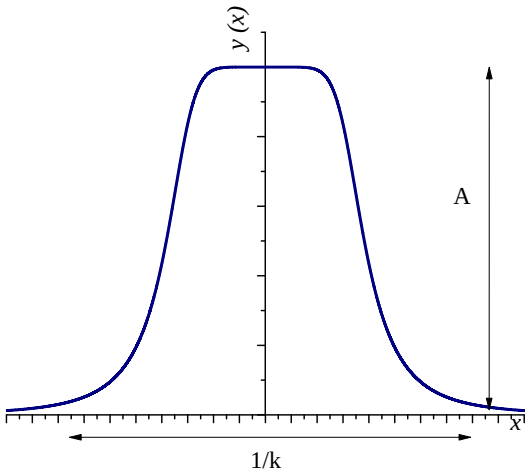

(a) Plateau: $y = \sqrt{A^2/(1+(kx)^8)}$

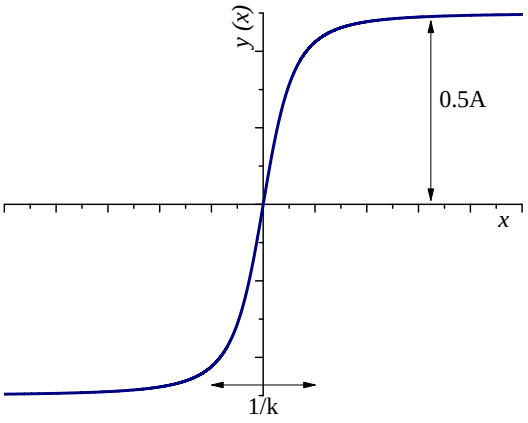

(b) Jog: $y = Akx/\sqrt{1+4k^2x^2}$

FIGURE 1.12: Isolated track defects II

- D3: $70 \text{ m} < \lambda < 150 \text{ m}$ (cross level),
  $70 \text{ m} < \lambda < 200 \text{ m}$ (alignment)

In these ranges, there exist different limits that are defined in such a way that when they are exceeded, corrective actions must be taken. These limits depends on the vehicle forward velocity, the most important factor when evaluating a track quality, and are defined as:

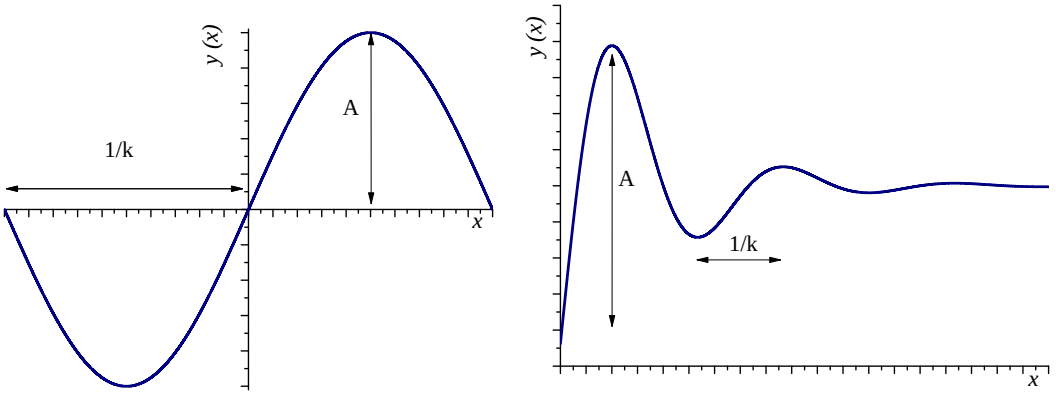

(a) Sinusoid: $y = A\sin(\pi kx)$ (b) Jog: $y = Ae^{-kx}\cos(\pi kx)$

FIGURE 1.13: Isolated track defects III

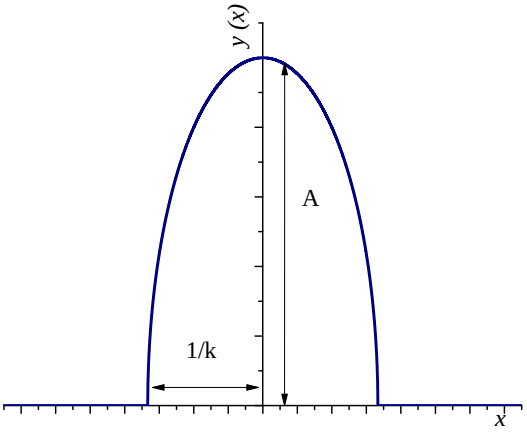

(a) Sinusoid: $y = A\sin(\pi kx)$

FIGURE 1.14: Isolated track defects IV

- IAL, *Immediate Action Limit*. When exceeded, urgent activities must be done to lower the derailment risk.
- IL, *Intervention Limit*. When exceeded, corrective actions should be applied to avoid the IAL limit in future inspections.
- AL, *Alert Limit*. When exceeded, the railroad track should be analysed for proper corrective decisions.

For instance, if vehicles speed is between 160 km/h and 230 km/h, the IAL limit of categories D1 and D2 (D3 does not account for safety but passengers comfort) are:

- D1: 20 mm (cross level),
  12 mm (alignment)
- D2: 33 mm (cross level),
  24 mm (alignment)

Concerning other track safety regulations, one can find for the *British Railways* indexes for comfort and smoothness of railroad vehicles [24]. Likewise, the european EN 12299 [1] gathers indexes for passangers comfort of railroad vehicles. Furthermore, for *The Association of American Railroad*, the regulation "Track safety standards" [64], specifies what railroad vehicles cannot exceed for safety or comfort issues. These parameters are:

- Wheel vertical load:
  Never under 10% of static load
- Roll angle of passengers car:
  Lower than 6^{o}
- Vertical acceleration of passengers car:
  Lower than $0.6g$ (g =acceleration of gravity)

1.3 Modeling railroad vehicle dynamics

Analysis and simulation of vehicle dynamics is one of the fields of study in the Multibody System Dynamic approach (MSD). As said at the beginning of the chapter, the strategy of trying and error with a noticeable number of real prototypes is a habit of learning from the past. The cost savings that computer simulations provide is of major importance while experiments with real prototypes are set aside to a minimum for

validation purposes. However, when vehicle analysis deal with railroad systems, it is first advisable to determine two well-known features for proper computer simulations: the vehicle is guided along the rails and huge contact forces produced in small contact areas arise in the wheel/rail contact scenario. This causes that a general procedure to account for MSD needs to be enhanced by capable and remarkable specific modeling characteristics before it can be used in railroad vehicles.

The interaction between railway vehicles and track has been of interest in many investigations. It is a complex dynamical system in engineering because it can be defined by many bodies and thus, it may include many degrees of freedom. In addition, these bodies can be interconnected in numerous ways and then, coupled to the ground by the complex and non-conservative phenomena of the wheel/rail contact. It was in the early 20^{th} century when Carter [8] presented the first realistic model of the lateral dynamics of a railway vehicle. He later introduced the effect of conicity and, by extending Hertz's theory of elastic contact, the concept of creep in the rolling stock whose combination could lead to a lateral dynamic instability [9], which can nowadays be referred as *hunting*. This instability arised from the pure kinematic description of conical wheelsets with square rails proposed by Klingel [46]. Nevertheless, as Carter's analysis required complex arithmetic together with the fact that railroad engineers were skeptical in that time, not many more research contributions were developed during the successive 20 years.

In the 1950s, research investigations started to focus on the instability of railroad vehicles and began to account for the suspension stiffnesses. It was after the competition held by the Office for Research and Experiments (ORE), when Matsudaira [14] developed a stability chart of a model, in which longitudinal and lateral suspension elements act between wheelsets and frame by using the principles of eigenalue analysis. This determined the essential factors of analytical models of lateral dynamics of railroad vehicles. In 1963, de Pater [12] studied a complete vehicle with many degrees of freedom following the creep analysis of Carter and assuming that the contact area is circular.

Nonetheless, it was Kalker [38] who applied the creep analysis to a general case and giving years later, a detailed and a simplified solution for the three dimensional problem with random creepages and perfect elastic bodies, which can be found respectively in [39] and [41].

However in the mid 1960s, Wickens at the Brithis Rail Research department (BRR) in Derby, determined comprehensive features of the behaviour of a simple wheelset, deducting that it is able to convert energy from the forward motion into energy for the lateral motion [106]. It was then realised the importance of the suspension elements in the study of the stability of railroad vehicles. In addition, the angular motion of a wheelset around the normal vector to the contact plane, called the *spin*, started to be accounted for in the equations and showing a reduced influence of gravitational stiffness and leading to full-scale experiments, as those developed in [26], where a complete hunting limit cycle was detected. Here, two impediments were challenged: the complexity of the wheel/rail geometry and the existence of creep saturation.

Once the stability analysis of railroad vehicles was generally acepted, researchers started to focus on curve negotiation and dynamic response due to track geometry. With regard to curving, the first linear theories appeared in 1969 independently by Newland [60] and Boocock [7], the latter one being validated with experimental results. In these linear theories, there exists a great correlation when large radius curves where considered because their main assumptions relied on neglecting spin creepage, gravitational stiffness and wheelset roll. It was not until 1977 when it was developed a nonlinear approach for railroad vehicles in curves by Elkins and Gostling [17]. In this work, the contact patch moves and changes in size and shape from the tread to the flange considering only one contact point while the matematical aspects of the two points contact scenario were not considered until the 1990s [65]. On the other hand, regarding railroad dynamic responses due to track geometry one can refer to the work presented by Jenkins et al. in 1974 [37] where the vertical response of a railroad vehicle was studied passing over a dipped joint and identifying two different transients related to the track

stiffness and rail mass. It was later in the 1980s, when track irregularities started to be studied as a stochastic process and research work was published in that field, as the one presented by Clark et al. [10]. Then, the concepts of passenger comfort and ride quality arised and international standards were first defined. Furthermore, in the BRR, the first evaluation of track irregularities was carried out in [25] by applying the power spectra density approach and resulting in power spectra of track irregularities that were later used for future designs.

It was by the 1970s when efficient methods of computation became accessible to be applied at complicated and nonlinear railroad vehicle models. They first started as a specific problems whose equations of motion were manually calculated and integrated into computer programs to determine stability analysis or curve negotiation. This lead to a change in the way railroad vehicles were designed as a function of the results of dynamic simulations and consequently, complete simulation packages started to appear. They were first reviewed in the 1990s by Schiehlen [87] and by Kortum [48] who identified a great variation of their degree of generality in them. In the most general case, those packages called *multibody* programs, where those in which a general vehicle model with the theory and basis of the MBD approach could be simulated. Others involve different formulations of the equations of motions, use a set of minimal generalized coordinates or treat the constraints associated with the motion in alternative ways. The majority of them have evolved to the current days with a great capability in solving the non-linearities of railroad vehicles together with their interaction to the track. Some well-known simulation packages can be listed as:

- SIMPACK MBS Software [81, 88]
- MSC ADAMS/Rail Software [56, 83]
- VAMPIRE DeltaRail [73]
- NUCARS Software [45]

- GENSYS Rail [15]
- ROBOTRAN [23]
- SAMS/2000 [90]

Nevertheless, specific and accurate dynamic analysis of any type of rail-guided vehicles demands accurate description of track geometry together with specialized and unique computer subroutines in order to perform customized tasks. This is usually common in the railroad research field, where not only the vehicle design is the main scope of the study. That is the reason why many of these computer packages are generally adapted to user-defined subroutines. However, even when a software is capable of receiving user-defined subroutines, they are not commonly user-friendly and it is not possible to access to the source code, mainly due to licenses issues. As a consequence, many recent research work has been done with independent programs coded individually by researchers for their particular case of study. In this sense, in the work of Escalona et al. [21], there is a extense review of the research trends in the field of multibody dynamics for railroad vehicles, specially focused on high-speed trains.

When modeling the dynamics of railroad vehicles, one has to consider the high computational cost that solving all the non linearities of the multibody system entails. As a summary, computational cost depends on the model of study, on how the equations of motion are formulated, how they are integrated forward in time and how it is all implemented [11]. Paying attention to the model of study, one can realize that the highest computational cost derives from the solution of the wheel/rail contact problem.

In Multibody Dynamics, the wheel/rail contact problem is assumed to occur in a single point where the normal and tangential contact forces are applied. In this context, it can be solved in three steps: first, it has to be determined the solution of the contact geometry in order to find the position of the contact points. Secondly, it is computed the relative velocities and creepages at the contact point using the kinematic description

of the system. Finally, using contact mechanics, contact forces are calculated. With regard to the geometry, wheel/rail contact can be classified as a non-conformal contact, which means that the geometry of the bodies in contact in the vicinity of the contact area is smooth and the curvatures of both surfaces are different such that Hertz contact theory applies. In this sense, the non-conformal contact can be simulated using one of these two well-known basic procedures: the *Constraint Method* (also called Rigid Contact Method) and the *Elastic Method* (also known as Penalty Method).

On the one hand, in the Constraint Method contact is assumed to occur in a single point in each body that occupies the same position in space, and it is guaranteed by the use of kinematic constraints. Also, there are surface parameters that define the position of the contact points and they are part of the system coordinates. Here, normal contact forces are calculated as reaction forces associated with the contact constraints. However, as the contact points occupy the same position in both bodies by the kinematic constraints, the numeric simulation of this approach can lead to difficulties when accounting for the separation of bodies. On the other hand, in the Elastic Method the contact point in each body can occupy a different position in space, allowing to occur indentation (this is, penetration between bodies in contact). As a consequence, it requires a contact search algorithm to identify the position of the contact points within the surface of each body in contact. Here, the normal contact force is a function of the indentation and velocity of indentation and as the contact points occupy different position in space, the simulation of bodies separation can very easily be implemented.

One of the first works that employed the constraint approach was published in 1988 by de Pater [13]. He considered a wheelset on a rigid track using four degrees of freedom (DOFs) to then, apply the first-order theory to reduce the problem to four equations with four variables. More modern, in Shabana et al. [92], an augmented formulation for mechanical systems with non-generalized coordinates is applied to general rigid body contact to then, be implemented in the wheel/rail contact defining the wheel and rail surfaces as a function of four non-generalized parameters (*surface parameters*) [91] and

imposing as contraints that the contact point in the wheel surface occupies the same position as the contact point in the rail surface and that the tangent plane to the contact point in the wheel is parallel to the tangent plane to the rail at the contact point. This is developed by five constraints equations. Therefore, as there are only four surface parameters, the constraint contact approach eliminate one DOF.

The Elastic Method has also been widely used in the literature. For instance, Kik and Steinborn [43] developed a primary work of this approach where the location of the contact points was reduced to a two-dimensional problem. Later Shabana et al. [94, 95] introduced a methodology to account for the rail arc length trajectory coordinate traveled by the wheelset in order to evaluate the position in which the plane that contains the contact points lies. Knowing this plane, the position of the contact points is reduced to a two-dimensional problem. Other works related to the Elastic Method can be found in [67, 68] where a general formulation for an accurate prediction of independent contact points, both in the wheel tread and flange and with the possibility to remain in different planes, is proposed.

In terms of computational efficiency, the location of the wheel/rail contact points in the solution of the contact problem, is one of the most demanding operations that has to be carried out when railroad vehicles are simulated and that is the reason why several numerical procedures have been published for an efficient and accurate prediction of them in the literature. In general, the search of the contact points can be done in two ways: the *online* and the *offline* approach. In the *online* approach, the search of the contact points is done "online", which means that it is accounted for throughout the numeric simulation by solving the geometric equations that govern both the rigid or the elastic contact. In the *offline* approach, the solution of the contact points is computed in a preprocessing stage and stored in a table called *contact look-up table*. A wheel/rail contact lookup table has solutions for specific wheelset positions relative to the track and can have their spatial derivatives and other geometric data associated with the contact points that are needed for the numerical simulations. Also, in these tables,

the influence of track irregularities can be accounted for by increasing the number of independent variables, whose number depends on the elastic or rigid method proposed together with the simplifications assumed.

In relation to the online approach for the contact point detection, many numeric procedures have been proposed in the literature. In [94], an optimized approach for searching all possible contact points in which each candidate point is grouped into a region of penetration called batch, is presented. Also, in [93], four different nonlinear dynamic formulations for the analysis of the wheel/rail contact using both the elastic and rigid approach, are discussed. In [54], Malvezzi et al. presented two semi-analytic procedures for the contact point detection between wheel and rail and based on the known analytic expressions of the surfaces in contact. In [2], one of these efficient semi-analytic methods is implemented in which an analytical reduction to a simple scalar equation is achieved for computational efficiency purposes. Furthermore, Sugiyama et al. [101], presents a numerical procedure based on the constraint formulation where tread, flange and back-of-flange contacts are allowed to evaluate.

With regard to the offline approach for the contact point detection, the concept of the previously defined contact lookup table arises. Schupp et al. [89], proposed a *quasi-elastic* contact model that accounts qualitatively for the elastic deformation of the contact interface and approximates by two-dimensional splines the contact solution, whose coefficients are stored as a table in a pre-processing step. This model has been implemented in the already defined simulation package Simpack MBS [81]. Other works using the lookup table approach are those presented in [19, 55, 85, 100]. In Malvezzi et al. [55], the compass search together with the simplex numerical algorithm is used for the point detection, which is based on an analytical procedure that runs offline. Santamaría et al. [85] developed a procedure that accounts for the elastic contact in a lookup table approach. Here, four initial DOFs define the relative position of the wheelset with respect to the rail that are later reduced to three DOFs with the assumption that the

contact point lies on radial sections at the wheel. Using an optimal number of discretized positions and the symmetric property of the problem, a reduced-size with 3 DOFs lookup table is obtained. Additionally to the offline approach, Sugiyama et al. [100] developed a hybrid procedure to account for the contact points both online and offline, in which a lookup table is used for evaluating the candidate points in the wheel tread while an iterative search is employed for predicting flange contact.

When evaluating the wheel-rail contact points, it is of major importance to include the effect of track irregularities, since its locations are highly influenced by these defects. In addition, track irregularites are the main responsible for the railroad vehicle dynamic response as it has been the scope of many research work in the literature [4, 37, 49, 50, 61, 63, 99]. The vehicle response to track irregularities cannot be studied independently apart from the vehicle itself. As presented by Luber [53], there is no representative correlation between the track geometry regulation EN-13848-5 [71] and the vehicle response since different vehicles can manifest a completely different dynamic behaviour when affected by the same track irregularities. That is the reason why each railroad vehicle must be analyzed running on the permissible track defects. In the works of Li et al. [51] and Berggren et al. [4], it is shown by simulation purposes, the need of evaluating track quality in terms of the track defects and vehicle response.

The consideration of track irregularities in the wheel/rail contact problem using contact lookup tables is a difficult but challenging task. Notwithstanding it alows a great reduction in the computacional cost of searching the contact points, it also augments the number of independent variables or entries to the table and therefore, not many research work has been done in that field, which is one of the goals of this thesis.

Moreover, as the computational efficiency of proposed models increased together with computer performance, MBS simulations in the real-time domain became important. Rulka and Pankiewicz [82] presented the transition from offline MBS models to real-time ones by turning the differential algebraic equations of motion into ordinary differential equations. Kim and Jeong [44], proposed a synthesis method based on the generalized

coordinate partitioning method [105], where an approximate function approach is used for a real-time MB model of a full car. Also, Meli et al. [57] presented a detailed real-time three-dimensional model of the dynamics of a railway vehicle running on a generic track for Hardware In the Loop (HIL) systems.

Finally, the use of prototype vehicles for the investigation of railway vehicle dynamics has been necessary in the railroad industry. Even with the previous improvement in simulation techniques, the possibility to validate simulating results with experimental data is always of great interest. Examples of railroad vehicle prototypes in the literature are mainly focalized into roller rigs for wheelsets or bogie vehicles, as those presented in [108], [35] or [30], although full railroad vehicles have also been used. Regardless of the high economic costs that the use of experimental tests involve, its application has been useful and advantageous in the railroad research field.

1.4 Outline of the thesis

The contents of this thesis are summarized as follows:

- **Kinematics and dynamics of railroad vehicles**. In this chapter, the formulation of the equations of motion for railroad vehicles based on the Track Frame formulation (TF) are presented. The kinematic description of railroad vehicles is first described and then, the dynamic formulation of the system, which is based on the Newton - Euler equations of rigid bodies, defined. Here, the different reference frames that allow a systematic and efficient formulation of wheelsets kinematics are introduced. Also the procedure to develop a contact *lookup table* that accounts for track irregularities is derived. Finally, some kinematic assumptions that allow a simplification in the equations of motion are proposed.

- **Design and testing**. The design of a 5-inch scaled railroad vehicle is presented together with their parameter identification. The vehicle, which is formed by

four wheelsets, two bogie frames and a carbody, is assembled by 24 springs and four dampers. Three different inertial measurement units (IMU) are installed at the wheelset, frame, and carbody plane to account for the dynamic behaviour of primary and secondary suspensions. In addition, two distance lasers measure the vertical deflection of these two suspensions. Moreover it is presented the experimental procedure followed to account for track irregularities in the 5-inch railroad track and the analytical scheme derived in order to obtain the reference and irregular geometry of it.

- **Numerical modeling**. In this chapter, the multibody model of the scaled vehicle is presented. Mass and inertia properties are described and simulated on the measured 5-inch track. The proposed model is simulated at the variable forward velocity measured at the experimental test. The definition and implementation of this variable forward velocity constraint is also derived. Furthermore, it is presented a brief summary of the track preprocessor used to implement the ideal and irregular measured track.

- **Numerical results and comparison**. The results obtained in the experimental tests and those obtained in the numeric simulations, both with the non-linearized and linearized kinematics, are shown, compared and discussed.

- **Closure**. Finally, a brief chapter is included to give a summary and conclusions of the work as well as some topics that could continue the current investigation and results.

Chapter 2

Kinematics and Dynamics of Railroad Vehicles

2.1 Introduction

The work developed in this thesis is based on the Track Frame formulation (TF). The TF formulation is quite typical in the description of ground vehicles and it is characterized by a moving frame of reference in which the bodies' description are referred to it [70, 78]. This allows a better understanding of the bodies' coordinates when compared to a global method, in which all coordinates are referred with respect to the inercial frame, specially when simulations accounts for different track topologies. It also has the capability to achieve appropriate eigenvalue analysis and the consideration of the flexibility of the track [75, 76]. There are different formulations where a moving reference frame is used. Some of them [96] use only one moving frame that accompanies the vehicle movement. In those formulations the definition of the bodies coordinates is referred with respect to the moving frame. However, there are others where there is a moving reference frame for each body of the system [47] involving the initial disadvantage of computing a set of track calculations for every body in the system.

The procedure presented in this work is a combination of both approaches. On the one hand, it accounts for a main moving frame called Track Frame (TF) where all bodies' coordinates are referred to it, but on the other hand, it also accounts for a set of special trajectory frames for wheelset bodies that are usefull for the kinematic description of wheelsets with the use of pre-calculated contact lookup tables.

This chapter is organized as follows: in Section 2.2 it is defined the kinematics of the TF formulation and how it is applied to railroad vehicles. Section 2.3 shows the applied dynamics to railroad vehicles. The procedured derived to create a contact lookup table that accounts for track irregularities is shown in Section 2.4 and Section 2.5 shows a linearization of equations of motion subject to be used in numeric simulations.

2.2 Kinematic formulation of railroad vehicles

2.2.1 Notation

Before the definition of the kinematics of railroad vehicles, it is basic to state a clear description of the employed notation. As it will be shown in the following sections, there are a considerable number of reference frames involved in the formulation that can be confusing and easy to mislead, particularly when position vectors are used. For this reason, it is left to the reader to return to this section for a complete understanding of any position vector symbol, superscript or overline presented throughout this work.

Position vector symbols: (see Fig. 2.1)

- **R**: Position vector $\vec{R}$ which origin coincides with the GF
- **r**: Position vector $\vec{r}$ which origin coincides with the TF
- **u**: Position vector $\vec{u}$ which origin coincides with the BF, WF and WIF
- **w**: Position vector $\vec{w}$ which origin coincides with the BTF and WTF

where GF: Global Frame; TF: Track Frame; BF: Body Frame; WF: Wheelset Frame; WIF: Wheelset Intermediate Frame; BTF: Body Track Frame; WTF: Wheelset Track Frame; RHF: Rail-Head Frame.

Note that as explain later, for a better understanding of figures, the WF and WTF coincide with the BF and BTF respectively when the body is a wheelset.

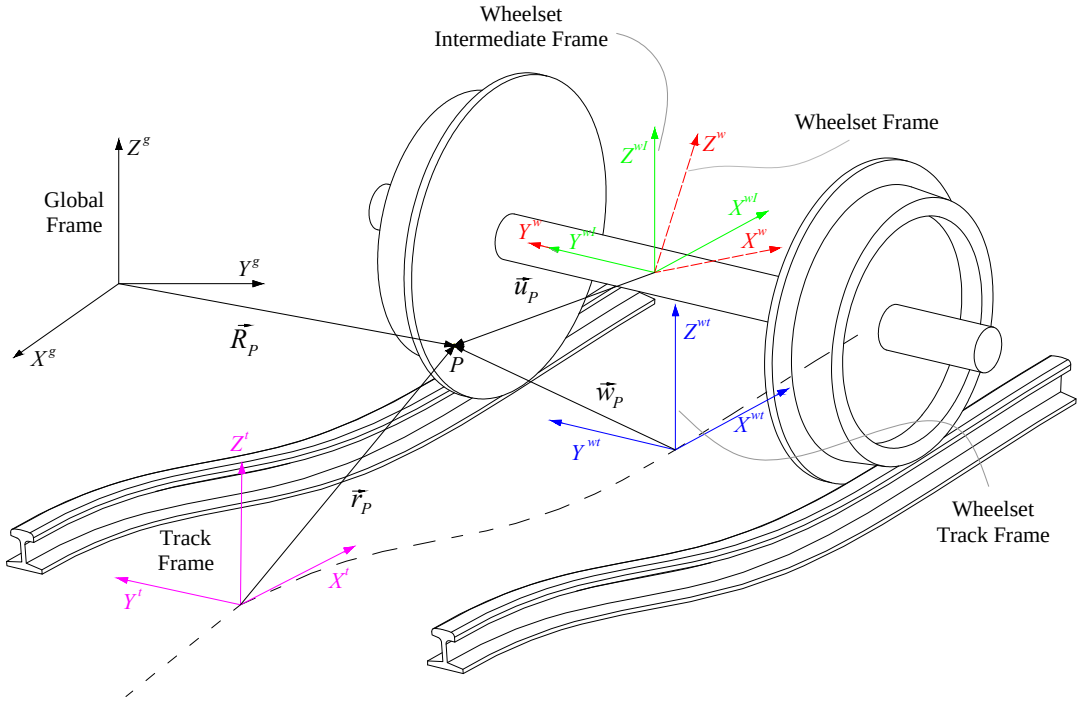

FIGURE 2.1: Position vector symbols of an arbitrary point P

Superscripts:

- g: The magnitude refers to the GF
- t: The magnitude refers to the TF
- bt: The magnitude refers to the BTF
- wt: The magnitude refers to the WTF
- wI: The magnitude refers to the WIF

- w: The magnitude refers to a WF
- rh: The magnitude refers to a RHF
- i: The magnitude refers to BF i
- j: The magnitude refers to BF j

Note: superscripts separated by a comma (i.e. 't, i') refer to the second superscript with respect to the first one. This is, in the case of the transformation matrix $\mathbf{A}^{t,i}$, superscript 't, i' refers to the transformation matrix of Body Frame i with respect to the Track Frame.

Overlines:

- Bold symbols withouth overline, like $\mathbf{r}$, mean that the column matrix that contains the components of the position vector $\vec{r}$ are given in the GF.
- Bold symbols with 'bar' overline, like $\bar{\mathbf{r}}$, mean that the column matrix that contains the components of the position vector $\vec{r}$ are given in the TF.
- Bold symbols with 'hat' overline, like $\hat{\mathbf{r}}$, mean that the column matrix that contains the components of the position vector $\vec{r}$ are given in the BF (which is the WF for wheelset bodies).
- Bold symbols with 'arc' overline, like $\widehat{\mathbf{r}}$, mean that the column matrix that contains the components of the position vector $\vec{r}$ are given in the BTF (which is the WTF for wheelset bodies).
- Bold symbols with 'inverted arc' overline, like $\breve{\mathbf{r}}$, mean that the column matrix that contains the components of the position vector $\vec{r}$ are given in the WIF.

2.2.2 Kinematics of the track frame

As the TF runs along the centerline of the railroad track geometry and the coordinates are defined with respect to it, it is essential to generate the necessary information of the motion of this frame of reference with respect to an inertial frame in order to set up the equations of motions. In the movement of the TF $[O^t(X^tY^tZ^t)]$, it is assumed to keep its axis X^t tangent to the track centerline. The arc length along the track centerline traveled by the TF is denoted as s^t and it is the input together with its first and second time derivatives for the so-called "track preprocessor" that generates such a necessary information of the motion of the TF (see Chapter 4). The track preprocessor gives, for each arc length, the position and orientation of the TF and geometric vectors and matrices that are needed to set up the equations of motion. Figure 2.2 shows a vehicle body in an arbitrary position.

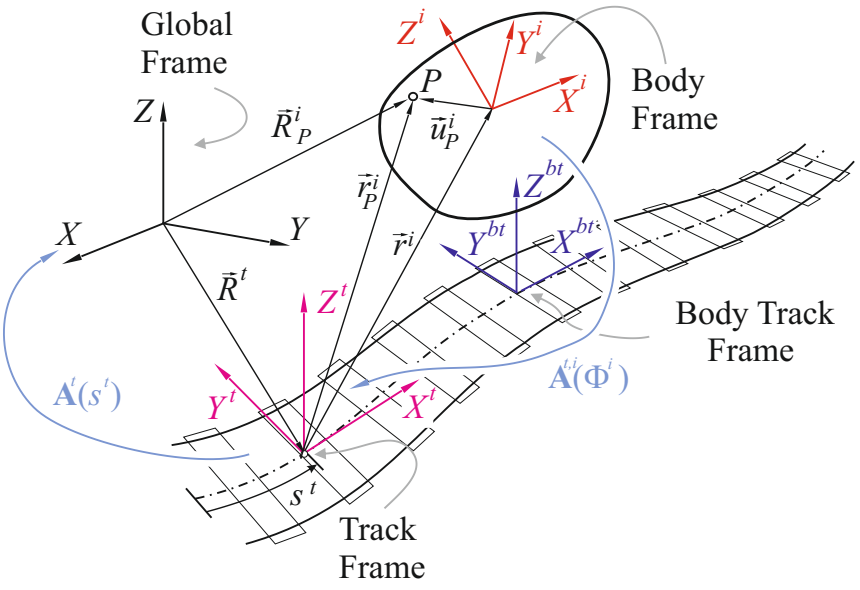

FIGURE 2.2: Kinematics of an arbitrary body in the TF formulation

The coordinates that describe the position of the origin and orientation of the TF with respect to the GF are:

$$\mathbf{q}^t = \begin{bmatrix} x^t & y^t & z^t & \varphi^t & \theta^t & \psi^t \end{bmatrix}^T, \tag{2.1}$$

where $\mathbf{R}^t = [\ x^t \quad y^t \quad z^t\ ]^T$ is the position vector of the origin of the TF O^t with respect to the GF and $\mathbf{\Phi}^t = [\ \varphi^t \quad \theta^t \quad \psi^t\ ]^T$ is a set of three Euler angles that describe the orientation of the TF with respect to the GF. The coordinates of the TF are known functions of the track centerline geometry, this is $\mathbf{q}^t = \mathbf{q}^t(s^t)$.

The orientation of the TF with respect to the GF is defined using a set of three consecutive rotations applied to the GF that make it parallel to the TF. Applying the *right-hand* rule, these consecutive rotations start with the yaw angle ψ^t about the positive direction of axis Z^g, followed by a pitch rotation θ^t about the negative direction defined by the rotated axis Y', and followed by a roll rotation φ^t about the negative direction defined by the rotated axis X''. The use of *negative* rotations is necessary to be consistent with the angles usually defined in the railway industry. Therefore, the rotation matrix of the TF with respect to the GF $\mathbf{A}^t$ is given as the product of the three consecutive rotation matrices $\mathbf{A}^t = \mathbf{A}^t_\psi \mathbf{A}^t_\theta \mathbf{A}^t_\varphi$ by:

$$\mathbf{A}^t = \begin{bmatrix} \cos\psi^t & -\sin\psi^t & 0 \\ \sin\psi^t & \cos\psi^t & 0 \\ 0 & 0 & 1 \end{bmatrix} \begin{bmatrix} \cos\theta^t & 0 & -\sin\theta^t \\ 0 & 1 & 0 \\ \sin\theta^t & 0 & \cos\theta^t \end{bmatrix} \begin{bmatrix} 1 & 0 & 0 \\ 0 & \cos\varphi^t & \sin\varphi^t \\ 0 & -\sin\varphi^t & \cos\varphi^t \end{bmatrix} \tag{2.2}$$

From a kinematic point of view, it is also relevant to define the matrix that linearly relates time derivatives of the the Euler angles to the angular velocity vector of the track frame $\boldsymbol{\omega}^t$. This relation is written as [90]:

$$\boldsymbol{\omega}^t = \mathbf{G}^t \dot{\mathbf{\Phi}}^t, \tag{2.3}$$

where $\dot{\mathbf{\Phi}}^t = [\ \dot{\varphi}^t \quad \dot{\theta}^t \quad \dot{\psi}^t\ ]^T$, and $\mathbf{G}^t$ is a function of the Euler angles that can be written as:

$$\mathbf{G}^t = \begin{bmatrix} -\cos\psi^t\cos\theta^t & \sin\psi^t & 0 \\ -\cos\theta^t\sin\psi^t & -\cos\psi^t & 0 \\ -\sin\theta^t & 0 & 1 \end{bmatrix} \tag{2.4}$$

This allows the definition of the absolute angular velocity of the TF as a function of the arc length and its first time derivative. This is, $\boldsymbol{\omega}^t = \boldsymbol{\omega}^t(s^t, \dot{s}^t)$

2.2.3 Kinematics of an arbitrary body

Every body in the system has its own body frame of reference (BF), which is located and orientated with respect to the TF (see Fig.2.2). For a body i, its position and orientation with respect to the TF is given by:

$$\mathbf{q}^i = \begin{bmatrix} x^i & y^i & z^i & \varphi^i & \theta^i & \psi^i \end{bmatrix}^T, \tag{2.5}$$

where $\bar{\mathbf{r}}^i = [\ x^i \quad y^i \quad z^i\ ]^T$ and $\mathbf{\Phi}^i = [\ \varphi^i \quad \theta^i \quad \psi^i\ ]^T$. Following the definitions presented in Section 2.2.1, $\bar{\mathbf{r}}^i$ is the position vector of the origin of the BF with respect to the TF given by its components in the TF while $\mathbf{\Phi}^i$ is the set of three Euler angles that describe the orientation of the BF with respect to the TF.

The orientation of the BF with respect to the TF is defined using a set of three consecutive rotations applied to the TF that make it parallel to the BF. If applying the *right-hand* rule, these consecutive rotations start with the yaw angle ψ^i about the positive direction of axis Z^t, followed by a roll rotation φ^i about the rotated axis X', and followed by a pitch rotation θ^i about the rotated axis Y''. In this case it is convenient to leave the pitch rotation (the *largest* angle rotated by the wheelsets) as the last one. Consequently, the rotation matrix of the BF with respect to the TF $\mathbf{A}^{t,i}$, is given as

the product of the three consecutive rotation matrices $\mathbf{A}^{t,i} = \mathbf{A}^i_\psi \mathbf{A}^i_\varphi \mathbf{A}^i_\theta$ by:

$$\mathbf{A}^{t,i} = \begin{bmatrix} \cos\psi^i & -\sin\psi^i & 0 \\ \sin\psi^i & \cos\psi^i & 0 \\ 0 & 0 & 1 \end{bmatrix} \begin{bmatrix} 1 & 0 & 0 \\ 0 & \cos\varphi^i & -\sin\varphi^i \\ 0 & \sin\varphi^i & \cos\varphi^i \end{bmatrix} \begin{bmatrix} \cos\theta^i & 0 & \sin\theta^i \\ 0 & 1 & 0 \\ -\sin\theta^i & 0 & \cos\theta^i \end{bmatrix} \tag{2.6}$$

According to Fig.2.2, the position vector $\mathbf{R}^i_P$ of an arbitrary point P of body i with respect to the GF is given by:

$$\mathbf{R}^i_P = \mathbf{R}^t + \mathbf{A}^t \bar{\mathbf{r}}^i_P, \tag{2.7}$$

where $\mathbf{R}^t$ is the position vector of the TF, and $\bar{\mathbf{r}}^i_P$ is the local position vector of the arbitrary point P on body i with respect to the TF. The latter one can be written as:

$$\bar{\mathbf{r}}^i_P = \bar{\mathbf{r}}^i + \mathbf{A}^{t,i} \hat{\mathbf{u}}^i_P, \tag{2.8}$$

in which $\hat{\mathbf{u}}^i_P$ is the local position vector of the arbitrary point P in body i with respect to its BF.

From the kinematic point of view, as shown in the preceeding subsection 2.2.2, it is convenient to define the linear relation on Euler angles derivatives that makes possible to obtain the bodies angular velocity with respect to the TF $\boldsymbol{\omega}^{t,i}$. This expression can be writen as:

$$\boldsymbol{\omega}^{t,i} = \mathbf{G}^{t,i} \dot{\boldsymbol{\Phi}}^i, \tag{2.9}$$

where $\dot{\mathbf{\Phi}}^i = [\ \dot{\varphi}^i \quad \dot{\theta}^i \quad \dot{\psi}^i\ ]^T$, and $\mathbf{G}^{t,i}$ is the well-known matrix function of trigonometric functions of the angular generalized coordinates of body i:

$$\mathbf{G}^{t,i} = \begin{bmatrix} 0 & \sin\psi^i & -\cos\psi^i\cos\theta^i \\ 0 & -\cos\psi^i & -\sin\psi^i\cos\theta^i \\ 1 & 0 & -\sin\theta^i \end{bmatrix} \tag{2.10}$$

Equation 2.9 can also be written to obtain the body angular velocity relative to the TF with its components in the BF. This expression takes the form:

$$\hat{\boldsymbol{\omega}}^{t,i} = \mathbf{A}^{t,i^T}\mathbf{G}^{t,i}\dot{\mathbf{\Phi}}^i = \hat{\mathbf{G}}^{t,i}\dot{\mathbf{\Phi}}^i \tag{2.11}$$

2.2.4 Wheelset kinematics

Once the kinematics of the TF and the kinematics of an arbitrary body in the TF formulation have been defined, the next step is the definition of the different frames used for an easy and efficient implementation of the equations of motion of railroad vehicles.

For wheelset bodies, three differente frames are introduced (see Fig.2.3) namely:

1. **Wheelset body Frame**, (WF): $[O^w(X^wY^wZ^w)]$.
   This is equivalent to the BF, whose orientation with respect to the track frame is given by the Euler angles $\mathbf{\Phi}^w = [\ \varphi^w \quad \theta^w \quad \psi^w\ ]^T$.

2. **Wheelset Intermediate Frame**, (WIF): $[O^{wI}(X^{wI}Y^{wI}Z^{wI})]$.
   This frame is the result of rotating the WF the pitch angle θ^w about the common Y^w axis. This is, the WF that shows no pitch rotation and whose orientation coordinates with respect to the TF are given by: $\mathbf{\Phi}^{wI} = [\ \varphi^w \quad 0 \quad \psi^w\ ]^T$.

3. **Wheelset Track Frame**, (WTF): $[O^{wt}(X^{wt}Y^{wt}Z^{wt})]$.
   This is a frame that accompanies the wheelset along the track centerline, as the

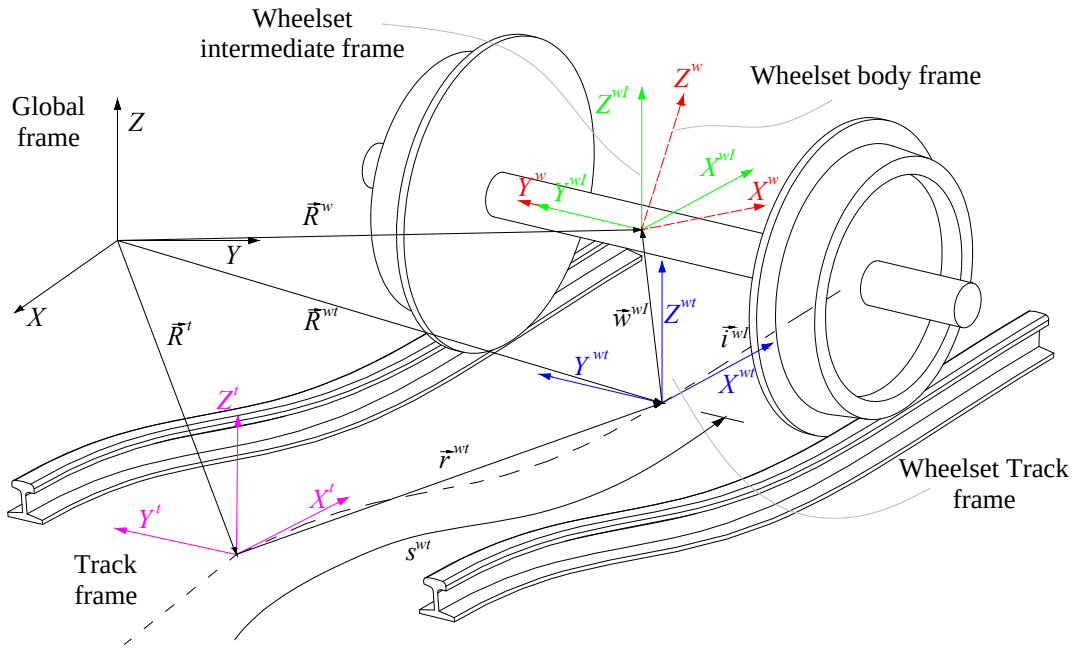

FIGURE 2.3: Different frames used for wheelset bodies

TF does, but keeping the wheelset longitudinal x-coordinate equal to zero. Its precise definition of position and orientation is explained next.

The definition of the WTF is convenient for the numerical treatment of the wheel-rail contact with lookup tables, as will be shown in Section 2.4. In order to find the position and orientation of the WTF, an arc-length parameter s^{wt} has to be associated at any time with each wheelset. This parameter is the arc length along the track centerline of the WTF. Given the coordinates of the WF $\mathbf{q}^w$, and the TF $\mathbf{q}^t$, the calculation of s^{wt} requires the solution of the following non-linear algebraic equation:

$$\mathbf{i}^{wI}\left(s^{wt}\right)^T\left(\mathbf{R}^w - \mathbf{R}^{wt}\left(s^{wt}\right)\right), \tag{2.12}$$

where $\mathbf{R}^{wt}(s)$ and $\mathbf{i}^{wI}(s)$ are the functions that provide the position and tangent vector of a point in the track centerline given the arc length s. Equation 2.12 states that

the position vector $\widehat{\mathbf{w}}^{wI}$ of the WIF with respect to the WTF is perpendicular to the tangent to the track at the body location. In other words, it states that the position vector has zero x-coordinate in the WTF.

In special cases such as tangent or circular tracks, there is no need to solve Eq. 2.12. One can easily observed that in a tangent track the body arc length parameter s^{wt} coincides with $(s^t + x^w)$, while for a circular track, one can find an analytical expression that provides the value of s^{wt} without solving Eq. 2.12. In other situations, for example when the TF is in a tangent stretch wherears the wheelset is at a transition or curved stretch, Eq. 2.12 has to be solved to find the value of s^{wt}.

Once the wheelset arc-length parameter s^{wt} has been computed, the position of the origin $\bar{\mathbf{r}}^{wt}$ and the transformation matrix $\mathbf{A}^{t,wt}$ from the WTF to the TF can be calculated using the rail preprocessor.

2.2.4.1 Definition of Rail-Head Frame

Implicitly related to the kinematics of a wheelset body for the wheel-rail contact scenario, it is fundamental to describe the Rail-Head Frame (RHF) as the left and right frames (one per rail) defined for each arc-length s in which the railroad track is characterized. The origin of these frames lies in the rail-head centerlines (see Fig. 2.4) and its main feature is to allow the definition of the global position of the rail contact points as it will be shown in Section 2.4.

The global position vector of the RHF both for the left and right rails, $\mathbf{R}_L^{rh}$, and $\mathbf{R}_R^{rh}$, is provided by the rail preprocessor as in the case of the TF and BTF/WTF. This means that solving the non-linear algebraic equation of Eq. 2.12, both left and right RHF frames are obtained as $\mathbf{R}_L^{rh} = \mathbf{R}_L^{rh}(s^{wt})$ and $\mathbf{R}_L^{rh} = \mathbf{R}_L^{rh}(s^{wt})$.

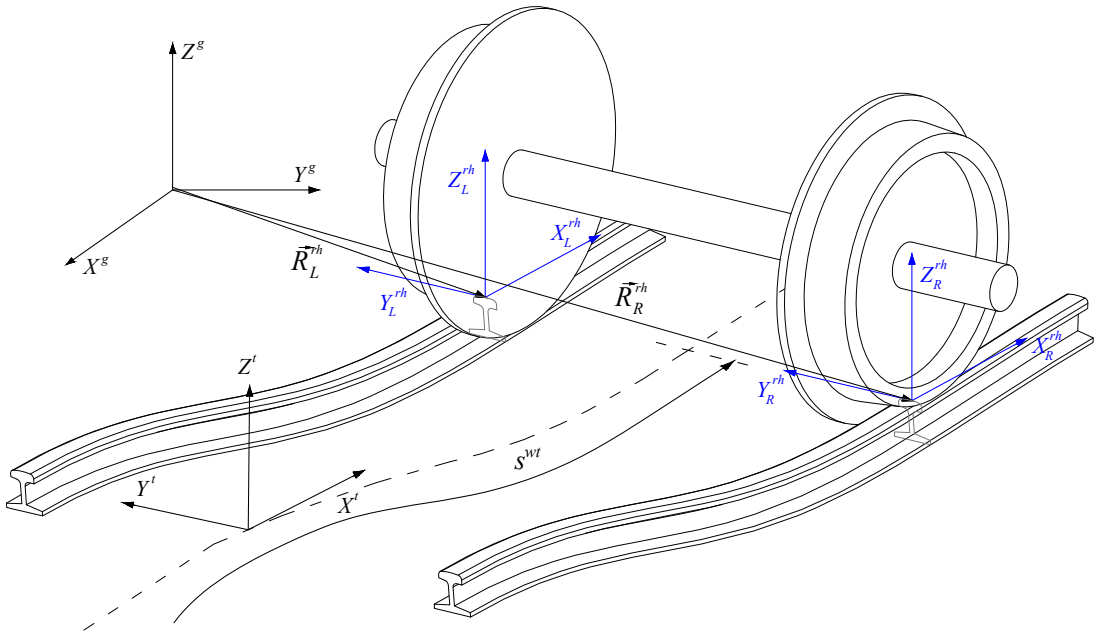

FIGURE 2.4: Rail-Head Frame definition

2.2.5 Velocity and acceleration expressions

In this section, the velocity and acceleration vectors together with the angular velocity and angular acceleration vectors are derived and written in terms of the generalized coordinates that will help in the definition of the equations of motion.

2.2.5.1 Spatial velocity and acceleration of an arbitrary point

As the position of an arbitrary point P of the vehicle body i is defined by Eqs. 2.7 and 2.8, the calculation of the velocity and acceleration vectors of the arbitrary point can be done by differentiating with respect to time. With regard to Eq. 2.7, it yields:

$$\mathbf{R}_P^i = \frac{\partial \mathbf{R}_P^i}{\partial \mathbf{q}^t}\dot{\mathbf{q}}^t + \frac{\partial \mathbf{R}_P^i}{\partial \mathbf{q}^i}\dot{\mathbf{q}}^i = \mathbf{H}_P^{t,i}\dot{\mathbf{q}}^t + \mathbf{H}_P^i\dot{\mathbf{q}}^i, \tag{2.13}$$

where the following jacobian matrices have been identitied:

$$\mathbf{H}_P^{t,i} = \frac{\partial \mathbf{R}_P^i}{\partial \mathbf{q}^t}, \qquad \mathbf{H}_P^i = \frac{\partial \mathbf{R}_P^i}{\partial \mathbf{q}^i}, \tag{2.14}$$

Both matrices $\mathbf{H}_P^{t,i}$, and $\mathbf{H}_P^i$ of Eq. 2.14 are functions of $\mathbf{q}^t$ and $\mathbf{q}^i$, and therefore, the acceleration of point P is obtained as:

$$\ddot{\mathbf{R}}_P^i = \mathbf{H}_P^{t,i}\ddot{\mathbf{q}}^t + \mathbf{H}_P^i\ddot{\mathbf{q}}^i + \mathbf{h}_P^{t,i}\dot{\mathbf{q}}^t + \mathbf{h}_P^i\dot{\mathbf{q}}^i \tag{2.15}$$

where, identifying terms as in the previous equation one as:

$$\mathbf{h}_P^{t,i} = \frac{\partial \dot{\mathbf{R}}_P^i}{\partial \mathbf{q}^t}, \qquad \mathbf{h}_P^i = \frac{\partial \dot{\mathbf{R}}_P^i}{\partial \mathbf{q}^i}, \tag{2.16}$$

As it will be shown in later sections, during the calculation of the vehicle equations of motion, the inertia forces of the vehicle bodies are projected in the TF. To this end, the expression of the absolute acceleration of the center of gravity Gi of body i projected in the TF is needed. This expression takes the form:

$$\ddot{\bar{\mathbf{R}}}_{Gi}^{\,i} = \mathbf{A}^{tT}\ddot{\mathbf{R}}_{Gi}^i = \bar{\mathbf{H}}_{Gi}^{t,i}\ddot{\mathbf{q}}^t + \bar{\mathbf{H}}_{Gi}^i\ddot{\mathbf{q}}^i + \bar{\mathbf{h}}_{Gi}^{t,i}\dot{\mathbf{q}}^t + \bar{\mathbf{h}}_{Gi}^i\dot{\mathbf{q}}^i, \tag{2.17}$$

where

$$\begin{aligned} \bar{\mathbf{H}}_{Gi}^{t,i} &= \mathbf{A}^{tT}\mathbf{H}_{Gi}^{t,i} \qquad & \bar{\mathbf{H}}_{Gi}^i &= \mathbf{A}^{t\,T}\mathbf{H}_{Gi}^i \\ \bar{\mathbf{h}}_{Gi}^{t,i} &= \mathbf{A}^{t\,T}\mathbf{h}_{Gi}^{t,i} \qquad & \bar{\mathbf{h}}_{Gi}^i &= \mathbf{A}^{t\,T}\mathbf{h}_{Gi}^i \end{aligned} \tag{2.18}$$

2.2.5.2 Angular velocity and acceleration of an arbitrary body

For the calculation of the absolute angular velocity of the vehicle body i, the following well-known kinematic relations between the angular velocity and the rotation matrix are used [97]:

$$\begin{aligned} \widetilde{\boldsymbol{\omega}}^i &= \dot{\mathbf{A}}^i \mathbf{A}^{i^T} \\ \widetilde{\hat{\boldsymbol{\omega}}}^i &= \mathbf{A}^{i^T} \dot{\mathbf{A}}^i \end{aligned} \tag{2.19}$$

where $\widetilde{\boldsymbol{\omega}}$ and $\widetilde{\hat{\boldsymbol{\omega}}}$ are the skew-symmetric matrices associated with the absolute angular velocity vector projected in the global frame $\boldsymbol{\omega}$ and body frame $\hat{\boldsymbol{\omega}}$ respectively. Here matrix $\mathbf{A}^i$ refers to the transformation matrix of the BF with respect to the GF and can be calculated as $\mathbf{A}^i = \mathbf{A}^t \mathbf{A}^{t,i}$. In addition, for the time derivative of the rotation matrix $\dot{\mathbf{A}}^i$ the chain rule can be applied.

Alternatively, the absolute angular velocity of the vehicle body i can also be calculated as the sum of the BF angular velocity with respect to the TF plus the angular velocity of the TF with respect to the GF. This expression projected in the BF yields:

$$\hat{\boldsymbol{\omega}}^i = \mathbf{A}^{i^T} \boldsymbol{\omega}^t + \hat{\boldsymbol{\omega}}^{t,i} \tag{2.20}$$

where the angular velocity vectors are extracted from the following skew-symmetric matrices:

$$\begin{aligned} \widetilde{\boldsymbol{\omega}}^t &= \dot{\mathbf{A}}^t \mathbf{A}^{t^T} \\ \widetilde{\hat{\boldsymbol{\omega}}}^{t,i} &= \mathbf{A}^{t,i^T} \dot{\mathbf{A}}^{t,i} \end{aligned} \tag{2.21}$$

As it will be shown in Section 2.3, during the calculation of the vehicle equations of motion, the moment of the inertia forces of the non-wheelset vehicles bodies are projected in the BF. To this end, the expression of the absolute angular acceleration of the non-wheelset body i projected in the BF is therefore needed. This expression takes the form:

$$\hat{\boldsymbol{\alpha}}^i = \dot{\hat{\boldsymbol{\omega}}}^i = \hat{\mathbf{G}}^{t,i}\ddot{\mathbf{q}}^t + \hat{\mathbf{G}}^i\ddot{\mathbf{q}}^i + \hat{\mathbf{g}}^{t,i}\dot{\mathbf{q}}^t + \hat{\mathbf{g}}^i\dot{\mathbf{q}}^i \tag{2.22}$$

where the following jacobian matrices are used:

$$\begin{aligned} \hat{\mathbf{G}}^{t,i} &= \frac{\partial \hat{\boldsymbol{\omega}}^i}{\partial \dot{\mathbf{q}}^t} \qquad & \hat{\mathbf{G}}^i &= \frac{\partial \hat{\boldsymbol{\omega}}^i}{\partial \dot{\mathbf{q}}^i} \\ \hat{\mathbf{g}}^{t,i} &= \frac{\partial \hat{\boldsymbol{\omega}}^i}{\partial \mathbf{q}^t} \qquad & \hat{\mathbf{g}}^i &= \frac{\partial \hat{\boldsymbol{\omega}}^i}{\partial \mathbf{q}^i} \end{aligned} \tag{2.23}$$

However for the vehicle wheelsets, Euler equations are projected in the WIF. This is one of the reasons of the definition of the WIF. In this case, the angular velocity of the wheelset projected in the WIF takes the form:

$$\breve{\boldsymbol{\omega}}^w = \mathbf{A}^{wI\,T}\boldsymbol{\omega}^t + \boldsymbol{\omega}^{wt} \tag{2.24}$$

where as stated in Section 2.2.1, the 'inverted arc' superscrip $\breve{}$ means that the vector components are given in the WIF. Matrix $\mathbf{A}^{wI} = \mathbf{A}^t\mathbf{A}^{t,wI}$ is the rotation matrix from the WIF to the GF thus, the angular acceleration of the wheelset projected in the WIF yields:

$$\breve{\boldsymbol{\alpha}}^w = \dot{\breve{\boldsymbol{\omega}}}^w = \breve{\mathbf{G}}^{w,t}\ddot{\mathbf{q}}^t + \breve{\mathbf{G}}^w\ddot{\mathbf{q}}^i + \breve{\mathbf{g}}^{w,t}\dot{\mathbf{q}}^t + \breve{\mathbf{g}}^w\dot{\mathbf{q}}^w \tag{2.25}$$

where the following jacobian matrices are used:

$$\breve{\mathbf{G}}^{w,t} = \frac{\partial \breve{\boldsymbol{\omega}}^{w}}{\partial \dot{\mathbf{q}}^{t}} \qquad \breve{\mathbf{G}}^{w} = \frac{\partial \breve{\boldsymbol{\omega}}^{w}}{\partial \dot{\mathbf{q}}^{w}}$$
$$\breve{\mathbf{g}}^{w,t} = \frac{\partial \breve{\boldsymbol{\omega}}^{w}}{\partial \mathbf{q}^{t}} \qquad \breve{\mathbf{g}}^{w} = \frac{\partial \breve{\boldsymbol{\omega}}^{w}}{\partial \mathbf{q}^{w}} \tag{2.26}$$

2.3 Dynamic formulation of railroad vehicles

2.3.1 Newton-Euler equations for vehicle bodies

In this section, the equations of motion of railroad vehicles are presented. The obtained equations of motion are based on the Newton-Euler equations of the rigid bodies that comprise the vehicle. In the case of Newton equations, they are projected in the TF in order to achieve clear and intuitive description of the dynamic behavior of the vehicle since it is referred to reference posisitions that the TF has. This definition is done as follows:

$$m^{i}\ddot{\mathbf{R}}^{i}_{Gi} = \bar{\mathbf{F}}^{i} \tag{2.27}$$

where $\ddot{\mathbf{R}}^{i}_{Gi}$ is the acceleration of the center of gravity of body i as given in Eq. 2.17 and $\bar{\mathbf{F}}^{i}$ is the sum of all forces applied to the body projected in the TF. This force vector includes applied forces such as gravity forces, suspension forces, aerodynamic forces and contact forces. It also includes the reaction forces associated with the constraints due to kinematic joints or other assumed rehonomic constraints. With regard to Euler equations, a division must be made between wheelsets and non-wheelset bodies. In case of non-wheelset bodies, Euler equations are projected in the BF because in these cases, the inertia tensor $\mathbf{I}$ remains constant in the BF. This projection is derived as follows:

$$\mathbf{I}^{nw}\hat{\boldsymbol{\alpha}}^{nw} = \hat{\mathbf{T}}^{nw} - \hat{\boldsymbol{\omega}}^{nw} \times (\mathbf{I}^{nw}\hat{\boldsymbol{\omega}}^{nw}) \tag{2.28}$$

where $\hat{\boldsymbol{\alpha}}^{nw}$ and $\hat{\boldsymbol{\omega}}^{nw}$ are the angular acceleration and angular velocity vector as given by Eqs.2.22 and 2.20 respectively, while superscript nw refers to non-wheelset body. $\mathbf{I}^{nw}$ is the inertia tensor of the non-wheelset body in the BF and $\hat{\mathbf{T}}^{nw}$ is the vector sum of moments applied with respect to the center of gravity projected in the BF.

In the case of wheelset bodies, Euler equations are not projected in the BF but to the WIF. This is explained by the definition of the wheel-rail contact that will be shown in further sectios. As the WIF does not experience pitch rotation, a more intuitive description of the wheel/rail contact scenario can be derived if the equations of motion are projected in the WIF. In addition, as the wheelset is a sold of revolution with two planes of symmetry such that $I_x = I_z$, the inertia tensor in the WIF coincides with the inertia tensor in the BF. Therefore, Euler equations projected in the WIF take the form:

$$\mathbf{I}^{w}\breve{\boldsymbol{\alpha}}^{w} = \breve{\mathbf{T}}^{w} - \breve{\boldsymbol{\omega}}^{w} \times \left(\mathbf{I}^{w}\breve{\boldsymbol{\omega}}^{w}\right) \tag{2.29}$$

where $\breve{\boldsymbol{\alpha}}^{w}$ and $\breve{\boldsymbol{\omega}}^{w}$ are the angular acceleration and angular velocity vector as given by Eqs.2.25 and 2.24 respectively. Here superscript w refers to wheelset body. $\mathbf{I}^{w}$ is the inertia tensor of the wheelset body in the WIF and $\breve{\mathbf{T}}^{w}$ is the vector sum of moments applied with respect to the center of gravity projected in the WIF.

Then, the Newton-Euler equations for the vehicle bodies can be written in matrix form as:

$$\begin{bmatrix} m^i\mathbf{1} & \mathbf{0} \\ \mathbf{0} & \mathbf{I}^{ni} \end{bmatrix} \begin{bmatrix} \ddot{\hat{\mathbf{R}}}^{\,i}_{Gi} \\ \hat{\boldsymbol{\alpha}}^i \end{bmatrix} = \begin{bmatrix} \bar{\mathbf{F}}^i \\ \hat{\mathbf{T}}^i \end{bmatrix} + \begin{bmatrix} \mathbf{0} \\ -\hat{\boldsymbol{\omega}}^i \times \left(\mathbf{I}^i\hat{\boldsymbol{\omega}}^i\right) \end{bmatrix} \tag{2.30}$$

where $\mathbf{1}$ is the 3×3 identity matrix that relates the inertia terms of the Newton equations of body i. Equation 2.30 can finally be rearranged as:

$$\mathbf{M}^i_{NE}\mathbf{a}^i = \mathbf{Q}^i_{NE} + \mathbf{Q}^i_{vNE} \tag{2.31}$$

in which $\mathbf{M}^i_{NE}$ is here called the Newton-Euler mass matrix, $\mathbf{a}^i$ is the vector that contains the translational and angular acceleration of the body, which does not coincide with the second derivative of the body coordinates, $\mathbf{Q}^i_{NE}$ is here called the Newton-Euler generalized forces and $\mathbf{Q}^i_{vNE}$ is the Newton-Euler quadratic-velocity generalized inertia forces. Equation 2.30 is also valid for the wheelsets if Euler equation 2.29 is used instead of Eq. 2.28.

Equation 2.31 is the Newton-Euler equations of motion for arbritary or wheelset bodies. However, this equation is not written in terms of the generalized coordinates so, in what follows, the procedure followed the write Newton-Euler equations as a function of the generalized coordinates is explained:

Combining Eq. 2.17 and Eq. 2.25, the vector of accelerations for the case of wheelset bodies is given by:

$$\mathbf{a}^i = \begin{bmatrix} \ddot{\mathbf{R}}^i_{Gi} \\ \hat{\boldsymbol{\alpha}}^i \end{bmatrix} = \begin{bmatrix} \bar{\mathbf{H}}^{t,i}_{Gi} \\ \hat{\mathbf{G}}^{t,i} \end{bmatrix} \ddot{\mathbf{q}}^t + \begin{bmatrix} \bar{\mathbf{H}}^i_{Gi} \\ \hat{\mathbf{G}}^i \end{bmatrix} \ddot{\mathbf{q}}^i + \begin{bmatrix} \bar{\mathbf{h}}^{t,i}_{Gi} \\ \hat{\mathbf{g}}^{t,i} \end{bmatrix} \dot{\mathbf{q}}^t + \begin{bmatrix} \bar{\mathbf{h}}^i_{Gi} \\ \hat{\mathbf{g}}^i \end{bmatrix} \dot{\mathbf{q}}^i \tag{2.32}$$

Note that for the case of non-wheelset bodies, the procedure is similar and straightforward, and in consequence, only the case of wheelset bodies is considered.

Equation 2.32 can be rearranged as:

$$\mathbf{a}^i = \mathbf{L}^{t,i}\ddot{\mathbf{q}}^t + \mathbf{L}^i\ddot{\mathbf{q}}^i + \mathbf{l}^{t,i}\dot{\mathbf{q}}^t + \mathbf{l}^i\dot{\mathbf{q}}^i \tag{2.33}$$

where the 6×6 jacobian matrices $\mathbf{L}^{t,i}$, $\mathbf{L}^i$, $\mathbf{l}^{t,i}$, and $\mathbf{l}^i$ are identified.

Now that the acceleration vector $\mathbf{a}^i$ of body i is written in terms of the generalized coordinates, one can substitute Eq. 2.33 into Eq. 2.31. Rearranging this substitution,

it yields:

$$\mathbf{M}^i_{NE}\mathbf{L}^i\ddot{\mathbf{q}}^i = \mathbf{Q}^i_{NE} + \mathbf{Q}^i_{vNE} - \mathbf{M}^i_{NE}\left(\mathbf{L}^{t,i}\ddot{\mathbf{q}}^t + \mathbf{l}^{t,i}\dot{\mathbf{q}}^t + \mathbf{l}^i\dot{\mathbf{q}}^i\right) \tag{2.34}$$

Finally, premultiplying Eq. 2.34 by $\mathbf{L}^{i^T}$ and rearranging, it leads to the final expression of the Newton-Euler equations of motion written as a function of the generalized coordinates as:

$$\mathbf{M}^i\ddot{\mathbf{q}}^i = \mathbf{Q}^i + \mathbf{Q}^i_v + \mathbf{Q}^i_{TFin} \tag{2.35}$$

where $\mathbf{M}^i$ is the mass matrix of the system, $\mathbf{Q}^i$ is the vector of generalized forces, $\mathbf{Q}^i_v$ is the vector of quadratic velocity inertia forces due to the relative motion of the BF with respect to TF and $\mathbf{Q}^i_{TFin}$ is the vector of inertia forces due to the TF motion. These terms are defined below:

$$\begin{aligned}
\mathbf{M}^i &= \mathbf{L}^{i^T}\mathbf{M}^i_{NE}\mathbf{L}^i \\
\mathbf{Q}^i &= \mathbf{L}^{i^T}\mathbf{Q}^i_{NE} \\
\mathbf{Q}^i_v &= \mathbf{L}^{i^T}\left(\mathbf{Q}^i_{vNE} - \mathbf{M}^i_{NE}\mathbf{l}^i\dot{\mathbf{q}}^i\right) \\
\mathbf{Q}^i_{TFin} &= -\mathbf{L}^{i^T}\mathbf{M}^i_{NE}\left(\mathbf{L}^{t,i}\ddot{\mathbf{q}}^t + \mathbf{l}^{t,i}\dot{\mathbf{q}}^t + \mathbf{l}^i\dot{\mathbf{q}}^i\right)
\end{aligned} \tag{2.36}$$

2.3.2 Equations of motion of unconstrained railroad vehicles

For a general railroad vehicle that accounts for a large number of bodies, there can be mechanical joints and force elements that interconnect them. With regard to mechanical joints such as, revolute, spherical, prismatic or cylindrical joints, they reduce the number of degrees of freedom of the system by imposing constraints, in most cases formulated as a set of nonlinear algebraic equations of the system generalized coordiantes [96]. However, some simplified vehicle models assume that the relative motion of all vehicle bodies is unconstrained being their interaction due to spring-damper suspension elements. For these unconstrained vehicles, the equations of motion are simply

obtained by assempling the equations of motion of the vehicle bodies as given at Eq. 2.35. The equations of motion of the unconstrained vehicle are given by:

$$\mathbf{M}\ddot{\mathbf{q}} = \mathbf{Q} + \mathbf{Q}_v + \mathbf{Q}_{TFin} + \mathbf{Q}_{susp} + \mathbf{Q}_{cntact} \tag{2.37}$$

where the mass matrix $\mathbf{M}$ and force vectors of the railroad system are defined as:

$$\begin{gathered}\mathbf{M} = \begin{bmatrix} \mathbf{M}^1 & & & \\ & \mathbf{M}^2 & & \\ & & \ddots & \\ & & & \mathbf{M}^{nb} \end{bmatrix} \quad \mathbf{Q} = \begin{bmatrix} \mathbf{Q}^1 \\ \mathbf{Q}^2 \\ \vdots \\ \mathbf{Q}^{nb} \end{bmatrix} \\ \mathbf{Q}_v = \begin{bmatrix} \mathbf{Q}_v^1 \\ \mathbf{Q}_v^2 \\ \vdots \\ \mathbf{Q}_v^{nb} \end{bmatrix} \quad \mathbf{Q}_{TFin} = \begin{bmatrix} \mathbf{Q}_{TFin}^1 \\ \mathbf{Q}_{TFin}^2 \\ \vdots \\ \mathbf{Q}_{TFin}^{nb} \end{bmatrix} \quad \mathbf{Q}_{cntact} = \begin{bmatrix} \mathbf{Q}_{cntact}^1 \\ \mathbf{Q}_{cntact}^2 \\ \vdots \\ \mathbf{Q}_{cntact}^{nb} \end{bmatrix}\end{gathered} \tag{2.38}$$

being $\mathbf{Q}$, $\mathbf{Q_v}$, $\mathbf{Q}_{TFin}$, $\mathbf{Q}_{susp}$ and $\mathbf{Q}_{cntact}$, the generalized externally applied forces, cuadratic velocity terms forces, Track-Frame related forces, suspension forces and contact forces respectively, while superscript nb refers to the number of bodies of the system. In the following sections, the calculation of the vector of generalized suspension forces and tangential contact forces are derived.

2.3.3 Generalized suspension forces

The vector of generalized suspension forces generated by a spring-damper element is derived in this section. To this end, a spring and a damper element are assumed to be installed between two generic rigid bodies i and j as shown in Fig. 2.5.

In this system, the spring stiffness is denoted by k, and the damping coefficient is symbolized by c. If P and Q are the connecting points between body i and body j at

Fig. 2.5, the resultant force f_s of the suspension elements is calculated as:

$$f_s = k(l - l_0) + c\dot{l} \tag{2.39}$$

where l is the instantaneous spring length, l_0 is the initial length of the spring in the undeformed configuration and $\dot{l}$ is the time derivative of the spring length. In Eq. 2.39, the terms $c\dot{l}$ and $k(l - l_0)$ are damping and spring forces respectively, which are nonlinear function of the generalized coordinates.

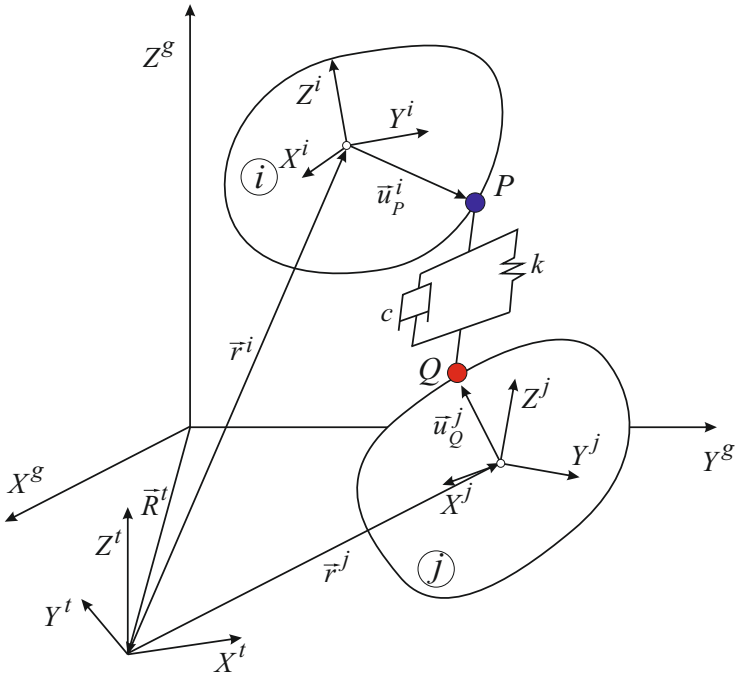

FIGURE 2.5: Spring-damper element between two arbitrary bodies

The position vector in the TF of the two connecting points P and Q with respect to the TF can be written as:

$$\begin{aligned} \bar{\mathbf{r}}_P^i &= \bar{\mathbf{r}}^i + \mathbf{A}^{t,i}\hat{\mathbf{u}}_P^i \\ \bar{\mathbf{r}}_Q^j &= \bar{\mathbf{r}}^j + \mathbf{A}^{t,j}\hat{\mathbf{u}}_Q^j \end{aligned} \tag{2.40}$$

The position vector of point P with respect to the point Q in the TF is calculated as the vector:

$$\bar{\mathbf{r}}_{PQ} = \bar{\mathbf{r}}^i + \mathbf{A}^{t,i}\hat{\mathbf{u}}_P^i - \bar{\mathbf{r}}^j - \mathbf{A}^{t,j}\hat{\mathbf{u}}_Q^j \tag{2.41}$$

Then, the stantaneous length of the vector that joins the two connecting points is obtained as:

$$l = \sqrt{(\bar{\mathbf{r}}_{PQ})^T \bar{\mathbf{r}}_{PQ}} \tag{2.42}$$

And finally, the time derivative of the spring length $\dot{l}$, which must also be calculated, is obtained by applying the chain rule as:

$$\dot{l} = \frac{\partial l}{\partial \mathbf{q}}\dot{\mathbf{q}} \tag{2.43}$$

As the geometric terms have been calculated, the potencial energy $\mathrm{U_s}$ and the Rayleigh dissipation function $\mathrm{F_d}$ associated with the spring and damper elements can be calculated as:

$$\mathrm{U}_s = \frac{1}{2}k(l - l_0)^2, \qquad \mathrm{F}_d = \frac{1}{2}c\dot{l}^2 \tag{2.44}$$

and the generalized suspension force vector associated with the system coordinates can be calculated as:

$$\mathbf{Q}_s^i = -\frac{\partial \mathrm{U}_s}{\partial \mathbf{q}^i} - \frac{\partial \mathrm{F}_d}{\partial \dot{\mathbf{q}}^i}, \qquad \mathbf{Q}_s^j = -\frac{\partial \mathrm{U}_s}{\partial \mathbf{q}^j} - \frac{\partial \mathrm{F}_d}{\partial \dot{\mathbf{q}}^j} \tag{2.45}$$

Here, vectors $\mathbf{Q}_s^i$ and $\mathbf{Q}_s^j$ are the 6×1 vectors of generalized suspension forces affecting to bodies i and j respectively where the connecting points are. As the Newton-Euler equations of motion are written in the TF for the Newton's, and in the BF for the Euler equations, a last updating procedure must be carried out. Regarding the cartesian components of $\mathbf{Q}_s^i$ and $\mathbf{Q}_s^j$, no further modifications have to be done since the calculation

of Eq. 2.42 is derived in the TF. Nonetheless, that is the reason why for the components affecting the rotational coordinates, this is, the last three coordinates of vectors $\mathbf{Q}_s^i$ and $\mathbf{Q}_s^j$, a transformation needs to be accomplished so as Euler equations are written in the BF. This transformation can be achieved by:

$$\mathbf{Q}_{susp}^i = \mathbf{B}_{susp}^{t,i}\mathbf{Q}_s^i, \qquad \mathbf{Q}_{susp}^j = \mathbf{B}_{susp}^{t,j}\mathbf{Q}_s^j \tag{2.46}$$

where $\mathbf{Q}_{susp}^i$ and $\mathbf{Q}_{susp}^j$ are the generalized force vector associated with the system coordinates and written in accordance with the Newton-Euler equations, and $\mathbf{B}_{susp}^{t,i}$ and $\mathbf{B}_{susp}^{t,j}$ the 6×6 transformation matrices for bodies i and j that are defined below:

$$\mathbf{B}_{susp}^{t,i} = \begin{bmatrix} \mathbf{1} & \mathbf{0} \\ \mathbf{0} & \mathbf{A}^{t,i^T} \end{bmatrix}, \qquad \mathbf{B}_{susp}^{t,j} = \begin{bmatrix} \mathbf{1} & \mathbf{0} \\ \mathbf{0} & \mathbf{A}^{t,j^T} \end{bmatrix} \tag{2.47}$$

Note that in Eq. 2.47, $\mathbf{1}$ refers to the 3×3 identity matrix, $\mathbf{0}$ to the 3×3 null matrix, and $\mathbf{A}^{t,i}$ and $\mathbf{A}^{t,j}$ to the 3×3 transformation matrices of the BF i and j with respect to the TF.

2.3.4 Contact forces

The computation of the contact forces is crucial in the dynamic analysis of railroad vehicles since they are essential for its dynamic stability and therefore, an accurate procedure to account for them results indispensable. They can be divided into two different categories: Normal and tangential contact forces.

The approach followed in this thesis regarding normal contact forces derives from the use of contact lookup tables by imposing constraints (see Section 2.4.5), and as a consequence, the generalized normal contact forces are obtained as reaction forces throughout the Lagrange multipliers associated with the constraints.

However, for the calculation of the tangential contact forces, the linear Kalker's theory has been used [40], which is characterized for the linear relationship between the tangential contact forces and the dimensionless relative velocities known as creepages. It is well-known that this theory is not appropriate for gross-sliding, which commonly occurs at the accelerating of braking scenarios and for this reason, smooth accelerations scenarios will be proposed in future sections. For a wheelset body i, the 3×1 tangential contact force vector $\mathbf{F}^i_{cntact}$ is linearly calculated as:

$$\mathbf{F}^i_{cntact} = \mathbf{D}^i\boldsymbol{\varepsilon}^i = \begin{pmatrix} d^i_{11} & 0 & 0 \\ 0 & d^i_{22} & d^i_{23} \\ 0 & -d^i_{23} & d^i_{33} \end{pmatrix} \begin{pmatrix} \xi^i \\ \eta^i \\ \phi^i \end{pmatrix} \tag{2.48}$$

where $\mathbf{D}^i$ is the well-known matrix of linear coefficients that depend on the wheel-rail profile geometry, area of contact and material used [96], and ξ^i, η^i and ϕ^i the dimensionless longitudinal, lateral and non-dimensionless spin creepages computed as the ratio between the contact point velocity and body forward velocity as shown in Eq. 2.49. Note that in Eq. 2.49, superscript i of body i is omitted for simplicity, V is the body forward velocity, and v_x and v_y are the longitudinal and lateral components of the absolute contact point velocity projected in the local frame of the contact point. This contact point frame is obtained by the two geometric tangents and normal vector calculated in Section 2.4.4. Similarly, ω_z is the third component of the absolute contact point angular velocity vector projected in the local frame of the contact point.

$$\xi = \frac{v_x}{V}, \qquad \eta = \frac{v_y}{V}, \qquad \phi = \frac{\omega_z}{V} \tag{2.49}$$

Then, in order to compute the 6×1 vector of generalized tangential forces $\mathbf{Q}^i_{cntact}$ of Eq. 2.38 and consistent with the formulation proposed, the equilibrium equations are applied and the Cartesian components are projected to the TF while for the angular components to the WIF.

Figure 2.6 shows a sketch of the longitudinal creepage ξ in a wheel of a nominal radiuss R, forward velocity V and angular velocity ω.

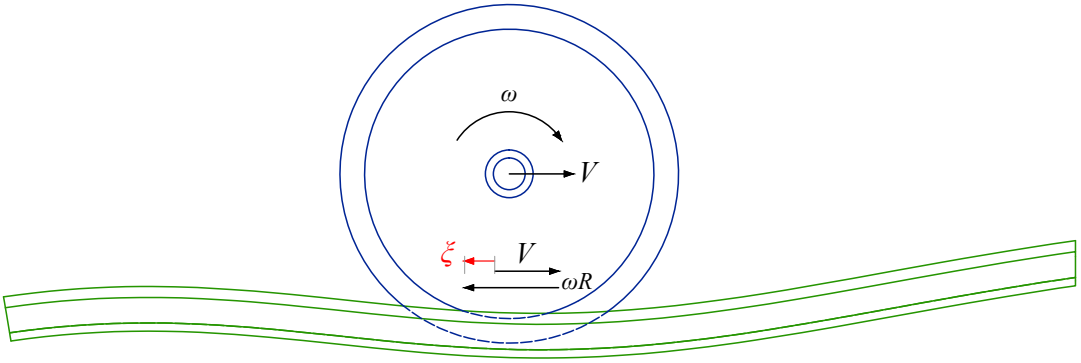

FIGURE 2.6: Longitudinal creepage

2.3.4.1 Flange contact forces

Flange contact forces appear when the wheel flange touches the inner side of the railhead profile. There are many factors that influence in the appearance of flange contact forces, such as the vehicle forward velocity in curve negotiations, curve radius, wheel tread conicity, and lateral gap between the rail and the wheel flange. In summary, it is a complex dynamic phenomenon that can lead to the so-called wheel-climb scenario that results in railroad wheel derailment.

In this thesis, a simplified but effective procedure to account for the flange contact is derived. Its main properties can be listed as:

- Flange contact forces are divided into normal and tangential contact forces F_f^N and F_f^T respectively.
- Normal flange contact forces are calculated based on the indentantion between the wheel flange and railhead δ. They can also account for viscosity effects that

depend on the velocity of indentation between the wheel flange and railhead:

$$F_f^N = k_f \delta^n + c_f \dot{\delta} \, |\delta| \tag{2.50}$$

where k_f is the flange stiffness, n is the exponential term of the indentation, usually $n = 1.5$ for Hertzian contact, c_f is the flange damping and $\dot{\delta}$ is the speed of indentation. Note that the absolute term $|\delta|$ avoids a damping force component when there is no indentation.

- Tangential flange contact forces are calculated by a Coulomb friction model assuming that there is relative movement between the contact surfaces such as:

$$F_f^T = \mu_f F_f^N \tag{2.51}$$

being μ_f the Coulumb friction coefficient between the wheel-flange and railhead surfaces.

These forces are written in vector form by projecting F_f^T in the direcction of the velocity of the flange contact point in its local X-Y components and F_f^N in the normal vector of the flange contact point.

2.3.5 Symbolic computation of equations of motion

The procedure presented in Sections 2.2 and 2.3 alows the possiblity to account for analytical expressions of the majority of the terms of the equation of motion of railroad vehicles.

Starting at the kinematic description of arbritary bodies in the TF formulation in Section 2.2, one can obtain, step by step, the analytical expresion of the jacobian matrices of Eqs. 2.14, 2.16, 2.23 and 2.26. Then, the equations of motion of 2.35 can easily be derived by substituing in the defined procedure of Section 2.3.

The advantages of the computation of symbolic expressions of the terms of the equations of motion are, among other things, a considerable reduction in the computational cost, since it is only necessary to substitute the specific parameters for each body in the expressions [84]. It also increases the portability of a multibody model with respect to other specific environments since analytical expressiones for general case studies are obtained. That is the reason why in the work presented in this thesis, the equations of motion of railroad vehicles are derived symbolically for general vehicle bodies following the procedure presented throughout Chapter 2.

2.4 Wheel-rail contact with precalculated lookup tables

2.4.1 Constraint approach

In this thesis, wheel-rail contact is treated with the constraint approach. As defined in Section 1.3, a set of contact constraints that allow four relative degrees of freedom of the wheelset with respect to the track is used. A single contact point, as shown in Fig.2.7, is assumed for each wheel-rail pair that constrains one degree of freedom of relative motion.

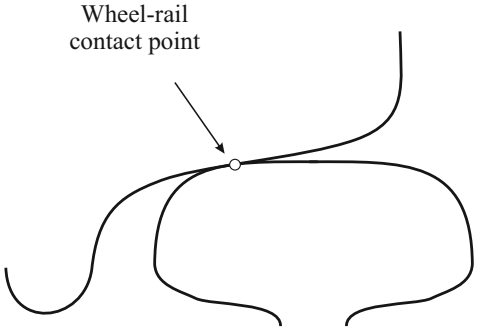

FIGURE 2.7: Single wheel-rail contact point

The constraint equations at each wheel-rail contact can be written as:

$$\mathbf{C}_j^C\left(\mathbf{q}^w,\mathbf{s}\right)=\begin{bmatrix}\bar{\mathbf{r}}_C^w\left(\mathbf{q}^w,\mathbf{s}^w\right)-\bar{\mathbf{r}}_C^r\left(\mathbf{s}^r,s^{wt}\right)\\ \bar{\mathbf{t}}_{1C}^{w\,T}\bar{\mathbf{n}}_C^r\\ \bar{\mathbf{t}}_{2C}^{w\,T}\bar{\mathbf{n}}_C^r\end{bmatrix}=\mathbf{0},\quad j=L,R \tag{2.52}$$

where L and R stand for left or right wheel-rail contact respectively. The first vector equation (3 scalar equations) is called *contact point position constraint* whereas the two last equations represent the *contact point orientation constraints*. In Eq. 2.52, $\mathbf{C}^C$ is the constraint vector of the contact point C, $\bar{\mathbf{r}}_C^w$ and $\bar{\mathbf{r}}_C^r$ are the position vectors of the contact point with respect to the TF in the wheel and rail respectively and $\bar{\mathbf{t}}_{1C}^w$, $\bar{\mathbf{t}}_{2C}^w$ and $\bar{\mathbf{n}}_C^r$ are the two tangent vectors of the contact point in the wheel and the normal vector to the contact point in the rail, projected also into the TF as it can be seen in Fig. 2.8 for the case of the right contact.

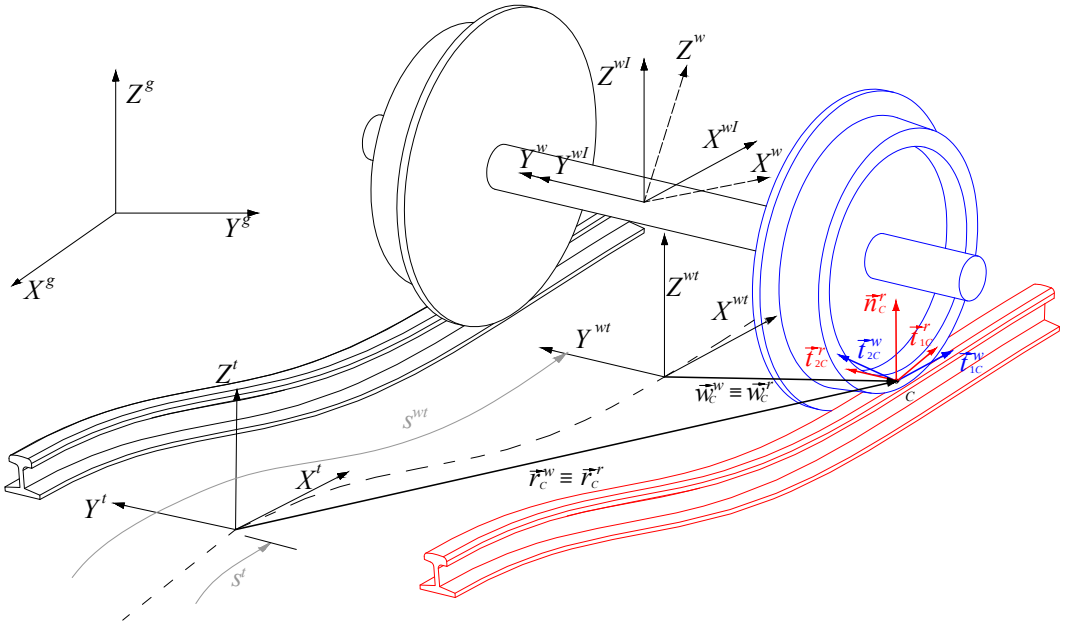

FIGURE 2.8: Wheel-rail contact geometric vectors

These constraint equations of 2.52 are used to impose the non-conformal contact of two bodies with smooth surfaces. Contact point constraint guarantee that there is a point on the wheel, the contact point C on the wheel, that instantaneously occupies the same

position in space that other point on the rail, the contact point C on the rail. The contact point orientation constraints guarantee that the tangent plane to the wheel at the contact point is parallel to the tangent plane to the rail at the contact point. Note that all vectors in Eq. 2.52 are defined with respect to the TF. In addition, for the definition of the contact point position on the wheel $\bar{\mathbf{r}}_C^w$ and on the rail $\bar{\mathbf{r}}_C^r$, the wheel-rail surfaces in contact are defined as functions of the so-called surface parameters of the wheel $\mathbf{s}^w$ and rail $\mathbf{s}^r$. In this work, four surface parameters are used, two to define the wheel profile surface $\mathbf{s}^w = \begin{bmatrix} s_1^w & s_2^w \end{bmatrix}^T$ and other two for the rail-head profile surface $\mathbf{s}^r = \begin{bmatrix} s_1^r & s_2^r \end{bmatrix}^T$. They are the curvilinear coordinates used to locate an arbitrary point on the surfaces. Their physical meaning is shown in Fig. 2.9.

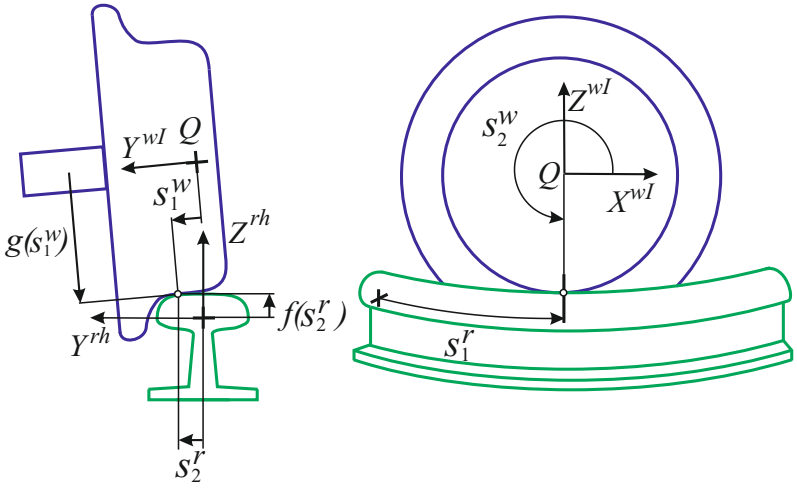

FIGURE 2.9: Wheel and rail surface parameters

The position of arbitrary points on the surface of the wheel and the rail with respect to the TF are given by:

$$\begin{aligned} \bar{\mathbf{r}}_C^w &= \bar{\mathbf{r}}^w + \mathbf{A}^{t,wI} \breve{\mathbf{w}}_C^w \\ \bar{\mathbf{r}}_C^r &= \mathbf{A}^{tT} \left(\mathbf{R}_C^r - \mathbf{R}^t \right) \end{aligned} \tag{2.53}$$

where for the case of the right contact, it yields:

$$\breve{\mathbf{w}}_C^w = \begin{bmatrix} -g\left(s_1^w\right)\sin s_2^w \\ -d + s_1^w \\ -g\left(s_1^w\right)\cos s_2^w \end{bmatrix}, \quad \mathbf{R}_C^r = \mathbf{R}_R^{rh}\left(s_1^r\right) + \mathbf{A}_R^{rh}\left(s_1^r\right)\begin{bmatrix} 0 \\ s_2^r \\ f\left(s_2^r\right) \end{bmatrix} \tag{2.54}$$

In Eq. 2.53, the definition of the WIF (wheelset intermediate frame, see Section 2.2.4) becomes necessary since $\breve{\mathbf{w}}_C^w$ is the position vector of the contact point on the wheel in the WIF defined in Eq. 2.54, that depends on the wheelset surface parameters and on the lateral distance d from the WIF to the center of the wheel. $\mathbf{A}^{t,wI}$ is the transformation matrix of the WIF with respect to the TF and $\mathbf{R}_C^r$ is the global position of the contact point in the rail. Also note that for the calculation of $\mathbf{R}_C^r$ in Eq. 2.54, the global position of the origin of the right rail profile frame $\mathbf{R}_R^{rh}$ together with its orientation matrix $\mathbf{A}_R^{rh}$ defined in Section 2.2.4.1 are needed. They are functions of the arc-length rail parameter s_1^r provided by the track preprocessor. Finally, $f(s_2^r)$ and $g(s_1^w)$ are the rail head and wheel profiles, respectively, as functions of the transverse surface parameters. In this work, these functions are analytically defined by spline functions that extrapolate the coordinates of a set of surface points given in tables.

With regard to the three geometric vectors that appear in the contact point orientation constraints, the two tangents to the wheel at the contact point $\bar{\mathbf{t}}_{1C}^w$ and $\bar{\mathbf{t}}_{2C}^w$, and the normal to the rail at the contact point $\bar{\mathbf{n}}_C^r$, they can be calculated as follows:

$$\begin{aligned} \bar{\mathbf{t}}_{1C}^w &= \frac{\partial \bar{\mathbf{r}}_C^w}{\partial s_1^w}, \quad \bar{\mathbf{t}}_{2C}^w = \frac{\partial \bar{\mathbf{r}}_C^w}{\partial s_2^w} \\ \bar{\mathbf{t}}_{1C}^r &= \frac{\partial \bar{\mathbf{r}}_C^r}{\partial s_1^r}, \quad \bar{\mathbf{t}}_{2C}^r = \frac{\partial \bar{\mathbf{r}}_C^r}{\partial s_2^w} \\ \bar{\mathbf{n}}_C^r &= \bar{\mathbf{t}}_{1C}^r \times \bar{\mathbf{t}}_{2C}^r \end{aligned} \tag{2.55}$$

where the two tangents to the rail at the contact point, $\bar{\mathbf{t}}_{1C}^r$ and $\bar{\mathbf{t}}_{2C}^r$ are used for the computation of $\bar{\mathbf{n}}_C^r$.

The contact constraints vector $\mathbf{C}^C$ given in Eq. 2.52 includes five constraint equations but it also adds four new coordinates to the system: the four surface parameters associated with the contact point on the wheel $\mathbf{s}^w$ and on the rail $\mathbf{s}^r$. Therefore, each wheel-rail contact eliminates only one degree of freedom of relative motion.

2.4.2 Contact lookup table

In order to create the wheel-rail contact lookup tables, the contact constraint equations given in Eq. 2.52 are solved for a set of values of the wheelset coordinates $\mathbf{q}^w$. Every wheelset having one contact point on the left wheel and one contact point on the right wheel is subject to the ten contact constraints given by $\mathbf{C}_L^C$ and $\mathbf{C}_R^C$. These constrains are 10 non-linear algebraic equations which are functions of 14 coordinates; the 6 wheelset generalized coordiantes given in $\mathbf{q}^w$ plus the 8 surface parameters associated with the two contacts: $\mathbf{s}_L^w$, $\mathbf{s}_L^r$, $\mathbf{s}_R^w$ and $\mathbf{s}_R^r$.

However, looking carefully to the contact constraint equations in Eq. 2.52, it can be assumed that they do not depend on the *pitch*-coordinate of the wheelset θ^w since the wheelset contact point local position vector is given in the WIF, which does not show pitch rotation. The number of unknowns is thus reduced from 14 to 13.

To create the contact look-up table, the wheelset coordinate x^w is assumed to be zero, this is, it is assumed that there is no longitudinal displacement between the wheelset and the TF. This is equivalent to solve the contact constraint equations in the WTF instead of the TF. The position and orientation of the WIF with respect to the WTF are given by $\widehat{\mathbf{w}}^{wI}$ and $\mathbf{A}^{wt,wI}$ respectively as shown in Eq. 2.57. Nevertheless, for the transformation matrix of the WIF with respect to the WTF, $\mathbf{A}^{wt,wI}$, the small angle assumption has been used. This is, following the rotation sequence in the axes $< Z, X', Y'' >$ with the angles ψ^{wI}, φ^{wI} and θ^{wI}, the original transformation matrix stands as $\mathbf{A}^{wt,wI} = \mathbf{A}_{\psi^{wI}}\mathbf{A}_{\varphi^{wI}}\mathbf{A}_{\theta^{wI}}$ and yields:

$$\mathbf{A}^{wt,wI} = \begin{bmatrix} \mathrm{c}\psi^{wI}\mathrm{c}\theta^{wI} - \mathrm{s}\varphi^{wI}\mathrm{s}\psi^{wI}\mathrm{s}\theta^{wI} & -\mathrm{c}\varphi^{wI}\mathrm{s}\psi^{wI} & \mathrm{c}\psi^{wI}\mathrm{s}\theta^{wI} + \mathrm{c}\theta^{wI}\mathrm{s}\varphi^{wI}\mathrm{s}\psi^{wI} \\ \mathrm{c}\theta^{wI}\mathrm{s}\psi^{wI} + \mathrm{c}\psi^{wI}\mathrm{s}\varphi^{wI}\mathrm{s}\theta^{wI} & \mathrm{c}\varphi^{wI}\mathrm{c}\psi^{wI} & \mathrm{s}\psi^{wI}\mathrm{s}\theta^{wI} - \mathrm{c}\psi^{wI}\mathrm{c}\theta^{wI}\mathrm{s}\varphi^{wI} \\ -\mathrm{c}\varphi^{wI}\mathrm{s}\theta^{wI} & \mathrm{s}\varphi^{wI} & \mathrm{c}\varphi^{wI}\mathrm{c}\theta^{wI} \end{bmatrix} \tag{2.56}$$

where c = cos and s = sin. Therefore, assuming small angles one can adopt that $\sin\alpha \simeq \alpha$ and that $\cos\alpha \simeq 1$ being α and arbitrary angular coordinate of the WIF with respect to the WTF. This assumption leads to:

$$\widehat{\mathbf{w}}^{wI} = \begin{bmatrix} 0 \\ y^{wI} \\ z^{wI} \end{bmatrix}, \qquad \mathbf{A}^{wt,wI} \cong \begin{bmatrix} 1 & -\psi^{wI} & \theta^{wI} \\ \psi^{wI} & 1 & -\varphi^{wI} \\ -\theta^{wI} & \varphi^{wI} & 1 \end{bmatrix} \tag{2.57}$$

To form the lookup table numerical values are given to the independent coordinates to solve the non-linear algebraic equations of Eq. 2.52 that govern the wheel-rail contact. As the *pitch* coordinate θ^w is irrelevant in the location of the contact point in the WIF and the longitudinal coordinate x^w is also pointless when the contact constraint equations are solved in the WTF, the two selected independent coordinates are the wheelset lateral displacement y^{wI} and *yaw* angle ψ^{wI} in the WIF.

Accordingly, numerical values are given to y^{wI} and ψ^{wI}, where the initial and final positions are the left and right flange contact scenarios. Then, the 10 non-linear algebraic equations $\mathbf{C}_L^C$ and $\mathbf{C}_R^C$ are solved to provide 10 unknowns: the remaining wheelset coordinates, z^{wI} and φ^{wI}, and the 8 surface parameters $\mathbf{s}_L^w$, $\mathbf{s}_L^r$, $\mathbf{s}_R^w$ and $\mathbf{s}_R^r$. In this stage, the lookup table has two entries (y^{wI} and ψ^{wI}) and it provides, among other data, the vertical wheelset displacement and roll angle as follows:

$$\begin{aligned} z^{wI} &= f\left(y^{wI}, \psi^{wI}\right) \\ \varphi^{wI} &= g\left(y^{wI}, \psi^{wI}\right) \end{aligned} \tag{2.58}$$

If the wheelset yaw angle is small, as it uses to be in the case of railroad dynamics, the dependency of the vertical displacement and the roll angle on it is insignificant. Thus, for simplicity, one can assume that there is no such dependency and Eq. 2.58 can be rewritten as:

$$\begin{aligned} z^{wI} &\approx f\left(y^{wI}, 0\right) = f\left(y^{wI}\right) \\ \varphi^{wI} &\approx g\left(y^{wI}, 0\right) = g\left(y^{wI}\right) \end{aligned} \tag{2.59}$$

The number of entries (or independent variables) of the lookup table is thus reduced from two to one. Due to the contact constraints, the position of the origin $\widehat{\mathbf{w}}^{wI}$ and orientation matrix of the WIF with respect to the WTF $\mathbf{A}^{wt,wI}$ given at Eq. 2.57 become:

$$\widehat{\mathbf{w}}^{wI} = \begin{bmatrix} 0 \\ y^{wI} \\ f(y^{wI}) \end{bmatrix}, \qquad \mathbf{A}^{wt,wI} = \begin{bmatrix} 1 & -\psi^{wI} & \theta^{wI} \\ \psi^{wI} & 1 & -g(y^{wI}) \\ -\theta^{wI} & g(y^{wI}) & 1 \end{bmatrix} \tag{2.60}$$

Equation 2.59 can be considered as the two constraint equations to the wheelset motion. Nevertheless these constraints cannot be used directly in the equations of motion because they are not written in terms of the generalized coordinates of the wheelset $\mathbf{q}^w$. In what follows, Eq. 2.59 is transformed to a set of constraints in terms of $\mathbf{q}^w$.

In order to use the contact lookup table, the wheelset arc length parameter s^{wt} (see Fig. 2.3) has to be determined by solving the nonlinear algebraic equation 2.12 for a general track. Then, the position of the WIF with respect to the TF can be obtained as:

$$\bar{\mathbf{r}}^w = \bar{\mathbf{r}}^{wt}\left(s^t, s^{wt}\right) + \mathbf{A}^{t,wt}\left(s^t, s^{wt}\right)\ \widehat{\mathbf{w}}^{wI}\left(y^{wI}\right) \tag{2.61}$$

In this equation, the position vector $\bar{\mathbf{r}}^{wt}$ and orientation matrix of the WTF with respect to the TF $\mathbf{A}^{t,wt}$, are obtained from the rail preprocessor as follows:

$$\begin{aligned} \bar{\mathbf{r}}^{wt} &= \mathbf{A}^{t}\left(s^{t}\right)^{T}\left(\mathbf{R}^{wt}\left(s^{wt}\right)-\mathbf{R}^{t}\left(s^{t}\right)\right) \\ \mathbf{A}^{t,wt} &= \mathbf{A}^{t}\left(s^{t}\right)^{T}\mathbf{A}^{wt}\left(s^{wt}\right) \end{aligned} \tag{2.62}$$

And the orientation of the WIF with respect to the WTF can be obtained by:

$$\mathbf{A}^{wt,wI} = \mathbf{A}^{t,wt^{T}}\mathbf{A}^{t,wI} \tag{2.63}$$

where

$$\mathbf{A}^{t,wI} = \begin{bmatrix} \cos\psi^{w} & -\sin\psi^{w}\cos\phi^{w} & \sin\psi^{w}\sin\phi^{w} \\ \sin\psi^{w} & \cos\psi^{w}\cos\phi^{w} & -\cos\psi^{w}\sin\phi^{w} \\ 0 & \sin\phi^{w} & \cos\phi^{w} \end{bmatrix} \tag{2.64}$$

The two independent wheelset constraint equations due to wheel-rail contact can be extracted from the 'z' component of vector $\bar{\mathbf{r}}^{w}$ given in Eq. 2.61 and the term (3,2) (*third* row, *second* column) of the transformation matrix $\mathbf{A}^{t,wI}$ given in Eq. 2.64 as follows:

$$\begin{aligned} & z^{w} - \left(z^{wt}\left(s^{t},s^{wt}\right) + \mathbf{A}_{r3}^{t,wt}\left(s^{t},s^{wt}\right) \begin{bmatrix} 0 \\ y^{wI} \\ f(y^{wI}) \end{bmatrix} \right) = 0 \\ & \mathbf{A}_{c3}^{t,wt^{T}}\left(s^{t},s^{wt}\right)\mathbf{A}_{c2}^{t,wI}\left(\mathbf{q}^{w}\right) - g(y^{wI}) = 0 \end{aligned} \tag{2.65}$$

where in matrices $\mathbf{A}_{r3}^{t,wt}$, $\mathbf{A}_{c3}^{t,wt}$ and $\mathbf{A}_{c2}^{t,wI}$ subscript $r3$, $c3$ and $c2$ refer to the the third row, third column and second column respectively of the corresponding matrices.

Equation 2.65 includes the two non-linear constraint equations of the wheelset due to wheel-rail contact implemented with lookup tables $\left(f(y^{wI}),\ g(y^{wI})\right)$. In the particular case of a tangent track $\left(\mathbf{A}^{t,wt} = \mathbf{I}\right)$, without vertical slope $\left(z^{wt}\left(s^t, s^{wt}\right) = 0\right)$, $\left(y^{wI} = y^w\right)$, Eq. 2.65 reduces to:

$$\begin{aligned} z^w - f(y^w) &= 0 \\ \sin\varphi^w - g(y^w) &= 0 \end{aligned} \tag{2.66}$$

In an arbitrary track, the lateral displacement y^{wI} with respect to the WTF can be obtained from Eq. 2.61 as

$$\begin{aligned} \widehat{\mathbf{w}}^{wI} = \mathbf{A}^{t,wt^T}\left(\bar{\mathbf{r}}^w - \bar{\mathbf{r}}^{wt}\right) \Rightarrow \\ y^{wI} = \mathbf{A}_{c2}^{t,wt^T}\left(\bar{\mathbf{r}}^w - \bar{\mathbf{r}}^{wt}\right) \end{aligned} \tag{2.67}$$

where as in the previous equations, subscript $c2$ refers to the second column of the transformation matrix $\mathbf{A}^{t,wt}$.

Considering that the TF arc length parameter s^t is usually prescribed and that s^{wt} is an implicit function of the wheelset coordinates $\mathbf{q}^w$ as established in Eq. 2.12, and y^{wt} is in turn a function of $\mathbf{q}^w$, s^t and s^{wt} as establish in Eq. 2.67, then the constraint equations 2.65 take the vector form:

$$\mathbf{C}^{wr}\left(\mathbf{q}^w\right) = \mathbf{0} \tag{2.68}$$

2.4.3 Derivatives of the contact constraints

In multibody dynamics, constraint equations can be treated at position level, as given in Eq. 2.65, velocity level and acceleration level [90]. In the case of holonomic and scleronomic constraints the velocity and acceleration level equations yield:

$$\begin{aligned} \mathbf{C}_{\mathbf{q}w}^{wr}\dot{\mathbf{q}}^{w} &= \mathbf{0} \\ \mathbf{C}_{\mathbf{q}w}^{wr}\ddot{\mathbf{q}}^{w} + \dot{\mathbf{C}}_{\mathbf{q}w}^{wr}\dot{\mathbf{q}}^{w} &= \mathbf{0} \end{aligned} \tag{2.69}$$

where

$$\begin{aligned} \mathbf{C}_{\mathbf{q}w}^{wr} &= \frac{\partial \mathbf{C}^{wr}}{\partial \mathbf{q}^{wT}} \\ \dot{\mathbf{C}}_{\mathbf{q}w}^{wr} = \frac{d\mathbf{C}_{\mathbf{q}w}^{wr}}{dt} &= \frac{\partial\left(\mathbf{C}_{\mathbf{q}w}^{wr}\dot{\mathbf{q}}^{w}\right)}{\partial \mathbf{q}^{wT}} \end{aligned} \tag{2.70}$$

The two matrices that appear in this equation have to be evaluated with the help of the contact lookup tables too. A symbolic computation of these matrices requires the computation of the partial derivatives s^{wt} and y^{wt} with respect to $\mathbf{q}^{w}$. In this thesis, the dependency of s^{wt} with $\mathbf{q}^{w}$ is neglected in terms of the calculation of the Jacobian matrix of the constraints $\mathbf{C}_{\mathbf{q}w}^{wr}$. This is equivalent to assume that during the vehicle motion, the WTF is at a constant distance to the TF along the track regardless of the coordinates $\mathbf{q}^{w}$. This assumption is not exact, and that is why Eq. 2.12 has to be solved each time step, but it is a reasonable assumption for the calculation of the Jacobian matrix.

With regard to the lateral displacement y^{wt}, the following partial derivative is obtained from Eq. 2.67

$$\frac{\partial y^{wI}}{\partial \mathbf{q}^{wT}} = \begin{bmatrix} \mathbf{A}_{c2}^{t,wtT} & 0 & 0 & 0 \end{bmatrix} \tag{2.71}$$

Calling C_1^{wr} C_2^{wr} to the two constraint equations in Eq. 2.65, the rows of the contact constraint Jacobian matrix $\mathbf{C}_{\mathbf{q}w}^{wr}$ become:

$$\frac{\partial C_1^{wr}}{\partial \mathbf{q}^{wT}} = \begin{bmatrix} 0 & 0 & 1 & 0 & 0 & 0 \end{bmatrix} - \mathbf{A}_{r3}^{t,wt} \begin{bmatrix} 0 \\ 1 \\ f'(y^{wI}) \end{bmatrix} \frac{\partial y^{wI}}{\partial \mathbf{q}^{wT}}$$
$$\frac{\partial C_2^{wr}}{\partial \mathbf{q}^{wT}} = \mathbf{A}_{c3}^{t,wt^T} \frac{\partial \mathbf{A}_{c2}^{t,wI}}{\partial \mathbf{q}^{wT}} - g'(y^{wI}) \frac{\partial y^{wI}}{\partial \mathbf{q}^{wT}} \tag{2.72}$$

where f' and g' are the derivatives of the lookup table functions with respect to the input parameter y^{wI}. The jacobian matrix $\partial \mathbf{A}_{c2}^{t,wI} / \partial \mathbf{q}^{wT}$ is calculated as:

$$\frac{\partial \mathbf{A}_{c2}^{t,wI}}{\partial \mathbf{q}^{wT}} = \begin{bmatrix} 0 & 0 & 0 & \sin\psi^w \sin\varphi^w & 0 & -\cos\psi^w \cos\varphi^w \\ 0 & 0 & 0 & -\cos\psi^w \sin\varphi^w & 0 & -\sin\psi^w \cos\varphi^w \\ 0 & 0 & 0 & \cos\varphi^w & 0 & 0 \end{bmatrix} \tag{2.73}$$

The time derivative of the two terms in Eq. 2.72 provides the rows of the matrix $\dot{\mathbf{C}}_{\mathbf{q}w}^{wr}$. With regard to the first constraint C_1^{wr} it yields:

$$\frac{d}{dt}\left(\frac{\partial C_1^{wr}}{\partial \mathbf{q}^{wT}}\right) = -\dot{\mathbf{A}}_{r3}^{t,wt} \begin{bmatrix} 0 \\ 1 \\ f'(y^{wI}) \end{bmatrix} \frac{\partial y^{wI}}{\partial \mathbf{q}^{wT}}$$
$$-\mathbf{A}_{r3}^{t,wt} \left(\begin{bmatrix} 0 \\ 0 \\ f''(y^{wI}) \end{bmatrix} \frac{\partial y^{wI}}{\partial \mathbf{q}^{wT}} \dot{\mathbf{q}}^w \frac{\partial y^{wI}}{\partial \mathbf{q}^{wT}} + \begin{bmatrix} 0 \\ 1 \\ f'(y^{wI}) \end{bmatrix} \frac{d}{dt}\left(\frac{\partial y^{wI}}{\partial \mathbf{q}^{wT}}\right) \right) \tag{2.74}$$

While for the second constraint C_2^{wr} one has:

$$\begin{aligned}\frac{d}{dt}\left(\frac{\partial C_2^{wr}}{\partial \mathbf{q}^{wT}}\right) &= \dot{\mathbf{A}}_{c3}^{t,wt^T}\frac{\partial \mathbf{A}_{c2}^{t,wI}}{\partial \mathbf{q}^{wT}} \\ +\mathbf{A}_{c3}^{t,wt^T}\frac{d}{dt}\left(\frac{\partial \mathbf{A}_{c2}^{t,wI}}{\partial \mathbf{q}^{wT}}\right) &- g''(y^{wI})\frac{\partial y^{wI}}{\partial \mathbf{q}^{wT}}\dot{\mathbf{q}}^w\frac{\partial y^{wI}}{\partial \mathbf{q}^{wT}} - g'(y^{wI})\frac{d}{dt}\left(\frac{\partial y^{wI}}{\partial \mathbf{q}^{wT}}\right)\end{aligned} \tag{2.75}$$

where f'' and g'' are the second derivatives of the lookup table functions with respect to the input parameter y^{wI}.

In the particular case of a tangent track ($\mathbf{A}^{t,wt} = \mathbf{I}$) without vertical slope $y^{wI} = y^w$, ($z^{wt}\left(s^t, s^{wt}\right) = 0$), matrices $\mathbf{C}_{\mathbf{q}w}^{wr}$ and $\dot{\mathbf{C}}_{\mathbf{q}w}^{wr}$ reduce to:

$$\begin{aligned}\mathbf{C}_{\mathbf{q}w}^{wr} &= \begin{bmatrix} 0 & -f' & 1 & 0 & 0 & 0 \\ 0 & -g' & 0 & \cos\varphi^w & 0 & 0 \end{bmatrix} \\ \dot{\mathbf{C}}_{\mathbf{q}w}^{wr} &= \begin{bmatrix} 0 & -f''\,\dot{y}^w & 0 & 0 & 0 & 0 \\ 0 & -g''\,\dot{y}^w & 0 & -\sin\varphi^w\dot{\varphi}^w & 0 & 0 \end{bmatrix}\end{aligned} \tag{2.76}$$

2.4.4 Additional contact geometric vectors

In the creation of the lookup table, the solution of the contact constraints of Eq. 2.52 is obtained for different values of the wheelset coordinates $\mathbf{q}^w$. As shown through Section 2.4.2, the considered assumptions allow to obtain the solution of the wheel-rail contact as a function of only the wheelset lateral displacement with respect to its WTF y^{wI}. This is, the wheel-rail contact is solved by knowing only one function of the wheelset coordinates.

In adddition to the solution of the wheel-rail contact, additional geometric terms can also be stored as a function of y^{wI} that will help in the dynamic simulation of railroad

vehicles. This is the case of the already defined lookup table functions f, g of Eq. 2.59 and its derivatives f', g', f'' and g'' with respect to the input parameter y^{wI}.

Moreover, geometric vectors at the contact point positions are also stored. These geometric vectors can be seen in Fig. 2.10, $\mathbf{t}_1^r$, $\mathbf{t}_2^r$, $\mathbf{n}^r$, $\mathbf{t}_1^w$, $\mathbf{t}_2^2$ and $\mathbf{n}^w$, where for visualization purposes, the contact point in the wheel and rail do not coincide as they should in the constraint approach.

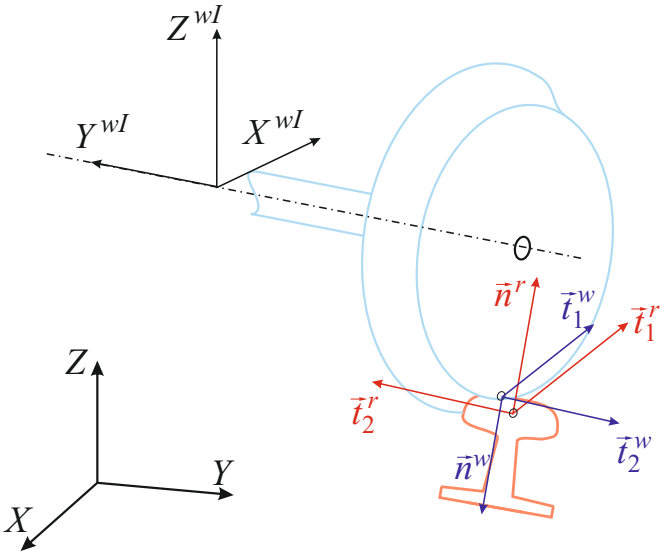

FIGURE 2.10: Geometric vectors stored in the lookup table

Their calculation is straightforward in the process of solving the contact constraint equations $\mathbf{C}^C$ and its value is necessary when tangential contact forces are evaluated. As tangential creep forces are evaluated at every time step of the dynamic simulation of railroad vehicles, having the geometric vector at the contact points reduces considerably the computional cost.

2.4.5 Calculation of generalized normal contact forces

Since the wheel-rail contact is accounted for in this formulation using a constraint approach, the generalized wheel-rail normal contact forces appear in the equations of

motion as reaction forces associated with these constraints, as follows

$$\mathbf{Q}_{normal} = -\mathbf{C}_{\mathbf{q}}^{wr^T} \boldsymbol{\lambda}^{wr} \tag{2.77}$$

where the jacobian matrix $\mathbf{C}_{\mathbf{q}}^{wr}$ is obtained by assembling the jacobian matrices associated with all wheelsets in the vehicle, as follows:

$$\mathbf{C}_{\mathbf{q}}^{wr} = \begin{bmatrix} \mathbf{C}_{\mathbf{q}w1}^{wr1} \\ \vdots \\ \mathbf{C}_{\mathbf{q}wp}^{wrp} \end{bmatrix} \tag{2.78}$$

being p the total number of wheelsets in the vehicle. Vector $\boldsymbol{\lambda}^{wr}$ in Eq. 2.77 is the vector of Lagrange multipliers associated with the contact constraints. This expression of the generalized normal contact forces is now inserted into the equations of motion of the vehicle that are given by Eq. 2.37. Augmenting the resulting equations with the constraint equations yield:

$$\begin{aligned} &\mathbf{M}\ddot{\mathbf{q}} + \mathbf{C}_{\mathbf{q}}^{wrT} \boldsymbol{\lambda}^{wr} = \mathbf{Q} + \mathbf{Q}_v + \mathbf{Q}_{TFin} + \mathbf{Q}_{susp} + \mathbf{Q}_{cntact} \\ &\mathbf{C}^{wr}(\mathbf{q}) = \mathbf{0} \end{aligned} \tag{2.79}$$

The equations of motion have now become a system of Differential-Algebraic Equations (DAE).

2.4.6 Augmenting lookup tables with track irregularities

The use of the contact lookup table has difficulties when dealing with track irregularities. Simulation of track irregular geometry is essential in railroad dynamics since this is the main source of vehicle vibrations. In this thesis, this problem is solved by

increasing by one the number of entrance in the lookup table. This new entrance is the track gauge d (see Fig. 2.11).

The wheel-rail contact constraints are solved as a function of the lateral displacement of the wheelset for a set of values of the gauge d. Then, the lookup table contains pre-computed values of the following functions:

$$z^{wI} = f\left(y^{wI}, d\right), \qquad \varphi^{wI} = g\left(y^{wI}, d\right) \tag{2.80}$$

Due to the track irregularities, the left and right rail cross-sections experience displacements u_y^L, u_z^L, u_y^R and u_z^R (see Fig. 2.11).

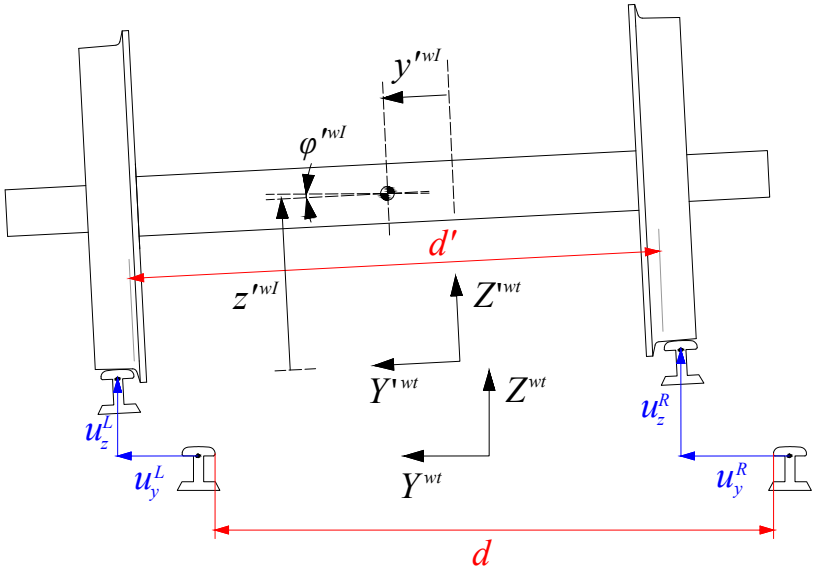

FIGURE 2.11: Rail centerline irregularities

In order to obtain the vertical position and roll angle of the wheelset on the irregular track using the two entries of the lookup table, an *irregular Wheel Track Frame* $< Y'^{wt}, Z'^{wt} >$ system is defined. This frame has a lateral displacement $(u_y^L + u_y^R)/2$ and a roll angle $(u_z^L - u_z^R)/d'$ with respect to the Wheel Track Frame WTF, where $d' = d + (u_y^L - u_y^R)$ is the gauge that has to be used as an entry to the lookup table

defined in Eq. 2.83. The wheelset vertical displacement z'^{wI} and roll angle φ'^{wI} in the irregular wheel-track frame are calculated as:

$$z'^{wI} = f\left(y'^{wI}, d'\right), \qquad \varphi'^{wI} = g\left(y'^{wI}, d'\right) \tag{2.81}$$

where $y'^{wI} = y^{wI} + (u_y^L - u_y^R)/2$. The wheelset vertical displacement and roll angle in the original wheel-track frame are finally given by:

$$\begin{aligned} z^{wI} &= z'^{wI} + \frac{\left(u_z^L + u_z^R\right)}{2} \\ \varphi^{wI} &= \varphi'^{wI} + \frac{\left(u_z^L - u_z^R\right)}{d'} \end{aligned} \tag{2.82}$$

2.5 Linearization of equations of motion

The DAE equations of motion presented in Eq. 2.79 can be partially linearized in order to accomplish efficient numeric simulations. However, linearization of this kind of equations is a difficult task, since the assumptions made are only valid in certain situations.

Applying linearization to the equations of motion requires its reduction to the first order terms of its Taylor expansion. It can be applied in two different views. From the kinematic point of view, and from the dynamic point of view. In this thesis, linearization is applied to the kinematic point of view and compared to the original formulation for accurate and efficient purposes. In addition, linearization of the dynamic equations of motion is proposed as the concepts for future work since a reduction of the nonlinearities of a dynamical system is essential for the purpose of real-time simulations.

2.5.1 Kinematic linearization

In Section 2.2.2, the kinematics of the TF is defined. This frame that follows the gross motion of the vehicle, has its X-axis tangent to the trajectory followed, as shown again in Fig. 2.12.

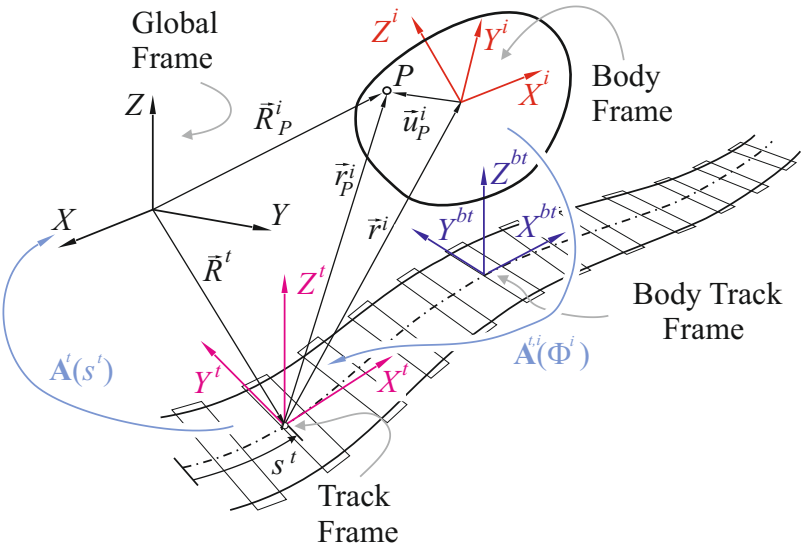

FIGURE 2.12: Kinematics of an arbitrary body in the TF formulation

The orientation of the TF with respect to the GF is defined by three consecutive rotations applied in the sequence $< Z^g, -Y', -X'' >$ with the angles ψ^t, $-\theta^t$ and $-\varphi^t$ respectively. Note that the negative rotations in the sequence of the TF are to be consistent with the railway industry because it employs a moving frame whose X and Z axis are in opposite direction than the TF. Then, the orientation matrix is defined by $\mathbf{A}^t = \mathbf{A}_{\psi^t}\mathbf{A}_{\theta^t}\mathbf{A}_{\varphi^t}$.

However, some assumptions in the transformation matrix can be made: firstly, the *pitch* angle θ^t of the TF with respect to the GF can be assumed small since it coincides with the slope or ramp of the track which usually is lower than 1%. Secondly, the *roll* angle of the TF φ^t, can also be assumed small since it corresponds to the bank angle of the track. This makes that the orientation matrix $\mathbf{A}^t$ of Eq. 2.2 can be simplified as:

$$\mathbf{A}^t = \mathbf{A}_{\psi^t}\mathbf{A}_{\theta^t}\mathbf{A}_{\varphi^t} \approx \begin{bmatrix} \cos\psi^t & -\sin\psi^t & 0 \\ \sin\psi^t & \cos\psi^t & 0 \\ 0 & 0 & 1 \end{bmatrix} \begin{bmatrix} 1 & 0 & -\theta^t \\ 0 & 1 & 0 \\ \theta^t & 0 & 1 \end{bmatrix} \begin{bmatrix} 1 & 0 & 0 \\ 0 & 1 & \varphi^t \\ 0 & -\varphi^t & 1 \end{bmatrix} \tag{2.83}$$

$$\mathbf{A}^t = \begin{bmatrix} \cos\psi^t & -\sin\psi^t & -\theta^t\cos\psi^t - \varphi^t\sin\psi^t \\ \sin\psi^t & \cos\psi^t & \varphi^t\cos\psi^t - \theta^t\sin\psi^t \\ \theta^t & -\varphi^t & 1 \end{bmatrix}$$

Note that the *yaw* angle of the TF ψ^t is not subject to be linearized since it can acount for large values as a function of the track geometry. .

Following the same procedure, the transformation matrix of an arbitrary body i with respect to the TF $\mathbf{A}^{t,i}$ of Eq. 2.6 can also be linearized. In this case, the orientation of the BF with respect to the TF is defined by three consecutive rotations applied in the sequence $< Z, X', Y'' >$ with the angles ψ^i, φ^i and θ^i respectively. Here, arbitrary bodies in a railroad system (all non-wheelsets bodies) are subject to experience small rotation angles and as a consequence, the three consecutive rotations can be linearized as follows:

$$\mathbf{A}^{t,i} = \mathbf{A}^i_\psi\mathbf{A}^i_\varphi\mathbf{A}^i_\theta \approx \begin{bmatrix} 1 & -\psi^i & 0 \\ \psi^i & 1 & 0 \\ 0 & 0 & 1 \end{bmatrix} \begin{bmatrix} 1 & 0 & 0 \\ 0 & 1 & -\varphi^i \\ 0 & \varphi^i & 1 \end{bmatrix} \begin{bmatrix} 1 & 0 & \theta^i \\ 0 & 1 & 0 \\ -\theta^i & 0 & 1 \end{bmatrix} \tag{2.84}$$

$$\mathbf{A}^{t,i} = \begin{bmatrix} 1 & -\psi^t & \theta^t \\ \psi^t & 1 & -\varphi^t \\ -\theta^t & \varphi^t & 1 \end{bmatrix}$$

where the product of small angles is neglected.

Special attention should be paid at the transformation matrix of a wheelset body w with respect to the TF $\mathbf{A}^{t,w}$. This orientation matrix has the same sequence that the one for arbitrary bodies $\mathbf{A}^{t,i}$ of Eq. 2.84. Nevertheless, the *pitch* coordinate of wheelset bodies θ^w experiences high values since it accounts for the revolution around the Y-axis of the wheelset. As a result, $\mathbf{A}^{t,w}$ cannot be linearized with respect to the *pitch*, so it yields as:

$$\mathbf{A}^{t,w} \approx \begin{bmatrix} 1 & -\psi^w & 0 \\ \psi^w & 1 & 0 \\ 0 & 0 & 1 \end{bmatrix} \begin{bmatrix} 1 & 0 & 0 \\ 0 & 1 & -\varphi^w \\ 0 & \varphi^w & 1 \end{bmatrix} \begin{bmatrix} \cos\theta^w & 0 & \sin\theta^w \\ 0 & 1 & 0 \\ -\sin\theta^w & 0 & \cos\theta^w \end{bmatrix} \tag{2.85}$$

$$\mathbf{A}^{t,w} = \begin{bmatrix} \cos\theta^w & -\psi^w & \sin\theta^w \\ \psi^w\cos\theta^w + \varphi^w\sin\theta^w & 1 & \psi^w\sin\theta^w - \varphi^w\cos\theta^w \\ -\sin\theta^w & \varphi^w & \cos\theta^w \end{bmatrix}$$

Note that the linearized rotations used in Eqs. 2.83, 2.84 and 2.85, involve that the resulting transformation matrices $\mathbf{A}^t$, $\mathbf{A}^{t,i}$, and $\mathbf{A}^{t,w}$, are no longer orthonormal.

2.5.2 Dynamic linearization

The dynamic linearization proposed in this thesis is not implemented in the results shown in further sections but it is derived as the basis for future work when efficient simulations are expected to compute.

The equations of motion of railroad vehicles are presented in Section 2.3 schematically in Eq. 2.37 and Eq. 2.79, the latter ones augmented with constraint equations. As a summary, they can be written as:

$$\begin{aligned} \mathbf{M}\ddot{\mathbf{q}} + \mathbf{C}_{\mathbf{q}}^T\lambda &= \mathbf{Q} \\ \mathbf{C}(\mathbf{q}, t) &= \mathbf{0} \end{aligned} \tag{2.86}$$

where $\mathbf{M}$ is the mass matrix, $\mathbf{C_q}$ is the jacobian matrix of the constraints vector $\mathbf{C}$, λ is the vector of Lagrange multipliers, $\mathbf{Q}$ is the vector of all generalized forces such as gravity, suspension, quadratic in system velocities or tangential contact forces, and $\ddot{\mathbf{q}}$ is the second-time derivative of the system generalized coordinates $\mathbf{q}$.

When the equations of motion are augmented with a constraint vector as in Eq. 2.86, they can be easily expressed in terms of independent coordinates $\mathbf{q}^{ind}$ if the constraint equations are not explicit fuctions of time (*scleronomous* system) [96]. As the lookup table constraint vector $\mathbf{C}^{wr}$ can be written as $\mathbf{C}^{wr} = \mathbf{C}^{wr}(\mathbf{q}^w, s^t, s^{wt}) = \mathbf{0}$, the first-time derivative vector of the coordinates $\dot{\mathbf{q}}^w$ can be written as:

$$\mathbf{C_q}\dot{\mathbf{q}}^w + \mathbf{C}_t = \mathbf{0} \tag{2.87}$$

where $\mathbf{C_q}$ and $\mathbf{C}_t$ are the Jacobian matrix and the partial time derivative vector of the constraints respectively. Identifying the independent and dependent coordinates and using the property that the Jacobian matrix of the dependent constraints is a square nonsingular matrix [97], it yields:

$$\mathbf{C}_\mathbf{q}^{ind}\dot{\mathbf{q}}^{ind} + \mathbf{C}_\mathbf{q}^{dep}\dot{\mathbf{q}}^{dep} = -\mathbf{C}_t \quad \rightarrow \quad \dot{\mathbf{q}}^{dep} = -\mathbf{C}_\mathbf{q}^{dep^{-1}}\left(\mathbf{C}_\mathbf{q}^{ind}\dot{\mathbf{q}}^{ind} + \mathbf{C}_t\right) \tag{2.88}$$

where the dependent and independent wheelset coordinates are $\mathbf{q}^{dep} = \begin{bmatrix} z^w & \varphi^w \end{bmatrix}^T$ and $\mathbf{q}^{ind} = \begin{bmatrix} x^w & y^w & \theta^w & \psi^w \end{bmatrix}^T$ respectively, and $\mathbf{C}_\mathbf{q}^{ind}$ and $\mathbf{C}_\mathbf{q}^{dep}$ are Jacobian sub-matrices associated with $\mathbf{q}^{ind}$ and $\mathbf{q}^{dep}$.

Rearranging the time derivative of the coordinates, one has:

$$\dot{\mathbf{q}}^w = \begin{bmatrix} \dot{\mathbf{q}}^{ind} \\ \dot{\mathbf{q}}^{dep} \end{bmatrix} = \begin{bmatrix} \mathbf{I} \\ -\mathbf{C}_\mathbf{q}^{dep^{-1}}\mathbf{C}_\mathbf{q}^{ind} \end{bmatrix}\dot{\mathbf{q}}^{ind} + \begin{bmatrix} \mathbf{0} \\ -\mathbf{C}_\mathbf{q}^{dep^{-1}}\mathbf{C}_t \end{bmatrix} \tag{2.89}$$

where, as the constraint equations are *scleronomic* constraints, $\mathbf{C}_t = \mathbf{0}$ and as a result, one can determine the matrix $\mathbf{B}$ that relates $\dot{\mathbf{q}}$ with $\dot{\mathbf{q}}^{ind}$ as:

$$\dot{\mathbf{q}}^{w} = \mathbf{B}\dot{\mathbf{q}}^{ind} = \begin{bmatrix} \mathbf{I} \\ -\mathbf{C}_{\mathbf{q}}^{dep^{-1}}\mathbf{C}_{\mathbf{q}}^{ind} \end{bmatrix} \dot{\mathbf{q}}^{ind} \tag{2.90}$$

The time derivative of Eq. 2.90 requires the computation of $\dot{\mathbf{B}}$. To this end, it is first necessary to calculate the time derivative Eq. 2.88 as:

$$\ddot{\mathbf{q}}^{dep} = -\mathbf{C}_{\mathbf{q}}^{dep^{-1}}\left[\mathbf{C}_{\mathbf{q}}^{ind}\ddot{\mathbf{q}}^{ind} - \dot{\mathbf{C}}_{\mathbf{q}}^{ind}\dot{\mathbf{q}}^{ind} - \dot{\mathbf{C}}_{\mathbf{q}}^{dep}\dot{\mathbf{q}}^{dep}\right] \tag{2.91}$$

Therefore $\dot{\mathbf{B}}$ can be obtained as:

$$\dot{\mathbf{B}} = \frac{d}{dt}\begin{bmatrix} \mathbf{I} \\ -\mathbf{C}_{\mathbf{q}}^{dep^{-1}}\mathbf{C}_{\mathbf{q}}^{ind} \end{bmatrix} = \begin{bmatrix} \mathbf{0} \\ -\mathbf{C}_{\mathbf{q}}^{dep^{-1}}\left(\dot{\mathbf{C}}_{\mathbf{q}}^{ind} - \dot{\mathbf{C}}_{\mathbf{q}}^{dep}\mathbf{C}_{\mathbf{q}}^{dep^{-1}}\mathbf{C}_{\mathbf{q}}^{ind}\right) \end{bmatrix} \tag{2.92}$$

The definition of $\dot{\mathbf{B}}$ at Eq. 2.92 allows to rewrite the augmented equations of motion of Eq. 2.86 in terms of the independent coordinates by substituing $\ddot{\mathbf{q}} = \mathbf{B}\ddot{\mathbf{q}}^{ind} + \dot{\mathbf{B}}\dot{\mathbf{q}}^{ind}$ as follows:

$$\mathbf{M}\left(\mathbf{B}\ddot{\mathbf{q}}^{ind} + \dot{\mathbf{B}}\dot{\mathbf{q}}^{ind}\right) + \mathbf{C}_{\mathbf{q}}^{wrT}\boldsymbol{\lambda}^{wr} = \mathbf{Q} \tag{2.93}$$

Premultiplying Eq. 2.93 by the traspose matrix $\mathbf{B}^T$ and knowing that the product $\mathbf{B}^T\mathbf{C}_{\mathbf{q}}^T$ is null [97], one can write the equations of motion in terms of the independent coordinates as:

$$\mathbf{B}^T\mathbf{M}\mathbf{B}\ddot{\mathbf{q}}^{ind} + \mathbf{B}^T\left(\mathbf{M}\dot{\mathbf{B}}\dot{\mathbf{q}}^{ind} - \mathbf{Q}\right) = \mathbf{0} \tag{2.94}$$

2.5.2.1 Partial linearization

The equations of motion of Eq. 2.94 can be written as a function vector $\mathbf{f}$ as

$$\mathbf{f}\left(\ddot{\mathbf{q}}^{ind}, \dot{\mathbf{q}}^{ind}, \mathbf{q}^{ind}\right) = \mathbf{0} \tag{2.95}$$

thus, neglecting the high order terms, they can numerically be linearized respect to a reference position $\mathbf{q}^{ref}$ as:

$$\left.\frac{\partial \mathbf{f}}{\partial \ddot{\mathbf{q}}^{ind}}\right|_{\mathbf{q}^{ref}} \left(\ddot{\mathbf{q}}^{ind} - \ddot{\mathbf{q}}^{ref}\right) + \left.\frac{\partial \mathbf{f}}{\partial \dot{\mathbf{q}}^{ind}}\right|_{\mathbf{q}^{ref}} \left(\dot{\mathbf{q}}^{ind} - \dot{\mathbf{q}}^{ref}\right) + \left.\frac{\partial \mathbf{f}}{\partial \mathbf{q}^{ind}}\right|_{\mathbf{q}^{ref}} \left(\mathbf{q}^{ind} - \mathbf{q}^{ref}\right) = \mathbf{0} \tag{2.96}$$

where the mass, damping and stiffness matrices $\mathbf{M}_{lin}$, $\mathbf{C}_{lin}$ and $\mathbf{K}_{lin}$ of the linearized system can be identified as

$$\left.\frac{\partial \mathbf{f}}{\partial \ddot{\mathbf{q}}^{ind}}\right|_{\mathbf{q}^{ref}} = \mathbf{M}_{lin}, \qquad \left.\frac{\partial \mathbf{f}}{\partial \dot{\mathbf{q}}^{ind}}\right|_{\mathbf{q}^{ref}} = \mathbf{C}_{lin}, \qquad \left.\frac{\partial \mathbf{f}}{\partial \mathbf{q}^{ind}}\right|_{\mathbf{q}^{ref}} = \mathbf{K}_{lin} \tag{2.97}$$

Equations 2.96 and 2.97 are particularized for the so-called reference position $\mathbf{q}^{ref}$. A reference position for a mechanical system is defined as the position that implies the equilibrium of forces in the system keeping the vehicle in a stationary state. A system reference position involves that slight changes in the system coordinates $\mathbf{q}$ with respect to the reference ones $\mathbf{q}^{ref}$ tend the system to recuperate the initial reference position. In railroad mechanical system, there are many reference positions. The most commonly one is the repose reference position, which can be calculated by solving Eq. 2.95 for $\ddot{\mathbf{q}}^{ind} = \mathbf{0}$ and $\dot{\mathbf{q}}^{ind} = \mathbf{0}$. Other common reference positions are obtained at constant curvature track strethces as a function of the vehicle forward velocity. In these ones, the use of the defined moving reference frame (TF) is crucial since the vehicle coordinates remain constant (except for the *pitch*) when negotiating the curve.

In this thesis a partial linearization of the equations of motion is proposed, because due to the high non-linear behaviour of the contact forces this term is not linearized while the suspension, inertia and quadratic terms in velocity forces are linearized. Consequently, the partially linearized equations of motion yield:

$$\mathbf{M}_{lin}\left(\ddot{\mathbf{q}}^{ind}-\ddot{\mathbf{q}}^{ref}\right)+\mathbf{C}_{lin}\left(\dot{\mathbf{q}}^{ind}-\dot{\mathbf{q}}^{ref}\right)+\mathbf{K}_{lin}\left(\mathbf{q}^{ind}-\mathbf{q}^{ref}\right)=\mathbf{B}^{T}\mathbf{Q}_{contact} \tag{2.98}$$

The stiffness, damping and mass matrices can be calculated numerically using many procedures that can be found in the literature such as the finite diference method with central differences where the function vector $\mathbf{f}$ of Eq. 2.96 is evaluated in the equilibrium position, velocity and acceleration respectively. Note that vector $\mathbf{f}$, no longer accounts for the contact forces $\mathbf{Q}_{contact}$.

2.5.2.2 Numerical interpolation in the linearized equations of motion

The partially linearized equations of motion presented in the previous section 2.5.2.1 can accurately reproduce the dynamic behaviour of a railroad vehicle if the vehicle movement is in the proximity of the equilibrium positions where the mass, damping and stiffness matrices were calculated. In order to account for precise results when a railroad vehicle is running on an arbitrary track, a preprocessing stage must be performed. This preprocessing stage is described below:

- The different track streches where the vehicle can reach stationary movement are identified and their corresponding positions are evaluated.
- Linearized mass, damping and stiffness matrices are evaluated according to the different calculated positions.

- A linear interpolation between the sequentially linearized mass, damping and stiffness matrices is carried out in order to generate an adequate number of matrices to be used when a vehicle body is running on transition streches.

Once this preprocessing stage is done and during the dynamic simulation of a railroad vehicle, each vehicle body identifies which of the precomputed mass, damping and stiffness matrices uses per time step.

Chapter 3

Design and Testing

3.1 Introduction

In this chapter, the design of a scaled railroad vehicle to be used in a 5-inch gauge railroad track and subject to specific requirements is derived. This vehicle, in which different inertial, guiding, recording and distance devices are installed, is mainly designed to be used in a 5-inch gauge railroad track and, as far as possible, designed in accordance to a real railroad vehicle. Thus, the different technical solutions adopted to achieve its current configuration are described in the following subsections. In addition, a parametric identification to obtain its mechanical parameters is accomplished in order to validate experimental tests with simulation results.

Moreover, a total track length of 70 m is measured on the 5-inch scaled railroad track where the vehicle is tested and whose purpose is to obtain a real track data to compare the simulation results. The innovative and accurate procedure followed to measured these track defects is also detailed. Finally, some experimental tests developed with the scaled vehicle in the measured track are carried out and its acquired results presented.

3.2 Design of a 5-inch scaled railroad vehicle

The design of a scaled railroad vehicle comprises a challenging task. On the one hand, it has to be representative with respect to a real train because one of its main purposes is to obtain dynamic data whose analysis will help in the simulation of full scale vehicles. In case this dynamic behavior is the primary area of interest, it should also account for the differences in the scaling such as geometric, inertial or suspension stiffness scaling factors that influence in the dynamic behavior. On the other hand, its reduced size implies a great difficulty in inserting different and important components such as sensors, transmission, or suspension elements.

In the following subsections, a review of different criteria for the similarity scaling in railroad vehicles is presented. Also, the concluding imperative design requirements, sensor positioning, wheel-rail geometry and the design of the primary and secondary suspensions together with the motor transmission in the scaled vehicle are described. Moreover, in Appendix A one can find the construction drawings of the prototype.

3.2.1 Similarity scaling

The use of prototype vehicles for the investigation of railway vehicle dynamics is important in the railroad industry. Even with the development of improvements in simulation techniques, which have lowered the necessity of prototype vehicles, the possibility to validate simulating results with experimental data is always of great interest. In addition, in order to reduce operational costs, the use of scaled vehicles provide a useful tool to easily account for experimental results. However and regardless of the cost savings, the use of scaled vehicles comprise disadvantages related to the geometry scalling that should be given due consideration to the consequences of these modifications.

Similarity laws are of particular interest when experimental results are obtained in scaled mechanisms. They were first introduced by Reynolds in 1883 [80], who applied

the scaling similarities to the hydrodynamics. Analogously, this approach can be applied to mechanical systems following different criteria as a function of the most interested physical parameters [34]. There exist different approaches to scaling, that can use dimensional analysis to obtain the scaling factors, and other approches that firstly derive the equations of motion to then identify the scaling factors to keep similarity. Some examples can be found by Jaschinski in [36] and by Illingworth in [32]. Also, in [34] it can be found the scaling strategies followed by three different institutions in the definition of a scaled rig; at the Manchester Metropolitan University (MMU), at the Institute for Robotics and System Dynamics of DLR and at the French National Research Institute (INRETS).

The general procedure for setting up a system of similarity starts by the definition of the length scaling factor φ_L and the time scaling factor φ_t as:

$$\varphi_L = \frac{L_1}{L_0}, \qquad \varphi_t = \frac{t_1}{t_0} \tag{3.1}$$

where L and t refer to the characteristic length and time and subscripts 1 and 0 to the full and scaled vehicle respectively. Likewise, scaling factors for velocity φ_v, acceleration φ_a and density φ_ρ can be calculated as:

$$\varphi_v = \frac{\varphi_L}{\varphi_t}, \qquad \varphi_a = \frac{\varphi_L}{\varphi_t^2}, \qquad \varphi_\rho = \frac{\rho_1}{\rho_0} \tag{3.2}$$

Then, the scaling factors for mass and rotational inertia, φ_m and φ_I can be obtained as:

$$\varphi_m = \varphi_\rho \varphi_L^3, \qquad \varphi_I = \varphi_m \varphi_l^2 \tag{3.3}$$

After these dimensionsless scaling factors have been calculated, a specific scaling strategy that depends on the main purpose of the prototype can be followed to obtain,

		MMU	**DLR**	**INRETS**
Length scaling	φ_L	5	5	5
Time scaling	φ_t	1	$\sqrt{5}$	4
Velocity scaling	φ_v	5	$\sqrt{5}$	1
Acceleration scaling	φ_a	5	1	4
Frequency scaling	φ_f	1	$1/\sqrt{5}$	1/4
Density scaling	φ_ρ	1	0.5	1
Mass scaling	φ_m	125	62.5	64
Rotational inertia scaling	φ_I	3125	1562.5	1024
Inertial force scaling	φ_F	625	62.5	16
Stiffness scaling	φ_k	125	12.5	4

TABLE 3.1: Comparison of scaling strategies

among other parameters, factors such as creep forces, Young's modulus, stress, strain, stiffness, damping, friction or frequency. Table 3.1 shows different scaling factors according to the scaling strategies followed at MMU, DLR and INRETS whose main target can be summarized as follows [34]:

- All scaled vehicles are designed in a 1/5 scale. The equivalent track gauge is 287mm, which is 1/5 of the standard track gauge of 1435mm.
- The goal of the MMU scaled vehicle is to investigate the dynamic behavior of independently driven wheelsets for light rail applications.
- The goal o the DLR scaled vehicle is the nonlinear running behavior of passenger vehicles and validation of numerical models.
- The goal of the INRETS scaled vehicle is to study and optimize the stability of the bogie when vertical loads are modified and different suspension elements used.

3.2.2 Initial requirements of scaled vehicle

As already stated in the previous section, the main purpose of a scaled vehicle should be mandatory when following a specific scaling strategy. In this work, the main objective

is to make a comparison between the numerical procedure presented in Chapter 2 with respect to experimental results of a vehicle running on a real 5-inch gauge railroad track that is already built. Therefore, it should be designed accordingly to this track and as a consequence, the length scaling factor φ_L with respect to a standard railroad track of 1435mm track gauge is:

$$\varphi_L = 11.3 \tag{3.4}$$

Additionally, once the scaled vehicle satisfies the length scaling factor it should account, as far as possible, for a similar dynamic behavior than a real railroad vehicle. In this case, the adopted vehicle model in which the design of the prototype is based on, is the 'ML-95' trainset that operates in the Lisbon subway company and is manufactured by Bombardier Inc. This trainset is modeled as a single wagon in [66], where the different mechanical properties can be obtained. Some of its features are listed below:

- Four wheelsets (mass = 933 kg)
- Eight axleboxes (mass = 176 kg)
- Two bogie frames (mass = 1982 kg)
- One carbody (mass = 11160 kg)
- Primary and secondary suspension elements
- Traction rods and transversal dampers for the carbody-bogie connection

However, a length scaling factor of $\varphi_L = 11.3$ involves a great size reduction in the scaled vehicle which derives in scaling factor conflicts, as it uses to happen when applying scaling criteria [34], such as the conflict in the scaling density φ_ρ or mass φ_m. In this case, to avoid wear problems, φ_ρ cannot be achieved because the same steel material is used for the wheel/rail design. Also, φ_m cannot be fulfilled because the number of sensors, batteries and electronic devices that will be mounted on the vehicle cannot be

predicted accurately. That is why the selected criterion for its design is a commitment between the mandatory φ_L and desired dynamic behaviour.

The adopted requirements that lead to the final design of the vehicle can be listed as:

1. **Average forward velocity**: The ML-95 vehicle is supposed to operate at a mean forward velocity of V =80 km/h. As the wheel radiuss is $R^{wh} = 0.43$m, that makes a total angular velocity ω^{wh} of:

$$\omega^{wh} = \frac{V}{R^{wh}} = 51.68 rad/s \tag{3.5}$$

   which is the nominal angular velocity that the wheelsets of the scaled vehicle should be able to reach.

2. **Vertical frequency**: Regardless of the fact that the scaled vehicle will be affected by track irregularities with a different pattern from those that affect to real tracks, the second main requirement of the vehicle is to design it with the same vertical frequency at wheelset-bogie level and at bogie-carbody level than the ML-95 one. This is, the vertical frequency that the primary and secondary suspensions have according to their suspended masses. To this end, a static estimation of the ML95 vehicle can be done as follows:

   - The total suspended mass of the ML95 vehicle m_{susp} can be calculated as:

$$m_{susp} = 2m^{bg} + m^{cb} = 15124 kg \tag{3.6}$$

     where m^{bg} is the mass of a bogie frame and m^{cb} is the mass of the carbody

   - Each wheelset is supossed to have two vertical springs (left and right side) whose vertical stiffness is $k^v = 1.28 \cdot 10^6$N/m.

   - The total suspended mass m_{susp} can be divided into the number of wheelsets n^{wh} in order to calculate the vertical frequency per wheelset in the primary

suspension ω_{ML95}^{prim} as:

$$\omega_{ML95}^{prim} = \sqrt{\frac{4k^v}{m_{susp}}} = 18.40 rad/s \tag{3.7}$$

- With regard to the secondary suspension, the suspended mass only comprises the mass of the carbody m^{cb}. Four *airsprings* characterized the vertical stiffness of the secondary suspension with $k_{air}^v = 250 \cdot 10^3$N/m. As there are two frames, the vertical frequency in the secondary suspension per frame ω_{ML95}^{second} can be obtained as:

$$\omega_{ML95}^{second} = \sqrt{\frac{4k_{air}^v}{m_{cb}}} = 9.47 rad/s \tag{3.8}$$

As a result, the scaled railroad vehicle should have as vertical frequencies, ω_{ML95}^{prim} and ω_{ML95}^{second} for the primary suspension per wheelset and for the secondary suspension per frame respectively.

3. **Sensor positioning**: The design of the scaled vehicle should allow the installation of inertial measurement units (IMU) at wheelset, frame and carbody level together with distance lasers to measure the deflection of the primary and secondary suspension. In addition, it has to allow a proper configuration of the transmission and space enough for the data acquisition system that will be laid on top of the carbody level.

3.2.3 Wheel - Rail surfaces

The design of the wheel rail surfaces is developed in this section. The rail real cross section is obtained as a bending of a sheet steel metal of 2 mm thickness whose cross section can be seen in Fig. 3.1.

Then, according to the formulation proposed in Chapter 2, it is necessary to obtain the rail cross section as a function of the transverse surface parameter s_2^r. Moreover, if one

FIGURE 3.1: Real cross section of the scaled rail

analyzes Fig. 3.1 by a 2D scanning image, it is possible to obtain a discretized number of points of the rail head. Table 3.2 shows this discretization whose representation is given in Fig. 3.2.

Note that the rail head is almost straight at the top of its surface. This means that, together with the wheel surface, the surfaces in contact are not convex, which may incur in infinite number of contact points. This singularity is avoided due to the bank angle of the rails, that is defined as the rotation of the profile frame about the tangent to the reference line.

Concerning the wheel, it has been designed based on the ML-95 wheel profile. This is, the wheel tread has a conicity of $\lambda^w = 1/30$ and its width (tread width) is 8.8 mm. The flange has a angle of attack of 75º and its width is 3 mm. With regard to the wheel radius, the first initial requirement has been adopted. As the wheel angular velocity of Eq. 3.5 must reach $\omega^{wh} = 51.68$ rad/s and the maximum longitudinal speed should not exceed 2 m/s, the designed wheel nominal radius R^{wh} is:

$$R^{wh} = \frac{V}{\omega^{wh}} \rightarrow R^{wh} = 38.1mm \tag{3.9}$$

Rail section			
y (mm)	z (mm)	y (mm)	z (mm)
-3.1359	-1.4859	0	0
-3.0931	-1.2003	0.3957	-0.0000
-3.0383	-1.0051	0.9815	-0.0002
-2.9626	-0.8109	1.6007	-0.0017
-2.7963	-0.5775	1.7851	-0.0167
-2.6104	-0.3892	1.9762	-0.0385
-2.4871	-0.2781	2.1865	-0.1063
-2.3574	-0.1823	2.3574	-0.1823
-2.1865	-0.1063	2.4871	-0.2781
-1.9762	-0.0385	2.6104	-0.3892
-1.7851	-0.0167	2.7963	-0.5775
-1.6007	-0.0017	2.9626	-0.8109
-0.9815	-0.0002	3.0383	-1.0051
-0.3957	-0.0000	3.0931	-1.2003
		3.1359	-1.4859

TABLE 3.2: Rail discretized points

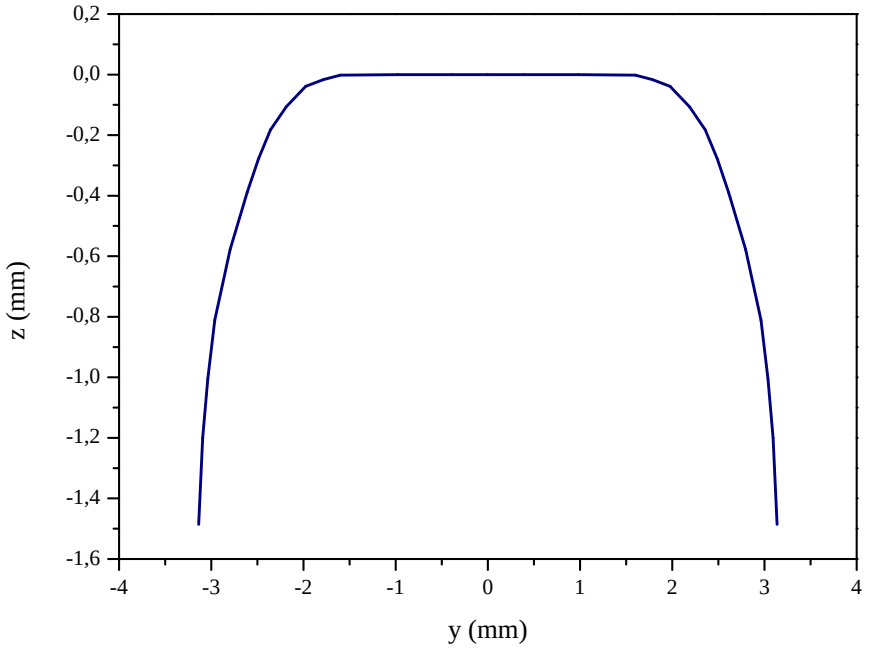

FIGURE 3.2: Cross section of the scaled rail

Wheel tread (left)							
y (mm)	z (mm)	y (mm)	z (mm)	y (mm)	z (mm)	y (mm)	z (mm)
-6.4000	38.2109	-3.1000	38.1021	0.2000	37.9934	3.5000	37.8847
-6.1000	38.2010	-2.8000	38.0923	0.5000	37.9835	3.8000	37.8748
-5.8000	38.1911	-2.5000	38.0824	0.8000	37.9736	4.1000	37.8649
-5.5000	38.1812	-2.2000	38.0725	1.1000	37.9637	4.4000	37.8550
-5.2000	38.1713	-1.9000	38.0626	1.4000	37.9539	4.7000	37.8451
-4.9000	38.1615	-1.6000	38.0527	1.7000	37.9440	5.0000	37.8352
-4.6000	38.1516	-1.3000	38.0428	2.0000	37.9341	5.3000	37.8253
-4.3000	38.1417	-1.0000	38.0329	2.3000	37.9242	5.6000	37.8155
-4.0000	38.1318	-0.7000	38.0231	2.6000	37.9143	5.9000	37.8056
-3.7000	38.1219	-0.4000	38.0132	2.9000	37.9044	6.2000	37.7957
-3.4000	38.1120	-0.1000	38.0033	3.2000	37.8945	6.5000	37.7858

TABLE 3.3: Rail discretized tread points

where, as shown in Fig. 3.3, due to the conicity of the tread, the nominal wheel radius R^{wh} is located in the center of the tread.

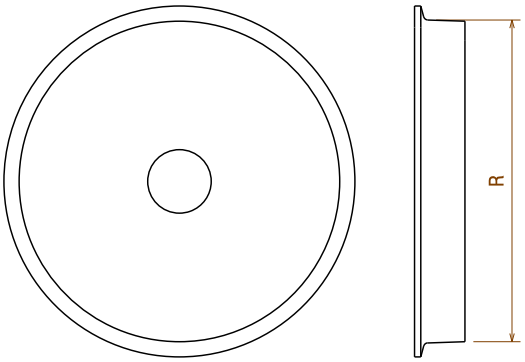

FIGURE 3.3: Wheel design

Knowing the exact geometry of the wheel, one can easily identify discretized points of the wheel surface. As a result of the proposed contact formulation of Section 2.4, the wheel tread and flange are discretized separately, and the corresponding nodal points are shown in Table 3.3 for the thread surface, and Table 3.4 for the flange one.

Finally, Fig. 3.4 shows the discretized points of the left wheel tread and flange in black and red line respectively. Note that in Fig. 3.4, flange and tread surfaces are discretized

Wheel flange (left)							
y (mm)	z (mm)	y (mm)	z (mm)	y (mm)	z (mm)	y (mm)	z (mm)
-5.0400	37.7424	-5.7000	40.2356	-6.3600	42.3665	-7.0200	42.7363
-5.1000	37.9690	-5.7600	40.4623	-6.4200	42.4830	-7.0800	42.6759
-5.1600	38.1957	-5.8200	40.6890	-6.4800	42.5989	-7.1400	42.5742
-5.2200	38.4224	-5.8800	40.9244	-6.5400	42.6956	-7.2000	42.4450
-5.2800	38.6490	-5.9400	41.1610	-6.6000	42.7450	-7.2600	42.2819
-5.3400	38.8757	-6.0000	41.3795	-6.6600	42.7595	-7.3200	42.0286
-5.4000	39.0996	-6.0600	41.5701	-6.7200	42.7697	-7.3800	41.6241
-5.4600	39.3263	-6.1200	41.7518	-6.7800	42.7747	-7.4400	40.4869
-5.5200	39.5543	-6.1800	41.9245	-6.8400	42.7736	-7.5000	37.8550
-5.5800	39.7822	-6.2400	42.0860	-6.9000	42.7668		
-5.6400	40.0090	-6.3000	42.2341	-6.9600	42.7551		

TABLE 3.4: Rail discretized flange points

independently, and as a result, there is intersection between them which does not affect to the dynamic simulations as will be shown in further sections.

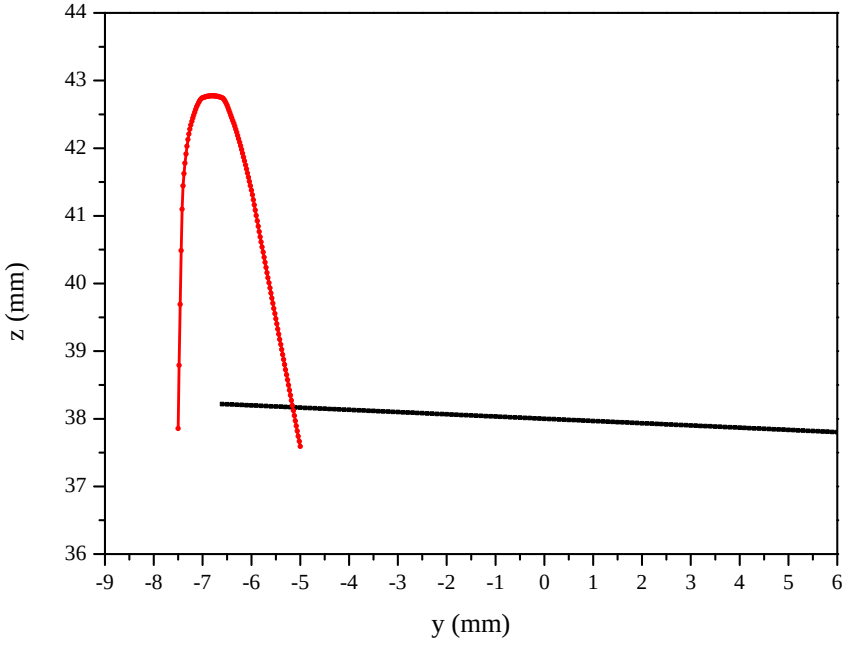

FIGURE 3.4: Wheel flange cross section

3.2.4 Design of primary suspension

Before deciding size, length and shape of suspension elements in the primary suspension, it is first necessary to set up the geometry of the connecting bodies. As the primary suspension transmits the loads from the bogie frames to the rotating wheelsets, the geometry of the axleboxes has to be designed.

Axleboxes are installed in each extremity of each wheelset and are formed by roller bearings that act as revolute joints between wheelsets and axleboxes. Therefore, it is possible to provide a horizontal plane where the suspension elements can be attached. Figure 3.5 shows the two axleboxes with their horizontal plane installed on one wheelset.

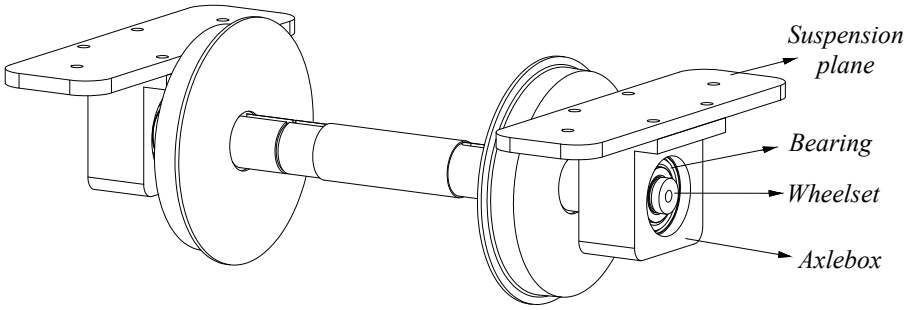

FIGURE 3.5: Axlebox in wheelset

Nevertheless, due to the third initial requirement of section 3.2.2, the location of a inertial IMU at the wheelset level requieres a special design for one of the axleboxes. In this case, axleboxes of one of the wheelsets are designed as shown in Fig. 3.6.

Primary suspension elements can be installed in the horizontal plane of Fig. 3.5. As the bogie frame is also a horizontal plane, the adopted solution for the attachment points is through *guiding supports*, which act as fixing elements that constraint the $X - Y$ movement of the suspension element as shown in Fig. 3.7.

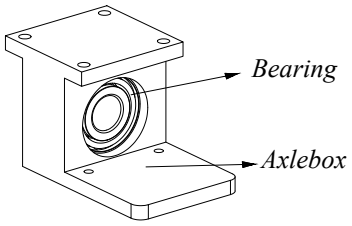

FIGURE 3.6: Axlebox for IMU installation

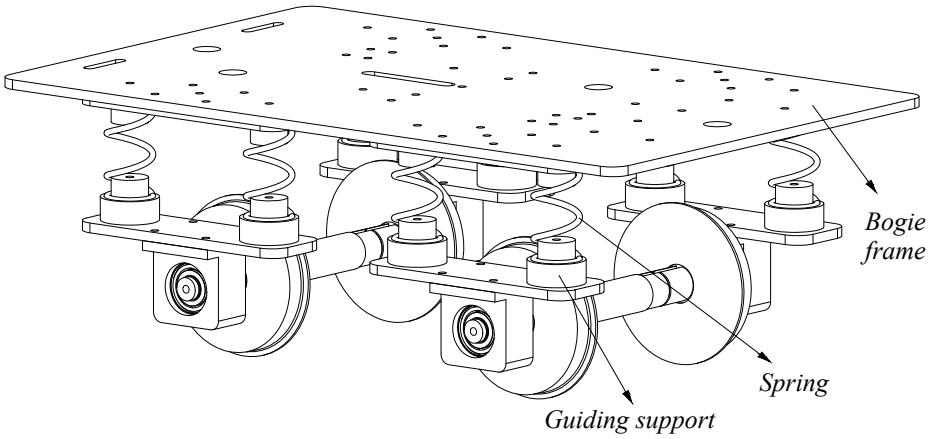

FIGURE 3.7: Primary suspension elements

Note that in Fig. 3.7, primary suspension elements are only set up in the vertical direction. There are no horizontal or lateral suspension elements, which means that the horizontal and lateral stiffness will be provided by the vertical springs when they are deformed in the horizontal $X-Y$ plane.

Once the technical solution for the primary suspension is defined, it is the turn for selecting the appropriate spring size according to the initial requirements. As shown in Eq. 3.7, the vertical frequency per wheelset is equal to $\omega_{prim} = 18.40$ rad/s. As there are four vertical springs per wheelset, one has that the stiffness of the vertical springs at the scaled vehicle k^v_{prim} can be calculated as:

$$k^v_{prim} = \frac{1}{4}\omega^2_{prim} m^{wh}_{susp} \tag{3.10}$$

Initial vertical spring - Primary suspension	
k^v_{prim}	392 N/m
L_0	90mm
L_{weight}	58.40mm
D_{int}	19mm
p	6 mm
e	1.5 mm
No. spirals	15

TABLE 3.5: Initial primary suspension features

where m^{wh}_{susp} is the suspended mass per wheelset. In a preliminar stage, m^{wh}_{susp} is assumed to be 4.5 kg and as a result, the initial vertical stiffness of each primary suspension spring is:

$$k^v_{prim} = 380N/m \tag{3.11}$$

which allows the use of the following spring for the primary suspension whose features are listed in Table 3.5

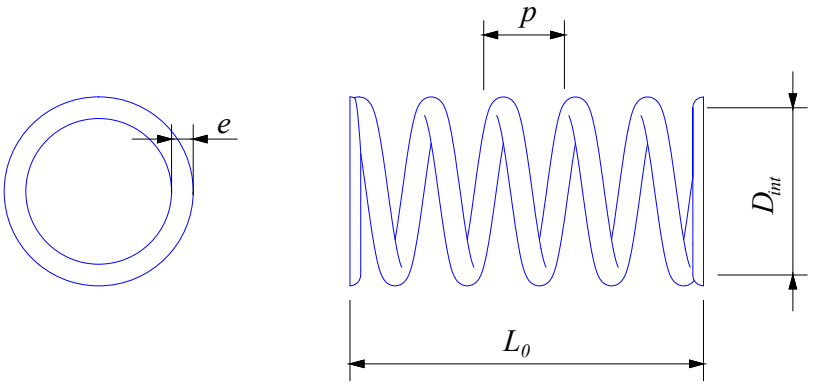

FIGURE 3.8: Primary suspension spring definition

The chosen spring for the primary suspension needs to satisfy the lateral stability of the system as they are the only elements that provide stiffness in the $X - Y$ plane.

Accordingly, in the following subsection a stability criterion to validate the springs lateral stiffness is presented.

3.2.4.1 Lateral stability of primary suspension

Figure 3.9 shows a vehicle laterally displaced an amount y. Assuming that the vertical load due to the weight is the only load, the lateral equilibrium of forces can be obtained as:

$$\sum F_y = 8k_y y - 8\frac{m_s g}{8}\sin\alpha \tag{3.12}$$

where m_s is the suspended mass of the vehicle, α is the angle of the spring force with respect to the vertical Z-axis and g is the gravity acceleration. Here, the number 8 comes from the number of suspension elements in the primary suspension per bogie frame, so m_s refers to the half of the suspended mass of the whole vehicle. If the small angle assumption is made and L_{weight} is the deformed spring length due to gravity, one has:

$$\sin\alpha \approx \alpha \approx \tan\alpha = \frac{y}{L_{weight}} \tag{3.13}$$

That can be substituted in Eq. 3.12 as:

$$\sum F_y = \left(8k_y - \frac{m_s g}{L_{weight}}\right)\cdot y \tag{3.14}$$

According to this stability criterion, the term in parenthesis of Eq. 3.14 is the lateral stiffness of the system. In order to be a stable system, its value has to be positive. Thus, the lateral stiffness of the vertical springs of the system k_y must be:

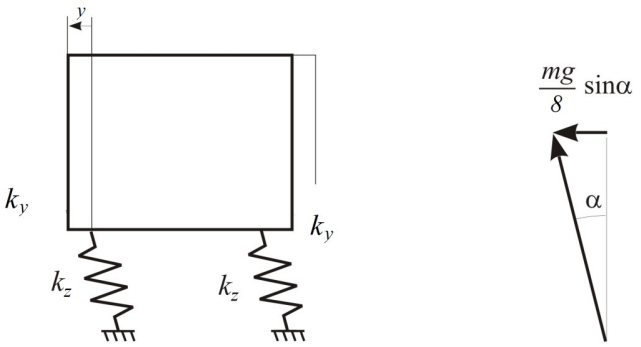

FIGURE 3.9: Lateral stability of primary suspension

$$8k_y - \frac{m_s g}{L_{weight}} > 0 \qquad \rightarrow \qquad k_y > \frac{m_s g}{8L_{weight}} \tag{3.15}$$

Replacing in Eq. 3.15 the values of the selected vertical springs for the primary suspension, and identifying m_s as the half of the total suspended mass of the vehicle as $m_s = 0.5 \cdot (m_{cb} + 2m_{bg})$ one has that the lateral stiffness of the vertical springs k_y^{prim} must be:

$$k_y^{prim} > 179.71 \frac{N}{m} \tag{3.16}$$

In order to calculate the lateral stiffness of the selected spring in the primary suspension, one can refer to the European standard DIN EN 13906-1 [16], where the design and calculation of cylindrical helical springs made of round wire and bars is proposed. As a summary, the value of the lateral stiffness for a spring is only constant for small deflections and is highly influenced by the joining conditions. Following the procedure presented in [16], the selected spring for the primary suspension of Table 3.5 has a lateral stiffness of $k_{y-initial}^{prim}$:

$$k_y^{prim} = 50.1 \frac{N}{m} \tag{3.17}$$

Selected vertical spring - Primary suspension	
k^v_{prim}	8700 N/m
L_0	50mm
L_{weight}	48.8mm
D_{int}	19mm
p	11.1 mm
e	2.5 mm
No. spirals	4.5
k^v_{y-prim}	4090 N/m

TABLE 3.6: Final primary suspension features

From Eq. 3.17 it is easily observed that the selected vertical spring for the lateral stiffness is no longer valid and therefore a stiffer suspension element has to be determined. This means that the initial requirement of vertical frequency is not accomplished. As a result and in order to account for considerable changes in the mass of the system, the vertical spring shown in Fig. 3.10 with the features given in Table 3.6 is selected.

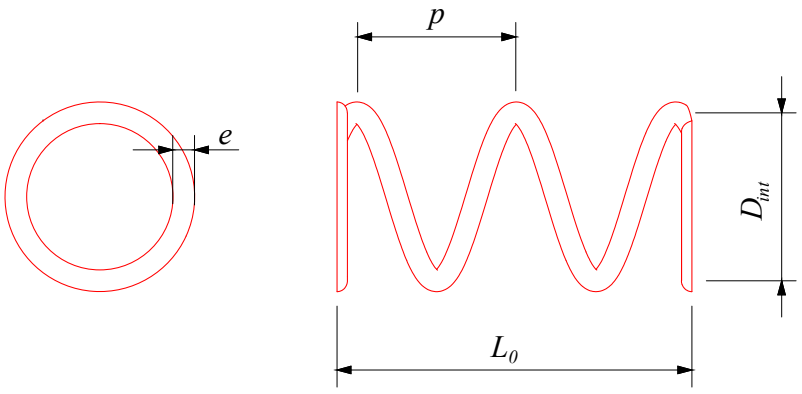

FIGURE 3.10: Final primary suspension spring definition

3.2.5 Design of secondary suspension

For the secondary suspension it is clear that the attachment points of the suspension elements between the carbody and the corresponding bogie frames remain in horizontal

planes due to their geometry as it can be seen in Fig. 3.11. Together with eight vertical springs and four per bogie frame, there is a total of four dampers whose main purpose is to increase the damping ratio of the carbody. Moreover it also has the possibility to include 4 anti-yaw spring-damper elements that can also be seen in Fig. 3.11. Finally, these anti-yaw suspension elements are not finally installed in the vehicle.

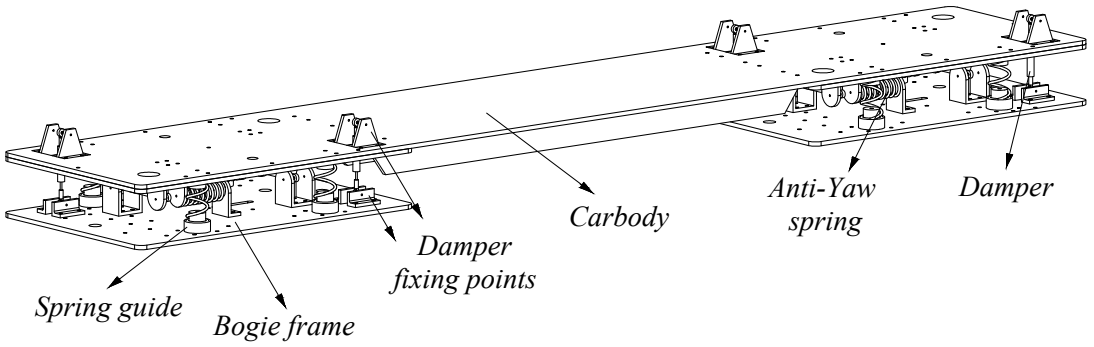

FIGURE 3.11: Secondary suspension

Following the same procedure that the one presented in Section 3.2.4, the initial requirement of the vertical frequency of the secondary suspension per frame $\omega_{second} = 9.47$ rad/s, one can obtain the stiffness of the vertical springs at the scaled vehicle k^v_{second} as:

$$k^v_{second} = \frac{1}{4}\omega^2_{second} m^{second}_{susp} \tag{3.18}$$

where m^{second}_{susp} is the suspended mass per frame, which coincides with the half of the carbody mass plus the estimated sensors and auxiliary elements mass. Equation 3.18 is divided by four because that is the number of vertical springs per frame. In a preliminar stage, m^{second}_{susp} is assumed to be 3.7 kg and as a result, the initial vertical stiffness of each secondary suspension element must be:

$$k^v_{second} = 83.3 N/m \tag{3.19}$$

Damper element	
A	61 mm
B	41 mm
C	2 mm
D	8 mm
E	2 mm
v_{max}^{115N}	0.25 m/s

TABLE 3.7: Damper element

which allows the use of springs for the secondary suspension that fulfill the requirements with properties such as initial undeformed length of $L_0 = 120$ mm, 18 mm spring inner diameter, 1 mm wire diameter and vertical stiffness of $k_{second}^{v} = 120$ N/m.

With regard to the damper elements and due to the small space available in its installation, four elements of the miniature model WM-Z of the Weforma GmbH company are used. The scheme and features are given in Fig. 3.12 and Table 3.7, respectively. Note that in Table 3.7, v_{max}^{115N} refers to the maximum speed of the damper when it is loaded at the maximum compression force of 115 N.

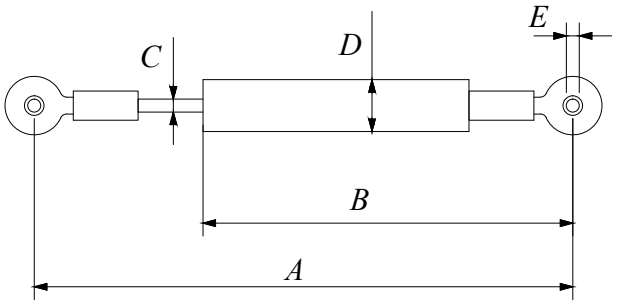

FIGURE 3.12: Damper element

3.2.5.1 Lateral stability of secondary suspension

The chosen spring for the secondary suspension also needs to satisfy the lateral stability of the system. Accordingly to the procedure follow for the primary suspension in Section

3.2.4.1, one can compute Eq. 3.15 to obtain:

$$k_y^{second} > 30.97 \frac{N}{m} \tag{3.20}$$

while for the initial spring of the secondary suspension and using the European standard DIN EN 13906-1 [16] one can obtain a lateral stiffness of $k_{y-second}^{v} = 2.15$ N/m. This means, that similarly to the primary suspension, the initial requirement of the vertical frequency in the secondary suspension cannot be achieved and as a result, a stiffer spring must be selected. To this end, the selected spring for the secondary suspension remains the same than for the primary suspension, with the difference in the number of suspension elements. This is, even when the springs for both suspensions are the same, there is a total of 16 and 8 elements for the primary and secondary suspension respectively.

3.2.6 Design of transmission

The design of the transmission of the scaled vehicle is a difficult task considering the lack of space between the primary suspension and wheelsets that requires a commitment between power and functionality. To this end, a preliminary design is derived based on the minimum power required to fulfill the initial requirements.

Wheels are expected to roll at $\omega^{wh} = 51.68$ rad/s as given by Eq. 3.5. According to the wheel radiuss ($R = 0.0381$ m), if the nominal forward velocity of $V = 2$ m/s is expected to be reached in x longitudinal meters at a constant rate and starting at static equilibrium, one has:

$$x = \frac{1}{2}\hat{a}\hat{t}^2 \qquad \rightarrow \qquad \hat{a} = \frac{V^2}{2x} \tag{3.21}$$

where $\hat{a}$ is the constant longitudinal acceleration, and $\hat{t} = V/\hat{a}$. Then, the required motor torque T_{motor} to get the required acceleration can be calculated as $T_{motor} = maR$ where m is the total mass of the vehicle. The required motor power $\dot{W}_{motor}$ can be computed as

$$\dot{W}_{motor} = T_{motor}\omega_{motor} \tag{3.22}$$

Note that ω_{motor} is the angular velocity of the motor, and it is related to the angular velocity of the wheelset ω^{wh} by $\omega_{motor} = \eta^{tr}\omega^{wh}$, where η^{tr} is the gear ratio.

Before selecting a DC motor that provides the power to the scaled train, it is first necessary to account for the power losses of the system. In this case, one has to account for the power loss in the transmission system together with the rolling resistance. Aerodynamic forces can be neglected due to the low forward velocity of the vehicle. With regard to the power loss in the transmission system $\dot{W}_{tr}$, one can estimate them as a 20% of the net power of the motor while for the rolling resistance T_{roll} one can predict it as the normal force displaced an eccentricity μ_r as shown in Fig. 3.13, where W is the weight of the vehicle, N is the normal force, F is the motor force and F_{roll} is the rolling resistance force.

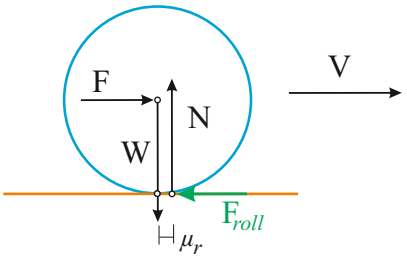

FIGURE 3.13: Rolling resistance

The eccentricity μ_r is calculated as in [107] by *railroad steel wheel on steel rail* whose value arises up to $\mu_r = 0.1$ mm accounting for the wheel radius. Therefore the rolling

Electric DC motor	
Motor Type	DC Motor with Encoder
Output Power (Mechanical)	$30W$
Rated Torque	$5.1\ kg \cdot cm$
Maximum speed	$588\ rpm$
Gear Ratio	$4\ \frac{1}{4} : 1$
Weight	$1.3kg$

TABLE 3.8: Electric DC motor

resistance torque T_{roll} can be calculated as $T_{roll} = \mu_r N$ and the power loss due to rolling resistance $\dot{W}_{roll}$ as:

$$\dot{W}_{roll} = T_{roll}\omega^{wh} \tag{3.23}$$

Finally, the total effective power of the DC motor $\dot{\dot{W}}_{motor}$ can be obtained as:

$$\dot{\dot{W}}_{motor} = \dot{W}_{motor} + \dot{W}_{roll} + \dot{W}_{tr} \tag{3.24}$$

Substituting x by 4 meters in Eq. 3.21 and 15 kg as the mass of the vehicle with all estimated sensors, one has that the minimum motor power at Eq. 3.24 must be $\dot{\dot{W}}_{motor} > 18.7$ W. As a result, the DC motor by Phidgets Inc. whose properties are detailed in Table 3.8 has been selected.

Once the DC motor has been selected, next step is the transmission design in order to transfer the motor power to the wheelsets. As the available space between bogie frame and wheelsets is limited and due to the fact that the size of the motor is relatively big, a bevel gear is used as shown in Fig. 3.14

The detailed definition of the transmission axis involves, among other things, section changes, roller bearings, and pinions. A exploded-view drawing can be seen in Fig. 3.15.

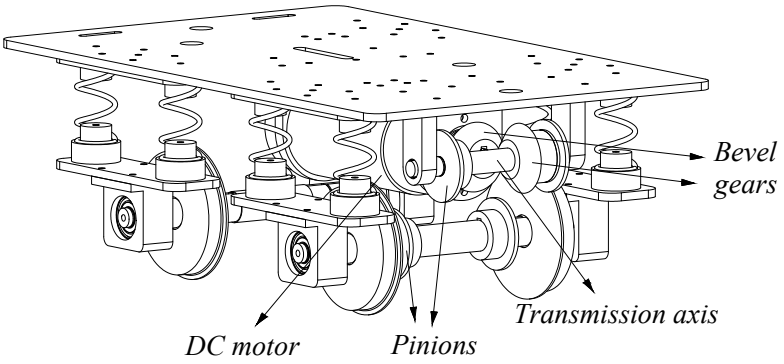

FIGURE 3.14: Transmission bogie

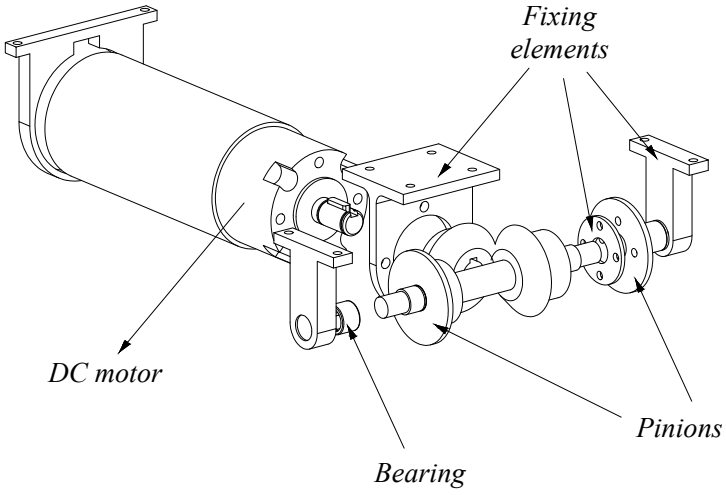

FIGURE 3.15: Transmission exploded-view

Finally, motor power is transmitted to the wheelset by two normalized metallic chains ISO 05B-1 - DIN 8187, as it can be seen in Fig. 3.16 characterized by a 8 mm gap among links.

3.2.7 Sensors

The main features of the inertial measurement units and distance lasers installed in the scaled vehicle is presented in this section. Its choice together with the Data Acquisition

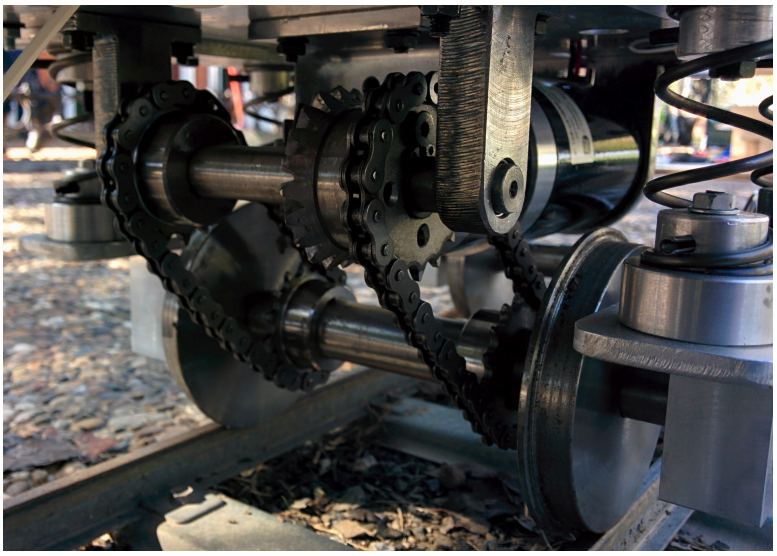

FIGURE 3.16: Scaled vehicle transmission

	Accels	**Gyros**
Measurement range	$\pm 5\ g$	$\pm 300\ ^{o}/s$
Initial bias error	$\pm 0.002\ g$	$\pm 0.25\ ^{o}/s$
Noise density	$80\ \mu g/\sqrt{\text{Hz}}$	$0.03\ ^{o}/s/\sqrt{\text{Hz}}$
Alignment error	$\pm 0.05\ ^{o}$	$\pm 0.05\ ^{o}$
Sampling rate	30 kHz	30 kHz
Scale factor stability	$\pm 0.05\ \%$	$\pm 0.05\ \%$
Model	3DM-GX3 -25	
Manufacturer	LORD MicroStrain Sensing Systems [59]	

TABLE 3.9: Inertial measurement unit features

system (DAQ), which is the responsible for processing the information given in sensors, were derived by the Virtualmech company [104]. In Table 3.9, the main features of the selected IMU model **3DM-GX3**® -25 by LORD MicroStrain® Sensing Systems [59] is presented. In addition, the features of the distance laser **ILD 1302-200** by Micro-Epsilon [58], are shown in Table 3.10.

Distance laser			
Measuring range	200mm	Start of measuring range	60mm
Resolution	100 μm	Measuring rate	750 Hz
Spot diameter	2200 μm	Operating temperature	0...+50°C
Model	ILD 1302-200	Manufacturer	Micro-Epsilon [58]

TABLE 3.10: Distance laser features

3.2.7.1 Sensor positioning

As defined in Section 3.2.2, a total of three inertial measurement units (IMU) at wheelset, frame and carbody levels together with two distance lasers to measure the vertical deflection between suspension planes are installed. For the IMU at wheelset level, the design of the axlebox is modified according to Fig. 3.17. This configuration of Fig. 3.17 allows to detect the wheelset acceleration and angular velocity with the exception of the pitch velocity that is not recorded due to the wheelset bearing.

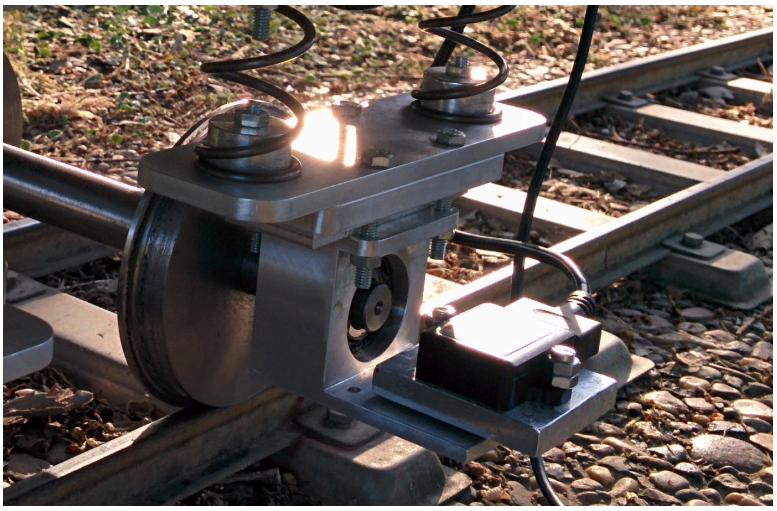

FIGURE 3.17: IMU at axlebox level

Moreover, for the IMUs located at bogie and carbody level, no further modifications need to be introduced as they are installed on the center of the frame and carbody respectively as shown in Fig. 3.18

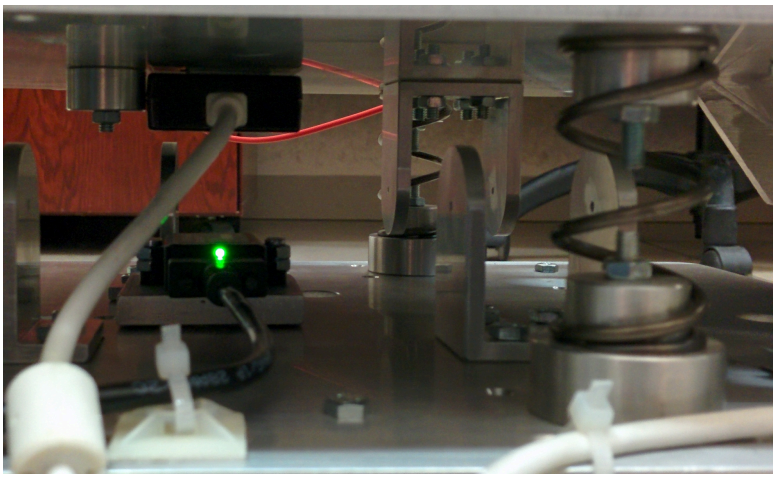

FIGURE 3.18: IMUs at bogie and carbody level

Finally, the distance lasers that measure the vertical deflection between primary and secondary suspensions are installed at the left and right edge of the bogie frame and carbody frame respectively pointing to the axlebox surfaces. This way, the acquired data refers to the vertical deflection of both suspension planes with respect to the wheelset planes and as a result, a postprocessing stage must be carried out to account for the relative displacement between primary and secondary suspensions. Figure 3.19 shows the lasers installation on the scaled vehicle.

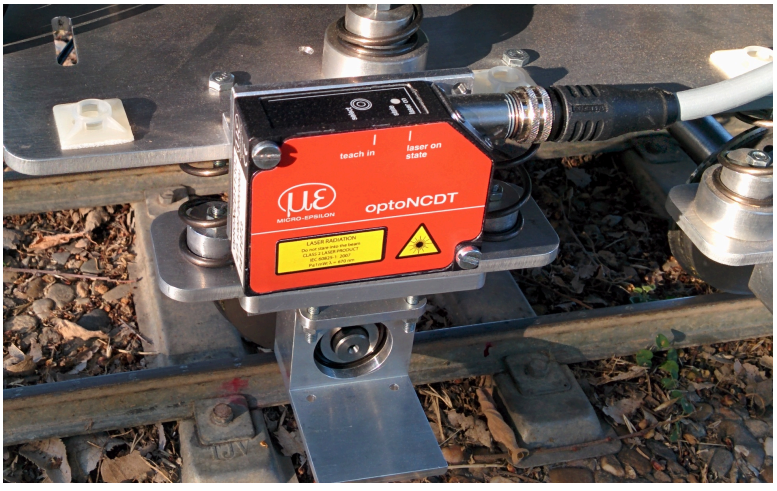

FIGURE 3.19: Bogie distance laser

3.3 Parameter identification

In this section it is explained the experimental procedure followed to obtain the real parameters of the vehicle. Some of the parameters, such as the suspension elements features, have a theoretical value that can be different from the real one, i.e. due to material defects or to the shape of the ends of the springs. In addition, as the design was developed in a preliminary stage, the number of sensors, batteries and other electronic devices mounted on the vehicle have modified the estimated intertial properties of the system, so a corrective estimation ot these parameters needs to be carried out.

3.3.1 Stiffness and damping properties

The identification of the stiffness and damping properties introduced by the suspension elements is derived by the modal analysis technique [22]. To this end, the dynamic response of the structure of the bogie frame attached to the ground by the suspension elements is studied when it is affected by different impulse forces. In Fig. 3.20 one can see the frame, the suspension elements, an accelerometer installed in the top of the frame and the hammer that provides the impulse force.

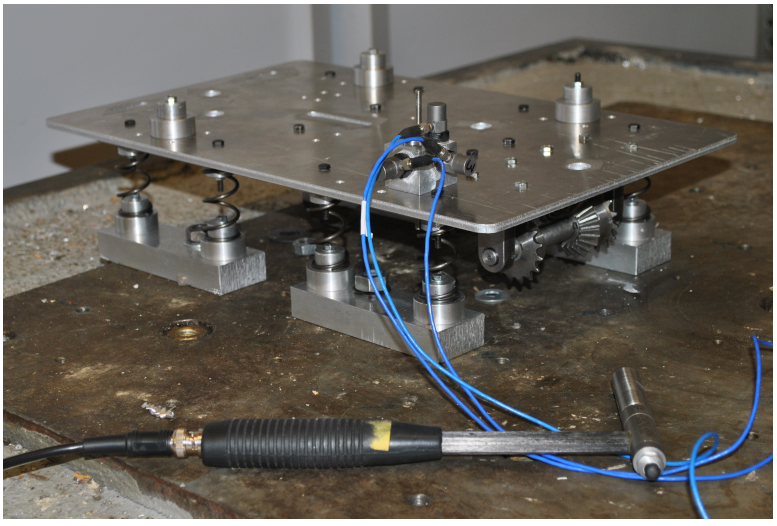

FIGURE 3.20: Parameter identification of suspension elements

In summary, this identification procedure can be developed by representing the system of Fig. 3.20 using ordinary differential equations (ODE) of the type:

$$\frac{d}{dt}\mathbf{X} = \mathbf{A}\mathbf{X} + \mathbf{B}\mathbf{u} \tag{3.25}$$

where $\mathbf{X}$ is the variables vector that includes the position and orientation coordinates and velocities of the frame, $\mathbf{A}$ is the state-space form system matrix, $\mathbf{u}$ is the input vector that accounts for the hammer force and $\mathbf{B}$ is the state matrix that linearly relates the inputs in the space-state equations. Note that Eq. 3.25 is a function of the inertia properties of the system that are expected to identify.

When the mechanical system is excited by impulse forces provided by the hammer in different directions, one can obtain the dynamic response captured by the accelerometer. The time response of the system for a vertical force is shown in Figure 3.21, where one can see on the left the experimental impulse force while on the right the vertical acceleration experienced by the bogie frame.

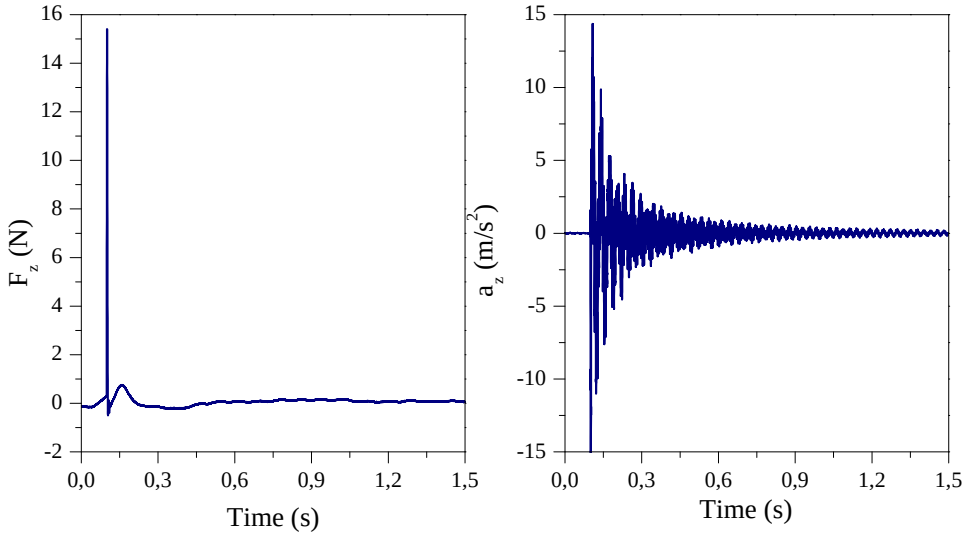

FIGURE 3.21: Vertical response at parameter identification

By comparing the results provided by the model and those obtained in the accelerometer it is straightforward to iteratively calculate the stiffness and damping properties introduced by the suspension elements that better fit the experimental results. To this purpose, the System Identification Toolbox [52] of the commercial software Matlab has been used and the results of the stiffness and damping properties k, c in the vertical, longitudinal and lateral direction of the springs selected in Sections 3.2.4 and 3.2.5 is calculated and shown in Eq. 3.26.

$$\begin{aligned} k_z &= 8585 \quad \text{N/m} \quad k_y = k_x = 9.15 \quad \text{N/m} \\ c_z &= 3.52 \quad \text{Ns/m} \quad c_y = c_x = 2505 \quad \text{Ns/m} \end{aligned} \tag{3.26}$$

From Eq. 3.26 one can realize that the vertical stiffness of the suspension element $k_z = 8585$ N/m is quite similar to the ideal stiffness provided by the manufacturer in Table 3.6 as $k^v_{prim} = 8700$ N/m. This slight difference is mainly attributed to the shape of the spring ends during their manufacturing process.

3.3.2 Mass and inertia estimation

Once the vehicle is installed with all necessary devices, it is weighed in the biomechanical system of Fig. 3.22 located in the Mechanical Engineering Department at the University of Seville, that is normally used for measuring the biomechanical portrayal of human walking.

In this system, which is formed by the two grey force plates model OR6-7 by AMTI Inc. [33], one can obtain the reaction forces and torques together with its position and orientation that the vehicle provides while it is in static equilibrium. Then, by applying the equilibrium of forces and torques equation one can estimate the position of the center of gravity of the system. Table 3.11 gathers the reaction forces at the two grey platforms of Fig. 3.22 in which F, Γ and r refer respectively, to the reaction force, torque and distance with respect to the reference frame of the scheme shown in Fig.

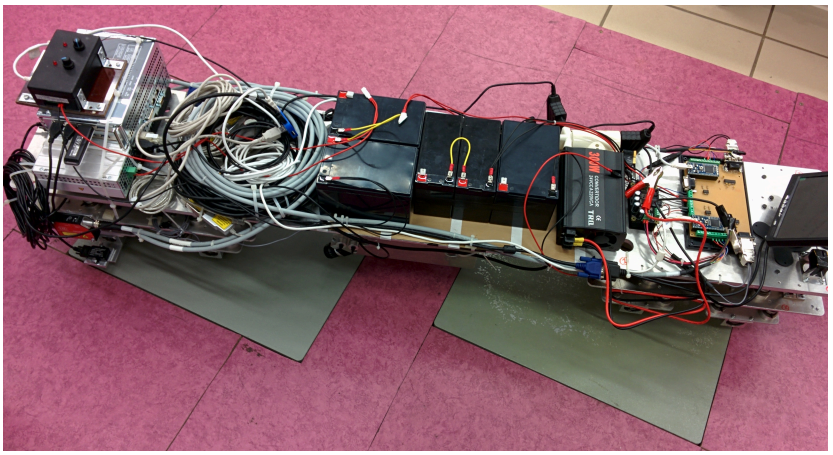

FIGURE 3.22: Scaled vehicle weighing

3.23, subscripts x, y and z to the Cartesian components, and platforms 1 and 2 to the left and right grey platforms of Fig. 3.22. Note that in Table 3.11, the total vertical force of the vehicle arises to $-443.17N$, which makes a total mass of:

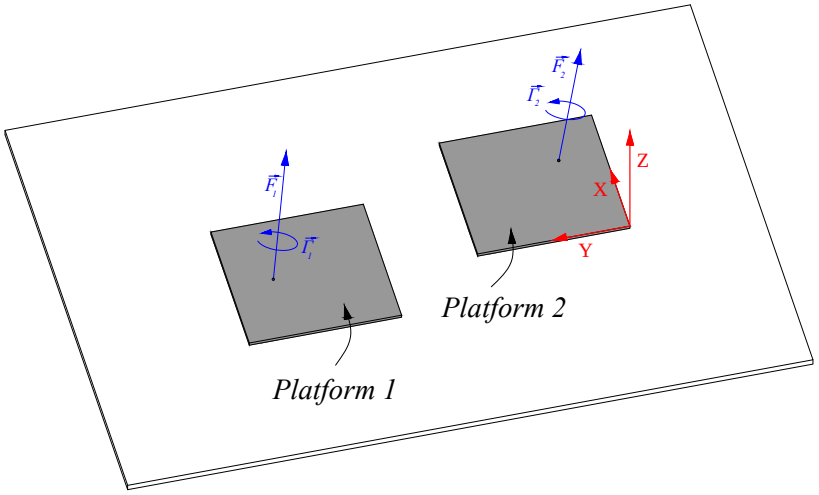

FIGURE 3.23: Vehicle weighing scheme

$$m_{vehicle} = 45.18kg \tag{3.27}$$

that is distributed in 25.18 kg for the instrumented bogie (*Platform 1*) and 20.01 kg for the driver one (*Platform 2*).

Platform 2		**Platform 1**	
F_x [N]	0.7978	F_x [N]	-0.7664
F_y [N]	-0.9430	F_y [N]	-1.7904
F_z [N]	-196.1532	F_z [N]	-247.0147
Γ_x [Nmm^2]	$1.8998{\cdot}10^4$	Γ_x [Nmm^2]	$-2.4595{\cdot}10^4$
Γ_y [Nmm^2]	$1.3207{\cdot}10^4$	Γ_y [Nmm^2]	$-1.2296{\cdot}10^4$
Γ_z [Nmm^2]	$-0.4450{\cdot}10^4$	Γ_z [Nmm^2]	$1.4983{\cdot}10^4$
r_x [mm]	299.1548	r_x [mm]	12.0218
r_y [mm]	157.1437	r_y [mm]	1041.5717
r_z [mm]	0.0	r_x [mm]	0.0

TABLE 3.11: Scaled vehicle reaction forces at repose

Regarding the calculation of the inertia tensor and due to the complexity of the whole vehicle, it has been calculated throughout CAD software. Assuming that all sensors are installed in the carbody except for the DC motor, inertia tensor of the remaining bodies is calculated by its CAD design and material properties. Then, the mass of the carbody is computed by the difference between the total mass of Eq. 3.27 and the mass of the remaining bodies, giving a value of $m_{carbody} = 32.04$ kg. This mass is installed on the carbody by adding an artificial density to the CAD design of the carbody and sensors that can be seen in Fig. 3.24 to then, compute the carbody inertia tensor as:

$$\mathbf{I}_{carbody} = \begin{pmatrix} 0.122 & -0.001 & 0.009 \\ -0.001 & 3.452 & 0 \\ 0.009 & 0 & 3.518 \end{pmatrix} \left[\mathrm{kg} \cdot \mathrm{m}^2\right] \tag{3.28}$$

Finally, in Chapter 4 one can find the mechanical properties of the whole system in the numerical model of the vehicle.

3.3.3 Definitive scaling factors

Once the scaled vehicle has been fully defined and mounted with its sensors, the scaling factors that apply to it with respect to the ML95 trainset vehicle are listed in Table

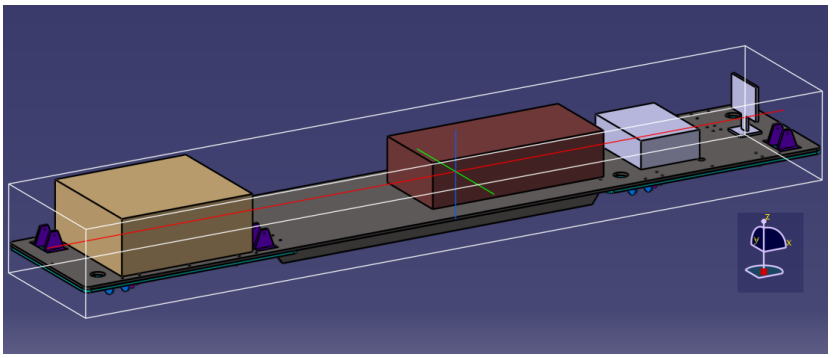

FIGURE 3.24: Carbody CAD design

3.12. These factors are compared to those obtained after the application of the similarity method proposed by Jaschinski [36] that would lead to a dynamically similar prototype.

As a result and due to the imperative length scaling factor, sensor positioning and the remaining desing criteria, the scaled vehicle does not accurately reproduce a similar dynamic behaviour than the ML-95 vehicle in which it is based on. That is, this vehicle is not appropriate for studying dynamic influences of external factors, such as i.e. derailment, improvement of active suspensions or evolution of wear and RCF, and extrapolate these conclusions to the full scale ML95 trainset, as in this case, the dynamic forces are not in accordance to the scaling of the problem. However, it is suitable for modeling validation as its properties are completely determined. In addition, it also satisfies one of its main objectives as future works, that is the estimation of the track irregularities as a function of the information collected by the sensors.

3.4 Track measurement

The definition of an ideal track centerline allows to describe the track geometry through a combination of analytical expressions. As it has been reported in the literature, railroad tracks can be defined using the three concepts listed below [13, 74]:

Scaling Factor	**Scaled Vehicle**	**Jaschinski** [36]	**Scaling Factor**	**Scaled Vehicle**	**Jaschinski** [36]
Length φ_L	11.3	11.3	Vert. Damping Primary Susp. $\varphi_{c^z_{prim}}$	15741.4	1442.9
Time φ_t	1	1	Vert. Damping Secondary Susp. $\varphi_{c^z_{sec}}$	19471.6	1442.9
Velocity φ_v	11.3	11.3	Vert. Stiffness Primary Susp. $\varphi_{k^z_{prim}}$	29.1	1442.9
Acceleration φ_a	11.3	11.3	Vert. Stiffness Secondary Susp. $\varphi_{k^z_{sec}}$	149.1	1442.9
Density φ_ρ	1	1	Long. Damping Primary Susp. $\varphi_{c^x_{prim}}$	9430.6	1442.9
Mass φ_m	448.3	1442.9	Long. Damping Secondary Susp. $\varphi_{c^x_{sec}}$	1422.6	1442.9
Inertial force φ_F	5065.8	16304.8	Long. Stiffness Primary Susp. $\varphi_{k^x_{prim}}$	2479.0	1442.9
Inertia carbody $\varphi_{I^{cb}}$	$5.72{\cdot}10^4$	$18.41{\cdot}10^4$	Long. Stiffness Secondary Susp. $\varphi_{k^x_{sec}}$	149.71	1442.9
Inertia bogie $\varphi_{I^{bog}}$	$11.11{\cdot}10^4$	$18.41{\cdot}10^4$	Lat. Damping Primary Susp. $\varphi_{c^y_{prim}}$	3840.9	1442.9
Inertia wheelset $\varphi_{I^{wh}}$	$6.73{\cdot}10^4$	$18.41{\cdot}10^4$	Lat. Damping Secondary Susp. $\varphi_{c^y_{sec}}$	1422.9	1442.9
Lat. Stiffness Primary Susp. $\varphi_{k^y_{prim}}$	411.18	1442.9	Lat. Stiff. Secondary Susp. $\varphi_{k^y_{sec}}$	411.18	1442.9

TABLE 3.12: Scaling factor comparison comparison

- **Projection**; it is the planar curve achieved when projecting the track centerline onto the horizontal plane. It is formed by tangent, curve and transition stretches
- **Development**; it defines the vertical profile of the track
- **Super-elevation**; it is the angle that defines the vertical distance between rails

In this section, the procedure followed to measure the scaled track geometry and its irregularities is described. The track is located in Seville (Spain) at Alamillo's park. The initial and ideal geometry is extracted from construction drawings and it is considered as a 35-meter tangent stretch followed by a 15-meter curvature curve that ends in a 2-meter tangent stretch as shown in Fig. 3.25.

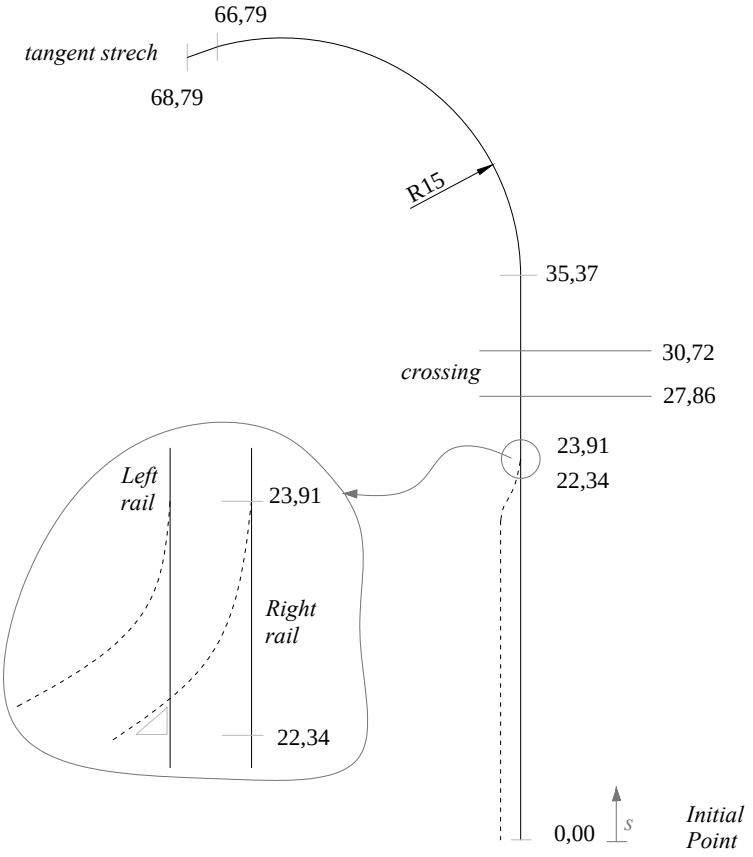

FIGURE 3.25: Track constructive drawing - Plan view

	Input	Tolerance	Output	Measurement uncertainty
Horizontal deviation (Gon)	0.0003	0.0003	0.0003	0.0002
Vertical deviation (Gon)	0.0003	0.0003	0.0003	0.0002
Distance deviation (mm)				
Infrared measurement	1	1mm + 1.5ppm	1	0.5
Laser measurement	2	2mm + 2ppm	2	1.5

TABLE 3.13: Leica TS15 R400 features

However, as it is common in the railroad industry, the real track presents important differences with respect to the ideal one extracted from construction drawings, mainly due to track irregularities. From Section 3.4.1 to 3.4.4 it is explained the experimental technique developed to measure the irregularities, topographic devices used and how the measured points are organized. In Section 3.4.5, the postprocess analysis to account for the appropriate data needed for simulation purposes is detailed. Finally, Section 3.4.6 presents the measured track lateral and vertical deviations with respect to the ideal track.

3.4.1 Experimental track measurement

In order to account for the track irregularities, an accurate topographic system must be used. In this case, a total topographic station by Leica Geosystems model TS15 P 1" R400 shown in Fig. 3.26 has been used. It is a modern electronic device that combines the ability to measure a position horizontally and vertically at the same time. It has two parts, the so-called *total station* which is mounted on a static tripod, and a *target prism*, which is moved along the real heads to make the measurements. The calibration properties of the system are described in Table 3.13.

FIGURE 3.26: Total station device

In what follows, the different stages for the track measurement are described.

3.4.2 Track marking

In a preprocessing stage, the track is marked in the top of the rail head every 2 centimeters as it is shown in Fig. 3.27. As the track length is about 68 meters, there is a total estimated number of measured points of 6800 between the left and the right rail respectively. The purpose of this marking is to guide the target prism while the total station is measuring as shown in Fig. 3.28.

3.4.3 Orientation of the total station

Once the track has been marked, the next step is the positioning of the total station. At this stage, it is necessary to find a suitable position for the device in order to refer the measured points to a global frame. Due to the fact that the measuring field has obstacles such as trees and ground ramps, two different positions of the total station were used. These two global position coordinates are listed in Table 3.14

FIGURE 3.27: Track marking

	x (m)	**y (m)**	**z (m)**
Position 1	1000.0000	1000.0000	0.0000
Position 2	1028.1288	998.5230	-0.0356

TABLE 3.14: Global positions of the total station

Knowing the global position of the different locations that the total station stands, it automatically refers the measured points to the global frame. Consequently, no further actions are required regarding the change of the total station position.

3.4.4 Track measuring

The measurement of the marked points is done with the help of the target prism. As it can be seen in Fig. 3.28, the target prism is located above each marked point and oriented to the total station. When the prism is vertically aligned the total station measures the point.

This procedure is repeated along the track. However, as it is a long process that took five consecutive days and ten people involved, the following strategy in the measurement was followed:

FIGURE 3.28: Track measuring

- Points are measured consecutively every meter in each rail. That means, every meter is divided in left and right rail and the points are measured consecutively. If the distance between points is 2 centimeter, 50 consecutive points are measured per meter in the left rail first, and then, the corresponding 50 points in the right rail.

- Points are named with a prefix followed by the number of the point (i.e. A1, A2,...,B1,B2,...).

- When the total station is changed or newly installed (i.e. at the beginning of the day), the prefix of the points is changed. This allows to identify constant errors when orientating the device respect to preceding measured points. Also, in order to identify this possible error, 10 overlappping points are measured twice, before and after the change of the total station position.

Figure 3.29 shows the measured points in blue and red together with their corresponding prefix. Also the two positions of the total station respect to the global frame can be seen. The change between blue and red of the measured points refers to points with

different prefix. That is, a group of points that were measured before the total station was changed or newly installed.

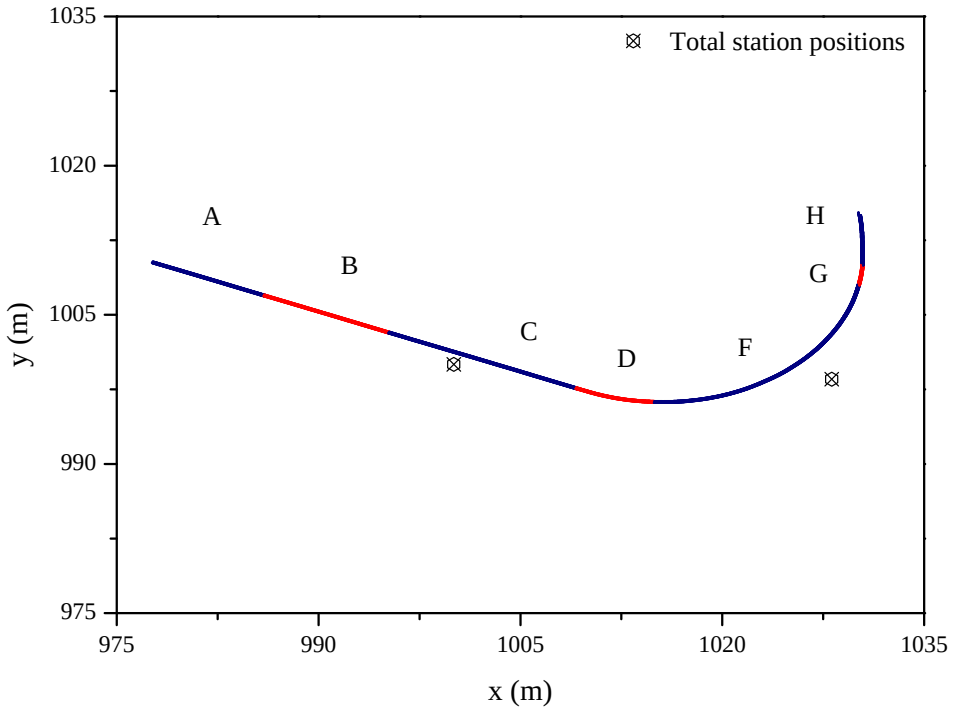

FIGURE 3.29: Initial track measured points

3.4.5 Postprocessing of measured track data

Measured points in the left and right rail need to be transformed into quantitative irregularities, such as vertical and lateral displacements of the rail heads with respect to the undeformed track configuration [20] as shown in Fig. 2.11. However, the data obtained after the experimental measurement needs to be processed first to account for possible errors or numerical solutions that are not compatible with simulation procedures (i.e. high discontinuities).

The postprocessing procedure applied to the experimental data is listed below:

Prefix	*No. Points*	*Comments*
A	A1 - A905	9 meters
B	B1 - B1012	10 meters
C	C1 - C1510	15 meters
D	D1 - D610	6 meters
E	E1 - E7	7 Reference points
F	F1 - F2112	21 meters
G	G1 - G213	2 meters
H	H1 - H509	5 meters
	6878 points	**68 Total measured meters**

TABLE 3.15: Initial organization of measured points

- Reorganization of the data grouping points in left and right rail respectively
- Remove duplicated points
- Minimize the error produced due to the change of the total station position
- Identification of the track centerline
- Computation of track irregularities as in Fig. 2.11
- Data filtering

3.4.5.1 Data reorganization

Initially there is a total of 6878 measured points that are first organized as shown in Table 3.15.

As explained in Section 3.4.4, every measured meter is divided into 50 consecutive points for the left rail and other 50 consecutive points for the right. However, due to the repetitiveness of the process, some points can be measured twice while others can be skipped. That explains why there are not exactly 100 points per measured meter as pointed out in Table 3.15. Consequently, they need to be grouped carefully and

individually into left and right rail. Moreover, once the points are grouped into left and right rail, duplicated points are removed to avoid computational errors.

3.4.5.2 Error minimization

The purpose of this section is to show the procedure followed to minimize the error made when positioning the total station. As the experimental measurement was made along five days, it is obvious that the topographic device had to be installed in the field many times. This involved a certain error when orientating it with respect to the original position as it can be seen in Fig. 3.30, which is a zoom of Fig. 3.29. In this figure, it is shown in red the points measured during one day (D-prefix) and in blue the points measured in the following day (F-prefix). Here, the 10 common points that are described in Section 3.4.4 are clearly identified and show the misalignment error made.

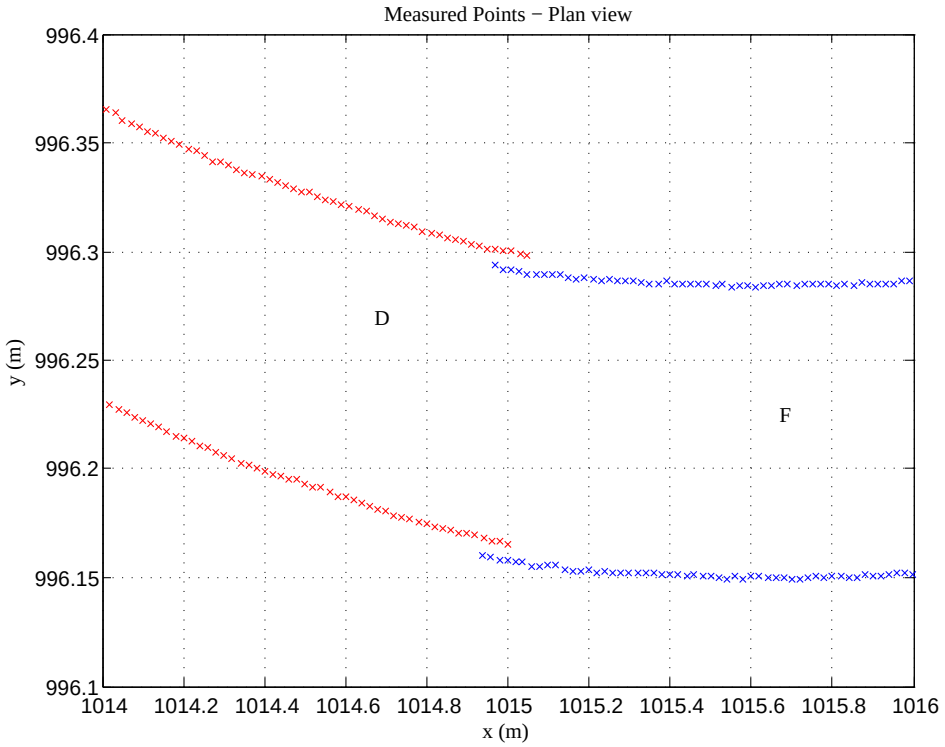

FIGURE 3.30: Misalignment error in measured points

In order to minimize this misalignment, the following statistical procedure has been done:

- If A is the index attached to the points measured in one day and B is the index for those measured in the next day, one has:

$$\Delta \mathbf{r}_i = \mathbf{r}_i^A - \mathbf{r}_i^B, \qquad i = 1, ..., n_c \tag{3.29}$$

where n_c is the numbe of points in common between the A and B group of points, $\mathbf{r}_i^A$ is the global position vector of point i in the group A while $\mathbf{r}_i^B$ is for the group B as shown in Fig. 3.31. Here, $\Delta \mathbf{r}_i$ can be considered as the translation vector that point i in the B configuration must be moved to coincide with the same point i in the A configuration.

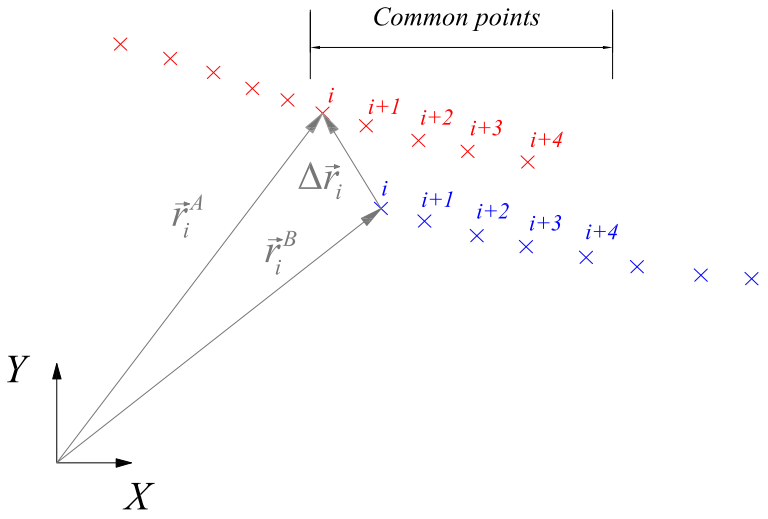

FIGURE 3.31: Misalignment estimation in one rail
×: A-measured points ×: B-measured points

- Once the n_c distance vectors are computed, the mean distance vector $\Delta\bar{\mathbf{r}}$, and the standard deviation $\boldsymbol{\sigma} = [\sigma_x \quad \sigma_y \quad \sigma_z]^T$ are calculated as:

$$\Delta\bar{\mathbf{r}} = \frac{\sum_{i=1}^{n_c} \Delta\mathbf{r}_i}{n_c}, \qquad \sigma_J = \sqrt{\frac{1}{n_c - 1}\sum_{i=1}^{n_c} (\Delta\mathbf{r}_{Ji} - \Delta\bar{\mathbf{r}}_J)^2}, \quad J = x, y, z \tag{3.30}$$

  The mean distance vector $\Delta\bar{\mathbf{r}}$ can be considered as the translation vector that every point in the B configuration must be moved to minimize the misalignment error produced by the topographic device while the standard deviation $\boldsymbol{\sigma}$ quantifies the amount of dispersion of the mean distance vector with respect to each $\Delta\mathbf{r}_i$. Note that in this statistical procedure derived to minimize the total station positioning error, the 'bar' overline only refers to the arithmetic mean.

  Therefore, if $\boldsymbol{\sigma}$ is smaller than $\Delta\bar{\mathbf{r}}$, the group of points is translated as a rigid body as:

$$\mathbf{r}_j = \mathbf{r}_{j0} + \Delta\bar{\mathbf{r}}, \qquad j = 1, ..., n_P \tag{3.31}$$

  where n_P is the number of points of the group subject to translation and subindex 0 refers to the non-translated configuration. However in other cases when the standard deviation is representative with respect to the mean distance, a rotation together with a translation need to be applied.

According to Fig. 3.29, this procedure is developed for the six pairs of group of points available in the experimental data whose results are listed in Table 3.16.

In addition, in Fig. 3.32, the distance vector $\Delta\mathbf{r}_i$ for every pair of points i and for each group of points shown in Fig. 3.29 is plotted in continuous line. Blue, red and black lines refer to the x, y and z components and dashed-dotted lines refer to the mean distance vectors $\Delta\bar{\mathbf{r}}$. Here, some conclusions can be extracted from this figure. On the one hand, the group of points $C - B$, $D - C$, and $G - F$, presents a small mean distance vector whose norm is less than 1 mm (see Table 3.16). Taking into account

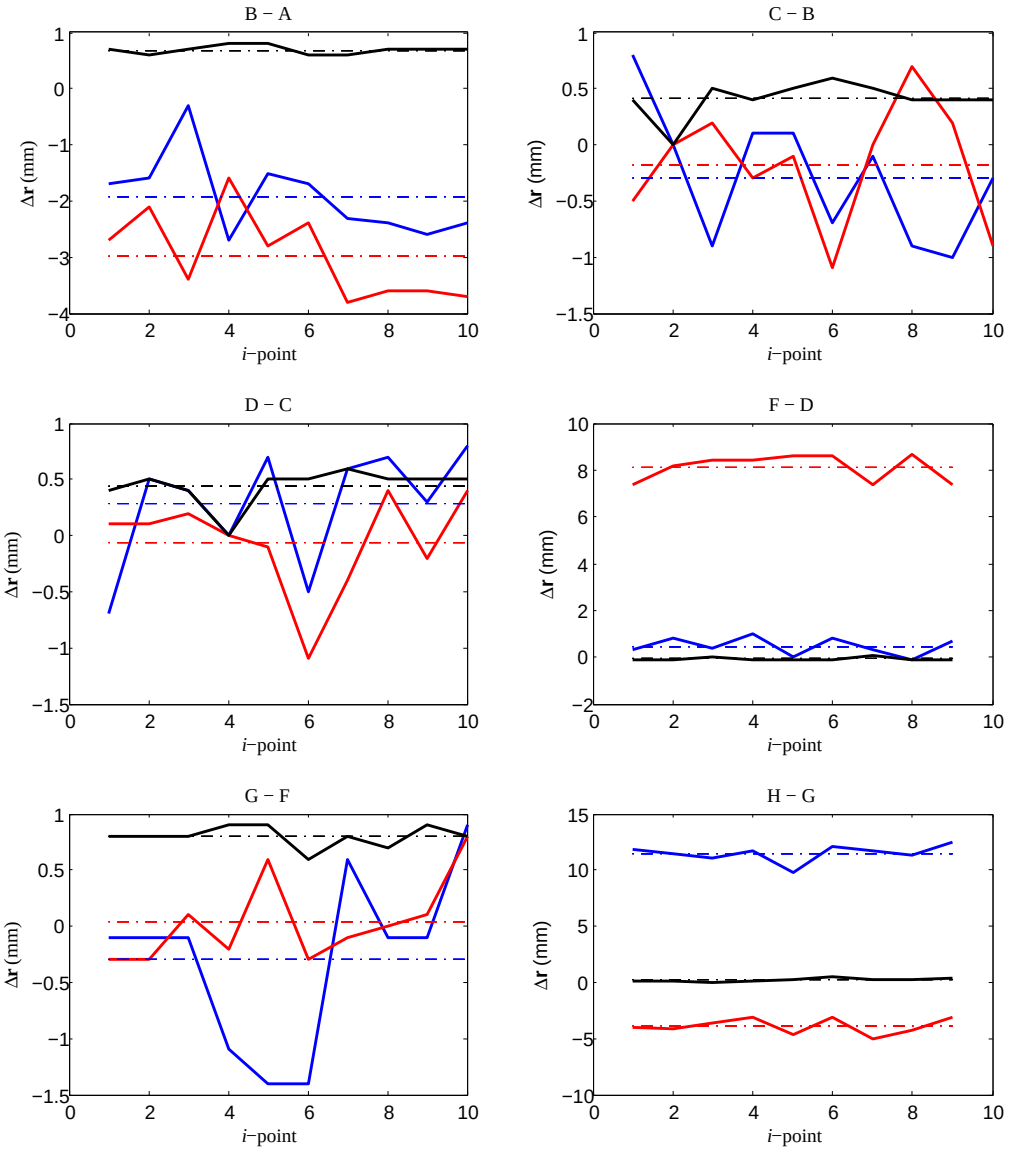

FIGURE 3.32: Translation vectors along the different group of measured points
$\Delta\mathbf{r}_i$ x-component $\Delta\mathbf{r}_i$ y-component $\Delta\mathbf{r}_i$ z-component
$\Delta\bar{\mathbf{r}}$ x-component $\Delta\bar{\mathbf{r}}$ y-component $\Delta\bar{\mathbf{r}}$ z-component

Pair of group of points	$\Delta\bar{\mathbf{r}}\,[mm]$	$\boldsymbol{\sigma}\,[mm]$
H - G	$\begin{bmatrix} 11.50 & -3.90 & 0.22 \end{bmatrix}^T$	$\begin{bmatrix} 0.77 & 0.72 & 0.16 \end{bmatrix}^T$
G - F	$\begin{bmatrix} -0.29 & 0.04 & 0.80 \end{bmatrix}^T$	$\begin{bmatrix} 0.78 & 0.38 & 0.09 \end{bmatrix}^T$
F - D	$\begin{bmatrix} 0.47 & 8.12 & -0.07 \end{bmatrix}^T$	$\begin{bmatrix} 0.38 & 0.56 & 0.07 \end{bmatrix}^T$
D - C	$\begin{bmatrix} 0.28 & -0.06 & 0.44 \end{bmatrix}^T$	$\begin{bmatrix} 0.52 & 0.44 & 0.16 \end{bmatrix}^T$
C - B	$\begin{bmatrix} -0.29 & -0.18 & 0.41 \end{bmatrix}^T$	$\begin{bmatrix} 0.58 & 0.54 & 0.16 \end{bmatrix}^T$
B - A	$\begin{bmatrix} -1.92 & -2.97 & 0.69 \end{bmatrix}^T$	$\begin{bmatrix} 0.72 & 0.76 & 0.07 \end{bmatrix}^T$

TABLE 3.16: Mean distance vector and standard deviation in measured group of points

that measurement uncertainty by the total station is about 0.5 mm and that the prism positioning implies a certain human error in the common points i, it can be assumed that no further modifications need to be done regarding these groups. On the other hand, the group of points $B-A$, $F-D$, and $H-G$, presents a clear mean distance vector that is representative when compared to its standard deviation. That means that in order to account for the misalignment produced by the total station positioning, these groups of points need to be translated its corresponding mean distance vectors $\Delta\bar{\mathbf{r}}$.

Therefore, according to Eq. 3.31, the following translations have been derived:

- Between G and H group of points, a translation of all points of group H of value $\Delta\bar{\mathbf{r}}_{HG} = \begin{bmatrix} 11.50 & -3.90 & 0.22 \end{bmatrix}^T$ is applied as:

$$\mathbf{r}_{H'} = \mathbf{r}_H + \Delta\bar{\mathbf{r}}_{HG} \tag{3.32}$$

  where $\mathbf{r}_H$ is the global position vector of points H and $\mathbf{r}_{H'}$ the global position vector of the translated points. Note that superscript $'$ denotes a translation of the points.

- Between D and the group of points FGH', a displacement to the FGH' group of value $\Delta\bar{\mathbf{r}}_{FD} = \begin{bmatrix} 0.47 & 8.12 & -0.07 \end{bmatrix}^T$ is applied as:

$$\mathbf{r}_{F'G'H''} = \mathbf{r}_{FGH'} + \Delta\bar{\mathbf{r}}_{FD} \tag{3.33}$$

- Between A and the group of points $BCDF'G'H''$, a displacement to the latter group of value $\Delta\bar{\mathbf{r}}_{BA} = \begin{bmatrix} -1.92 & -2.97 & 0.69 \end{bmatrix}^T$ is applied as:

$$\mathbf{r}_{B'C'D'F''G''H'''} = \mathbf{r}_{BCDF'G'H''} + \Delta\bar{\mathbf{r}}_{BA} \tag{3.34}$$

Figure 3.33 shows the original group of points D and F in red and blue crosses respectively, and their corresponding D' and F'' in black circles when this process is applied. Note that the red points D do not coincide with the black ones D' because the last translation described in Eq. 3.34, affects to the groups $BCDF'G'H''$.

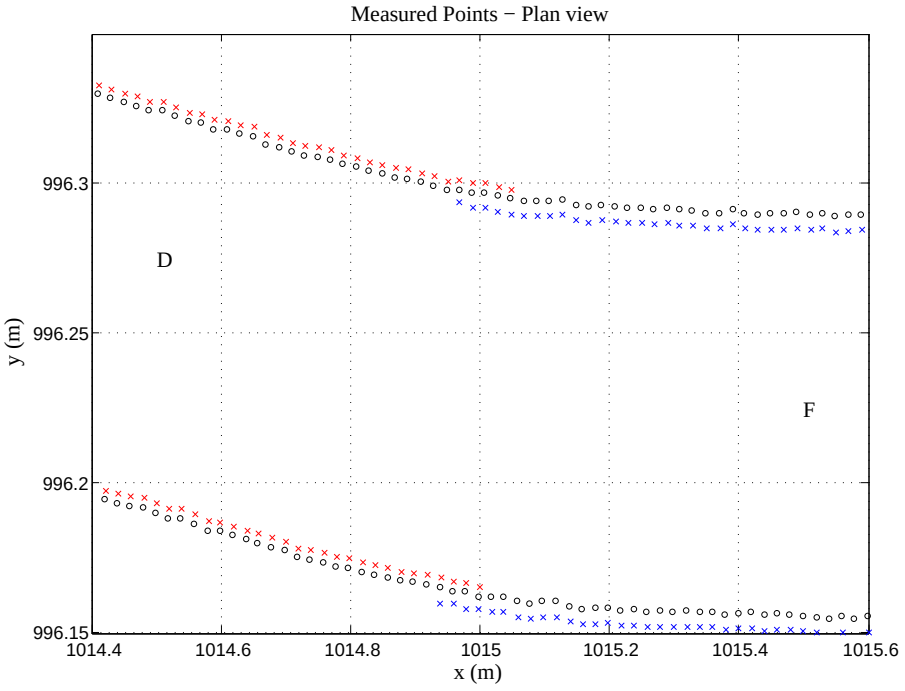

FIGURE 3.33: Initial and final D and F group of points
×: D-measured points ×: F-measured points ○: Corrected measured points

3.4.5.3 Arc-length coordinate of the track centerline

Before computing the irregularities in the left and right rails, it is necessary to calculate the real geometry of the track centerline. To this end, the arc-length coordinates of each rail s_R and s_L of Fig. 3.34 need to be expressed as a function of the arc-length coordinate of the track centerline s. This is, if n and m are the number of points measured in the left and right rail respectively, and f the number of points of the track centerline, being $n \neq m \neq f$, one has that $s_L = [s_L^1, s_L^2, \cdots, s_L^n]$ and $s_R = [s_R^1, s_R^2, \cdots, s_R^m]$. Therefore, the last arc-length element of the centerline vector s^f can be calculated as:

$$s^f = \frac{s_L^n + s_R^m}{2} \tag{3.35}$$

where f is the number of discretized points in the track centerline. Then, the incremental trajectory coordinate of the centerline can be calculated as $\Delta s = s^f/f$ and thus, the trajectory coordinate takes the form of:

$$s = [\Delta s, 2\Delta s, \cdots, f\Delta s] \tag{3.36}$$

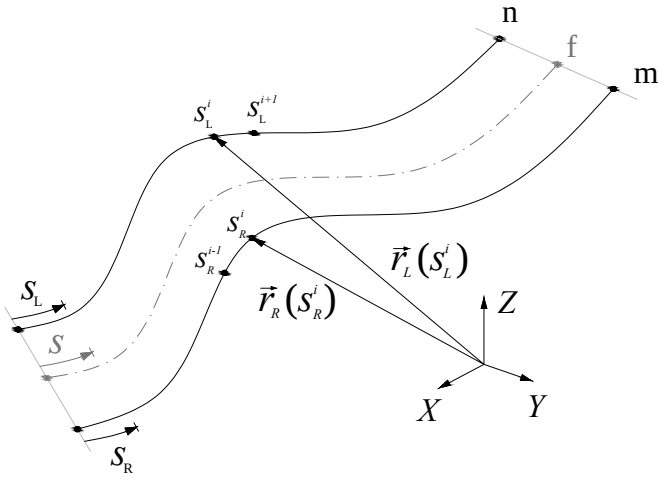

FIGURE 3.34: Different trajectory coordinates

As said before, once the trajectory coordinate of the track centerline is obtained, it is necessary to expressed the right and left rails trajectory coordinates s_R and s_L, as a function of s. Considering the arbitrary track of Fig. 3.34, one can observe that while in tangent stretches s_R and s_L coincide with s, in curve stretches this assumption is no longer valid because the exterior rail follows a longer path compared to the interior one. Consequently, to obtain $s_R(s)$ and $s_L(s)$ as plotted in Fig. 3.35, tangent and curve stretches in the centerline are first identified according to the ideal track plan view of Fig. 3.25. That is, a 35-meter tangent stretch followed by a 15-meter radius curve one that ends in a 2-meter tangent stretch. In tangent stretches it is assumed that the trajectory coordinates in both rails are the same as the trajectory coordinate in the track centerline, as shown in the first and third equations of Eq. 3.37, while in the curve stretch, a direct proportionality is used.

$$s_J^i = \begin{cases} (i-1)\,\Delta s & if \quad i = 1, ..., f_1 \\ s_J^{f_1} + (i-f_1)\left(\frac{s_J^{j2} - s_J^{j1}}{s^{f_2} - s^{f_1}}\right)\Delta s & if \quad i = f_1+1, ..., f_2 \\ s_J^{f_2} + (i-1)\,\Delta s & if \quad i = f_2+1, ..., f \end{cases} \tag{3.37}$$

Note that in Eq. 3.37, f_1 and f_2 refer to the position points where the curve stretch starts and ends respectively, and subscript J stands for L (left) or R (right) rail.

3.4.5.4 Real geometry of the track centerline

As the left and right arc-length coordinates have been expressed as a function of the arc-length coordinate s of the track centerline, it is then straightforward to obtain the real left and right rail geometry as a function of s. Therefore, the real geometry of the track centerline in Fig. 3.36, can be obtained as the half of the sum of the Cartesian left and right rail coordinates.

$$\mathbf{r}_{CL}^i\left(s^i\right) = \frac{\mathbf{r}_L^i\left(s^i\right) + \mathbf{r}_R^i\left(s^i\right)}{2}, \qquad i = 1, ..., f \tag{3.38}$$

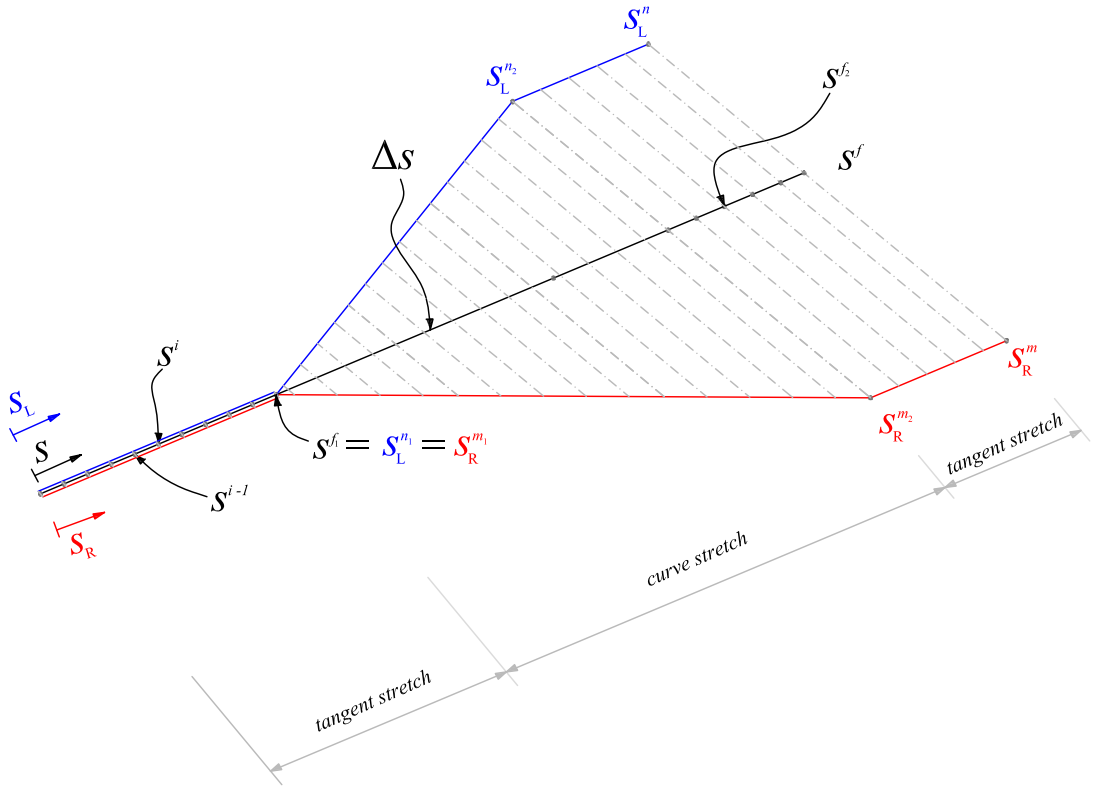

FIGURE 3.35: Direct proportionality of trajectory coordinates

where $\mathbf{r}_{CL}^i$ is the position vector of the track centerline at point i.

3.4.5.5 Ideal geometry of the track centerline

In the case of the targeted track and regardless of the fact that there is a curve, there is no cant angle, which means that both rails are supposed to have the same vertical coordinate in the ideal configuration. Therefore, by knowing the projection and the development, the targeted track centerline is fully defined and in order to obtain the analytical definition of the track centerline, it is necessary to find the function that better approximates the measured points of Eq. 3.38.

Ideal track centerline projection

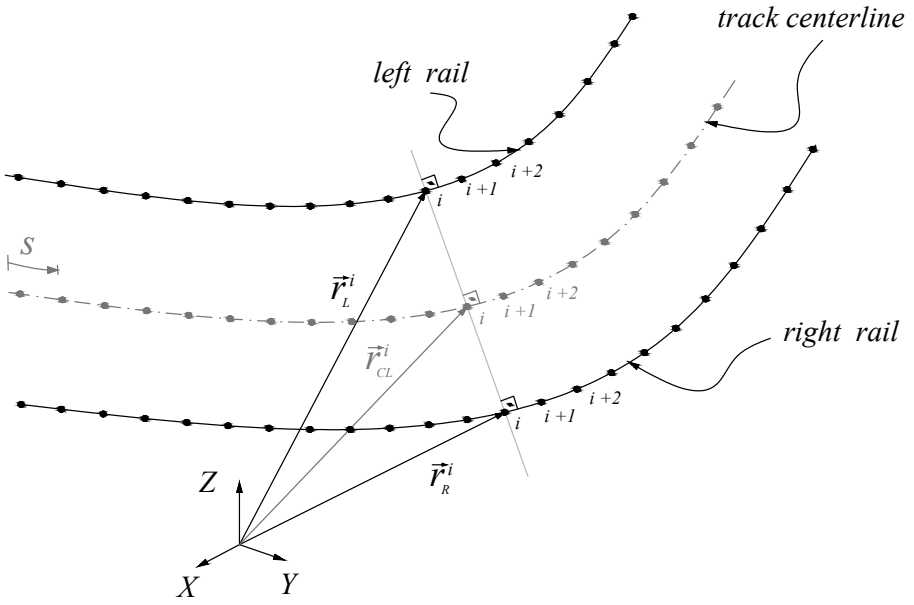

FIGURE 3.36: Track centerline geometry

The projection of the ideal track is formed by a tangent stretch followed by a curve one (see Section 3.4). There is no transition stretch, which implies that unexpected forces owed to the appearance of centrifugal forces are expected to act on the vehicle. As the track is formed by a tangent and a curve stretch, the problem reduces to find the analytical definition of a straight line together with the analytical definition of a circle that are subject to some geometrical constraints. Then, the position of an arbitrary point on the ideal track centerline $\mathbf{r}(s)$ can be defined as

$$\mathbf{r}\left(s\right)=\begin{cases}\mathbf{r}_A+\frac{\mathbf{r}_B-\mathbf{r}_A}{|\mathbf{r}_B-\mathbf{r}_A|}s & if \quad s\leq s_1\\ \mathbf{r}_C+R\Big[\begin{array}{cc}\cos\left(\beta+\frac{s-s_1}{R}\right) & \sin\left(\beta+\frac{s-s_1}{R}\right)\end{array}\Big]^T & if \quad s>s_1\end{cases} \tag{3.39}$$

where as shown in Fig. 3.37, $\mathbf{r}_A$ is the position vector of the initial point A, $\mathbf{r}_B$ is the position vector of point B that joins the tangent and the curve stretches, $\mathbf{r}_C$ is the position vector of the center of the curve stretch, s_1 is the trajectory coordinate where

the curve stretch starts, R is the curve radius and β is the orientation angle that defines the beginning of the curve and can be computed as:

$$\beta = atan2\left(\frac{y_B - y_C}{x_B - x_C}\right) \tag{3.40}$$

being $x_{C,B}$ and $y_{C,B}$ the Cartesian components of the vectors $\mathbf{r}_C$ and $\mathbf{r}_B$ respectively. Also note that s_1 can be calculated by substituting in Eq. 3.39, $s = s_1$ such as $\mathbf{r}(s_1) = \mathbf{r}_B$.

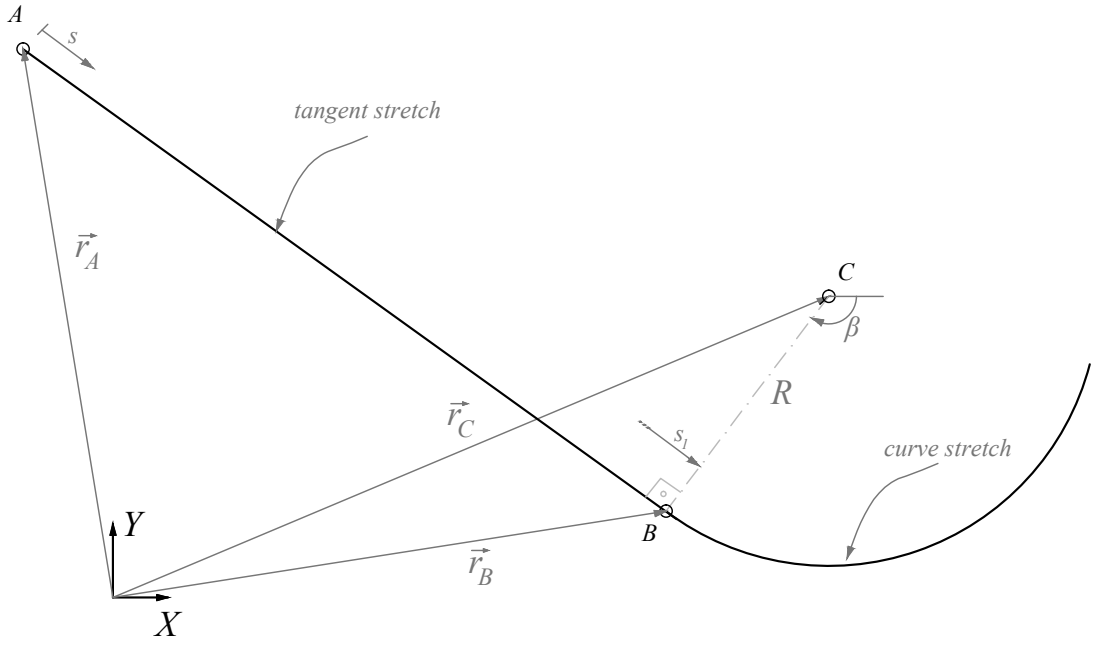

FIGURE 3.37: Ideal track centerline geometry

The analytical function of Eq. 3.39 that better fits the experimental data can be obtained by minimizing the quadratic distance between the measured centerline and the Eq. 3.39. This quadratic distance d^2 is computed as:

$$d^2 = \left[\mathbf{r}_{measured} - \mathbf{r}\left(s\right)\right]^T \left[\mathbf{r}_{measured} - \mathbf{r}\left(s\right)\right] \tag{3.41}$$

where $\mathbf{r}_{measured}$ is the position vector of the measured points in the track centerline. Therefore, the function that must be minimized can be written as:

$$f(\mathbf{u}) = \sum_{i=1}^{np} \left[\mathbf{r}^i_{measured} - \mathbf{r}\left(s^i\right)\right]^T \left[\mathbf{r}^i_{measured} - \mathbf{r}\left(s^i\right)\right]$$
$$\mathbf{u} = \begin{bmatrix} x_B & y_B & x_C & y_C & R \end{bmatrix}^T \tag{3.42}$$

Note that in Eq. 3.42, the Cartesian components of $\mathbf{r}_{measured}$ together with $\mathbf{r}(s^i)$ are known magnitudes. In order to minimize Eq. 3.42, it is necessary to impose constraints to ensure that the solution satisfy the geometric requirements. These two constrains are written in Eq. 3.43 that states that the distance between the center of the circle and the end of the tangent stretch is the radius of the circle and that the tangent vector at the beginning of the curve is normal to the position vector that joins the center of the radius with the beginning of the curve. The latter one is also known as the tangency condition.

$$\mathbf{g}(\mathbf{u}) = \begin{cases} (x_C - x_B)^2 + (y_C - y_B)^2 - R^2 = 0 \\ (\mathbf{r}_B - \mathbf{r}_A)^T (\mathbf{r}_C - \mathbf{r}_B) = 0 \end{cases} \tag{3.43}$$

As a result, minimizing Eq. 3.42 subject to the constraints of Eq. 3.43 can be done by using different optimization algorithms and methods. By adopting the method of Lagrange multipliers [5], this problem is equivalent to solve the following system of 7 non-linear algebraic equations of Eq. 3.44:

$$\frac{\partial f(\mathbf{u})}{\partial \mathbf{u}} + \boldsymbol{\lambda} \frac{\partial \mathbf{g}(\mathbf{u})}{\partial \mathbf{u}} = 0$$
$$\mathbf{g}(\mathbf{u}) = \mathbf{0} \tag{3.44}$$

where the unknown variables are the Lagrange multipliers of vector $\boldsymbol{\lambda} = \begin{bmatrix} \lambda_1 & \lambda_2 \end{bmatrix}^T$ together with the four components of $\mathbf{u} = \begin{bmatrix} x_B & y_B & x_C & y_C & R \end{bmatrix}^T$. By minimizing the function, it results

$$\begin{aligned} \mathbf{r}_B &= \begin{bmatrix} 1009.93 & 997.28 \end{bmatrix}^T \quad R = 14.9188\,\text{m} \\ \mathbf{r}_C &= \begin{bmatrix} 1015.53 & 1011.19 \end{bmatrix}^T \quad s_1 = 34.85\,\text{m} \end{aligned} \qquad \beta = -1.19\,\text{rad} \tag{3.45}$$

which means that the tangent stretch has a total length of $s_1 = 34.85$ m and a curved one of radius $R = 14.9188$ m.

Ideal track centerline development

The analytical definition of the vertical profile of the track centerline is achieved by straight lines with different slopes that pass through identified vertices. In these vertices, which join two consecutive lines with different slopes, there is a transition stretch obtained by a curve tangent to both consecutive lines. The procedure to obtain the transition curve between two straight lines, line i and line $i+1$ is shown in Fig. 3.38 and described below:

- The transition stretch between two consecutive lines is achieved by a quadratic polynomial of the form:

$$z\left(s_1\right) = as_1^2 + bs_1 + c \tag{3.46}$$

  where s_1 is the local trajectory parameter shown in Fig. 3.38 and calculated as $s_1 = s - s_m$. R_v is the vertical radius of the transition stretch while s_m and s_M are the initial and final point where the vertical transition takes place and α^i and α^{i+1} the angles with respect to the horizontal of the lines i and $i+1$ respectively. In addition, a, b, and c are the polynomial coefficients. Note that for the a coefficient, one can differenciate twice Eq. 3.46 with respect to s_1 to

obtain the curvature. It is then straightforward to calculate the a coefficient as $a = 1/(2R_v)$.

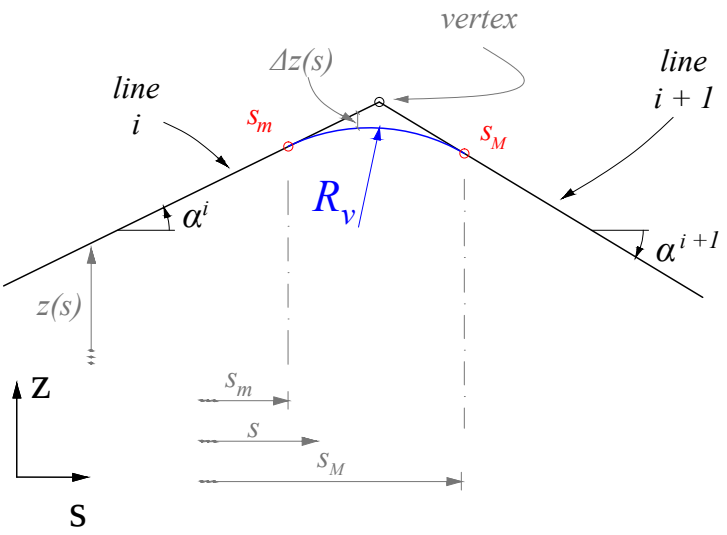

FIGURE 3.38: Vertical transition in track centerline development

- In order to fully determine the transition stretch, the four unknowns s_m, s_M, α^i and α^{i+1} have to be calculated. This is done by solving the four non-linear equations $\mathbf{C}$ of Eq. 3.47:

$$\mathbf{C} = \begin{bmatrix} z^i_{line}(s_m) - z(s_m) \\ z^{i+1}_{line}(s_M) - z(s_M) \\ z'(s_m) - \alpha^i \\ z'(s_M) - \alpha^{i+1} \end{bmatrix} = \mathbf{0} \tag{3.47}$$

Equation 3.47 states that the positions of the vertical coordinates at the beginning and at the end of the transition stretch, $z(s_m)$ and $z(s_M)$, occupy the same positions as those obtained in the tangent lines. It also states that the first derivative of the transition stretch, both at the beginning and at the end, $z'(s_m)$ and $z'(s_M)$, coincide with the slopes of the lines i and $i+1$ respectively.

$s(m)$	$z_{vertex}(mm)$	$R_v(m)$	$\tan\alpha^{i+1}$
0,00	0,00	0,0	-0,00010873
11,06	-44,067481	600	-0,00010873
17,20	-44,7350959	-300	-0,00800532
19,94	-66,6696854	300	-0,00157755
22,20	-70,2349445	500	0,00223998
24,18	-65,7997828	100	0,01450823
26,42	-33,3013445	-50	-0,00853771
27,78	-44,9126247	50	0,0023683
31,18	-36,8604145	200	0,00800979
32,44	-26,7680822	-150	0,00052663
37,18	-24,2718432	800	0,00222553
43,24	-10,7851049	200	0,01369653
48,46	60,7107628	-100	-0,00663193
55,00	17,3379393	100	0,00068662
57,18	18,8347616	150	0,00725257
59,16	33,1948544	-100	-0,0013333
62,42	28,8482992	0,0	0,00

TABLE 3.17: Parameters used in the definition of the track development

- Accordingly, this procedure is applied to the targeted track. As there is no development in the construction drawings of the scaled track, a total of 17 different vertices are manually selected and the corresponding tangent lines that join them, calculated as shown in Fig. 3.39 together with the measured vertical profile. In Table 3.17 it is shown the vertices positions, transition radii and the slope of the consecutive lines.

- After applying Eqs. 3.46 and 3.47, the transition stretches are calculated and then, the ideal track development can be evaluated. Figure 3.40 shows the ideal track development together with the measured one.

3.4.6 Track Irregularities

According to Fig. 3.41, rail irregularities can be defined as vertical and lateral displacements of the rail heads with respect to its ideal configuration. Thus, knowing the ideal

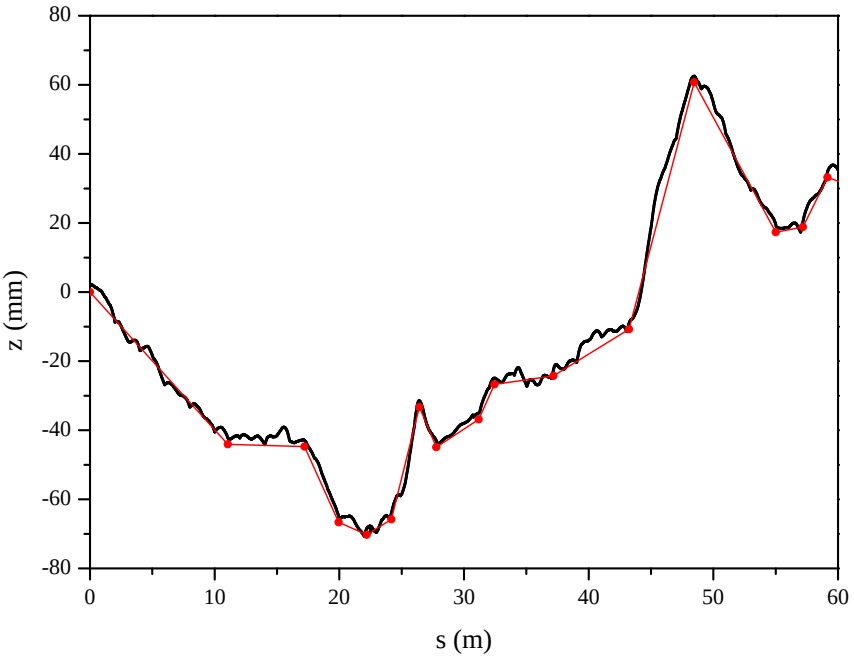

FIGURE 3.39: Identified vertices in track development
Measured vertical development — Identified vertices

geometry of the track centerline calculated in Section 3.4.5.5 and having identified the left and right rail geometry as a function of the trajectory coordinate s of the track centerline, lateral and vertical irregularities can be calculated.

3.4.6.1 Lateral Irregularities

In order to account for the track alignment, it is necessary to identify the ideal position of the left and right rail heads. Then, the 5-inch track gauge is centrally superposed along the track centerline as shown in Fig. 3.42, where for simplicity, only the left rail is considered. This process is described as follows:

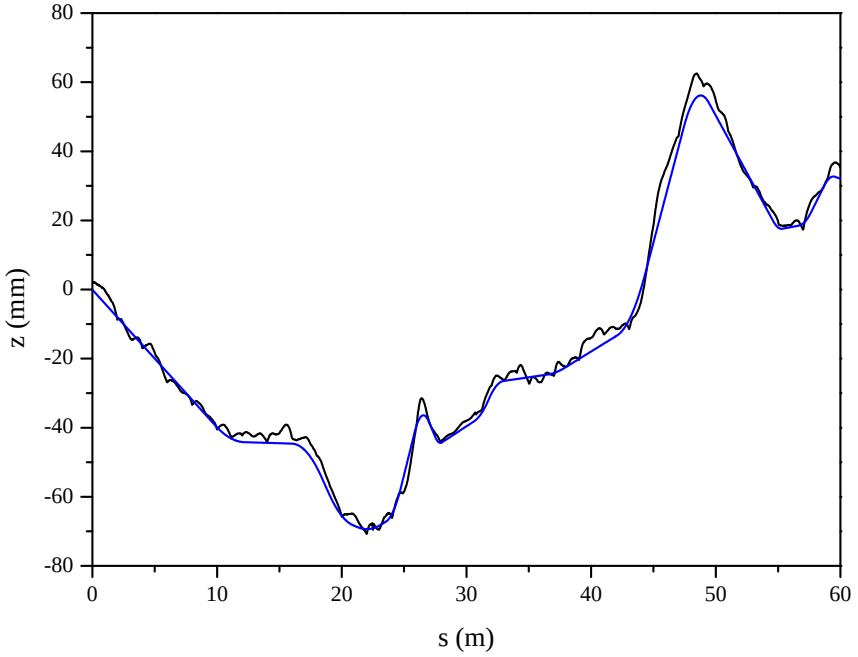

FIGURE 3.40: Ideal track development
Measured vertical development — Ideal track development

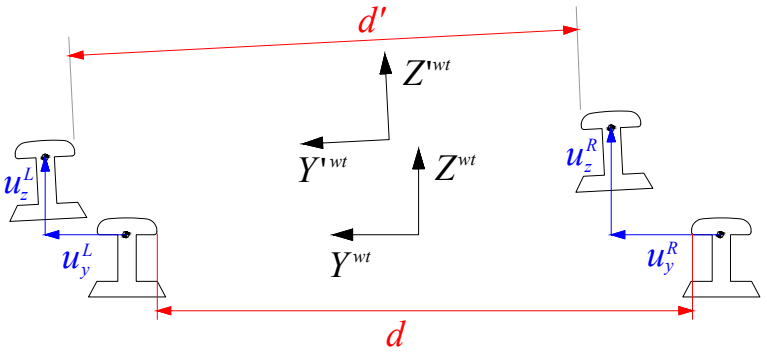

FIGURE 3.41: Discretization of track irregularities

- First, the unitary vector for the left rail at point i, $\mathbf{j}_L^i$ can be computed as:

$$\mathbf{J}_L^i = \mathbf{r}_L^i - \mathbf{r}_{CL}^i \qquad \rightarrow \qquad \mathbf{j}_L^i = \frac{\mathbf{J}_L^i}{|\mathbf{J}_L^i|} \tag{3.48}$$

  where subscripts L and CL stand for the left rail and ideal centerline respectively and $\mathbf{J}_L^i$ refers to the position vector between the point i in the left rail and the corresponding point i in the track centerline.

- Then, the track gauge is centrally superposed as a *translated centerline* (see Fig. 3.42). If a is the track half gauge, this translation is obtained as $a\mathbf{j}_L^i$. Therefore, the vector $\mathbf{y}_L^i$ that accounts for the lateral irregularity in the left rail can be calculated as:

$$\mathbf{y}_L^i = \mathbf{r}_L^i - \left(\mathbf{r}_{CL}^i + a\mathbf{j}_L^i\right) \tag{3.49}$$

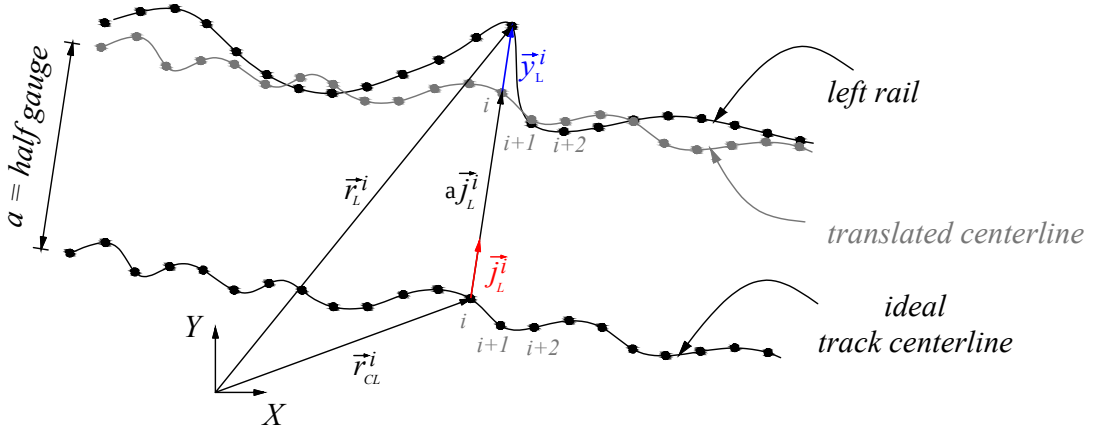

FIGURE 3.42: Computation of lateral irregularities in left rail

- Finally, the lateral left track irregularity at point i, u_y^{Li}, is obtained as $u_y^{Li} = \left|\mathbf{y}_L^i\right|$ but accounting for the sign of the irregularity in accordance with the local frames shown in the right figure of Fig. 3.41. This is, for the left rail, if $\mathbf{r}_L^i$ is larger than $\mathbf{r}_{CL}^i + a\mathbf{j}_L^i$, then u_y^{Li} is positive while for the right rail, if $\mathbf{r}_R^i$ is larger than $\mathbf{r}_{CL}^i + a\mathbf{j}_R^i$, the lateral right irregularity u_y^{Ri} is negative.

Figure 3.43 shows the left and right lateral irregularities u_y^L and u_y^R as a function of the trajectory coordinate s obtained after the application of the proposed postprocessing. It can be seen that both irregularities follow a similar pattern where similar high amplitudes are obtained. The reason for this behaviour is explained by the definition of the ideal track centerline as a tangent stretch followed by a perfect circular one. Even with the minimization procedure derived in Section 3.4.5.5, this ideal geometry does not perfectly match the measured centerline and that is why high deviations are obtained for both lateral irregularities. This will not affect to the numeric simulation since it is the relative lateral irregularity $u_y^L - u_y^R$ the magnitude that affects to the track gauge.

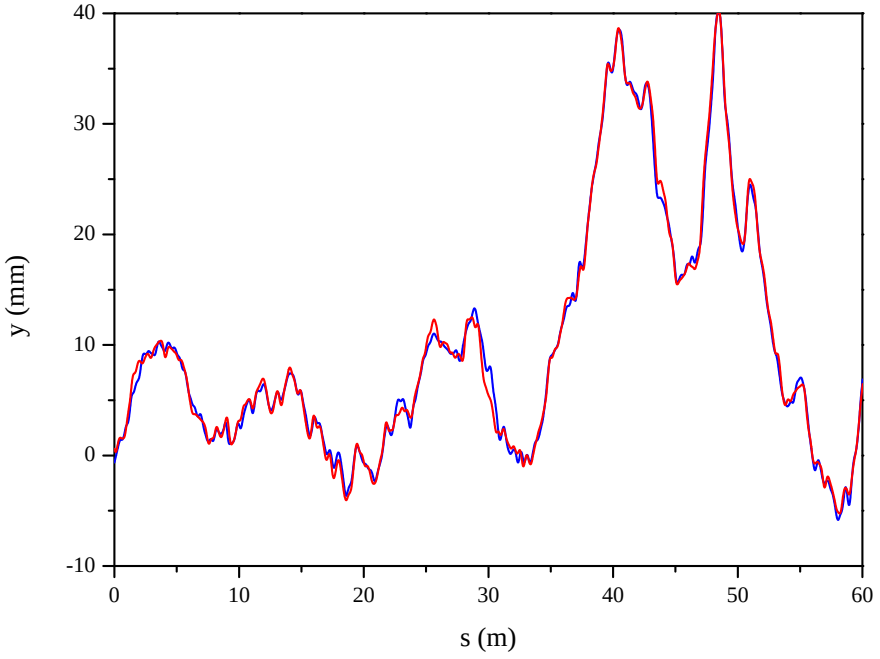

FIGURE 3.43: Computed lateral irregularities
Left rail u_y^L Right rail u_y^R

3.4.6.2 Vertical irregularities

In order to account for the vertical irregularities in the left and right rails, it is assumed that there is no cant angle in the ideal track, this is, the ideal vertical position of the left and right rails coincides with the track centerline development calculated in Section 3.4.5.5. Therefore the vertical irregularities u_z^L and u_z^R can be evaluated as the difference between the left and the right vertical component of $\mathbf{r}_L$ and $\mathbf{r}_R$ with respect to $\mathbf{r}_{CL}$ such as:

$$\begin{aligned} u_z^L &= (\mathbf{r}_L - \mathbf{r}_{CL})_z \\ u_z^R &= (\mathbf{r}_R - \mathbf{r}_{CL})_z \end{aligned} \tag{3.50}$$

Equation 3.50 can be evaluated numerically since $\mathbf{r}_L$, $\mathbf{r}_R$ and $\mathbf{r}_{CL}$ are discretized with the same trajectory parameter s of the track centerline. In Fig. 3.44 it can be seen the measured vertical irregularity in both rails as a function of s.

3.4.6.3 Gauge deviation and cross level

The lateral and vertical irregularities calculated in Section 3.4.6.1 and 3.4.6.2 can be transformed into the commonly known gauge deviation and cross level presented in Eq. 1.1 of Chapter 1. For this purpose, Fig. 3.45 shows the gauge deviation and cross level of the measured track.

3.5 Experimental tests

After the track measurement of Section 3.4 and the parameter identification of the prototype of Section 3.3, the vehicle has been tested on the track for the purpose of acquiring data through the sensors as it can be seen in the following subsections. As

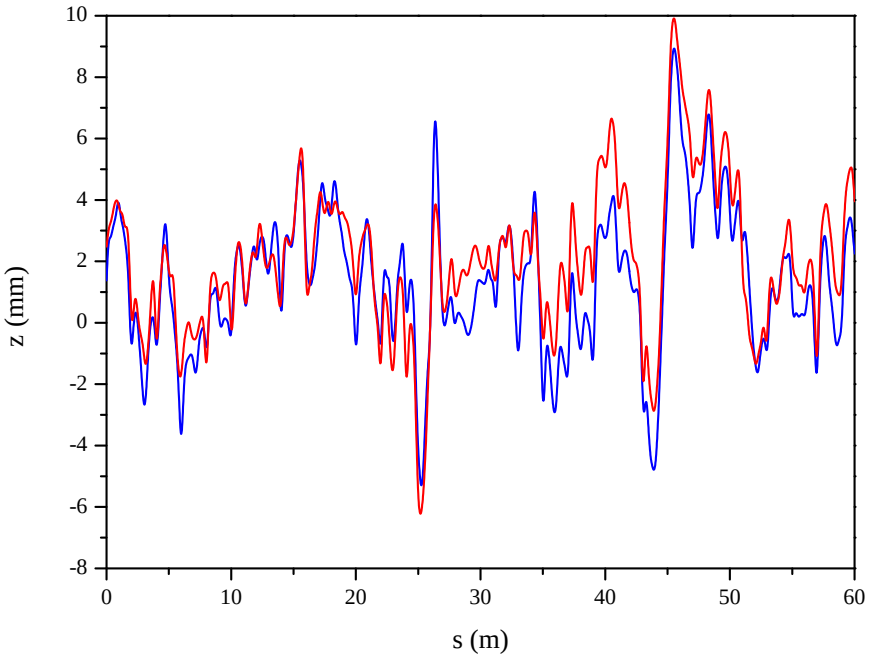

FIGURE 3.44: Computed vertical irregularities
Left rail u_z^L Right rail u_z^R

stated in Section 3.2.7, the instrumentation procedure of the scaled vehicle together with the Data Acquisition software (DAQ) were carried out by Virtualmech [104].

3.5.1 Features of the experimental tests

The characteristics that define the experimental campaing derived with the scaled vehicle can be listed as:

- The prototype is assembled in such a way that the instrumented bogie is the leading one while the driver bogie is the rear one.

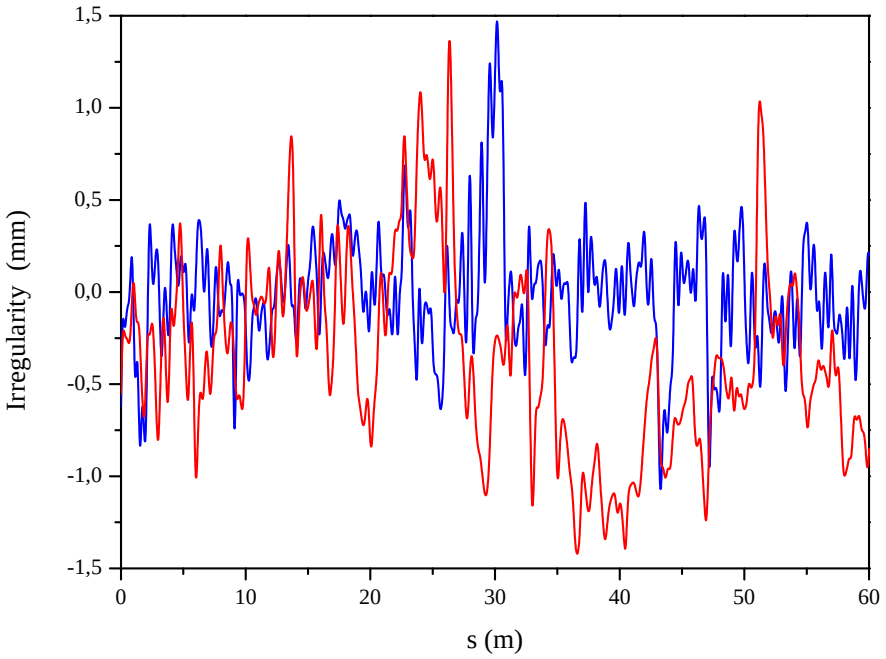

FIGURE 3.45: Gauge deviation and cross level
Gauge deviation Cross level

- The last wheelset at the driver bogie is initially positioned at the first point that was measured in the track. This is, the leading bogie is advanced with respect to the position of the track as shown in Fig. 3.46.

- All sensors (the three IMUs, two lasers and DC motor encoder), start recording data at the initial moment the motor begins rotating.

- In order to avoid the sliding of the wheelset that receives the motor energy with the rail, the motor is constrained with a constant acceleration starting from repose that is provided by the 10% of the total power until it reaches the maximum speed.

- To achieve repeatability, tests are duplicated to check the consistency of the experiments.

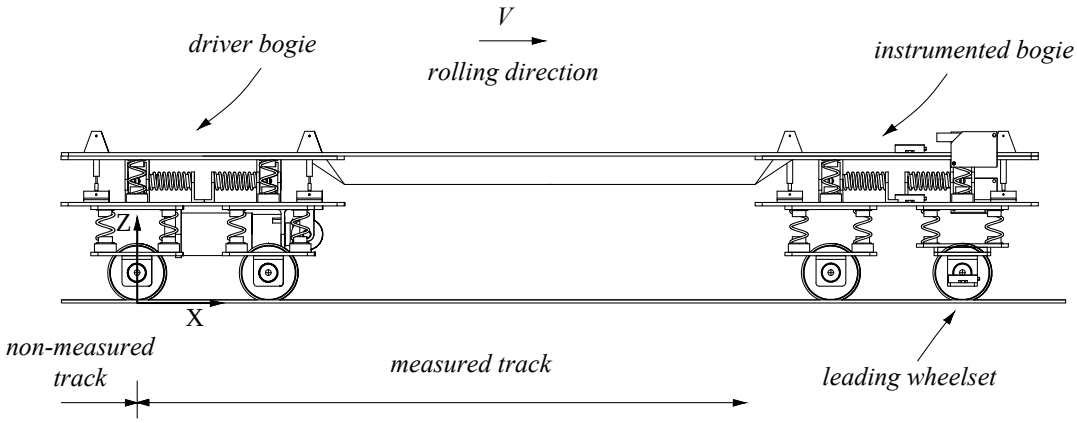

FIGURE 3.46: Initial position experimental tests

3.5.2 Sensors results

In this Section, the results acquired in the experiments are shown. Figure 3.47 on the right shows the forward velocity experienced by the vehicle that is measured throughtout the encoder of the DC motor and where the constant acceleration imposed as a constraint can be observed. In red it is plotted the data acquired by the sensor and in blue is plotted the filtered signal. On the left the distance traveled by the vehicle can be seen.

Figure 3.48 shows the relative vertical deflection with respect to the initial position measured by the distance lasers between the carbody and wheelset planes on the left and between the bogie and the wheelset planes on the right.

Furthermore, from Fig. 3.49 to Fig. 3.54 the acceleration and angular velocity obtained in the three IMUs installed at carbody, bogie frame and wheelset level are shown. Note in Fig. 3.54 the transition between the tangent and curve stretches, since yaw angular velocities experience a considerable constant amplitude.

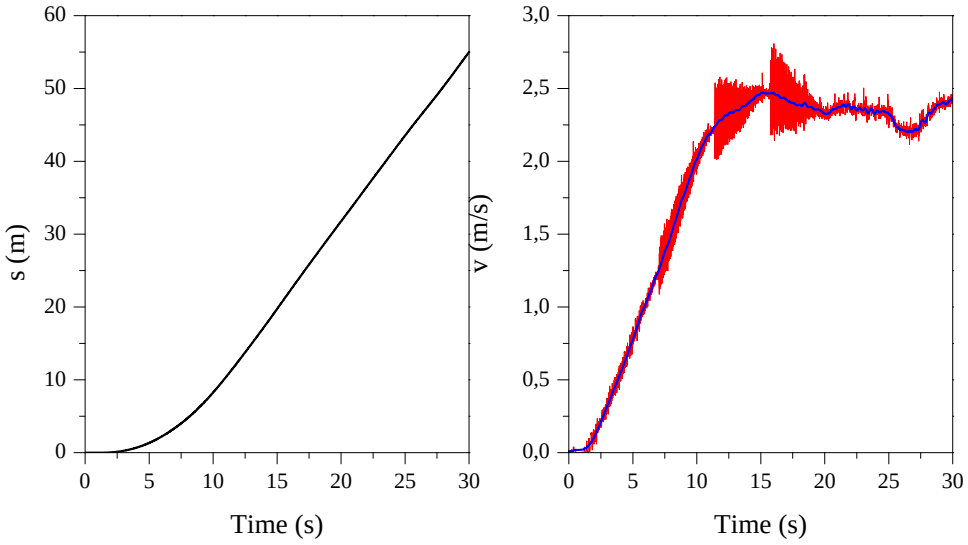

FIGURE 3.47: Distance traveled and forward velocity

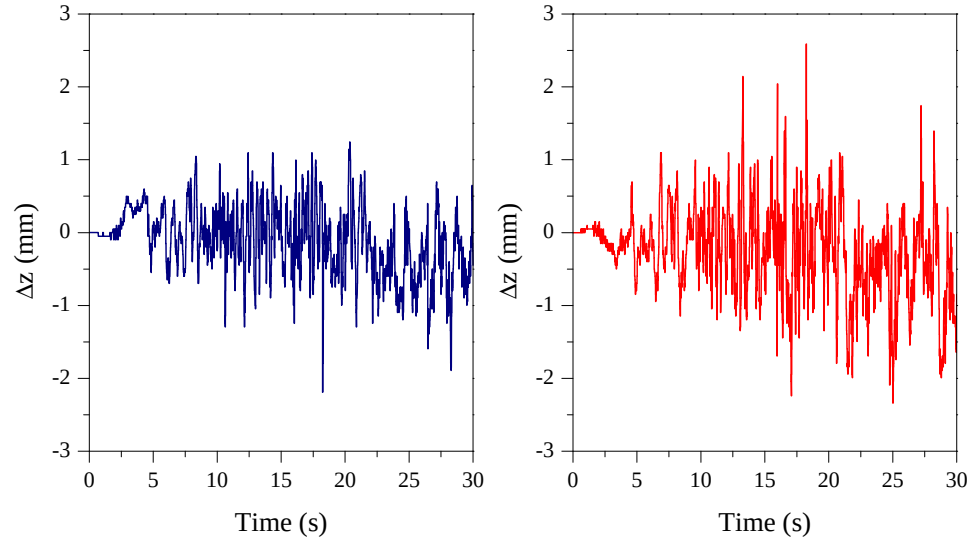

FIGURE 3.48: Relative vertical distance measured by lasers

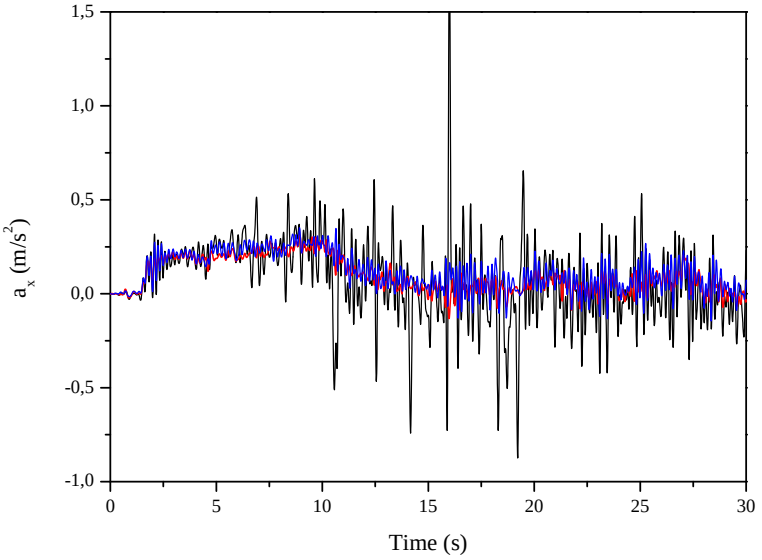

FIGURE 3.49: Longitudinal acceleration at IMUs
Bogie Carbody Wheelset

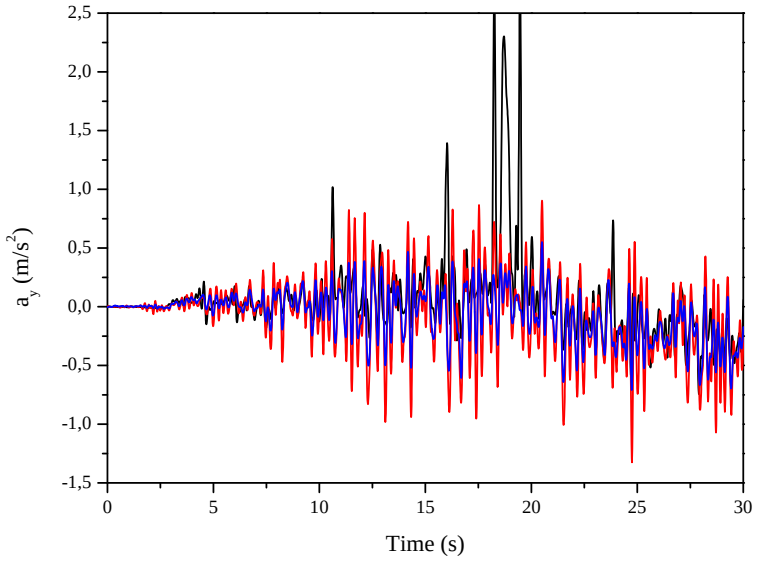

FIGURE 3.50: Lateral acceleration at IMUs
Bogie Carbody Wheelset

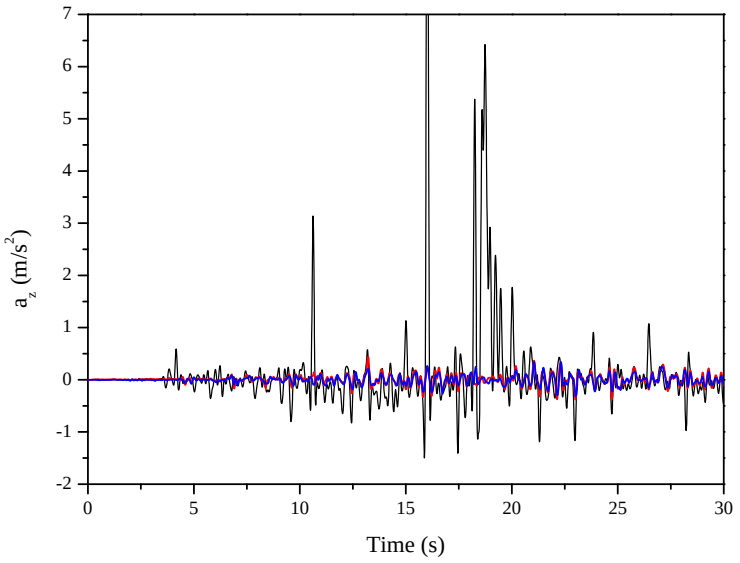

FIGURE 3.51: Vertical acceleration at IMUs
Bogie Carbody Wheelset

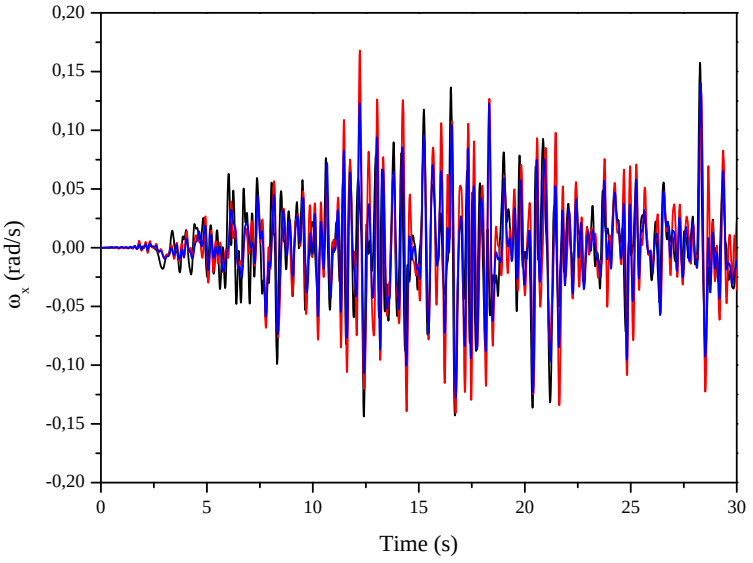

FIGURE 3.52: Longitudinal angular velocity at IMUs
Bogie Carbody Wheelset

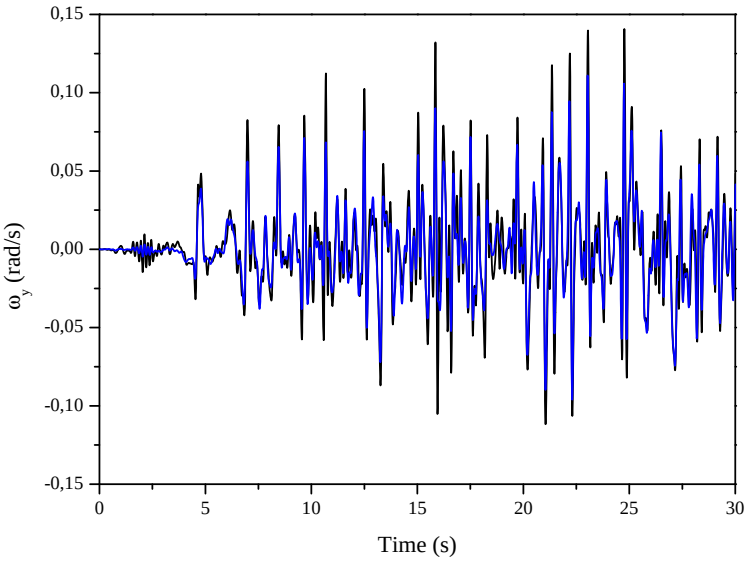

FIGURE 3.53: Lateral angular velocity at IMUs
Bogie Wheelset

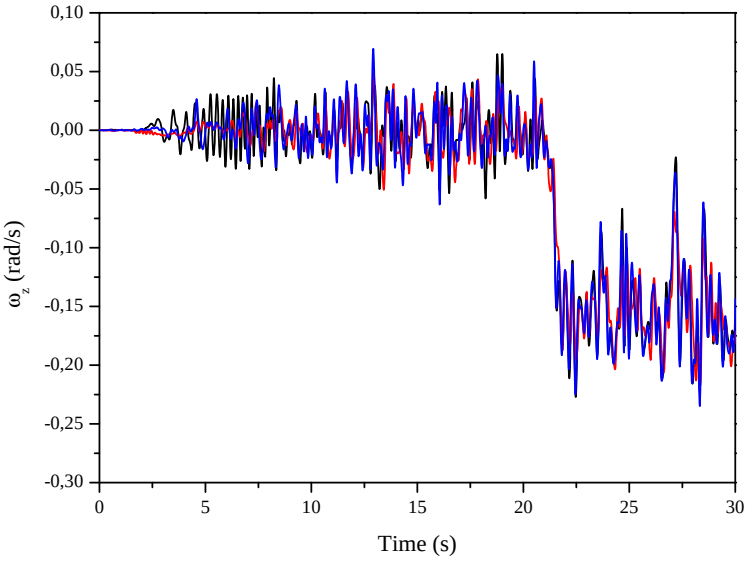

FIGURE 3.54: Vertical angular velocity at IMUs
Bogie Carbody Wheelset

Chapter 4

Numerical Modeling

4.1 Introduction

The objective of this chapter is the validation of the formulation proposed in Chapter 2 when it is applied to the scaled vehicle running on the measured track of Chapter 3 and compared with the experimental results acquired by its sensors. To this end, the mathematical description of the numerical model of the vehicle is presented in Section 4.2 where the mechanical properties, suspension elements, contact parameters and vehicle forward velocity constraint are defined. In Section 4.3 one can find the numerical simulation features, software used and the integration scheme.

4.2 Mathematical model of scaled vehicle

To firstly account for the multibody model of the vehicle, the number of bodies of the system needs to be identified. In this case, there is a total of 7 different bodies that interact among them and that can be listed as:

- **1.** Rear wheelset at rear bogie

- **2.** Front wheelset at rear bogie
- **3.** Rear bogie
- **4.** Rear wheelset at front bogie
- **5.** Front wheelset at front bogie
- **6.** Front bogie
- **7.** Carbody

This bodies' description can be seen in Fig. 4.1, where as it can be noted in Table 4.1, the definition of axleboxes is included in the definition of wheelsets (Bodies 1, 2, 3 and 4). From the mechanical point of view this assumption can be made since the local position vectors of the suspension elements that attach to the axleboxes are expressed in the so-called Wheelset Intermediate Frame (WIF, see Section 2.2.4), which occupies the same position and orientation in case a wheelset and its two axleboxes were considered separately.

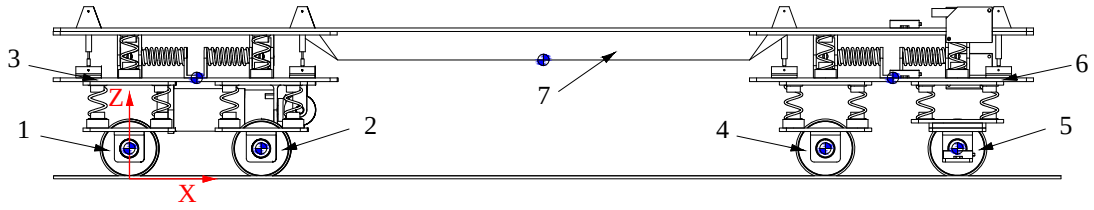

FIGURE 4.1: Scaled vehicle scheme

The vector **q** of initial position and orientation coordinates (*Euler angles*) of the bodies' COG with respect to the Track Frame (in red line at Fig. 4.1) are shown in Table 4.1. Regarding mass and inertia properties of the bodies, a combination of the experimental mass measurements of Section 3.3.2 and CAD software is derived and the obtained results are shown in Table 4.2.

Body	R_x $[m]$	R_y $[m]$	R_z $[m]$	φ $[rad]$	θ $[rad]$	ψ $[rad]$
1	0.0	0.0	0.0381	0.0	0.0	0.0
2	0.18585	0.0	0.0381	0.0	0.0	0.0
3	0.09273	0.0	0.1247	0.0	0.0	0.0
4	0.96480	0.0	0.0381	0.0	0.0	0.0
5	1.14990	0.0	0.0381	0.0	0.0	0.0
6	1.05566	0.0	0.1213	0.0	0.0	0.0
7	0.55433	0.0	0.1770	0.0	0.0	0.0

TABLE 4.1: Initial position and orientation coordinates of bodies

Body	m $[kg]$	I_{xx} $[kg \cdot m^2]$	I_{yy} $[kg \cdot m^2]$	I_{zz} $[kg \cdot m^2]$	I_{xy} $[kg \cdot m^2]$	I_{xz} $[kg \cdot m^2]$	I_{yz} $[kg \cdot m^2]$
1	1.598	0.009	0.001	0.009	0.0	0.0	0.0
2	1.598	0.009	0.001	0.009	0.0	0.0	0.0
3	4.096	0.017	0.046	0.055	0.0049	0.0049	0.0002
4	1.598	0.009	0.001	0.009	0.0	0.0	0.0
5	1.598	0.009	0.001	0.009	0.0	0.0	0.0
6	1.964	0.012	0.024	0.036	0.0007	0.0001	0.0
7	32.044	0.122	3.452	3.518	-0.001	0.009	0.0

TABLE 4.2: Mass and inertia properties of bodies

4.2.1 Suspension elements

Concerning suspension elements, there are only vertical springs and dampers acting on the real vehicle. However, these vertical elements introduce lateral and longitudinal damping and stiffness as described in Section 3.3.1. These properties in the X-Y plane are modeled as lateral and longitudinal suspension elements that initially start in its undeformed configuration. From Table 4.3 to Table 4.11 the mechanical features of the suspension elements are described. In those tables, *No.* refers to the suspension element number, i and j refer to the body in which the attachment points are situated, l_0 to the element undeformed length, k and c to the stiffness and damping coefficients, and $\hat{\mathbf{u}}^i$ and $\hat{\mathbf{u}}^j$ to the local position vectors of the attachment points in bodies i and j respectively.

Vertical primary suspension elements at rear bogie							
No.	i	j	l_0	k $[N/m]$	c $[N \cdot s/m]$	$\hat{\mathbf{u}}^i = \begin{bmatrix} u_x^i \\ u_y^i \\ u_z^i \end{bmatrix}$ $[m]$	$\hat{\mathbf{u}}^j = \begin{bmatrix} u_x^j \\ u_y^j \\ u_z^j \end{bmatrix}$ $[m]$
1	1	3	0.05	8585	3.52	$\begin{bmatrix} -0.044575 \\ -0.0968 \\ 0.0410 \end{bmatrix}$	$\begin{bmatrix} -0.1375 \\ -0.0968 \\ 0.00 \end{bmatrix}$
2	1	3	0.05	8585	3.52	$\begin{bmatrix} 0.044575 \\ -0.0968 \\ 0.0410 \end{bmatrix}$	$\begin{bmatrix} -0.04835 \\ -0.0968 \\ 0.00 \end{bmatrix}$
3	1	3	0.05	8585	3.52	$\begin{bmatrix} -0.044575 \\ 0.0968 \\ 0.0410 \end{bmatrix}$	$\begin{bmatrix} -0.1375 \\ 0.0968 \\ 0.00 \end{bmatrix}$
4	1	3	0.05	8585	3.52	$\begin{bmatrix} 0.044575 \\ 0.0968 \\ 0.0410 \end{bmatrix}$	$\begin{bmatrix} -0.04835 \\ 0.0968 \\ 0.00 \end{bmatrix}$
5	2	3	0.05	8585	3.52	$\begin{bmatrix} -0.044575 \\ -0.0968 \\ 0.0410 \end{bmatrix}$	$\begin{bmatrix} 0.04835 \\ -0.0968 \\ 0.00 \end{bmatrix}$
6	2	3	0.05	8585	3.52	$\begin{bmatrix} 0.044575 \\ -0.0968 \\ 0.0410 \end{bmatrix}$	$\begin{bmatrix} 0.1375 \\ -0.0968 \\ 0.00 \end{bmatrix}$
7	2	3	0.05	8585	3.52	$\begin{bmatrix} -0.044575 \\ 0.0968 \\ 0.0410 \end{bmatrix}$	$\begin{bmatrix} 0.04835 \\ 0.0968 \\ 0.00 \end{bmatrix}$
8	2	3	0.05	8585	3.52	$\begin{bmatrix} 0.044575 \\ 0.0968 \\ 0.0410 \end{bmatrix}$	$\begin{bmatrix} 0.1375 \\ 0.0968 \\ 0.00 \end{bmatrix}$

TABLE 4.3: Vertical primary suspension elements at rear bogie

Longitudinal primary suspension elements at rear bogie							
No.	i	j	l_0	k $[N/m]$	c $[N \cdot s/m]$	$\hat{\mathbf{u}}^i = \begin{bmatrix} u_x^i \\ u_y^i \\ u_z^i \end{bmatrix}$ $[m]$	$\hat{\mathbf{u}}^j = \begin{bmatrix} u_x^j \\ u_y^j \\ u_z^j \end{bmatrix}$ $[m]$
9	1	3	0.01	2505	9.15	$\begin{bmatrix} -0.044575 \\ -0.0968 \\ 0.0660 \end{bmatrix}$	$\begin{bmatrix} -0.1275 \\ -0.0968 \\ -0.025 \end{bmatrix}$
10	1	3	0.01	2505	9.15	$\begin{bmatrix} 0.044575 \\ -0.0968 \\ 0.0660 \end{bmatrix}$	$\begin{bmatrix} -0.03835 \\ -0.0968 \\ -0.025 \end{bmatrix}$
11	1	3	0.01	2505	9.15	$\begin{bmatrix} -0.044575 \\ 0.0968 \\ 0.0660 \end{bmatrix}$	$\begin{bmatrix} -0.1275 \\ 0.0968 \\ -0.025 \end{bmatrix}$
12	1	3	0.01	2505	9.15	$\begin{bmatrix} 0.044575 \\ 0.0968 \\ 0.0660 \end{bmatrix}$	$\begin{bmatrix} -0.03835 \\ 0.0968 \\ -0.025 \end{bmatrix}$
13	2	3	0.01	2505	9.15	$\begin{bmatrix} -0.044575 \\ -0.0968 \\ 0.0660 \end{bmatrix}$	$\begin{bmatrix} 0.03835 \\ -0.0968 \\ -0.025 \end{bmatrix}$
14	2	3	0.01	2505	9.15	$\begin{bmatrix} 0.044575 \\ -0.0968 \\ 0.0660 \end{bmatrix}$	$\begin{bmatrix} 0.1275 \\ -0.0968 \\ -0.025 \end{bmatrix}$
15	2	3	0.01	2505	9.15	$\begin{bmatrix} -0.044575 \\ 0.0968 \\ 0.0660 \end{bmatrix}$	$\begin{bmatrix} 0.03835 \\ 0.0968 \\ -0.025 \end{bmatrix}$
16	2	3	0.01	2505	9.15	$\begin{bmatrix} 0.044575 \\ 0.0968 \\ 0.0660 \end{bmatrix}$	$\begin{bmatrix} 0.1275 \\ 0.0968 \\ -0.025 \end{bmatrix}$

TABLE 4.4: Longitudinal primary suspension elements at rear bogie

Lateral primary suspension elements at rear bogie							
No.	i	j	l_0	k $[N/m]$	c $[N \cdot s/m]$	$\hat{\mathbf{u}}^i = \begin{bmatrix} u_x^i \\ u_y^i \\ u_z^i \end{bmatrix}$ $[m]$	$\hat{\mathbf{u}}^j = \begin{bmatrix} u_x^j \\ u_y^j \\ u_z^j \end{bmatrix}$ $[m]$
17	1	3	0.01	2505	9.15	$\begin{bmatrix} -0.044575 \\ -0.1068 \\ 0.0660 \end{bmatrix}$	$\begin{bmatrix} -0.1375 \\ -0.0968 \\ -0.025 \end{bmatrix}$
18	1	3	0.01	2505	9.15	$\begin{bmatrix} 0.044575 \\ -0.1068 \\ 0.0660 \end{bmatrix}$	$\begin{bmatrix} -0.04835 \\ -0.0968 \\ -0.025 \end{bmatrix}$
19	1	3	0.01	2505	9.15	$\begin{bmatrix} -0.044575 \\ 0.1068 \\ 0.0660 \end{bmatrix}$	$\begin{bmatrix} -0.1375 \\ 0.0968 \\ -0.025 \end{bmatrix}$
20	1	3	0.01	2505	9.15	$\begin{bmatrix} 0.044575 \\ 0.1068 \\ 0.0660 \end{bmatrix}$	$\begin{bmatrix} -0.04835 \\ 0.0968 \\ -0.025 \end{bmatrix}$
21	2	3	0.01	2505	9.15	$\begin{bmatrix} -0.044575 \\ -0.1068 \\ 0.0660 \end{bmatrix}$	$\begin{bmatrix} 0.04835 \\ -0.0968 \\ -0.025 \end{bmatrix}$
22	2	3	0.01	2505	9.15	$\begin{bmatrix} 0.044575 \\ -0.1068 \\ 0.0660 \end{bmatrix}$	$\begin{bmatrix} 0.1375 \\ -0.0968 \\ -0.025 \end{bmatrix}$
23	2	3	0.01	2505	9.15	$\begin{bmatrix} -0.044575 \\ 0.1068 \\ 0.0660 \end{bmatrix}$	$\begin{bmatrix} 0.04835 \\ 0.0968 \\ -0.025 \end{bmatrix}$
24	2	3	0.01	2505	9.15	$\begin{bmatrix} 0.044575 \\ 0.1068 \\ 0.0660 \end{bmatrix}$	$\begin{bmatrix} 0.1375 \\ 0.0968 \\ -0.025 \end{bmatrix}$

TABLE 4.5: Lateral primary suspension elements at rear bogie

Vertical primary suspension elements at front bogie							
No.	i	j	l_0	k $[N/m]$	c $[N \cdot s/m]$	$\hat{\mathbf{u}}^i = \begin{bmatrix} u_x^i \\ u_y^i \\ u_z^i \end{bmatrix}$ $[m]$	$\hat{\mathbf{u}}^j = \begin{bmatrix} u_x^j \\ u_y^j \\ u_z^j \end{bmatrix}$ $[m]$
25	4	6	0.05	8585	3.52	$\begin{bmatrix} -0.044575 \\ -0.0968 \\ 0.0410 \end{bmatrix}$	$\begin{bmatrix} -0.1375 \\ -0.0968 \\ 0.00 \end{bmatrix}$
26	4	6	0.05	8585	3.52	$\begin{bmatrix} 0.044575 \\ -0.0968 \\ 0.0410 \end{bmatrix}$	$\begin{bmatrix} -0.04835 \\ -0.0968 \\ 0.00 \end{bmatrix}$
27	4	6	0.05	8585	3.52	$\begin{bmatrix} -0.044575 \\ 0.0968 \\ 0.0410 \end{bmatrix}$	$\begin{bmatrix} -0.1375 \\ 0.0968 \\ 0.00 \end{bmatrix}$
28	4	6	0.05	8585	3.52	$\begin{bmatrix} 0.044575 \\ 0.0968 \\ 0.0410 \end{bmatrix}$	$\begin{bmatrix} -0.04835 \\ 0.0968 \\ 0.00 \end{bmatrix}$
29	5	6	0.05	8585	3.52	$\begin{bmatrix} -0.044575 \\ -0.0968 \\ 0.0410 \end{bmatrix}$	$\begin{bmatrix} 0.04835 \\ -0.0968 \\ 0.00 \end{bmatrix}$
30	5	6	0.05	8585	3.52	$\begin{bmatrix} 0.044575 \\ -0.0968 \\ 0.0410 \end{bmatrix}$	$\begin{bmatrix} 0.1375 \\ -0.0968 \\ 0.00 \end{bmatrix}$
31	5	6	0.05	8585	3.52	$\begin{bmatrix} -0.044575 \\ 0.0968 \\ 0.0410 \end{bmatrix}$	$\begin{bmatrix} 0.04835 \\ 0.0968 \\ 0.00 \end{bmatrix}$
32	5	6	0.05	8585	3.52	$\begin{bmatrix} 0.044575 \\ 0.0968 \\ 0.0410 \end{bmatrix}$	$\begin{bmatrix} 0.1375 \\ 0.0968 \\ 0.00 \end{bmatrix}$

TABLE 4.6: Vertical primary suspension elements at front bogie

Longitudinal primary suspension elements at front bogie							
No.	i	j	l_0	k $[N/m]$	c $[N \cdot s/m]$	$\hat{\mathbf{u}}^i = \begin{bmatrix} u_x^i \\ u_y^i \\ u_z^i \end{bmatrix}$ $[m]$	$\hat{\mathbf{u}}^j = \begin{bmatrix} u_x^j \\ u_y^j \\ u_z^j \end{bmatrix}$ $[m]$
33	4	6	0.01	2505	9.15	$\begin{bmatrix} -0.044575 \\ -0.0968 \\ 0.0660 \end{bmatrix}$	$\begin{bmatrix} -0.1275 \\ -0.0968 \\ -0.025 \end{bmatrix}$
34	4	6	0.01	2505	9.15	$\begin{bmatrix} 0.044575 \\ -0.0968 \\ 0.0660 \end{bmatrix}$	$\begin{bmatrix} -0.03835 \\ -0.0968 \\ -0.025 \end{bmatrix}$
35	4	6	0.01	2505	9.15	$\begin{bmatrix} -0.044575 \\ 0.0968 \\ 0.0660 \end{bmatrix}$	$\begin{bmatrix} -0.1275 \\ 0.0968 \\ -0.025 \end{bmatrix}$
36	4	6	0.01	2505	9.15	$\begin{bmatrix} 0.044575 \\ 0.0968 \\ 0.0660 \end{bmatrix}$	$\begin{bmatrix} -0.03835 \\ 0.0968 \\ -0.025 \end{bmatrix}$
37	5	6	0.01	2505	9.15	$\begin{bmatrix} -0.044575 \\ -0.0968 \\ 0.0660 \end{bmatrix}$	$\begin{bmatrix} 0.03835 \\ -0.0968 \\ -0.025 \end{bmatrix}$
38	5	6	0.01	2505	9.15	$\begin{bmatrix} 0.044575 \\ -0.0968 \\ 0.0660 \end{bmatrix}$	$\begin{bmatrix} 0.1275 \\ -0.0968 \\ -0.025 \end{bmatrix}$
39	5	6	0.01	2505	9.15	$\begin{bmatrix} -0.044575 \\ 0.0968 \\ 0.0660 \end{bmatrix}$	$\begin{bmatrix} 0.03835 \\ 0.0968 \\ -0.025 \end{bmatrix}$
40	5	6	0.01	2505	9.15	$\begin{bmatrix} 0.044575 \\ 0.0968 \\ 0.0660 \end{bmatrix}$	$\begin{bmatrix} 0.1275 \\ 0.0968 \\ -0.025 \end{bmatrix}$

TABLE 4.7: Longitudinal primary suspension elements at front bogie

Lateral primary suspension elements at front bogie							
No.	i	j	l_0	k $[N/m]$	c $[N \cdot s/m]$	$\hat{\mathbf{u}}^i = \begin{bmatrix} u_x^i \\ u_y^i \\ u_z^i \end{bmatrix}$ $[m]$	$\hat{\mathbf{u}}^j = \begin{bmatrix} u_x^j \\ u_y^j \\ u_z^j \end{bmatrix}$ $[m]$
41	4	6	0.01	2505	9.15	$\begin{bmatrix} -0.044575 \\ -0.1068 \\ 0.0660 \end{bmatrix}$	$\begin{bmatrix} -0.1375 \\ -0.0968 \\ -0.025 \end{bmatrix}$
42	4	6	0.01	2505	9.15	$\begin{bmatrix} 0.044575 \\ -0.1068 \\ 0.0660 \end{bmatrix}$	$\begin{bmatrix} -0.04835 \\ -0.0968 \\ -0.025 \end{bmatrix}$
43	4	6	0.01	2505	9.15	$\begin{bmatrix} -0.044575 \\ 0.1068 \\ 0.0660 \end{bmatrix}$	$\begin{bmatrix} -0.1375 \\ 0.0968 \\ -0.025 \end{bmatrix}$
44	4	6	0.01	2505	9.15	$\begin{bmatrix} 0.044575 \\ 0.1068 \\ 0.0660 \end{bmatrix}$	$\begin{bmatrix} -0.04835 \\ 0.0968 \\ -0.025 \end{bmatrix}$
45	5	6	0.01	2505	9.15	$\begin{bmatrix} -0.044575 \\ -0.1068 \\ 0.0660 \end{bmatrix}$	$\begin{bmatrix} 0.04835 \\ -0.0968 \\ -0.025 \end{bmatrix}$
46	5	6	0.01	2505	9.15	$\begin{bmatrix} 0.044575 \\ -0.1068 \\ 0.0660 \end{bmatrix}$	$\begin{bmatrix} 0.1375 \\ -0.0968 \\ -0.025 \end{bmatrix}$
47	5	6	0.01	2505	9.15	$\begin{bmatrix} -0.044575 \\ 0.1068 \\ 0.0660 \end{bmatrix}$	$\begin{bmatrix} 0.04835 \\ 0.0968 \\ -0.025 \end{bmatrix}$
48	5	6	0.01	2505	9.15	$\begin{bmatrix} 0.044575 \\ 0.1068 \\ 0.0660 \end{bmatrix}$	$\begin{bmatrix} 0.1375 \\ 0.0968 \\ -0.025 \end{bmatrix}$

TABLE 4.8: Lateral primary suspension elements at front bogie

Vertical primary suspension elements at front bogie							
No.	i	j	l_0	k $[N/m]$	c $[N \cdot s/m]$	$\hat{\mathbf{u}}^i = \begin{bmatrix} u_x^i \\ u_y^i \\ u_z^i \end{bmatrix}$ $[m]$	$\hat{\mathbf{u}}^j = \begin{bmatrix} u_x^j \\ u_y^j \\ u_z^j \end{bmatrix}$ $[m]$
49	3	7	0.05	8585	3.52	$\begin{bmatrix} -0.092925 \\ -0.0968 \\ 0.010 \end{bmatrix}$	$\begin{bmatrix} -0.55312 \\ -0.0968 \\ 0.00115 \end{bmatrix}$
50	3	7	0.05	8585	3.52	$\begin{bmatrix} 0.092925 \\ -0.0968 \\ 0.010 \end{bmatrix}$	$\begin{bmatrix} -0.36727 \\ -0.0968 \\ 0.00115 \end{bmatrix}$
51	3	7	0.05	8585	3.52	$\begin{bmatrix} -0.092925 \\ 0.0968 \\ 0.010 \end{bmatrix}$	$\begin{bmatrix} -0.55312 \\ 0.0968 \\ 0.00115 \end{bmatrix}$
52	3	7	0.05	8585	3.52	$\begin{bmatrix} 0.092925 \\ 0.0968 \\ 0.010 \end{bmatrix}$	$\begin{bmatrix} -0.36727 \\ 0.0968 \\ 0.00115 \end{bmatrix}$
53	6	7	0.05	8585	3.52	$\begin{bmatrix} -0.092925 \\ -0.0968 \\ 0.010 \end{bmatrix}$	$\begin{bmatrix} 0.42688 \\ -0.0968 \\ 0.00115 \end{bmatrix}$
54	6	7	0.05	8585	3.52	$\begin{bmatrix} 0.092925 \\ -0.0968 \\ 0.010 \end{bmatrix}$	$\begin{bmatrix} 0.61273 \\ -0.0968 \\ 0.00115 \end{bmatrix}$
55	6	7	0.05	8585	3.52	$\begin{bmatrix} -0.092925 \\ 0.0968 \\ 0.010 \end{bmatrix}$	$\begin{bmatrix} 0.42688 \\ 0.0968 \\ 0.00115 \end{bmatrix}$
56	6	7	0.05	8585	3.52	$\begin{bmatrix} 0.092925 \\ 0.0968 \\ 0.010 \end{bmatrix}$	$\begin{bmatrix} 0.61273 \\ 0.0968 \\ 0.00115 \end{bmatrix}$

TABLE 4.9: Vertical secondary suspension elements

Longitudinal secondary suspension elements							
No.	i	j	l_0	k $[N/m]$	c $[N \cdot s/m]$	$\hat{\mathbf{u}}^i = \begin{bmatrix} u_x^i \\ u_y^i \\ u_z^i \end{bmatrix}$ $[m]$	$\hat{\mathbf{u}}^j = \begin{bmatrix} u_x^j \\ u_y^j \\ u_z^j \end{bmatrix}$ $[m]$
57	3	7	0.01	2505	9.15	$\begin{bmatrix} -0.092925 \\ -0.0968 \\ 0.030 \end{bmatrix}$	$\begin{bmatrix} -0.54312 \\ -0.0968 \\ -0.02885 \end{bmatrix}$
58	3	7	0.01	2505	9.15	$\begin{bmatrix} 0.092925 \\ -0.0968 \\ 0.030 \end{bmatrix}$	$\begin{bmatrix} -0.35727 \\ -0.0968 \\ -0.02885 \end{bmatrix}$
59	3	7	0.01	2505	9.15	$\begin{bmatrix} -0.092925 \\ 0.0968 \\ 0.030 \end{bmatrix}$	$\begin{bmatrix} -0.54312 \\ 0.0968 \\ -0.02885 \end{bmatrix}$
60	3	7	0.01	2505	9.15	$\begin{bmatrix} 0.092925 \\ 0.0968 \\ 0.030 \end{bmatrix}$	$\begin{bmatrix} -0.35727 \\ 0.0968 \\ -0.02885 \end{bmatrix}$
61	6	7	0.01	2505	9.15	$\begin{bmatrix} -0.092925 \\ -0.0968 \\ 0.030 \end{bmatrix}$	$\begin{bmatrix} 0.41688 \\ -0.0968 \\ -0.02885 \end{bmatrix}$
62	6	7	0.01	2505	9.15	$\begin{bmatrix} 0.092925 \\ -0.0968 \\ 0.030 \end{bmatrix}$	$\begin{bmatrix} 0.60273 \\ -0.0968 \\ -0.02885 \end{bmatrix}$
63	6	7	0.01	2505	9.15	$\begin{bmatrix} -0.092925 \\ 0.0968 \\ 0.030 \end{bmatrix}$	$\begin{bmatrix} 0.41688 \\ 0.0968 \\ -0.02885 \end{bmatrix}$
64	6	7	0.01	2505	9.15	$\begin{bmatrix} 0.092925 \\ 0.0968 \\ 0.030 \end{bmatrix}$	$\begin{bmatrix} 0.60273 \\ 0.0968 \\ -0.02885 \end{bmatrix}$

TABLE 4.10: Longitudinal secondary suspension elements

Lateral secondary suspension elements							
No.	i	j	l_0	k $[N/m]$	c $[N \cdot s/m]$	$\hat{\mathbf{u}}^i = \begin{bmatrix} u_x^i \\ u_y^i \\ u_z^i \end{bmatrix}$ $[m]$	$\hat{\mathbf{u}}^j = \begin{bmatrix} u_x^j \\ u_y^j \\ u_z^j \end{bmatrix}$ $[m]$
65	3	7	0.01	2505	9.15	$\begin{bmatrix} -0.92925 \\ -0.1068 \\ 0.030 \end{bmatrix}$	$\begin{bmatrix} -0.55312 \\ -0.0968 \\ -0.02885 \end{bmatrix}$
66	3	7	0.01	2505	9.15	$\begin{bmatrix} 0.092925 \\ -0.1068 \\ 0.030 \end{bmatrix}$	$\begin{bmatrix} -0.36727 \\ -0.0968 \\ -0.02885 \end{bmatrix}$
67	3	7	0.01	2505	9.15	$\begin{bmatrix} -0.092925 \\ 0.1068 \\ 0.030 \end{bmatrix}$	$\begin{bmatrix} -0.55312 \\ 0.0968 \\ -0.02885 \end{bmatrix}$
68	3	7	0.01	2505	9.15	$\begin{bmatrix} 0.092925 \\ 0.1068 \\ 0.030 \end{bmatrix}$	$\begin{bmatrix} -0.36727 \\ 0.0968 \\ -0.02885 \end{bmatrix}$
69	4	7	0.01	2505	9.15	$\begin{bmatrix} -0.092925 \\ -0.1068 \\ 0.030 \end{bmatrix}$	$\begin{bmatrix} 0.42688 \\ -0.0968 \\ -0.02885 \end{bmatrix}$
70	4	7	0.01	2505	9.15	$\begin{bmatrix} 0.092925 \\ -0.1068 \\ 0.030 \end{bmatrix}$	$\begin{bmatrix} 0.61273 \\ -0.0968 \\ -0.02885 \end{bmatrix}$
71	4	7	0.01	2505	9.15	$\begin{bmatrix} -0.092925 \\ 0.1068 \\ 0.030 \end{bmatrix}$	$\begin{bmatrix} 0.42688 \\ 0.0968 \\ -0.02885 \end{bmatrix}$
72	4	7	0.01	2505	9.15	$\begin{bmatrix} 0.092925 \\ 0.1068 \\ 0.030 \end{bmatrix}$	$\begin{bmatrix} 0.61273 \\ 0.0968 \\ -0.02885 \end{bmatrix}$

TABLE 4.11: Lateral secondary suspension elements

4.2.2 Linear creep coefficients

As stated in Section 2.3.4, tangential tread contact forces are calculated using the Kalker simplified theory of rolling contact [41] where, in order to avoid the gross-sliding phenomenon that is not accurately reproduced by this theory, the numerical simulations account for a smoothed forward acceleration, as it is shown in Section 4.3. In this theory, the linear relation between the creepages $\boldsymbol{\varepsilon}$ and the creep forces and moment $\mathbf{F}_{cntact}$ are obtained by Eq. 2.48 as $\mathbf{F}_{cntact} = \mathbf{D}\boldsymbol{\varepsilon}$, where the coefficients of matrix $\mathbf{D}$ are calculated as follows:

$$\mathbf{D} = -Gab \begin{bmatrix} c_{11} & 0 & 0 \\ 0 & c_{22} & \sqrt{ab}c_{23} \\ 0 & -\sqrt{ab}c_{23} & c_{33} \end{bmatrix} \tag{4.1}$$

being G the modulus of rigidity, a the contact ellipse semi-axis in the rolling direction, b the contact ellipse semi-axis in the lateral direction and c_{11}, c_{22}, c_{33}, c_{12}, c_{23} the creepage coefficients that depend on Poisson's ratio and the ratio of contact ellipse semi-axes, as it can be found in [40]. In order to compute the contact ellipse semi-axes a and b, the contact area is assumed small compared with the size of the two bodies in contact. As a result, the requirements for the equilibrium of two bodies in contact proposed by Goldsmith [27], can be satisfied, which allows the computation of the contact ellipse semi-axes as a function of the normal contact force and the geometric parameter of the bodies in contact [96]. In addition, assuming that the semi-axes of the contact ellipse remain constant, matrix $\mathbf{D}$ that applies to the scaled railroad vehicle is calculated as:

$$\mathbf{D} = \begin{bmatrix} -9.1481 \cdot 10^3\,\mathrm{N} & 0 & 0 \\ 0 & -1.0008 \cdot 10^4\,\mathrm{N} & -1.1286\,\mathrm{N \cdot m} \\ 0 & 1.1286\,\mathrm{N \cdot m} & -1.11571 \cdot 10^{-4}\,\mathrm{N \cdot m^2} \end{bmatrix} \tag{4.2}$$

4.2.3 Flange contact features

Flange contact forces are calculated using an elastic method based on the indentation and on its first-time derivative between the rail-head profile and wheel flange surfaces as shown in Section 2.3.4.1 and in Eq. 2.50. To that end, a Hertzian contact stiffness k_f is assumed and calculated based on the geometry and material of the surfaces in contact [96] as:

$$k_f = \frac{4\beta}{3\left(K^r + K^w\right)\sqrt{A+B}} \tag{4.3}$$

where K^r and K^w are material properties of the two surfaces in contact (superscripts r and w for rail and wheel respectively) that depend on the Poisson's ratio ν and Young modulus E as in Eq. 4.4. Also, A and B are geometric parameters of the surfaces, that are calculated as a function of the surface principal radii of curvature R_1 and R_2 as shown in Eq. 4.5.

$$K^r = \frac{1-\left(\nu^r\right)^2}{\pi E^r}, \qquad K^w = \frac{1-\left(\nu^w\right)^2}{\pi E^w} \tag{4.4}$$

$$A = \frac{1}{2}\left(\frac{1}{R_1^r} + \frac{1}{R_1^w}\right), \qquad B = \frac{1}{2}\left(\frac{1}{R_2^r} + \frac{1}{R_2^w}\right) \tag{4.5}$$

Finally, β is a parameter that depends on the ratio A/B and is given by Goldsmith in [27] and in Table 4.12.

Assuming that in the scaled vehicle, $R_1^w = 38.10$ mm., $R_2^w = +\infty$, $R_1^r = +\infty$, $R_2^r = 1.306$ mm., $\nu^r = \nu^w = 0.3$, and $E^r = E^w = 200 \cdot 10^9$ N/m^2, the contact flange stiffness k_f is calculated as:

$$k_f = 1.509 \cdot 10^{10} \quad \text{N/m} \tag{4.6}$$

A/B	β
1.0	0.3180
0.7041	0.3215
0.4903	0.3322
0.3333	0.3505
0.2174	0.3819
0.1325	0.4300
0.0718	0.5132
0.0311	0.6662
0.00765	1.1450

TABLE 4.12: Goldsmith β-parameter [27]

Regarding the remaining flange parameters used in Eq. 2.50, n is assumed to be 1.5 as a Hertzian stiffness, and the damping ratio c_f, which is heuristically obtained, is assumed to be $c_f = 1.810 \cdot 10^9$ N·s/m. Note that for the selection of c_f of Eq. 2.50, one should avoid the appearance of traction forces as it occurs when the damping term is higher than the elastic one with opposite sign. In addition, the Coulomb dry friction parameter μ_f of Eq. 2.51 is assumed to be $\mu_f = 0.3$.

4.2.4 Forward velocity constraint

One of the advantages of the proposed Track Frame Formulation in Chapter 2, is the easy implementation of prescribed motions. As there is a body (fixing body) whose forward motion along the track centerline is constrained to be that of the TF (see Eq. 4.7), a prescribed motion only needs to be defined to the TF while it is left to the fixing body to pull the entire vehicle. If i is the fixing body, its constraint equation according to the coordinates vector $\mathbf{q}^i$ of Eq. 2.5 is:

$$x^i = 0 \tag{4.7}$$

As the position and orientation of the TF with respect to the GF is a function of the arc length parameter s^t provided by the track preprocessor subroutine, it is easy to prescribe the trajectory parameter and its first and second time derivatives s^t, $\dot{s}^t$ and $\ddot{s}^t$ as a function of time $s^t = s^t(t)$, $\dot{s}^t = \dot{s}^t(t)$ and $\ddot{s}^t = \ddot{s}^t(t)$.

In the case of the scaled vehicle, a DC motor with an encoder is used to provide the motion of the entire vehicle. The encoder registers the revolutions per second acquired by the motor when it starts rotating. Knowing the nominal wheel radius, it is straightforward to determine $s^t(t)$, $\dot{s}^t(t)$ and $\ddot{s}^t(t)$, and include them as prescribed coordinates of the TF. Figures 4.2, 4.3 and 4.4 show the trajectory coordinate and its filtered time derivatives as a function of time.

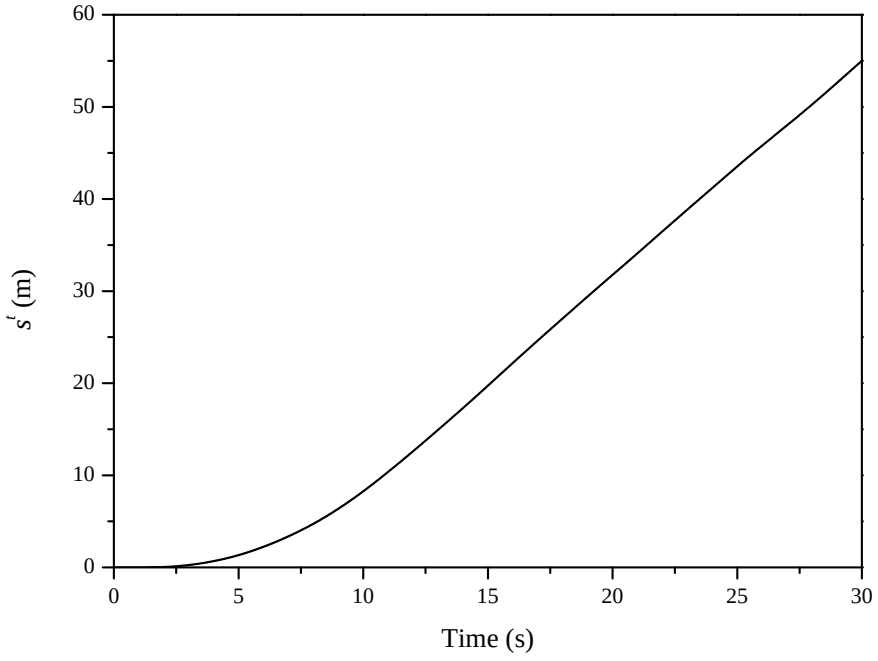

FIGURE 4.2: TF trajectory coordinate $s^t(t)$

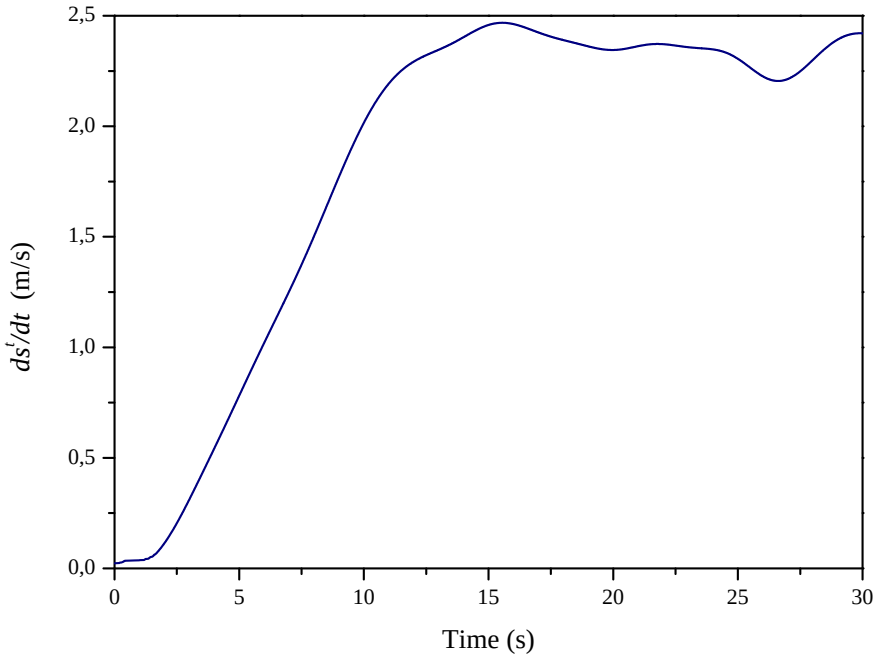

FIGURE 4.3: TF trajectory first time derivative $\dot{s}^t(t)$

4.3 Simulation features

The proposed formulation of Chapter 2 is implemented in Matlab® software in terms of the Object-Oriented Programming (OOP) concepts [79]. Before solving the equations of motion of Eq. 2.37 augmented with the contact lookup table constraints of Eq. 2.68 together with the fixing body constraint of Eq. 4.7 and with the prescribed TF motion of Figs. 4.2, 4.3 and 4.4, the following preprocessing procedure, also shown in Fig. 4.5, is derived:

1. Inertia and mechanical properties of the multibody model of the scaled train are first obtained.

2. Wheel-rail contact lookup tables are generated.

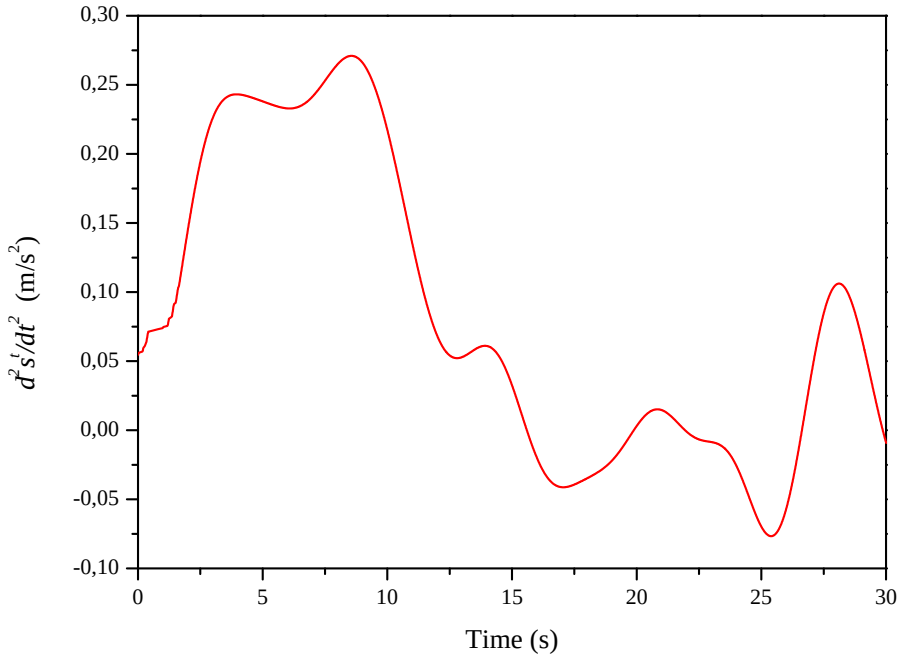

FIGURE 4.4: TF trajectory second time derivative $\ddot{s}^t(t)$

3. TF motion trajectory speed is obtained from the encoder file. Its position and acceleration as a function of the time are also calculated.

4. The ideal track geometry is first calculated together with its lateral and vertical irregularities.

5. Having identified the ideal track geometry and its irregularities, the real track is discretized as a combination of the ideal one plus track defects. The purpose of this discretization is to avoid the calculation of the right and left rail-head positions at every time step of the numeric simulation since it is only necessary to interpolate between the discretized real track positions.

6. Initial conditions (bodies static equilibrium positions and velocities) are set up.

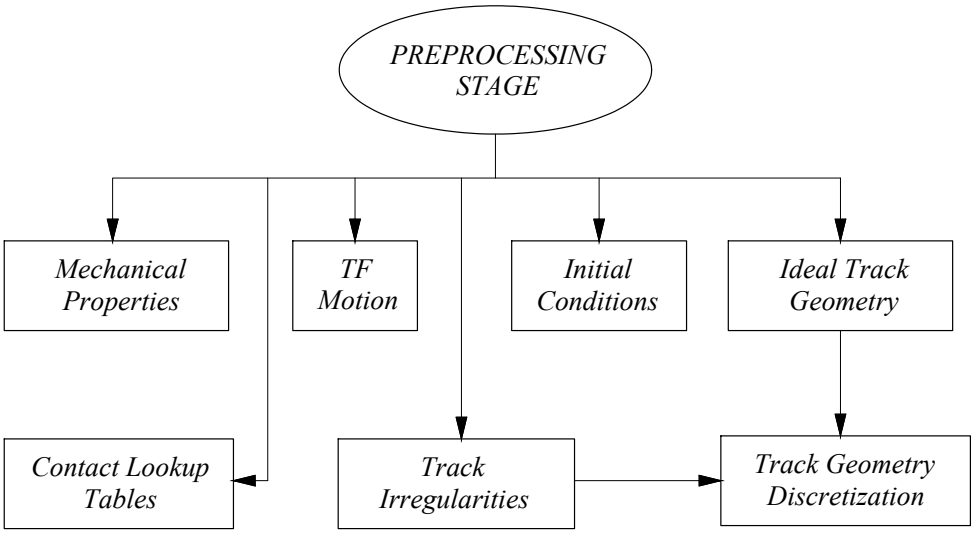

FIGURE 4.5: Preprocessing stage

4.3.1 Integration of equations of motion

After the preprocessing stage, the equations of motion are integrated forward in time. This process, which has been deeply studied in the literature, is of major importance in the accuracy of the results and in the computational cost involved. For this reason, in what follows it is explained the procedure derived to obtain the final form in which the equations of motion are integrated.

In this thesis, the equations of motion of unconstrained railroad vehicles of Eq. 2.37, are augmented with the constraints vector $\mathbf{C}$ as follows:

$$\begin{aligned} \mathbf{M}\ddot{\mathbf{q}} + \mathbf{C}_{\mathbf{q}}^{T}\boldsymbol{\lambda} &= \mathbf{Q} \\ \mathbf{C}\left(\mathbf{q}\right) &= \mathbf{0} \end{aligned} \tag{4.8}$$

where $\mathbf{q}$ is the vector of the system generalized coordinates, $\mathbf{M}$ is the mass matrix of the system, $\mathbf{Q}$ is the vector of generalized forces that accounts for the externally applied forces, suspension forces, TF inertia forces, cuadratic velocity term forces and

tangential contact forces, and $\mathbf{C_q}$ and $\boldsymbol{\lambda}$ the Jacobian matrix of the constraints and its Lagrange multipliers respectively. Note that the constraints vector $\mathbf{C}$ accounts for the contact lookup tables constraints (see Section 2.4.2) together with the fixing body constraint of Eq. 4.7, so the reaction forces associated with the constraints involve, among other things, the normal contact forces, and the fixing body constraint forces (traction force).

In order to integrate forward in time Eq. 4.8, the constraint vector equation $\mathbf{C}(\mathbf{q}) = \mathbf{0}$ can be differentiated twice with respect time such as:

$$\mathbf{C_q}\ddot{\mathbf{q}} = -\dot{\mathbf{C}}_\mathbf{q}\dot{\mathbf{q}} - \dot{\mathbf{C}}_t \tag{4.9}$$

where $\mathbf{C}_t$ is the partial time derivative of the constraints, which is null for this case study since the imposed constraints are not explicit functions of time. This allows the system equations of motion to take the matrix form of:

$$\begin{bmatrix} \mathbf{M} & \mathbf{C}_\mathbf{q}^T \\ \mathbf{C_q} & \mathbf{0} \end{bmatrix} \begin{bmatrix} \ddot{\mathbf{q}} \\ \boldsymbol{\lambda} \end{bmatrix} = \begin{bmatrix} \mathbf{Q} \\ -\dot{\mathbf{C}}_\mathbf{q}\dot{\mathbf{q}} \end{bmatrix} \tag{4.10}$$

The equations of motion of Eq. 4.10 may not exactly reproduce the dynamic behavior of the system since the constraint equations are satisfied in its second time derivative. This can contribute to errors that might accumulate (known as *constraint drift*) and leading to an inaccurate solution, which can be solved by using stabilization methods such as the Baumgarte one [3]. However, to avoid the use of a stabilization method, Eq. 4.10 is first solved for the independent coordinates and time derivatives of the system $\ddot{\mathbf{q}}^{ind}$, $\dot{\mathbf{q}}^{ind}$ and $\mathbf{q}^{ind}$ such as $\mathbf{q} = [\ \mathbf{q}^{ind} \quad \mathbf{q}^{dep}\ ]^T$. Here, if six are the generalized coordinates per body in the system as presented in Eq. 2.5 (omitting superscripts), the independent coordinates are $\mathbf{q}^{ind} = [\ x \quad y \quad \theta \quad \psi\ ]^T$ for wheelset bodies and $\mathbf{q}^{ind} = [\ x \quad y \quad z \quad \varphi \quad \theta \quad \psi\ ]^T$ for the remaining bodies. The dependent coordinates are only left to the wheelset bodies

as $\mathbf{q}^{dep} = [\ z \quad \varphi\ ]^T$. Additionally, in case of the fixing body (the one that has the constrained motion with respect to the TF), coordinate x is also dependent.

Then, the constraints equations $\mathbf{C}$ are solved to determine the remaining coordinates that allow to solve Eq. 4.10 without constraint drift, because the constraint equations are now solved in its original form.

As already stated, the formulation proposed in this thesis is implemented in Matlab software. In order to solve the system of Differential-Algebraic Equations (DAE) of index 2 of Eq. 4.10, a transformation into a system of Ordinary-Differencial Equations (ODE) is derived by doubling the number of equations of the DAE system. This procedure is achieved by renaming the variable vector $\mathbf{p}$ as:

$$\mathbf{p} = \begin{bmatrix} \mathbf{q} \\ \dot{\mathbf{q}} \end{bmatrix} \tag{4.11}$$

According to Eq. 4.11, its time derivative can be written as $\dot{\mathbf{p}} = [\ \dot{\mathbf{q}} \quad \ddot{\mathbf{q}}\ ]^T$, that allows to solve the system equations of motion of Eq. 4.10 by rewriting the time derivative $\dot{\mathbf{p}}$ as function vector $\dot{\mathbf{p}} = \mathbf{f}(\mathbf{p}, t)$, which is easily integrated by a Matlab ODE solver subroutine.

4.3.2 Integration scheme

The algorithm of the numeric integration of the equations of motion is described below and presented in Fig. 4.6:

1. Preprocessing stage. Initial conditions $\mathbf{q}_0^{ind}$ and $\dot{\mathbf{q}}_0^{ind}$ are obtained from vector $\mathbf{p}_0$ at time step $t = t_0$.

2. Constraint equations are solved ($\mathbf{C} = \mathbf{0}$ and $\mathbf{C_q}\dot{\mathbf{q}} = \mathbf{0}$) to obtain the dependent coordinates $\mathbf{q}_0^{dep}$ and velocities $\dot{\mathbf{q}}_0^{dep}$.

3. Mass matrix $\mathbf{M}$ and generalized applied forces $\mathbf{Q}$ of Eq. 4.10 are assembled.

4. Jacobian matrix $\mathbf{C_q}$ and its time derivative $\dot{\mathbf{C}}_\mathbf{q}$ of Eq. 4.10 are evaluated.

5. Equation 4.10 is solved to obtain $\ddot{\mathbf{q}}$ and $\boldsymbol{\lambda}$.

6. Vector $\dot{\mathbf{p}}$ of Eq. 4.11 is assembled since $\dot{\mathbf{q}}$ and $\ddot{\mathbf{q}}$ are known.

7. A numeric ODE solver is used to integrate vector $\dot{\mathbf{p}}$ in order to obtain $\mathbf{p}$ in time step $t + \Delta t$.

8. Time step t is updated to $t + \Delta t$ to check if the simulation continues or stops.

9. If the simulation continues, the independent coordinates $\mathbf{q}^{ind}$ and velocities $\dot{\mathbf{q}}^{ind}$ at time step $t + \Delta t$ are extracted from $\mathbf{p}$.

10. Return to step 2.

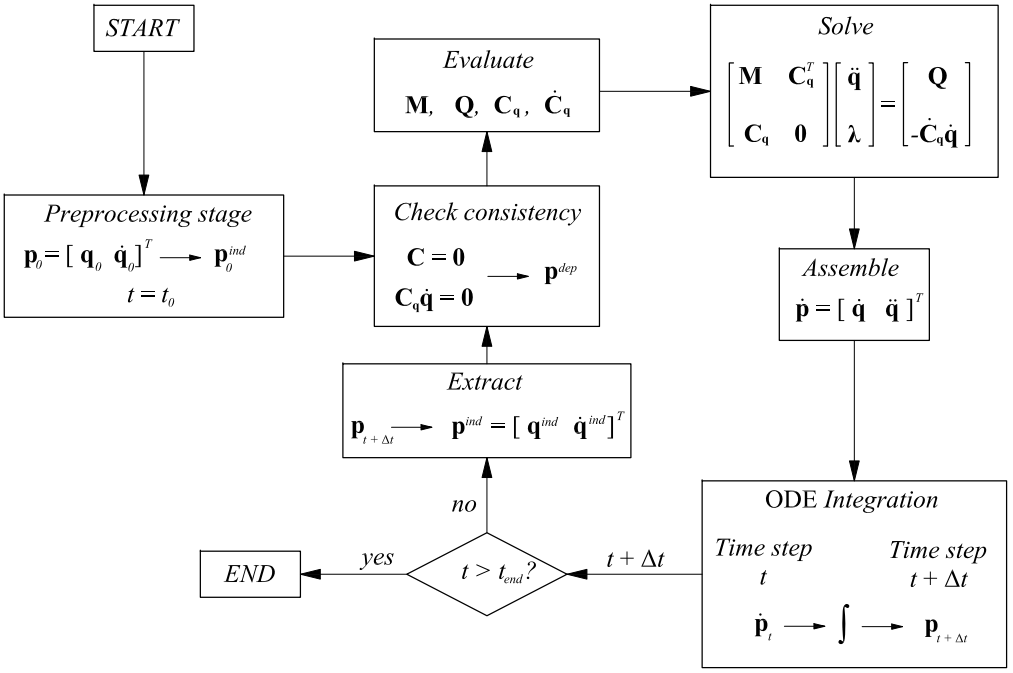

FIGURE 4.6: Integration scheme

Chapter 5

Numerical Results and Comparison

5.1 Introduction

In this Chapter, the experimental results acquired by the scaled railroad vehicle are compared with the numerical results provided by the proposed formulation. To this end, a first comparison between the numerical results of the kinematically simplified equations of Section 2.5.1 versus the non-simplified method described throughout Section 2.2 is developed in Section 5.2 to check the accuracy and efficiency of the assumptions. Then, the non-simplified approach is compared with the experimental results of Section 3.5 for validation purposes.

5.2 Comparison between numerical approaches

In this section the two numerical approaches, the kinematically simplified one (Section 2.5.1) versus the non-simplified one (Section 2.2, are compared in a simple case study.

This simple case study is characterized by the following features:

- The model studied is the scaled vehicle model presented in Section 4.2.
- A tangent track without irregularities is considered.
- The ideal development of the measured track at Alamillo's park of Fig. 3.40 is used.
- A constant forward velocity of $V = 1$ m/s is assumed.

In what follows, the most relevant results provided by the two approaches are presented from Fig. 5.1 to Fig. 5.8. Note that for a clear interpretation of the results, only the rearest wheelset (the one that has the imposed velocity constraint) and the leading one, are shown in the kinematically simplified method and the non-simplified one. Figure 5.1 and 5.2 show the wheelsets lateral and vertical displecement respectively, Figs. 5.3 and 5.4 the wheelsets lateral and vertical velocity, Figs. 5.5 and 5.6, the lateral and vertical creep forces acting on the selected wheelsets, Fig. 5.7 its vertical reaction forces and Fig. 5.8, the longitudinal reaction force acting on the driver wheelset.

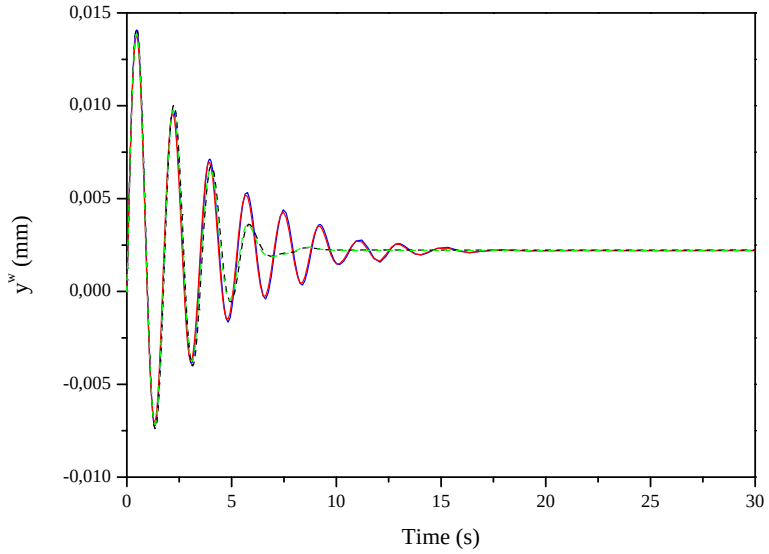

FIGURE 5.1: Wheelsets lateral displacement in case study 1
Rearest wheelset — Leading wheelset
Rearest wheelset lin. kinem. — Leading wheelset lin. kinem.

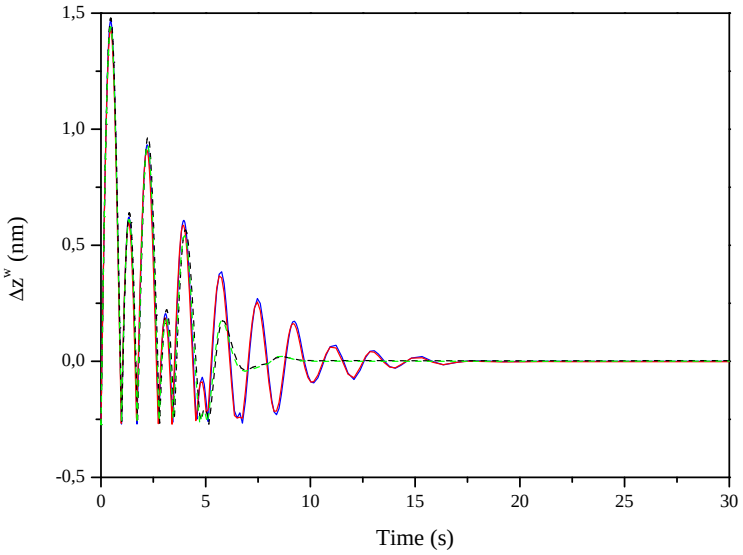

FIGURE 5.2: Wheelsets vertical displacement in case study 1
Rearest wheelset — Leading wheelset
Rearest wheelset lin. kinem. — Leading wheelset lin. kinem.

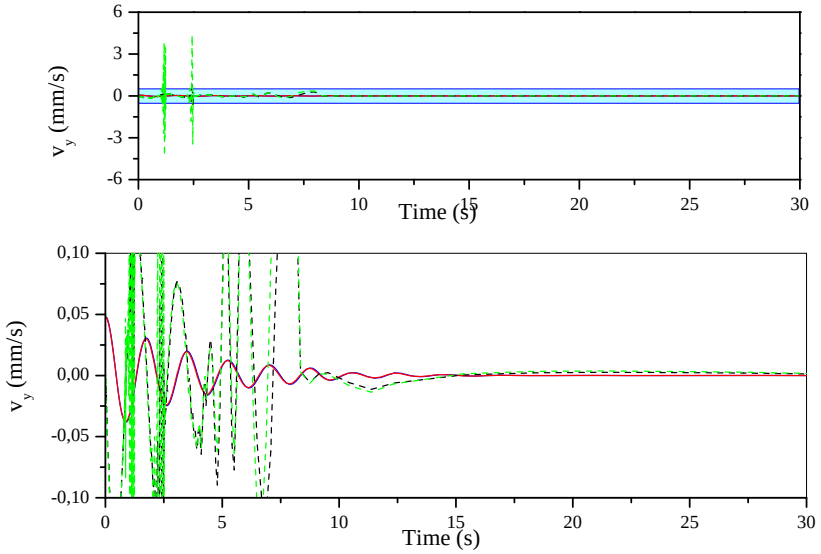

FIGURE 5.3: Wheelsets lateral velocity in case study 1
Rearest wheelset — Leading wheelset
Rearest wheelset lin. kinem. — Leading wheelset lin. kinem.

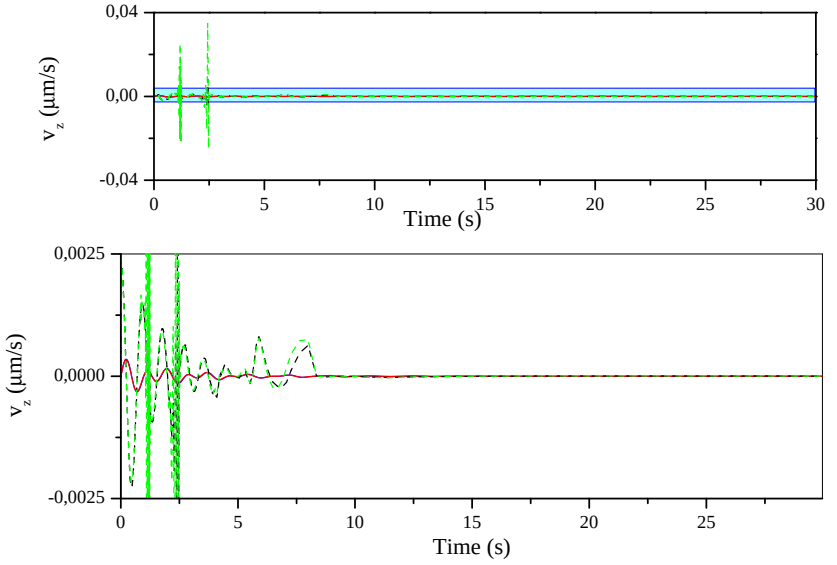

FIGURE 5.4: Wheelsets vertical velocity in case study 1
Rearest wheelset — Leading wheelset
Rearest wheelset lin. kinem. — Leading wheelset lin. kinem.

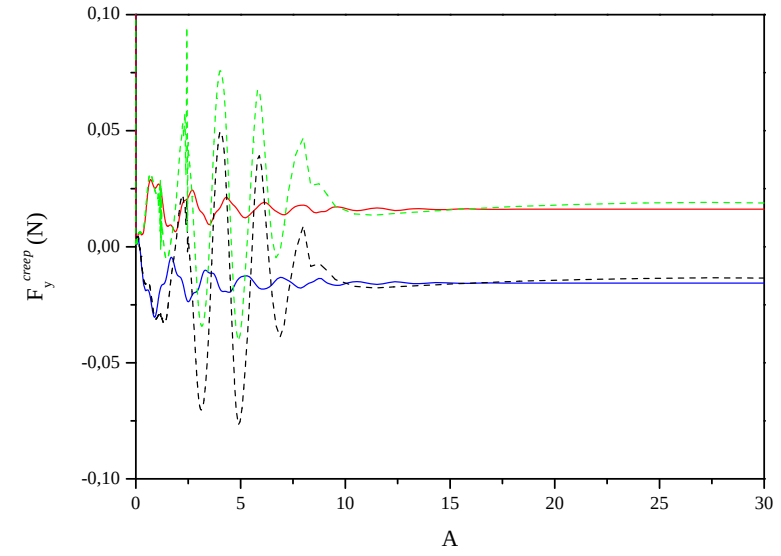

FIGURE 5.5: Wheelsets lateral creep forces in case study 1
Rearest wheelset — Leading wheelset
Rearest wheelset lin. kinem. — Leading wheelset lin. kinem.

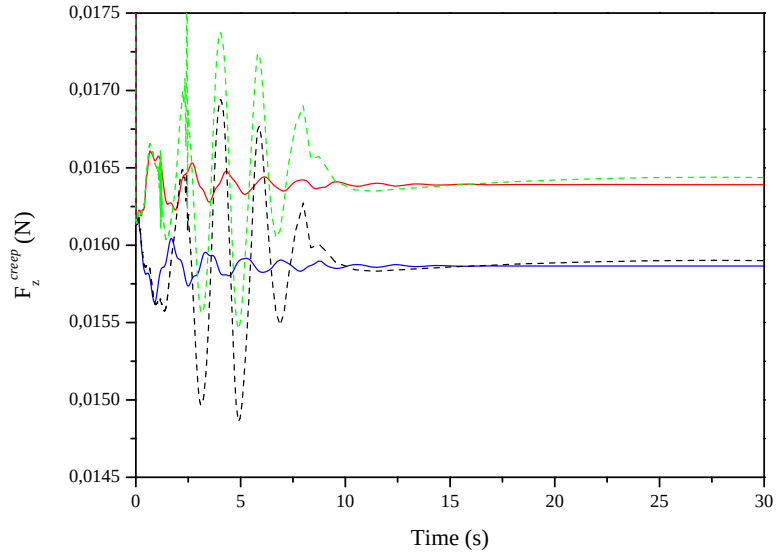

FIGURE 5.6: Wheelsets vertical creep forces in case study 1
Rearest wheelset — Leading wheelset
Rearest wheelset lin. kinem. — Leading wheelset lin. kinem.

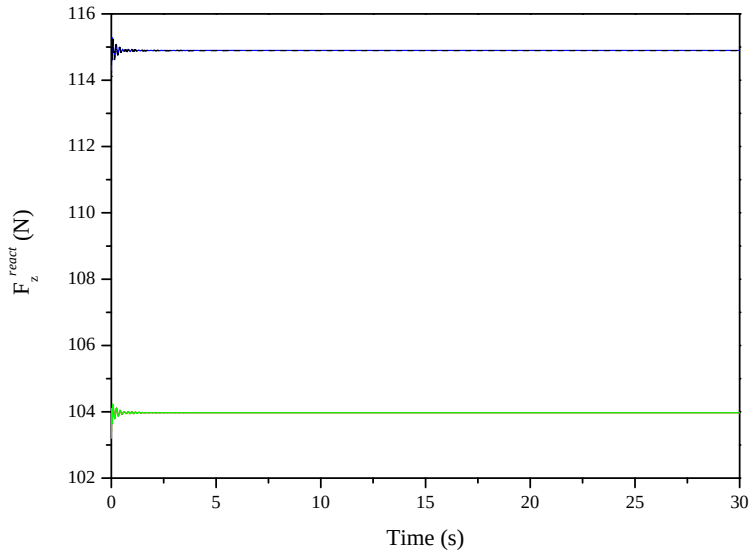

FIGURE 5.7: Wheelsets vertical reaction forces in case study 1
Rearest wheelset — Leading wheelset
Rearest wheelset lin. kinem. — Leading wheelset lin. kinem.

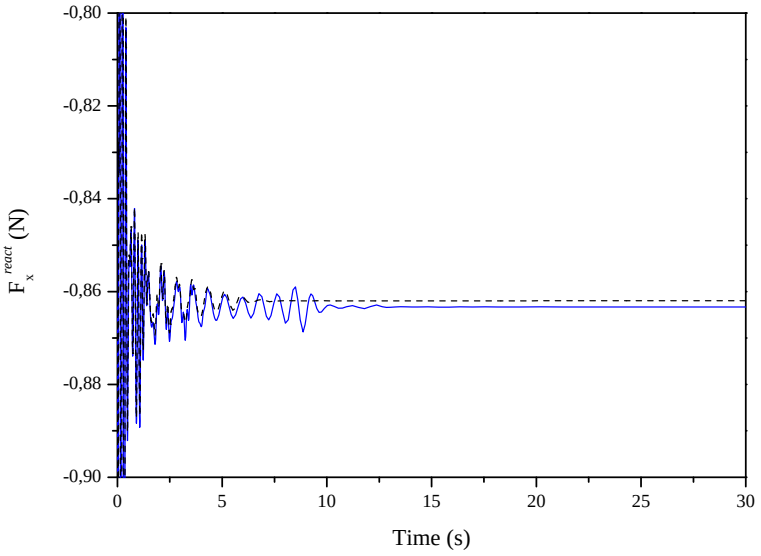

FIGURE 5.8: Wheelsets longitudinal reaction forces in case study 1
Rearest wheelset — Rearest wheelset lin. kinem.

5.2.1 Discussion between numerical approaches

Some conclusions can be extracted from the results presented among Figs. 5.1 and 5.8. Wheelsets lateral and vertical displacements are presented in Figs. 5.1 and 5.2, where due to the non-equilibrium conditions of the case study, some damped oscillations arise, being the kinematically linearized model the one that earlier reaches the equilibrium position. However, the lateral and vertical velocity of Figs. 5.3 and 5.4 show that the linearized one presents higher discontinuities at the beginning. This is, when the conditions are not close to the reference position (defined in Section 2.5.2.1), the kinematically linearized model loses accuracy. This fact is also seen on the creep forces of Figs. 5.5 and 5.6. In addition, in Fig. 5.7 the vertical reaction forces associated with the contact constraints for the same wheelsets are presented. As the mass of the vehicle is not uniformly distributed, different reaction forces are obtained at the equilibrium position. Finally, in Fig. 5.8 the longitudinal reaction force associated with the body fixed constraint is shown where the same discontinuities in the linearized approach can be observed.

The measurement of the computational cost of the two compared approaches is a difficult task that depends on a combination of hardware and software together with a proper code implementation. Here, for information purposes, the computational cost is compared when both models are simulated in a standard multi-core PC (without parallel programming) on a Matlab environment using as numerical integrator, the ODE-15s subroutine [98], which characterizes for the use of adapting (in size) time steps. To this end, the elapsed computational time for the kinematically simplified approach in the proposed case study is 82.08 s while for the non-simplified one, 122.97 s. This is, the kinematic linearization reduces the computational cost up to 33.25 %.

However, due to the high discontinuities that appear in the kinematically linearized approach with respect to the non-linearized one, it can be concluded that the linearized

approach is not capable of reproduce accurately the dynamic behavior of railroad vehicles when small perturbations with respect to the reference equilibrium positions appear. This statement is confirmed when a standard simulation that accounts for the track geometry and vehicle forward velocity measured at Sections 3.4 and 3.5.2 respectively, is developed for the kinematically simplified approach. There, the nonlinear phenomena such as flange contact or track irregularities, lead the simulation to singularity results and failure. Consequently, a railroad computational model that accurately accounts for arbitrary track with irregularities should avoid the proposed kinematic linearization of the equations of motion.

5.3 Comparison between numerical and experimental results

5.3.1 Simulated motion results

In this section, the simulated results of the non-simplified approach are presented. First, the wheelset trajectories together with the railroad track centerline are presented in Fig. 5.9, where a zoom of the tangent track is derived for a clear understanding. In Fig. 5.9, the simulated wheelset lateral displacements around the track centerline can be observed.

Similarly, wheelset vertical coordinates are shown in Fig. 5.10, where due to the distance between wheelsets, each one follows the track development at different time. In addition, in order to provide results according to the proposed Track Frame Formulation, some generalized position and velocity coordinates with respect to the TF are presented from Fig. 5.11 to Fig. 5.19 where, in some of wheelset cases and for a clearer understanding, only the rearest (the one with the constrained motion) and the leading one are presented. Here it is important to note that the TF follows the track centerline including its irregularities. To show the influence of the irregularities in the results,

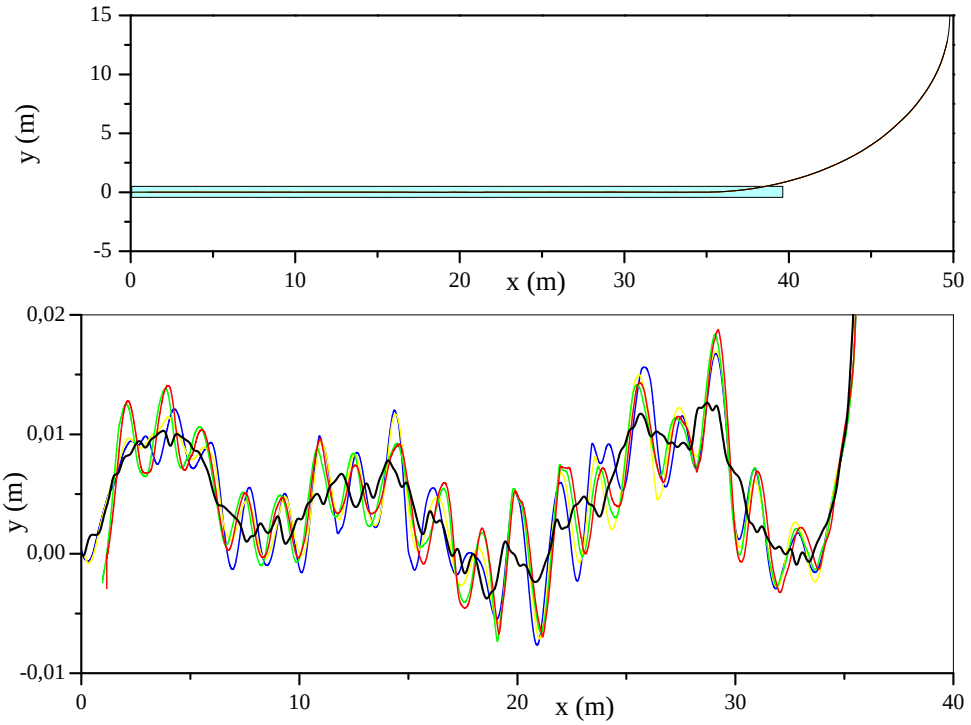

FIGURE 5.9: Simulated wheelsets trajectories and track geometry
Rear wheelset at rear bogie
Front wheelset at rear bogie
Front wheelset at rear bogie
Front wheelset at rear bogie
Track centerline

the lateral and vertical position coordinates of the wheelsets with respect to an ideal TF that follows the ideal centerline without irregularities are shown in Figs. 5.16 and 5.17 respectively. Additionally, global velocity in the longitudinal and lateral direction of the wheelsets are shown in Figs. 5.20 and 5.21 to be compared to the TF absolute velocities of Fig. 5.22.

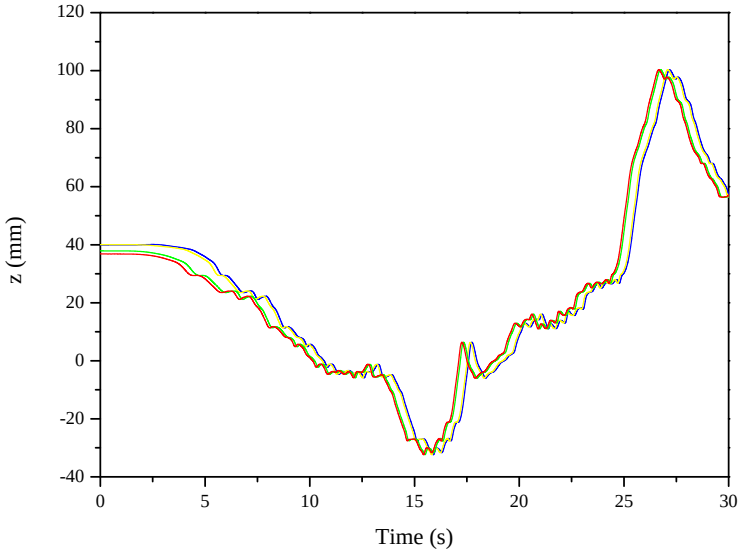

FIGURE 5.10: Simulated wheelsets z^w-coordinate
Rear wheelset at rear bogie
Front wheelset at rear bogie
Rear wheelset at front bogie
Front wheelset at front bogie

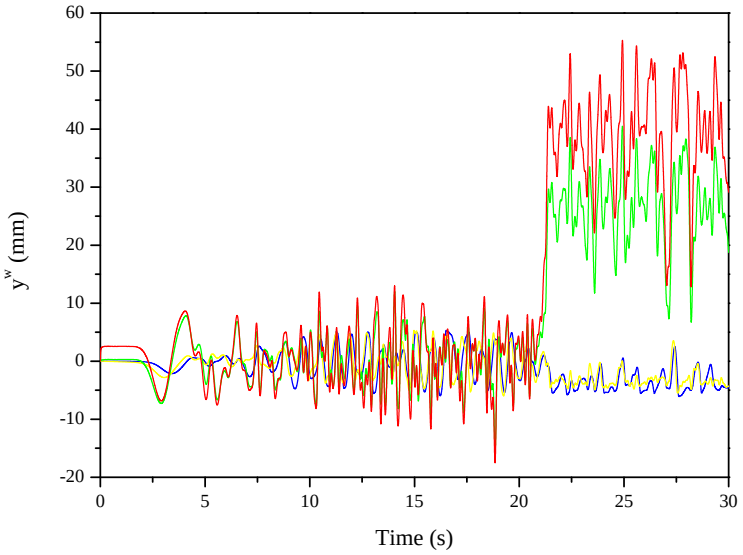

FIGURE 5.11: Simulated wheelsets y^w-coordinate with respect to TF
Rear wheelset at rear bogie
Front wheelset at rear bogie
Rear wheelset at front bogie
Front wheelset at front bogie

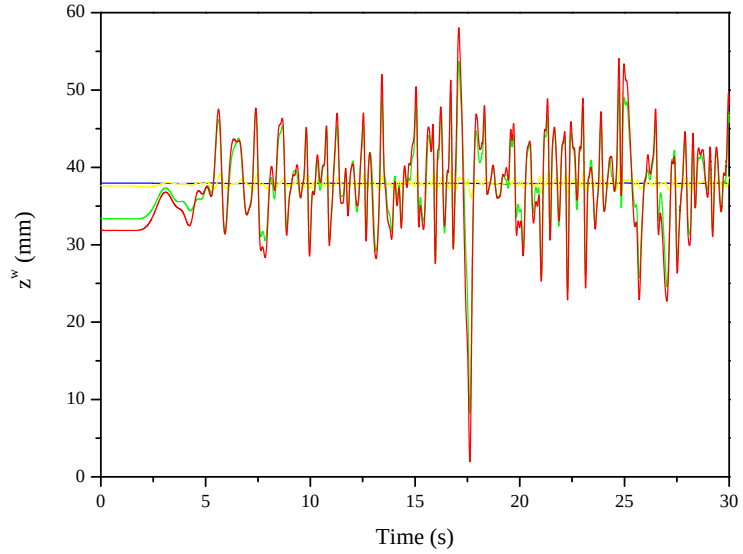

FIGURE 5.12: Simulated wheelsets z^w-coordinate with respect to TF
Rear wheelset at rear bogie — Front wheelset at rear bogie
Rear wheelset at front bogie — Front wheelset at front bogie

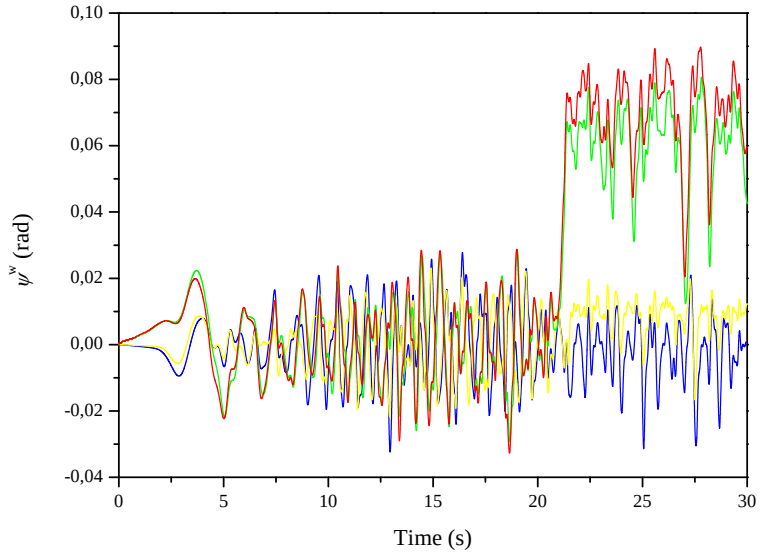

FIGURE 5.13: Simulated wheelsets ψ^w-coordinate with respect to TF
Rear wheelset at rear bogie — Front wheelset at rear bogie
Rear wheelset at front bogie — Front wheelset at front bogie

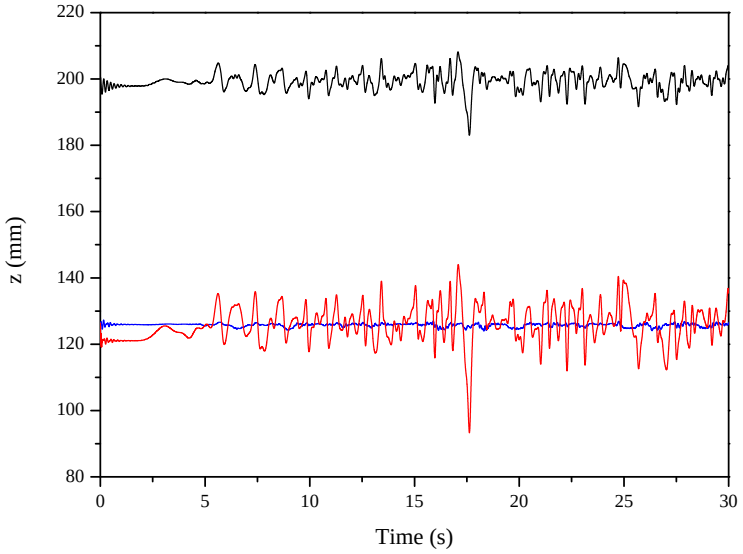

FIGURE 5.14: Simulated bogies and carbody z-coordinate with respect to TF
Rear bogie Front bogie
Carbody

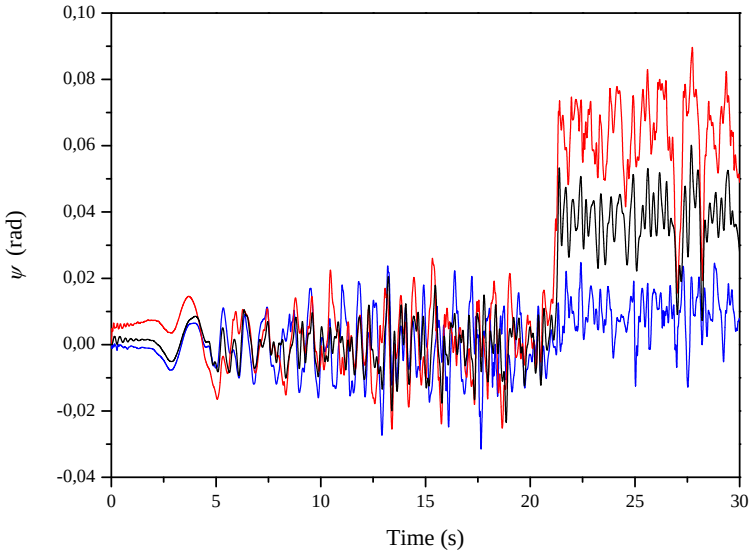

FIGURE 5.15: Simulated bogies and carbody ψ-coordinate with respect to TF
Rear bogie Front bogie
Carbody

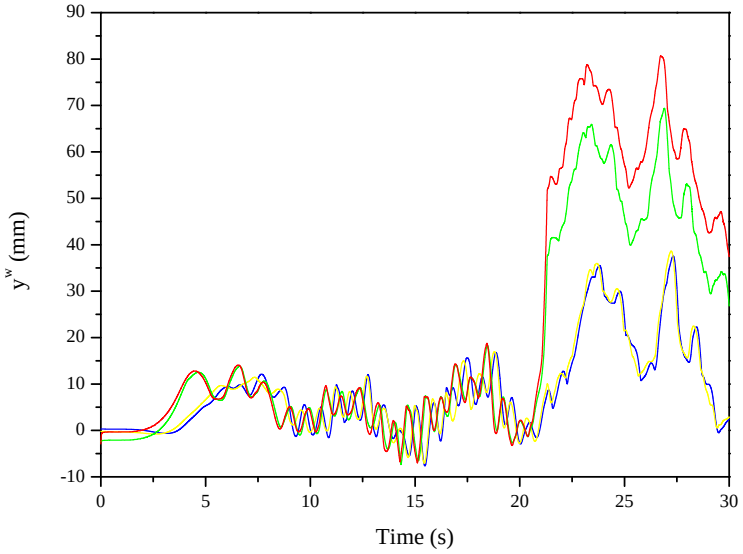

FIGURE 5.16: Simulated wheelsets y-position with respect to an ideal TF
Rear wheelset at rear bogie
Front wheelset at rear bogie
Rear wheelset at front bogie
Front wheelset at front bogie

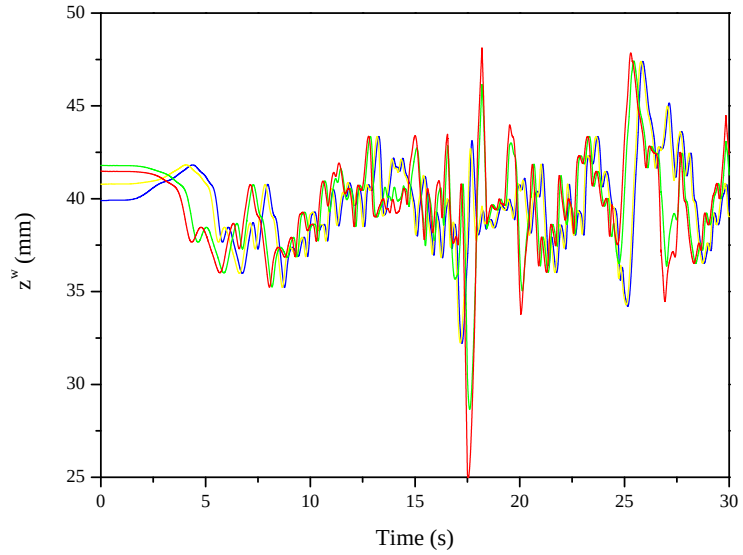

FIGURE 5.17: Simulated wheelsets z-position with respect to an ideal TF
Rear wheelset at rear bogie
Front wheelset at rear bogie
Rear wheelset at front bogie
Front wheelset at front bogie

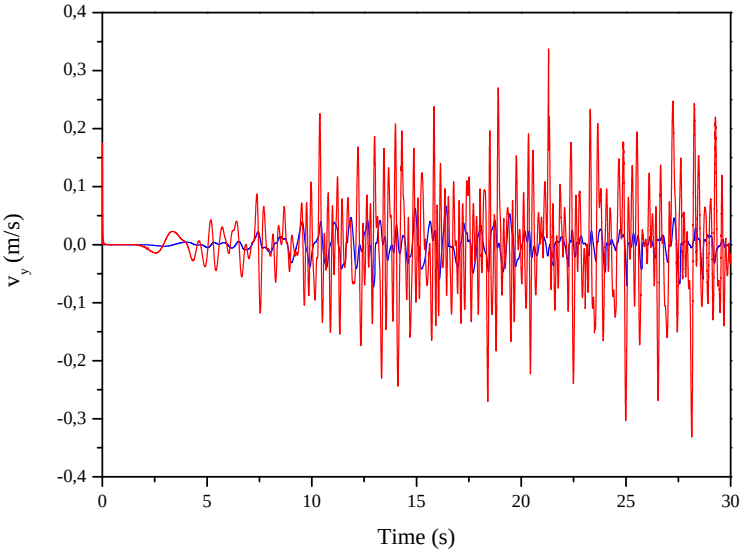

FIGURE 5.18: Simulated wheelsets y-velocity with respect to TF
Rear wheelset at rear bogie Front wheelset at front bogie

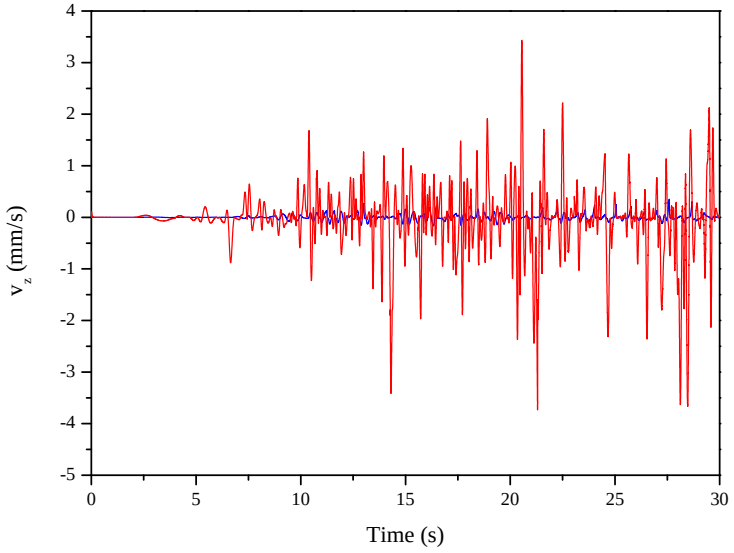

FIGURE 5.19: Simulated wheelsets z-velocity with respect to TF
Rear wheelset at rear bogie Front wheelset at front bogie

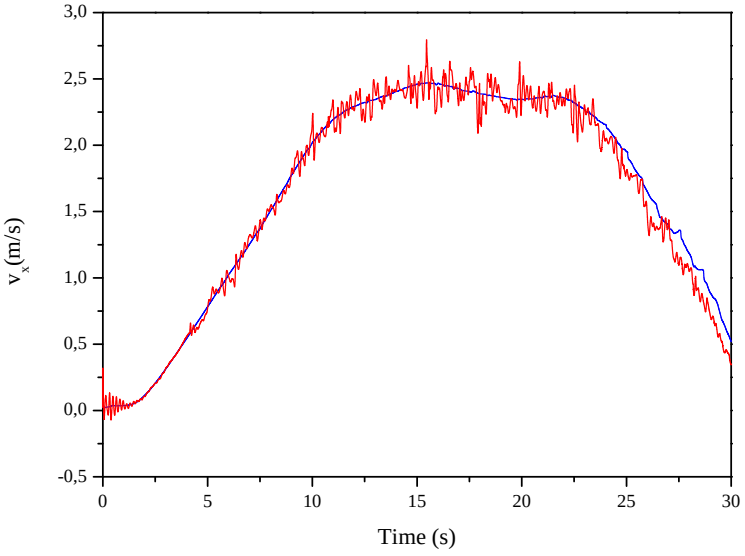

FIGURE 5.20: Simulated wheelsets absolute x-velocity
Rear wheelset at rear bogie Front wheelset at front bogie

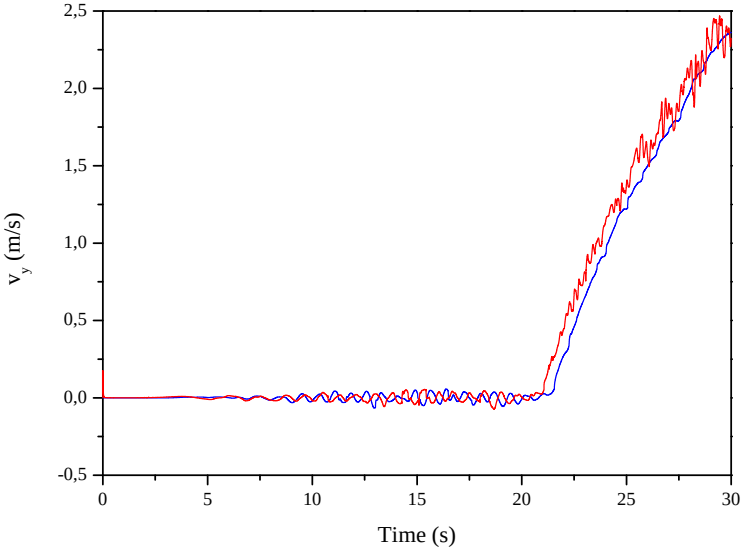

FIGURE 5.21: Simulated wheelsets absolute y-velocity
Rear wheelset at rear bogie Front wheelset at front bogie

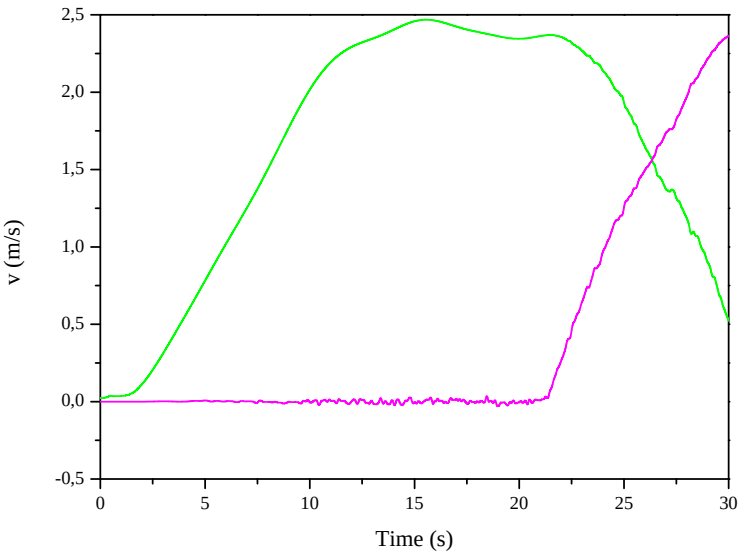

FIGURE 5.22: Simulated TF absolute x-y-velocity
x-longitudinal TF velocity y-lateral TF velocity

5.3.1.1 Discussion of motion results

At Fig. 5.9, the trajectory motion of the wheelsets around the irregular track centerline can easily be observed. Here, as the track lateral deviation is considerably high when compared to real railway tracks, the flange contact scenario is a common phenomenon that happens during the simulation since the hunting movements of wheelset bodies is not pure when its amplitude is maximum. This fact can be better observed at Section 5.3.2.1 of simulated force results. These wheelsets motions are projected to the TF where the lateral, vertical and yaw angle oscilliations with respect to it, are shown in Figs. 5.11, 5.12 and 5.13, respectively. As the TF follows the track centerline (including irregularities) and the rearest wheelset has the constrained longitudinal movement to be that of the TF, it is obvious that the leading wheelset experiences higher displacements and orientation angles with respect to the TF, as it can be seen in red line in Figs. 5.11, 5.12 and 5.13. In these figures, when the vehicle starts negotiating the curve (when $t > 20$ s), wheelsets at the front bogie undergo higher amplitudes (red and green line) than the wheelsets at the rear one. This is explained by the fact that the front bogie negotiates the curve before the TF does.

Regarding velocity figures with respect to the TF, such as wheelset lateral and vertical velocities of Figs. 5.18 and 5.19, it is clear that referring these magnitudes with respect to the TF do not provide meaningful information since the TF motion is also affected by the track irregularities. However, the bodies absolute velocity is an interesting magnitude when compared to the TF absolute velocity. In Figs. 5.20 and 5.21, wheelsets absolute longitudinal and lateral velocities are shown. It can be seen that these magnitudes follow the absolute TF velocities of Fig. 5.22, where its high frequency content is associated to the influence of the suspension elements and track irregularities. As explained before when negotiating the curve, note that the longitudinal direction of the absolute velocity of Fig. 5.20 decreases earlier in the leading wheelset than the rearest one and vice versa for its lateral direction of Fig. 5.21.

5.3.2 Simulated force results

Next, some results regarding forces acting on the different bodies of the model are presented. First, wheelsets creep forces in the lateral and longitudinal directions are presented in Figs. 5.23 and 5.24. Like in teh preceding section, Figure 5.25 shows for the rearest and leading wheelsets, the lateral component of the flange forces associated with the wheel indentation when flange contacts occur. Likewise, the vertical suspension element forces acting on these wheelsets are presented in Fig. 5.26 together with the vertical and lateral spring forces acting on bogies and carbody of Figs. 5.27 and 5.28, respectively. Also, wheelsets inertia forces associated with the TF motion together with its reaction forces in the vertical and longitudinal component are shown in Figs. 5.29, 5.30 and 5.31, respectively.

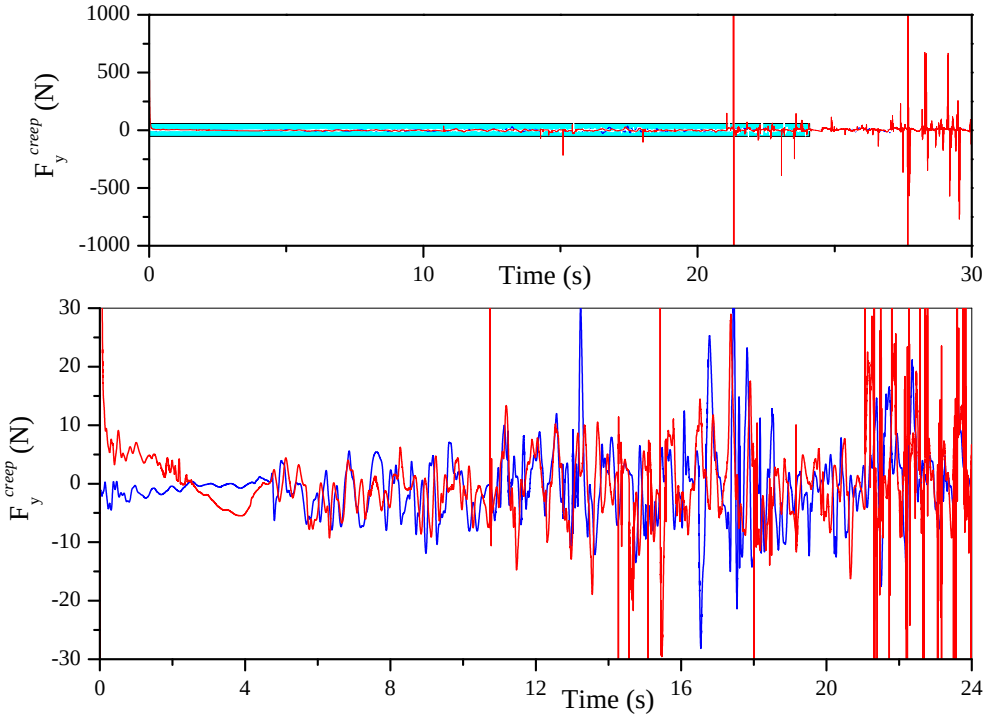

FIGURE 5.23: Simulated wheelsets lateral creep forces
Rear wheelset at rear bogie Front wheelset at front bogie

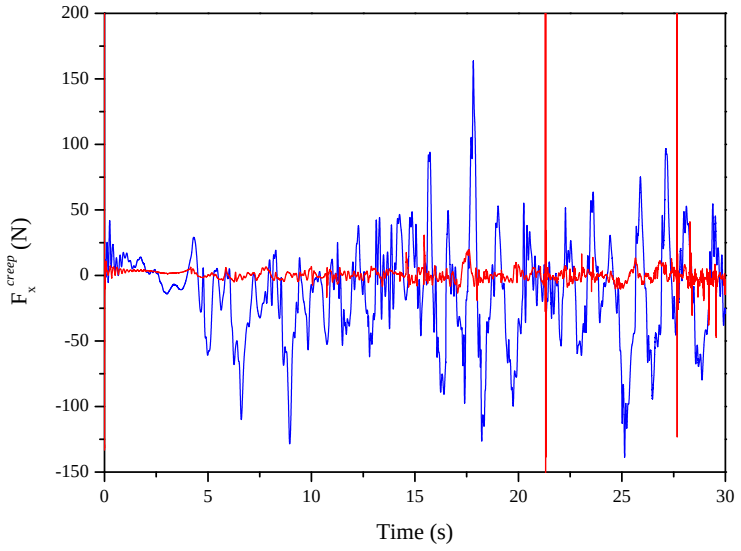

FIGURE 5.24: Simulated wheelsets longitudinal creep forces
Rear wheelset at rear bogie — Front wheelset at front bogie

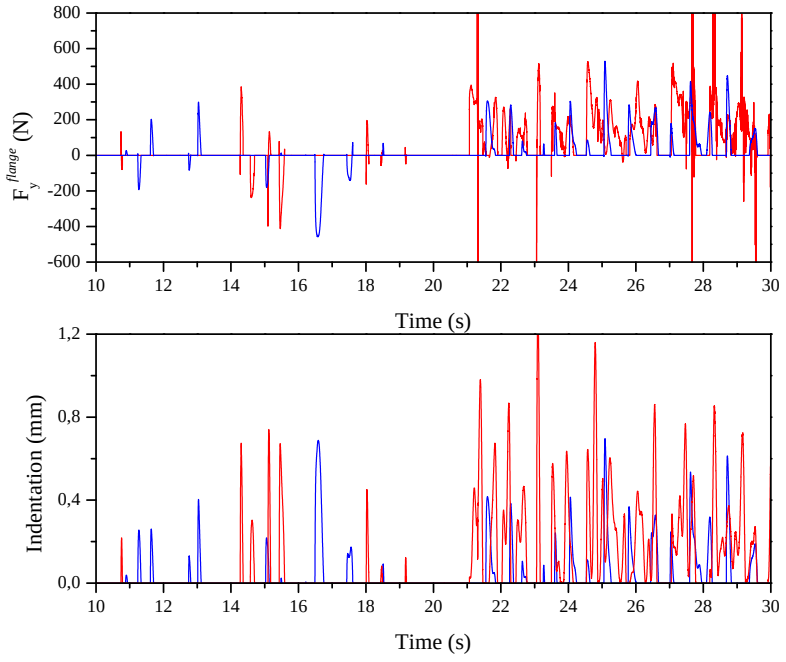

FIGURE 5.25: Simulated wheelsets flange forces and indentation
Rear wheelset at rear bogie — Front wheelset at front bogie

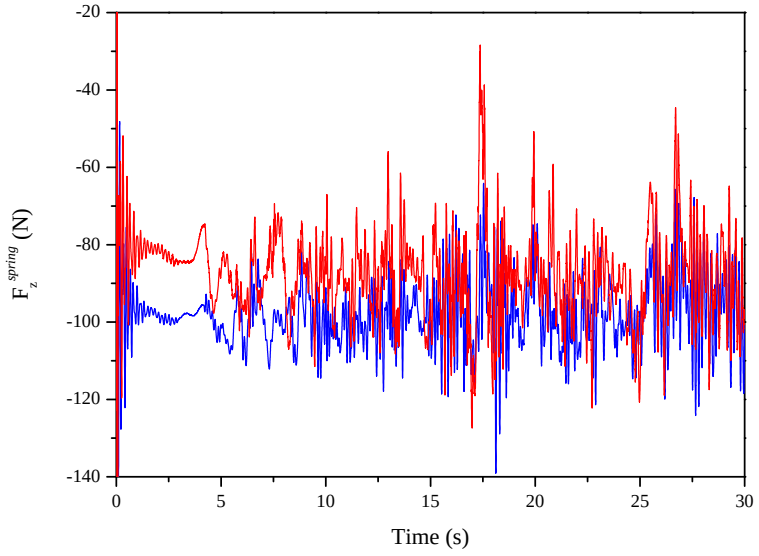

FIGURE 5.26: Simulated vertical spring forces acting on wheelsets
Rear wheelset at rear bogie Front wheelset at front bogie

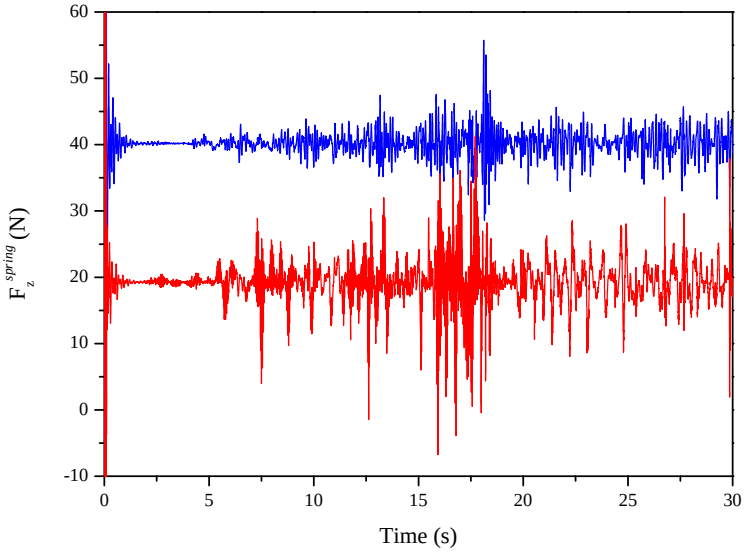

FIGURE 5.27: Simulated vertical spring forces acting on bogies
Rear bogie Front bogie

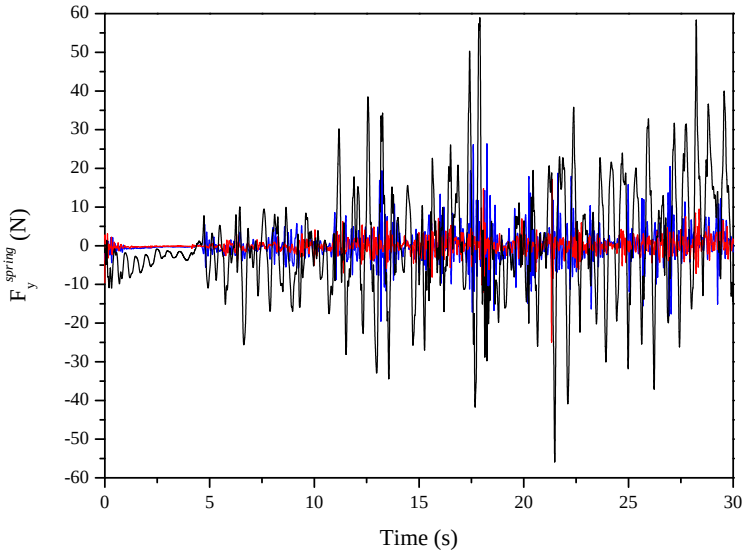

FIGURE 5.28: Simulated lateral spring forces acting on bogies and carbody
Rear bogie Front bogie
Carbody

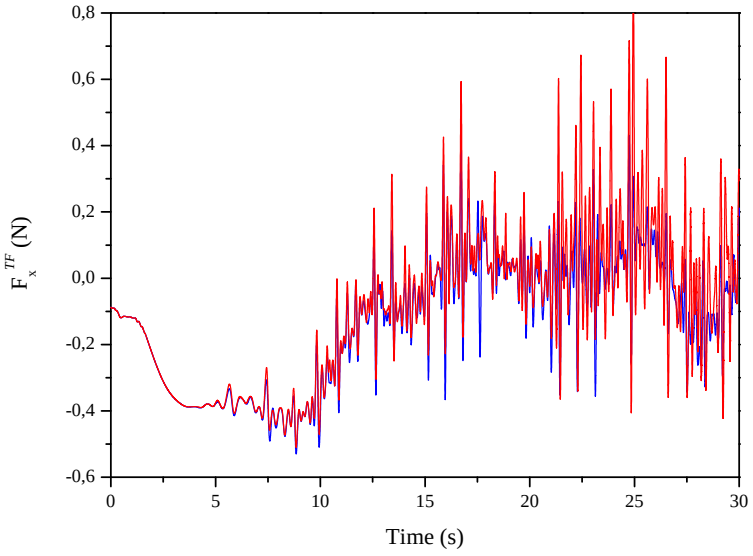

FIGURE 5.29: Simulated longitudinal TF forces acting on wheelsets
Rear wheelset at rear bogie Front wheelset at front bogie

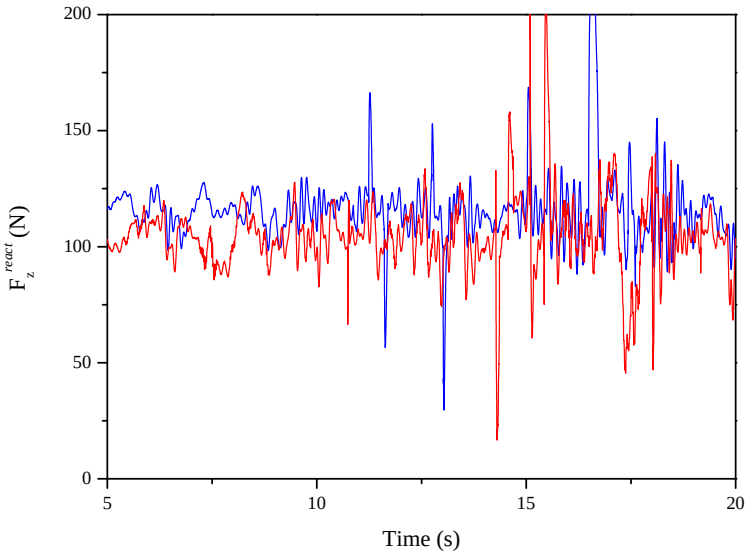

FIGURE 5.30: Simulated vertical reaction forces acting on wheelsets
Rear wheelset at rear bogie Front wheelset at front bogie

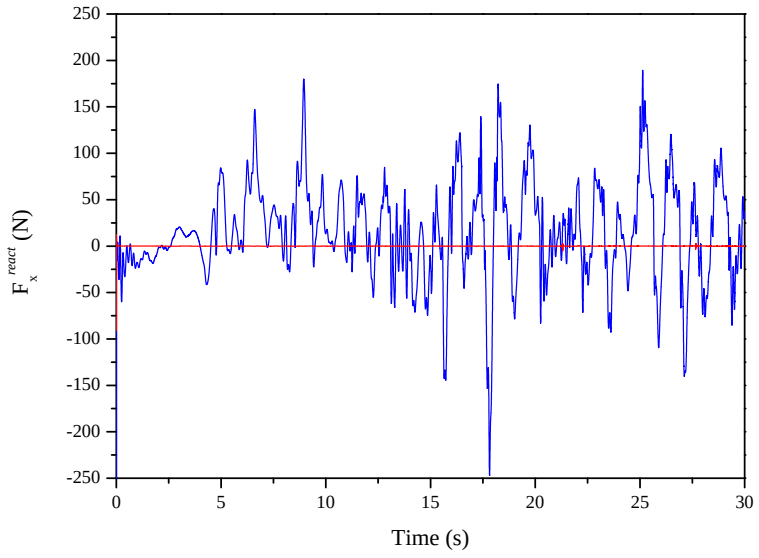

FIGURE 5.31: Simulated longitudinal reaction forces acting on wheelsets
Rear wheelset at rear bogie Front wheelset at front bogie

5.3.2.1 Discussion of force results

The main conclussion that can be extracted from the results presented in this section is that the model of the scaled vehicle is quite stiff when compared with real railroad vehicles since high-frequency components can be observed in all force figures. In Fig. 5.23, the wheelset lateral creep forces are presented. They oscillates, according to their lateral movement, with maximum magnitudes of around ± 25 N force as a function of the track geometry. However, when flange contact occurs, there are discontinuities that give sudden creep forces up to 1000 N. Figure 5.24 shows the wheelsets longitudinal creep forces. Here it is obvious that the imposed velocity constraint at the rearest wheelset (blue line) provides higher longitudinal creep forces than to the remaining wheelsets. Likewise it is necessary to mention that in the computation of the tangent contact forces derived in section 2.3.4, when the vehicle forward velocity is null, there is no definition of these forces. This certain case is solved by assuming that there is no tangential contact force when there is no vehicle forward velocity.

Wheel flange forces and indentation are presented in Fig. 5.25. At this figure, it can be extracted from the first 20 s, that in the tangent stretch flange contact occasionally occurs due to track irregularities, but in the curve stretch flange contact continously happens. Note that the leading wheelset in red line presents the highest peak forces as it is the first wheelset that negotiates the curve stretch. Regarding suspension element forces, it is noticeable the high frequency content that the vertical spring forces have on the bodies of the model in Fig. 5.26 for the wheelsets, and in Fig. 5.27 for the bogies and carbody. This is explained by the high stiffness of these force elements combined with the low mass of the vehicle (as presented in Chapter 3 by the scaling factors), which makes that even at the first instants of the simulation when the vehicle forward velocity is close to zero, the reference position is not easily achieved.

Additionally, the longitudinal TF inertia forces acting on the wheelsets, which are shown in Fig. 5.29, are closely related to the time derivative of Fig. 5.20. This is, Fig.

5.29 provides the wheelsets longitudinal acceleration showing a smooth pattern when the vehicle speed is low (when $t < 5$ s), keeping a value of $F_x^{TF} = -0.4$ N when the vehicle is accelerating and showing high influences of track defects when the maximum forward velocity is reached.

Finally, wheelsets vertical and longitudinal reaction forces are given by Figs. 5.30 and 5.31 respectively. These forces are associated with the system constraints. In case of the vertical reaction forces, their magnitudes oscilliate around their reference position provided in the former case study of Fig. 5.7. In case of the longitudinal reaction forces (Fig. 5.31), the imposed velocity constraint of the rearest wheelset (blue line) provides this high reaction force that balances the longitudinal creep forces of Fig. 5.24.

5.3.3 Experimental results

In what follows the comparison of the simulated results with the experimental ones acquired by the scaled railroad vehicle is derived. First, as a comparison in the frequency domain is of major importance, the specific features of the Data Acquisition system together with the noise introduced by sensors at the experiments are shown. Next, the comparison including the measurement of sensors, simulated results, and their Power Spectral Density functions (PSD), are compared for validation purposes.

5.3.3.1 Data Acquisition system

In Section 3.2.7, Tables 3.10 and 3.9 show the nominal caracteristics of the distance lasers and IMUs installed on the vehicle. There, it is noticeable the sensor maximum measuring rate, which is 750 Hz for the distance laser and 30 kHz for the accelerometer and gyroscope. However, as it is well-known in the use of sensors, the higher the frequency of sampling, the higher the added noise. For this reason, it is advisable to use a frequency of sampling that captures the dynamic behavior of the system without adding undesirable sensor noise.

In this experimental campaign, the DAQ was implemented by Virtualmech company [104], developing a user-defined software that stores the data provided by IMUs and distance lasers at a sampling rate of 167 Hz, which theoretically means 1 measure in each sensor per 6 ms. This sampling rate is approximately achieved at sensors, as it can be seen in Fig. 5.32 for the IMUs. The frequency of 167 Hz is a reasonable one since the proposed computational model is rigid and does not account for flexible bodies. This is, according to Popp [69], the experimental data should be able to capture the low-frequency range, which goes from 0 to 50 Hz, and where the interesting phenomena, such as derailment and hunting motion, are included. Note that in case of the simulated results, higher frequencies should not be comparable to those obtained by the sensors.

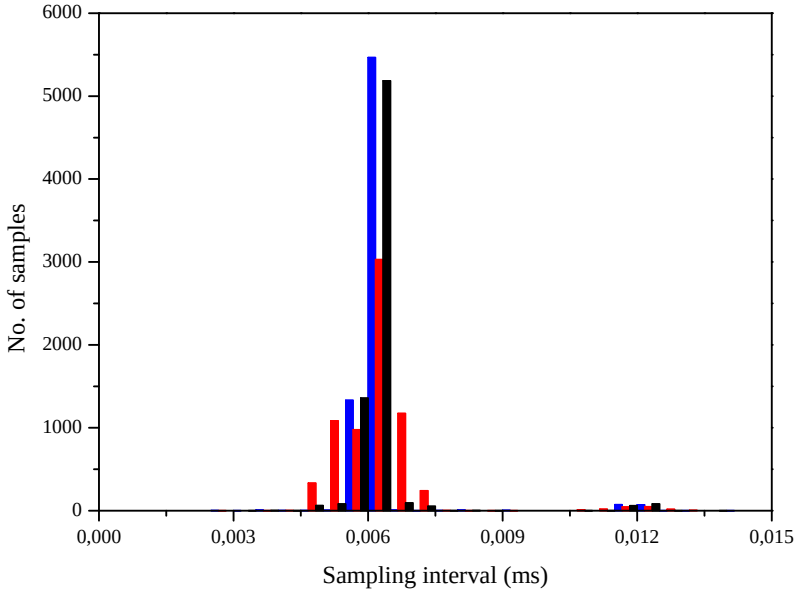

FIGURE 5.32: IMUs sampling rate histogram
Wheelset IMU Bogie IMU Carbody IMU

In addition to the definition of the DAQ system, the noise produced by IMUs is calculated based on the noise density properties of Table 3.9, which is 80 $\mu g/\sqrt{\text{Hz}}$ for the accelerometer and $0.03^{\text{o}}/s/\sqrt{\text{Hz}}$ for the gyroscope. If the sampling frequency is $f_s = 167$

Hz, accelerometers and gyroscopes produce a noise of 0.00731 m/s^2 and 0.00478 rad/s respectively.

5.3.3.2 Experimental comparison

Once the frequency of sampling of the DAQ system has ben defined, the comparison between the simulated and experimental results can be derived. In what follows, a series of figures related to distance, acceleration and angular velocity results, is presented together with their PSD functions in the frequency domain. Finally, the discussion of the presented results is derived in Section 5.3.3.3.

First, the relative vertical deflection measured by the distance lasers are presented in Figs. 5.33 and 5.34 for the secondary and primary suspensions. Then, from Fig. 5.35 to Fig. 5.42, the gyroscope angular velocities at wheelset, bogie and carbody levels are compared together with the Cartesian components of the acceleration at these three levels from Fig. 5.43 to 5.51. To conclude this section, PSD functions comparing experimental and simulated results are presented from Fig. 5.52 to Fig. 5.58.

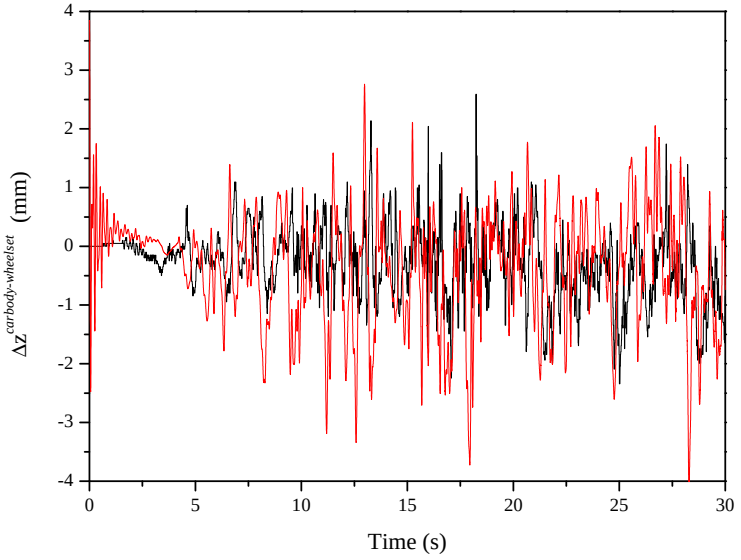

FIGURE 5.33: Relative vertical deflection between carbody frame and wheelset plane
Simulation Experiments

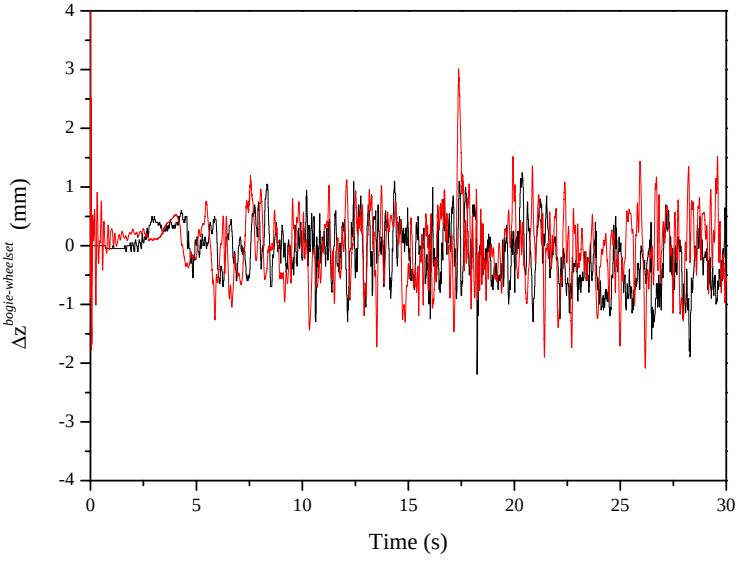

FIGURE 5.34: Relative vertical deflection between bogie frame and wheelset plane
Simulation Experiments

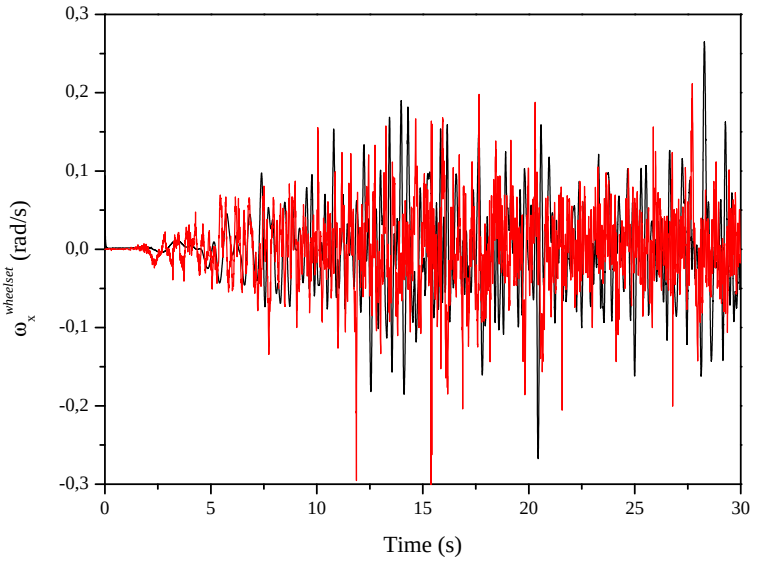

FIGURE 5.35: Wheelset longitudinal angular velocity
Simulation Experiments

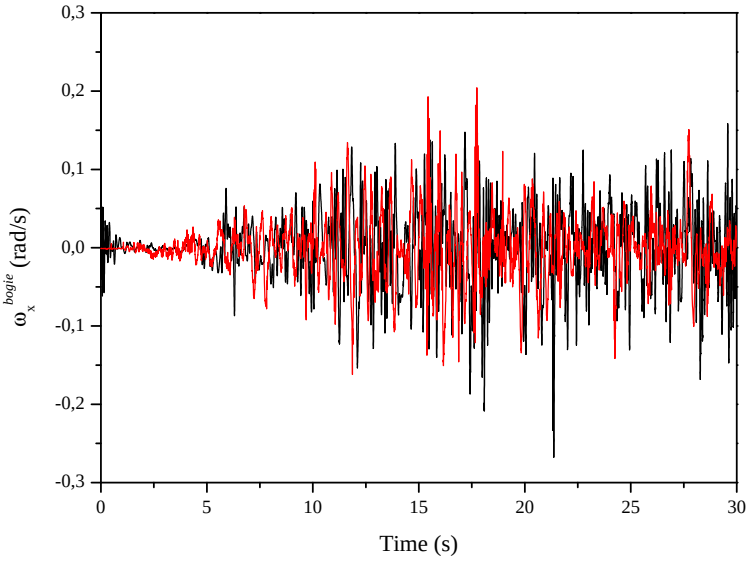

FIGURE 5.36: Bogie longitudinal angular velocity
Simulation Experiments

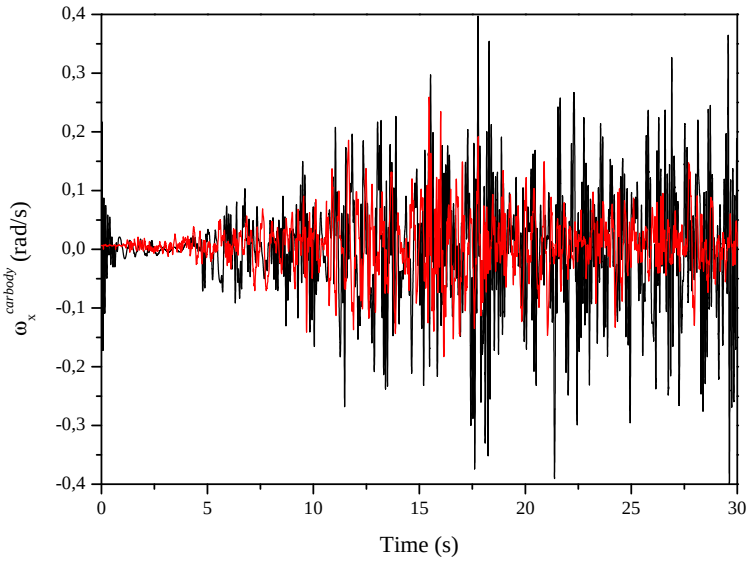

FIGURE 5.37: Carbody longitudinal angular velocity
Simulation Experiments

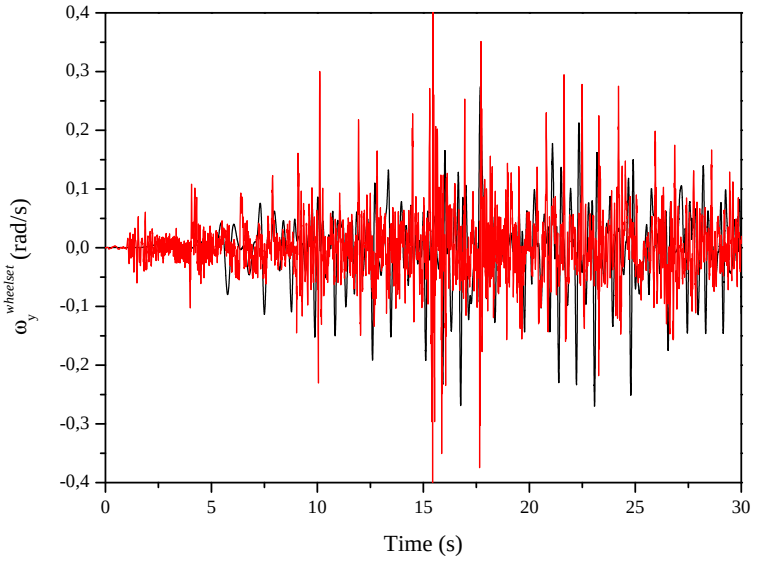

FIGURE 5.38: Wheelset lateral angular velocity
Simulation Experiments

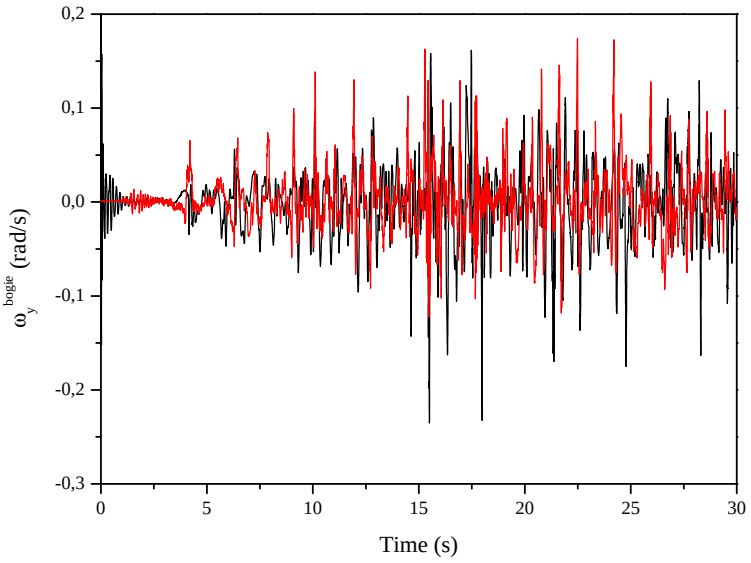

FIGURE 5.39: Bogie lateral angular velocity
Simulation Experiments

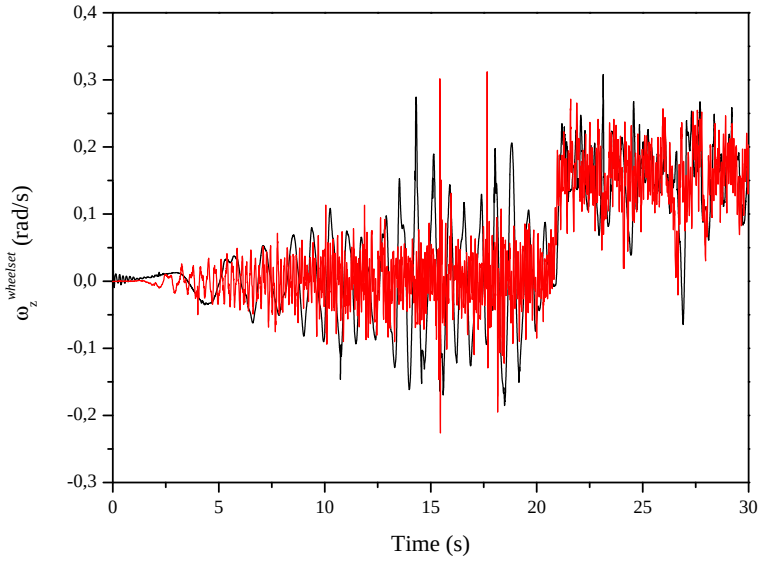

FIGURE 5.40: Wheelset vertical angular velocity
Simulation Experiments

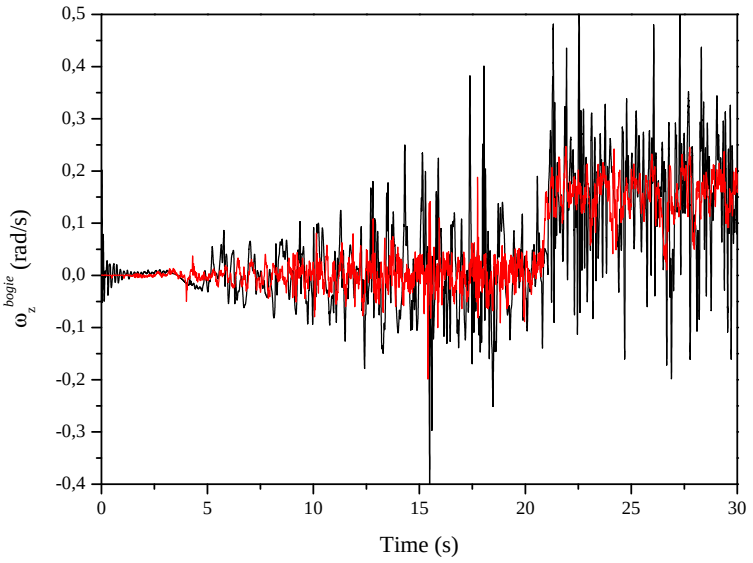

FIGURE 5.41: Bogie vertical angular velocity
Simulation Experiments

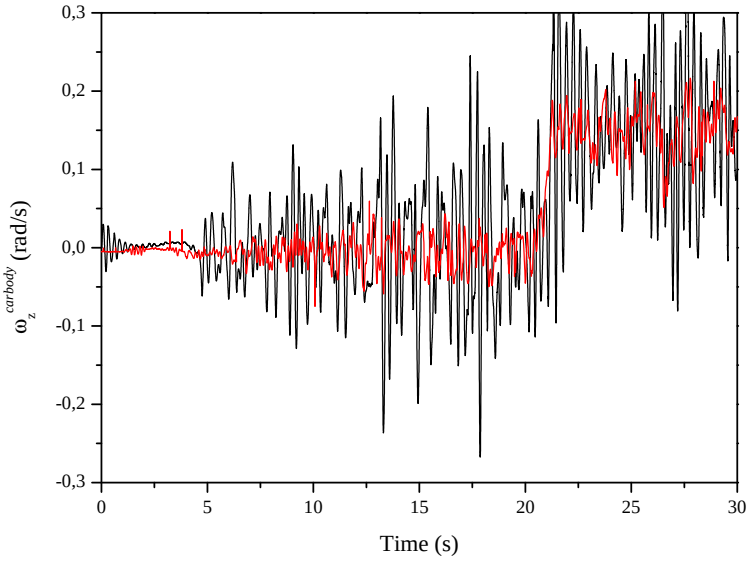

FIGURE 5.42: Carbody vertical angular velocity
Simulation Experiments

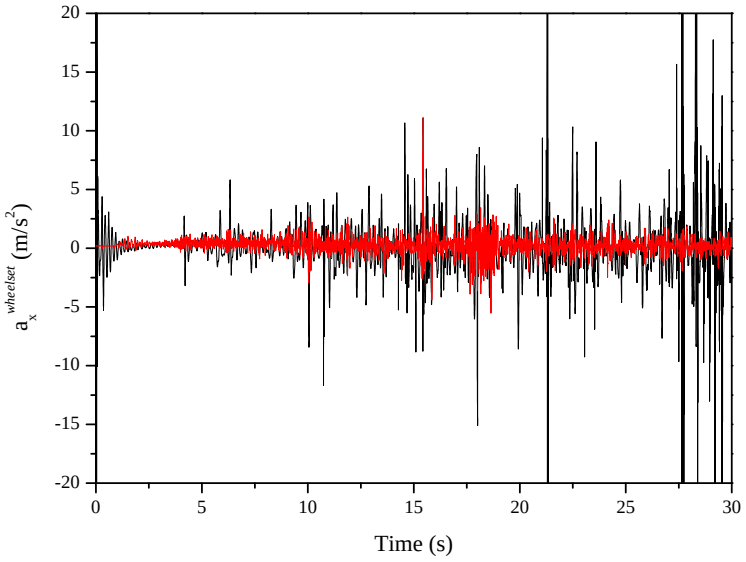

FIGURE 5.43: Wheelset longitudinal acceleration
Simulation Experiments

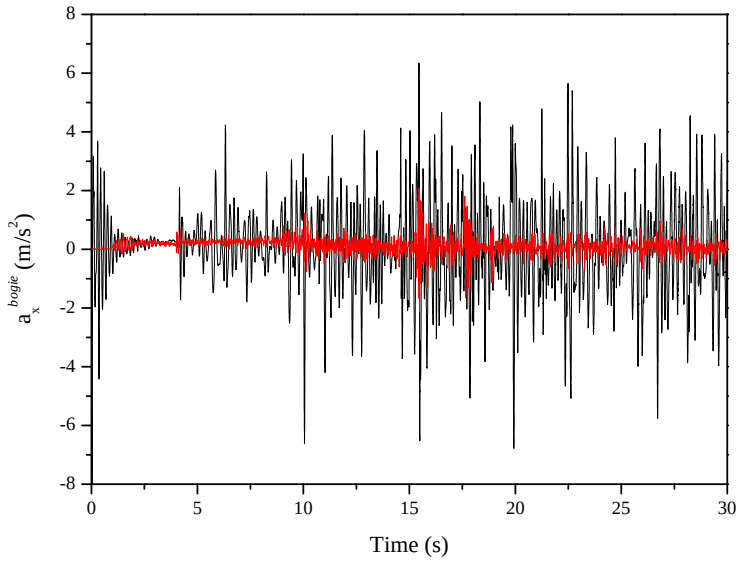

FIGURE 5.44: Bogie longitudinal acceleration
Simulation Experiments

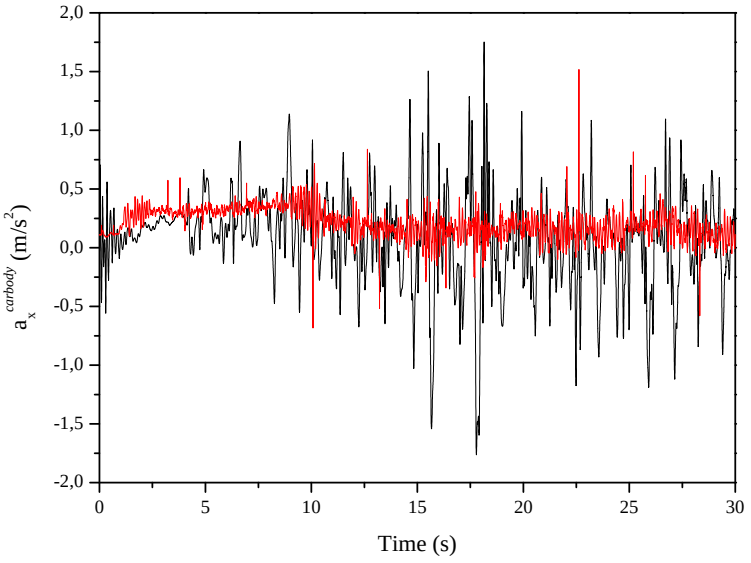

FIGURE 5.45: Carbody longitudinal acceleration
Simulation Experiments

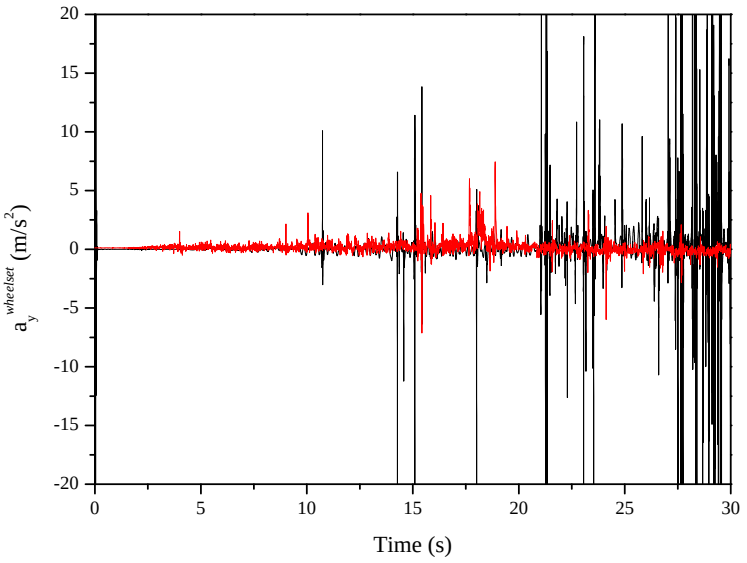

FIGURE 5.46: Wheelset lateral acceleration
Simulation Experiments

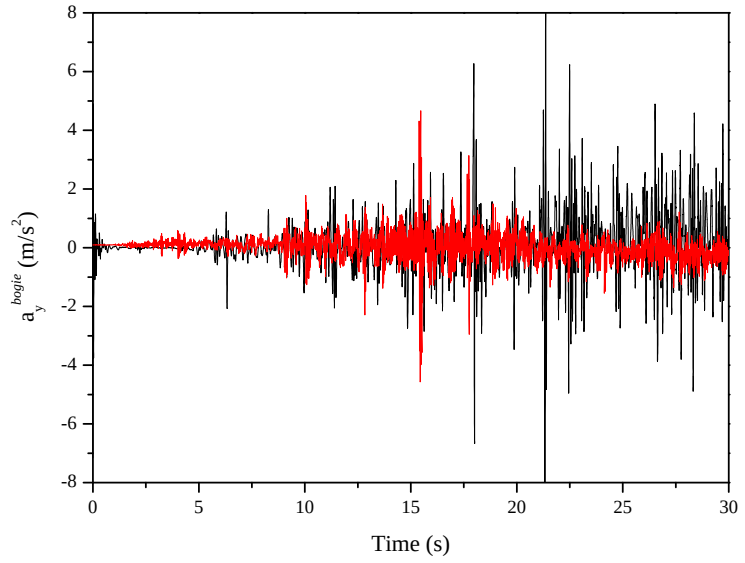

FIGURE 5.47: Bogie lateral acceleration
Simulation Experiments

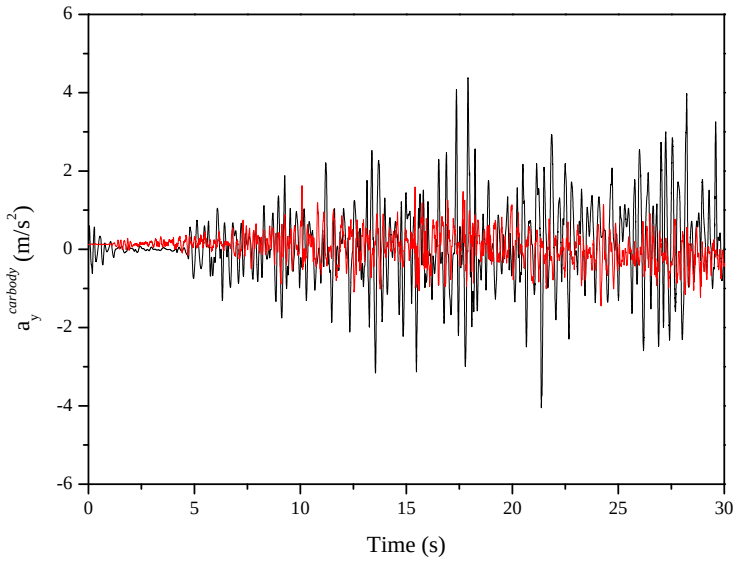

FIGURE 5.48: Carbody lateral acceleration
Simulation Experiments

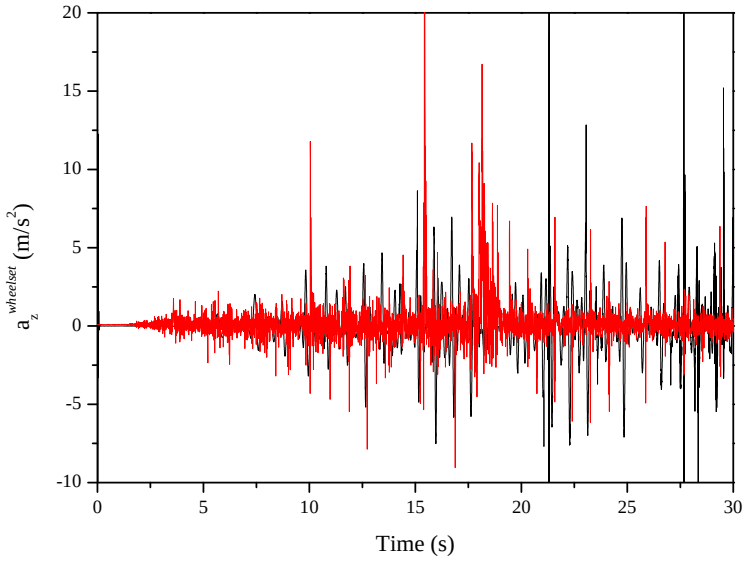

FIGURE 5.49: Wheelset vertical acceleration
Simulation Experiments

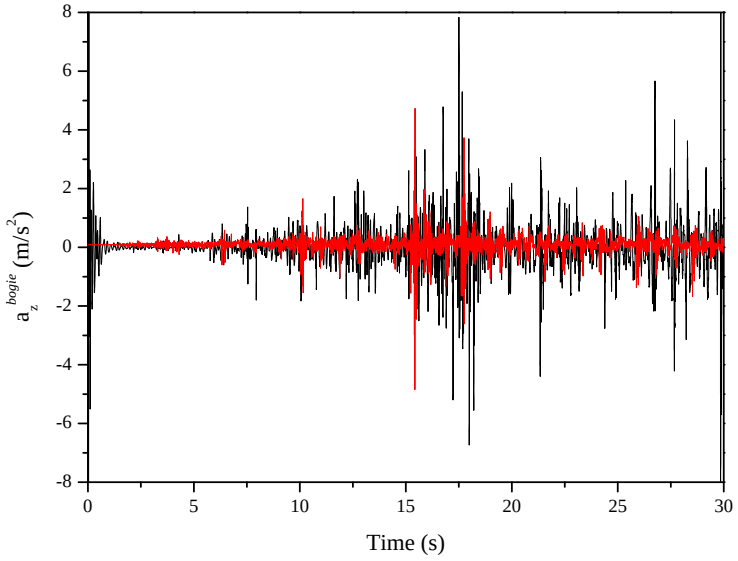

FIGURE 5.50: Bogie vertical acceleration
Simulation Experiments

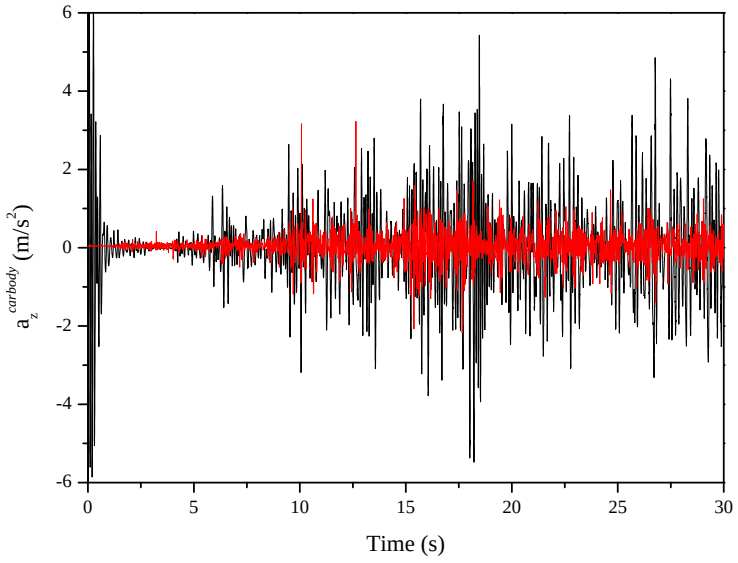

FIGURE 5.51: Carbody vertical acceleration
Simulation Experiments

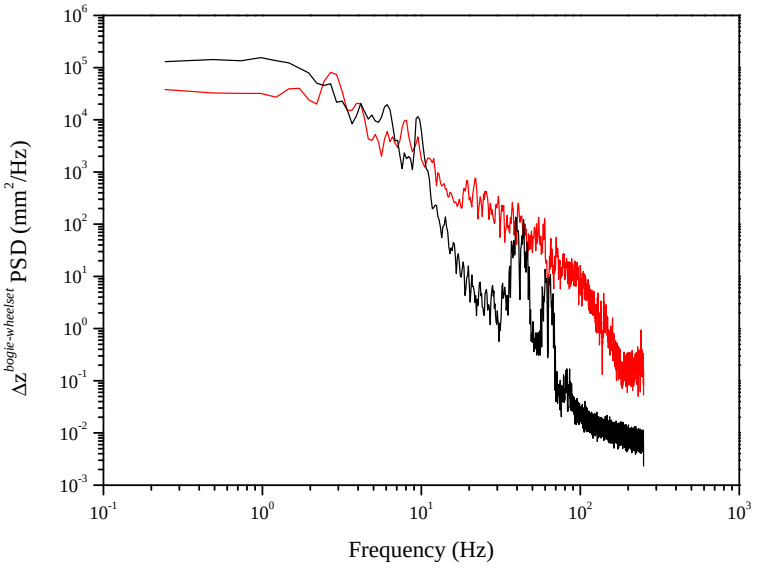

FIGURE 5.52: PSD at primary suspension
Simulation Experiments

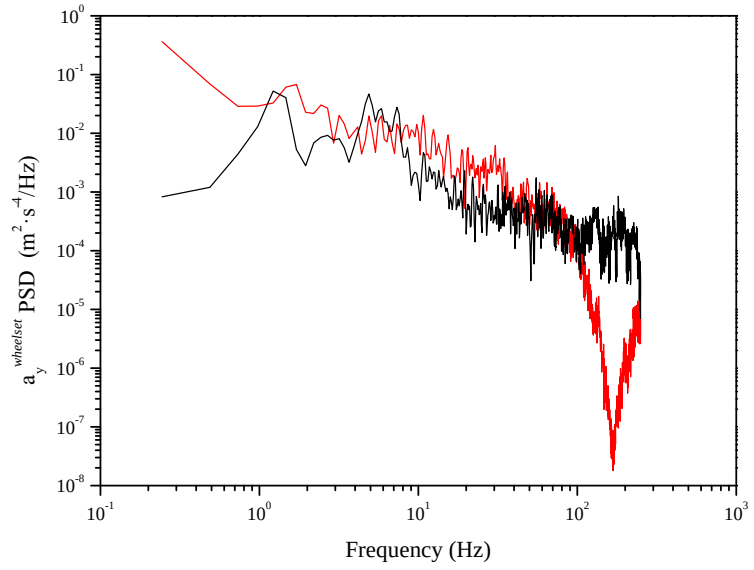

FIGURE 5.53: PSD - Lateral acceleration at wheelset
Simulation Experiments

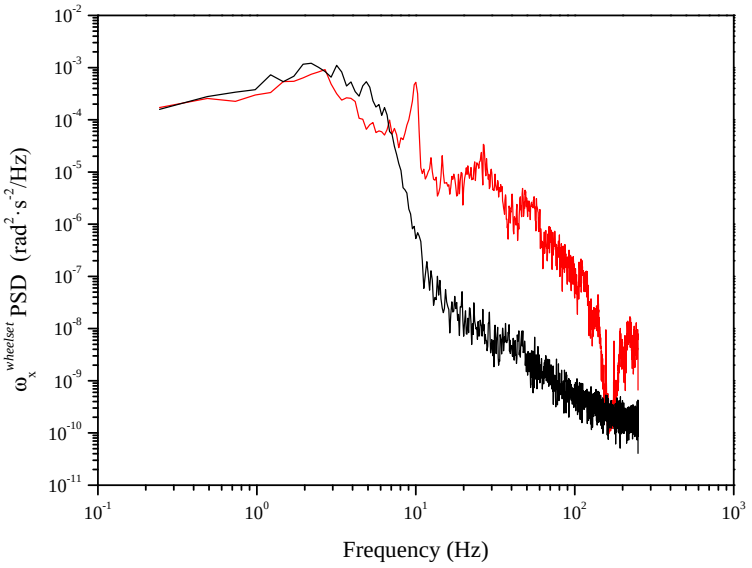

FIGURE 5.54: PSD - Longitudinal angular velocity at wheelset
Simulation Experiments

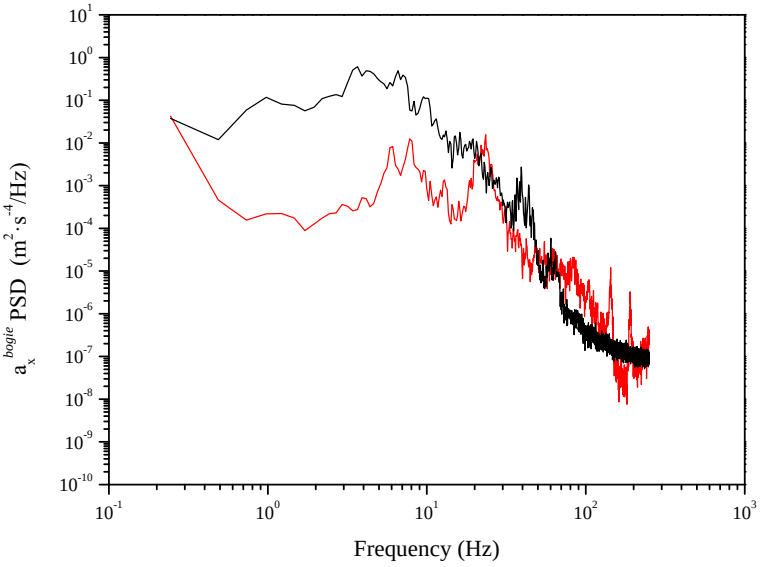

FIGURE 5.55: PSD - Longitudinal acceleration at bogie
Simulation Experiments

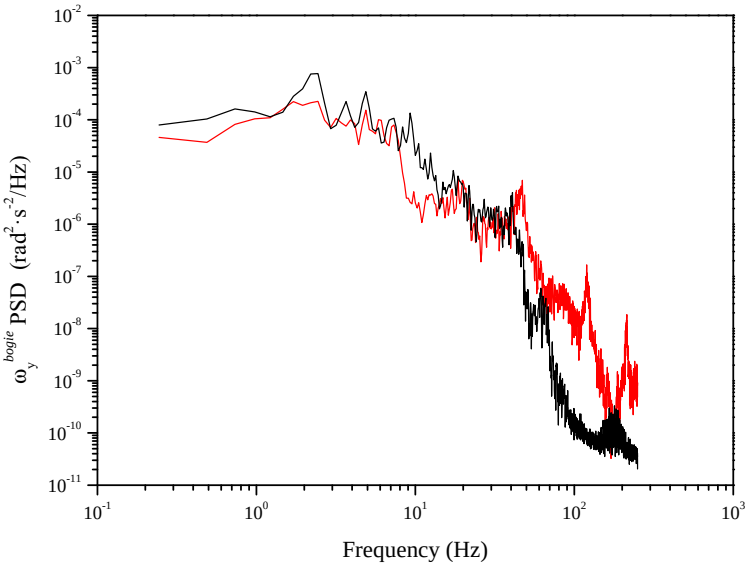

FIGURE 5.56: PSD - Lateral angular velocity at bogie
Simulation Experiments

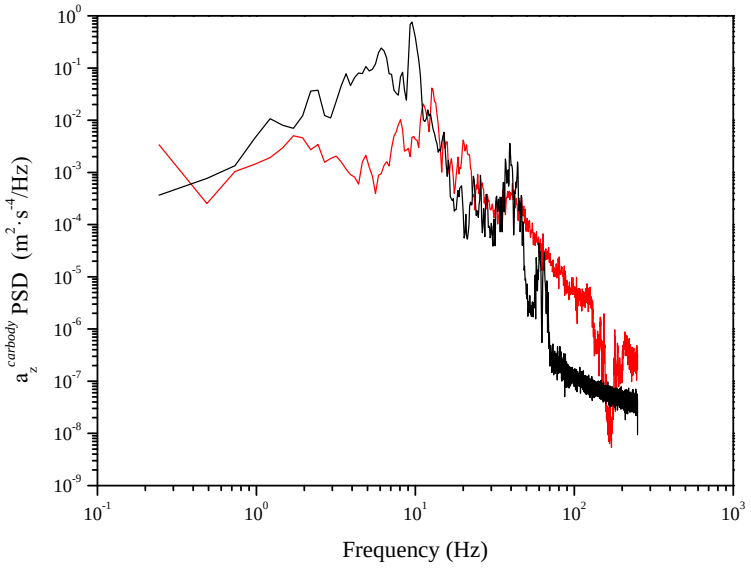

FIGURE 5.57: PSD - Vertical acceleration at carbody
Simulation Experiments

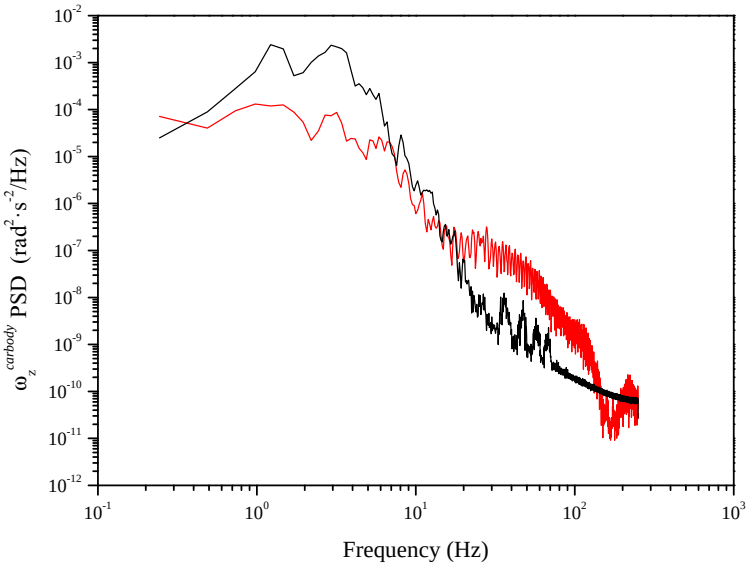

FIGURE 5.58: PSD - Vertical angular velocity at carbody
Simulation Experiments

5.3.3.3 Discussion of experimental comparison

In these results, a reasonable similar behavior between simulated and experimental results is obtained. First, it is necessary to point out that two important physical phenomena are not accounted for in the simulated results: the influence of the chain links in the transmission (ISO 05B-1 - DIN 8187) and the gap between consecutive rails. This gap has a width that ranges from 0.5 to 2 mm, being 2 meters the length of each rail. In addition, results presented in this section are the original ones. This is, no filtering process is applied to any of the experimental or simulated results.

In Figs. 5.33 and 5.34 the relative vertical deflection experienced in the secondary and primary suspension are presented. Here, quite similar results are obtained between simulated and experimental results, where the higher frequency content of the experimental ones can be attributed to the two physical phenomena described before. It is relevant to point out that for the measured distance between the carbody and wheelset planes in Fig. 5.33, the numerical model seems to provide higher deflections than the experimental results, which leads to the conclussion that the global vertical stiffness of the secondary suspension should be higher in the model.

Regarding the gyroscope results, comparable behaviors can be seen between experimental and simulated results, especially at the longitudinal and lateral angular velocities at wheelset, bogie and carbody of Figs. 5.35, 5.36, 5.37, 5.38 and 5.39. Only in the case of the carbody in Fig. 5.37, higher amplitudes in the simulated results, which are also attributed to the lower stiffness of the model, are obtained. However, for the vertical angular velocities at wheelset, bogie and carbody of Figs. 5.40, 5.41 and 5.42, two conclusions can be made: first, the transition from the tangent stretch to the curve one is clearly reproduced by the simulated results when compared to the experimental ones together with the values of these velocities, which are of the same order of magnitude. However, a clear difference in the frequency content between the simulated and experimental results is observed. The experimental results provide a much higher frequency

content in the vertical angular velocity provided by the gyroscopes, especially at the wheelset level. This fact can be attributed to some reasons: the joints of the suspension elements are modeled as linear spring-damper actuators in the three Cartesian components while in the real scaled vehicle, this kind of joint provides a nonlinear dynamic behavior that depends on the adjustment between springs and guiding supports (see Fig. 3.7), that might allow separation between springs and guiding supports during the experiment and producing these high frequencies.

Accelerometers results are presented from Fig. 5.43 to 5.51. Here, even though the noise at the sensors calculated in Section 5.3.3.1 is quite low, some differences between the simulated and experimental results can be observed. Simulated results follow the same pattern than the experimental ones but in case of wheelset accelerations of Figs. 5.43, 5.46 and 5.49, the influence of flange contacts clearly alters the simulated results in terms of sudden acceleration peaks. Accelerations at Figs. 5.43, 5.44 and 5.45, show the longitudinal acceleration provided by the TF but altered by a high frequency content that can be associated to the dynamic behavior of the suspension elements in the horizontal plane. Finally, vertical accelerations of Figs. 5.49, 5.50 and 5.51, show that the influence of the high stiffness of the model gives a different behavior between the simulated and experimental results but of a similar order of magnitude.

These differences between the experimental and simulated results can be better recognized by analyzing the PSD functions presented from Fig. 5.52 to Fig. 5.58. As stated before, the computational model does not account for flexible bodies so frequencies higher than 20-30 Hz are expected to disagree with the experimental results. For instance, this can be seen in the PSD content of the distance laser measurement at the primary suspension of Fig. 5.52 or in the PSD content of the longitudinal angular velocity at the wheelset of Fig. 5.54. Notwithstanding, there are magnitudes, such as the lateral acceleration at the wheelset or longitudinal one at the bogie, whose PSD functions also differ at low frequencies with respect to the experimental results (see Figs. 5.53 and 5.55 respectively). These unexpected results related to the dynamic

behavior of bodies in the horizontal plane, certainly indicate that the computational model does not fully reproduce the behavior of the scaled railroad vehicle in the low frequency range regarding mainly its longitudinal dynamics.

It can be concluded that, the proposed approach entails an important step in the efficient analysis of the dynamics of railroad vehicles. In addition, despite the future work that needs to be focused on improving the longitudinal dynamics of the computational model, such as a new parameter identification and the addition of the chain dynamics, it adequately reproduces the dynamics of railroad vehicles in the low-frecuency range up to 20 Hz, especially when the desired magnitudes are related to motion and angular velocities.

Chapter 6

Closure

6.1 Summary

In this thesis, a numerical approach for modeling railroad vehicles in arbitrary tracks with irregularities is presented and validated with experimental results. To this end, this work starts with an introductory chapter where the definition of track structure, track irregularities, and the state of the art in the simulation of railroad vehicles are presented. The kinematics and dynamics of railroad vehicles are presented in Chapter 2 where the use of the TF formulation characterized by a moving frame that accompanies the vehicle and where the bodies generalized coordinates are referred, is derived. Also, the Newton-Euler equations of motion have been developed analytically and the particular features of the formulation commented. Moreover, the definition of the wheel-rail contact by the use of contact lookup tables using a constraint approach is presented together with a partial linearization of the equations of motion that can be applied, subject to certain conditions, for efficient simulations.

The experimental campaign derived in this work in Chapter 3 involves the design and instrumentation of a scaled 5-inch gauge railroad vehicle, which has been tested in a

scaled railroad track previously measured to account for its real geometry. The novel procedure to accurately account for its geometry is also detailed in Chapter 3. Finally, the experimental results acquired by the instrumented vehicle are compared to the numerical model derived in Chapter 4, giving results and discussion in Chapter 5.

6.2 Conclusions

Accordingly to the motivations of this thesis that sought an accurate and efficient formulation to account for the dynamic behavior of railroad vehicles, the proposed formulation with the use of contact lookup tables that can be used in arbitrary railroad tracks with irregularities has proven to be realistic when its results are compared to the experimental ones acquired by the scaled vehicle in the low frequency range, especially at motion and angular velocity results.

However, there are important differences in the longitudinal dynamics of bodies that require future work in order to improve the accuracy of the proposed approach. The differences can be attributed to the following phenomena: the suspension element joints in the real scaled vehicle that allow separation between guiding supports and the springs. This provides a nonlinear dynamic behavior while in the computational model, the suspension elements are assumed to be linear spring-damper actuators in the three Cartesian coordinates. In addition, the influence of the chain links in the horizontal dynamics and the gap between consecutive rails are neglected, while during the experimental campaign, they seemed to affect to the longitudinal dynamic of the vehicle, especially the chain event. Finally, the differences in the vertical deflection between the experimental and simulated results at the secondary suspension suggests that a new parameter identification needs to be developed.

Regarding computational efficiency, the proposed formulation is programmed in the software Matlab®. This means that even though its computational efficiency is considerably more competent than the one available at the starting point of this dissertation,

quicker simulations could be achieved by switching the programming language, such as Fortran or C++.

6.3 Publications

During the realization of the thesis the following pieces of work were partly contributed by the candidate.

6.3.1 Journal papers

- A.M. Recuero, J.F. Aceituno, J.L. Escalona, and A.A. Shabana: *A nonlinear approach for modeling rail flexibility using the absolute nodal coordinate formulation*, Nonlinear Dynamics, **83**, pp. 463-481, 2016.
- J.F. Aceituno, P. Wang, L. Wang and A.A. Shabana: *Influence of rail flexibility in a wheel/rail wear prediction model*, Proceedings of the Institution of Mechanical Engineers, Part F: Journal of Rail and Rapid Transit, 2016. DOI: 10.1177/0954409715618426
- J.F. Aceituno, S. Muñoz and J.L. Escalona: *Comparison of a scaled railroad vehicle computational model with experimental results*, In preparation, XXX, XX-XX, 2016.
- O. Halminen, J.F. Aceituno, J.L. Escalona, J. Sopanen and A. Mikkola: *Models for dynamic analysis of backup ball bearings of an AMB-system*, Submitted for publication, XXX, XX-XX, 2016.

6.3.2 Conference papers

- J.F. Aceituno, J.L. Escalona and D. García-Vallejo: *Partially-Linearized Multibody Equations of Railroad Vehicles on Arbitrary Tracks for On-Board Applications*, ECCOMAS Thematic Conference on Multibody Dynamics, Barcelona, Spain, June 29 - July 2, 2015.

- J.L. Escalona and J.F. Aceituno: *Modeling Wheel-Rail Contact with Precalculated Lookup Tables in Arbitrary-Geometry Tracks with Irregularities*, Proceedings of the ASME 201 International Design Engineering Technical Conferences & Computers and Information in Engineering Conference IDETC/CIE 2015, Boston, Massachusetts, USA, August 2 - 5, 2015.

- J.F. Aceituno, S. Muñoz and J.L. Escalona: *Validation of a Scaled Railway Vehicle Computational Model with Experimental Results*, Accepted in The Third International Conference on Railway Technology: Research, Development and Maintenance, Cagliary, Sardinia, Italy, April 5 - 8, 2016.

- J.L. Escalona, J.F. Aceituno and A.M. Recuero : *Modelo de Vehículo Ferroviario con Cálculo Simbólico y Tablas Precalculadas para Simulaciones en Tiempo Real*, XX Congreso Nacional de Ingeniería Mecánica, Málaga, Spain, September 24-26, 2014.

- J.D. Carazo, J.F. Aceituno, F.J. Siles-Barrios, J.J. Jiménez de Cisneros y Fonfría and D. Carazo: *Design of Wind Resistant Structures for Monopich Canopies. An Application to Solar Trackers*, EUROSTEEL 2011, Budapest, Hungary, August 31 - September 2, 2011.

6.3.3 Non-indexed journal papers

- A.M. Recuero, J.F. Aceituno, J.L. Escalona and A.A. Shabana: *Nonlinear Track-Railroad Vehicle Interaction*, National University Rail Center - NURail, pp. 1-3, 2014.

Appendix A

Scaled vehicle construction drawings

In this appendix the construction drawings used in the manufacture of the scaled vehicles are included. Note that the scalling of the drawings is only achieved if they are printed in the paper size that they refer. These drawings can be listed as:

- Global perspective
- Power-driven bogie perspective
- Sensored bogie perspective
- Compressed shaft
- Transmission shaft
- Gear and pinions
- Compressed wheel
- Axleboxes

- Suspension fixing elements
- Laser fixing elements
- Suspension fixing elements 2
- Bogie frame
- Carbody subframe
- Carbody
- Carbody plates

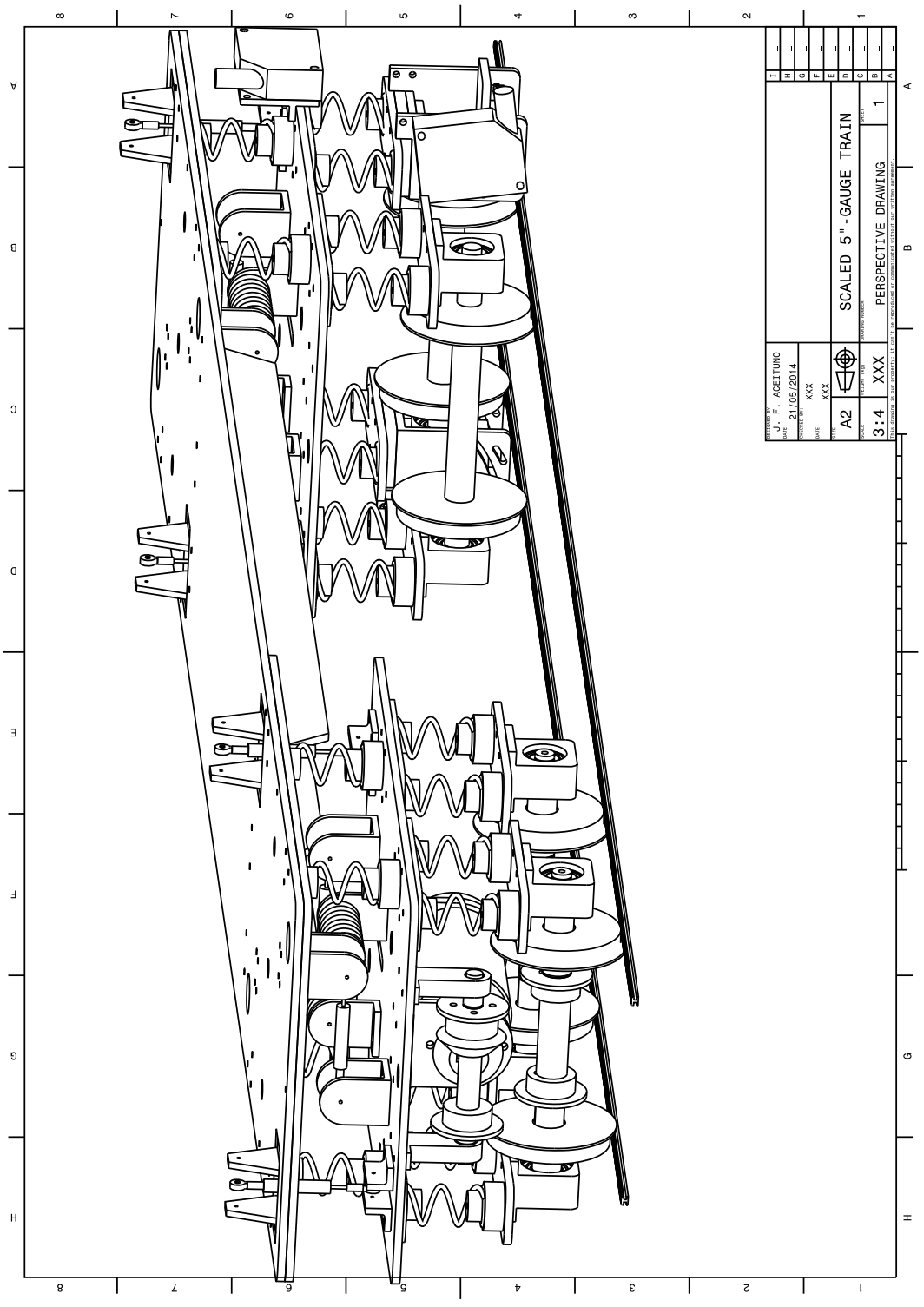

FIGURE A.1: Perspective drawing

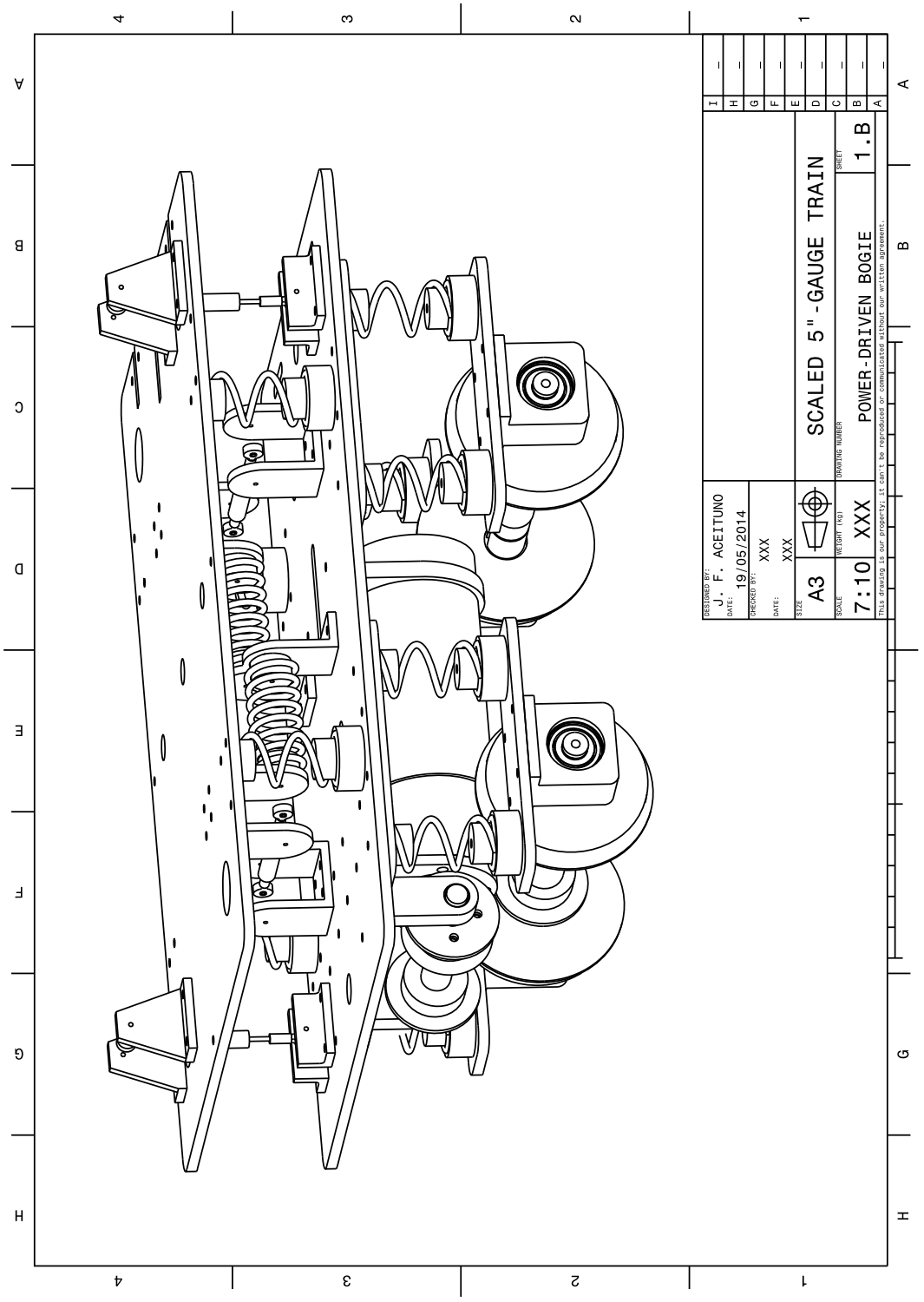

FIGURE A.2: Power-driven bogie

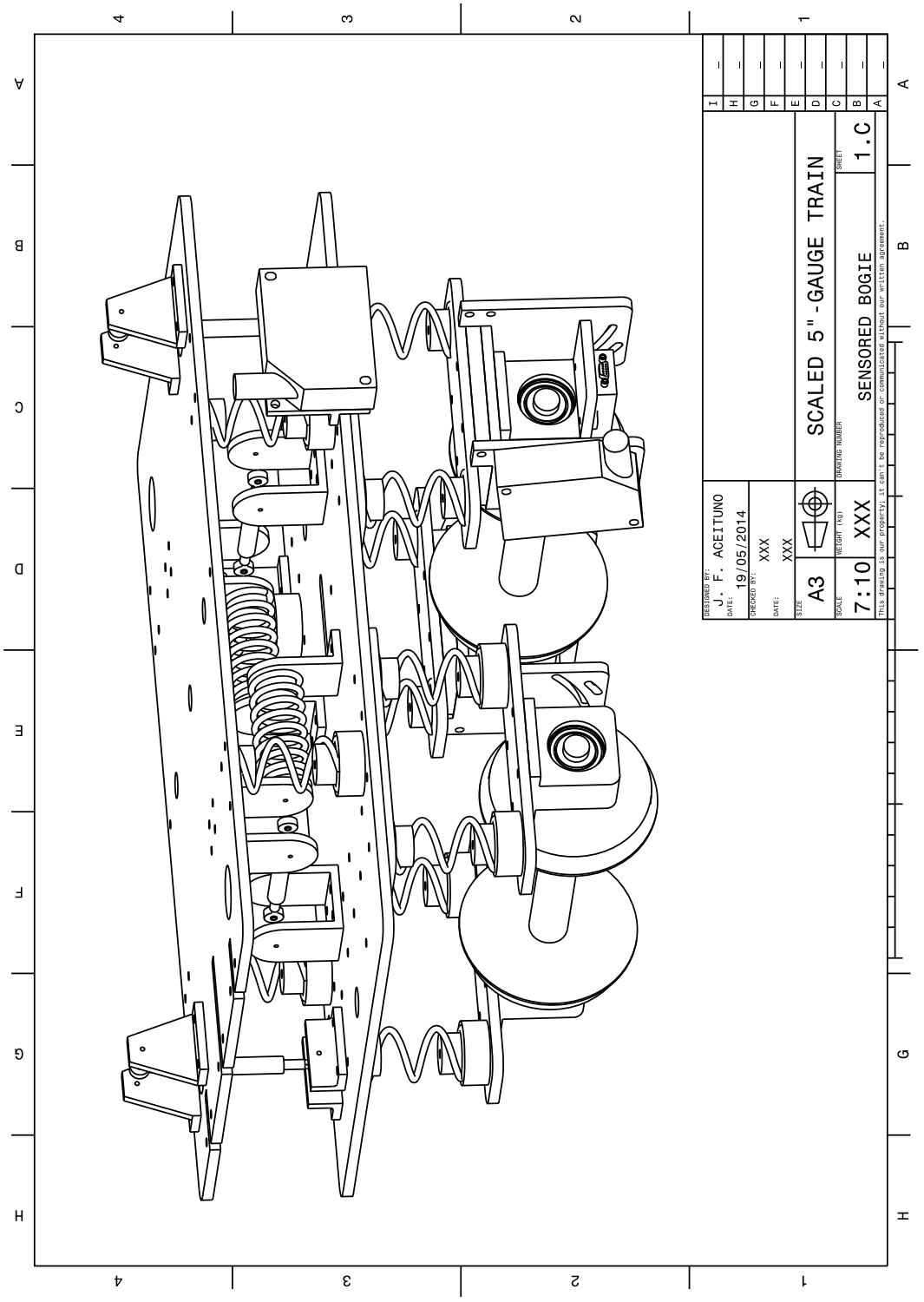

FIGURE A.3: Sensored bogie

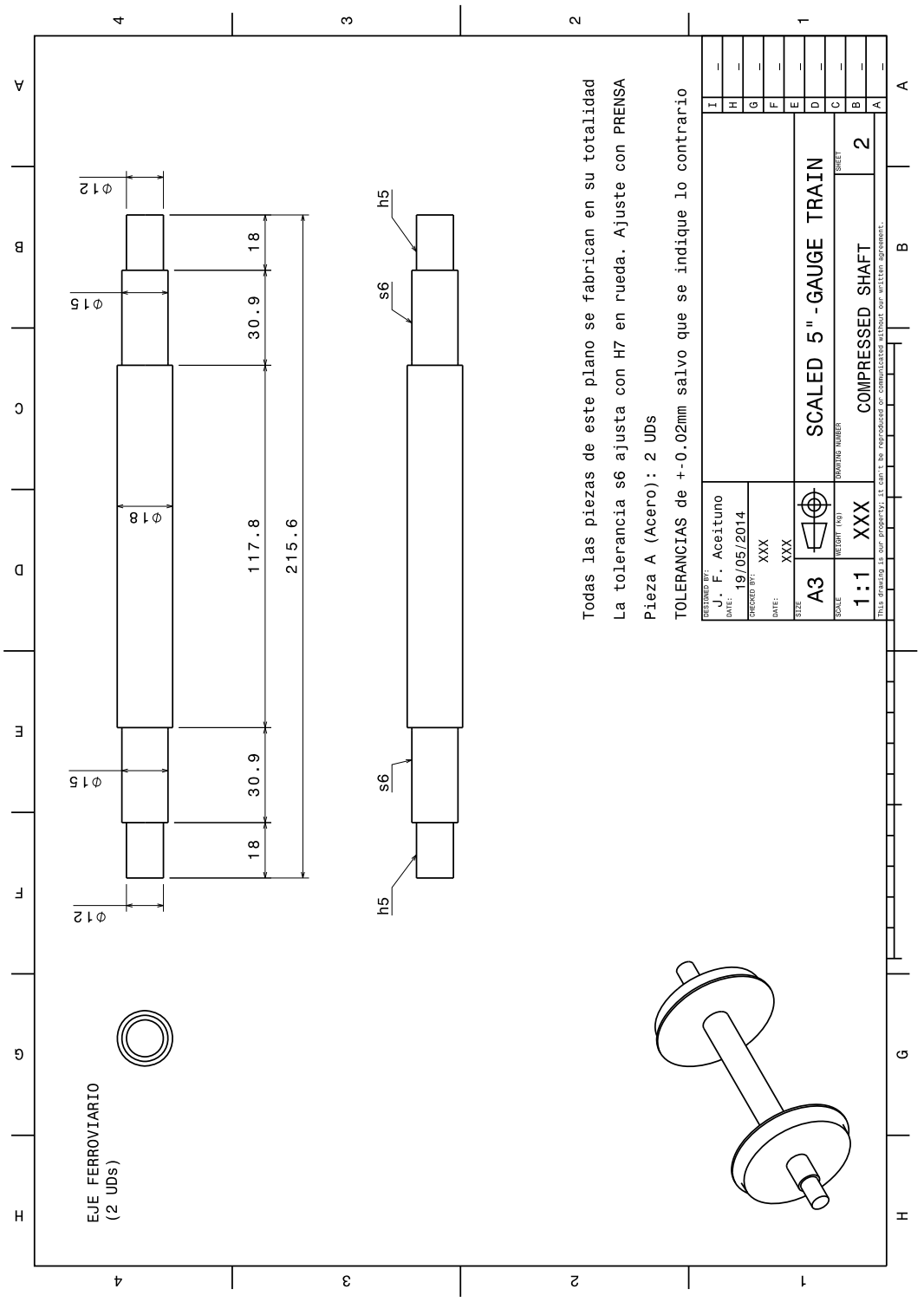

FIGURE A.4: Compressed shaft

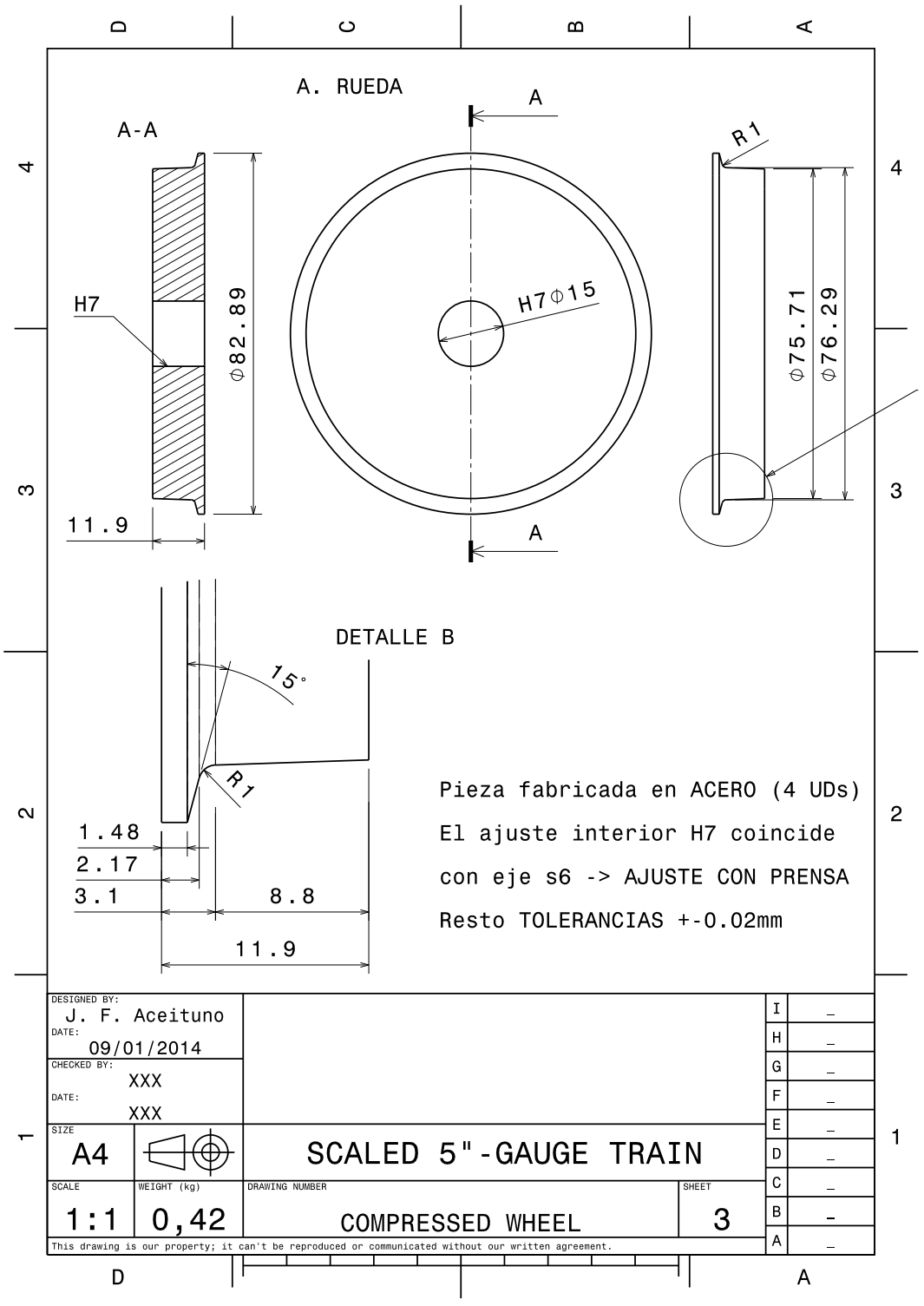

FIGURE A.5: Compressed wheel

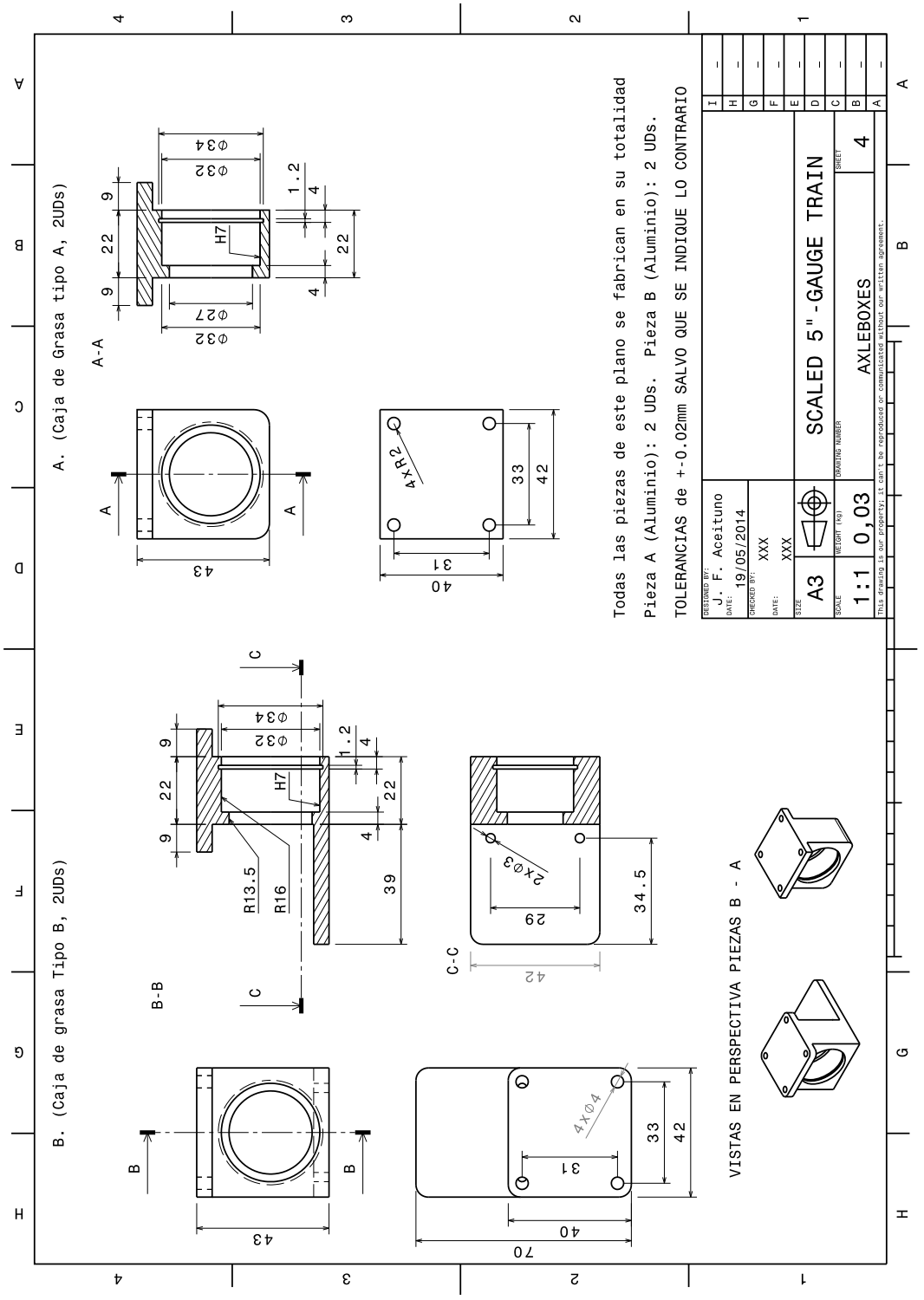

FIGURE A.6: Axleboxes

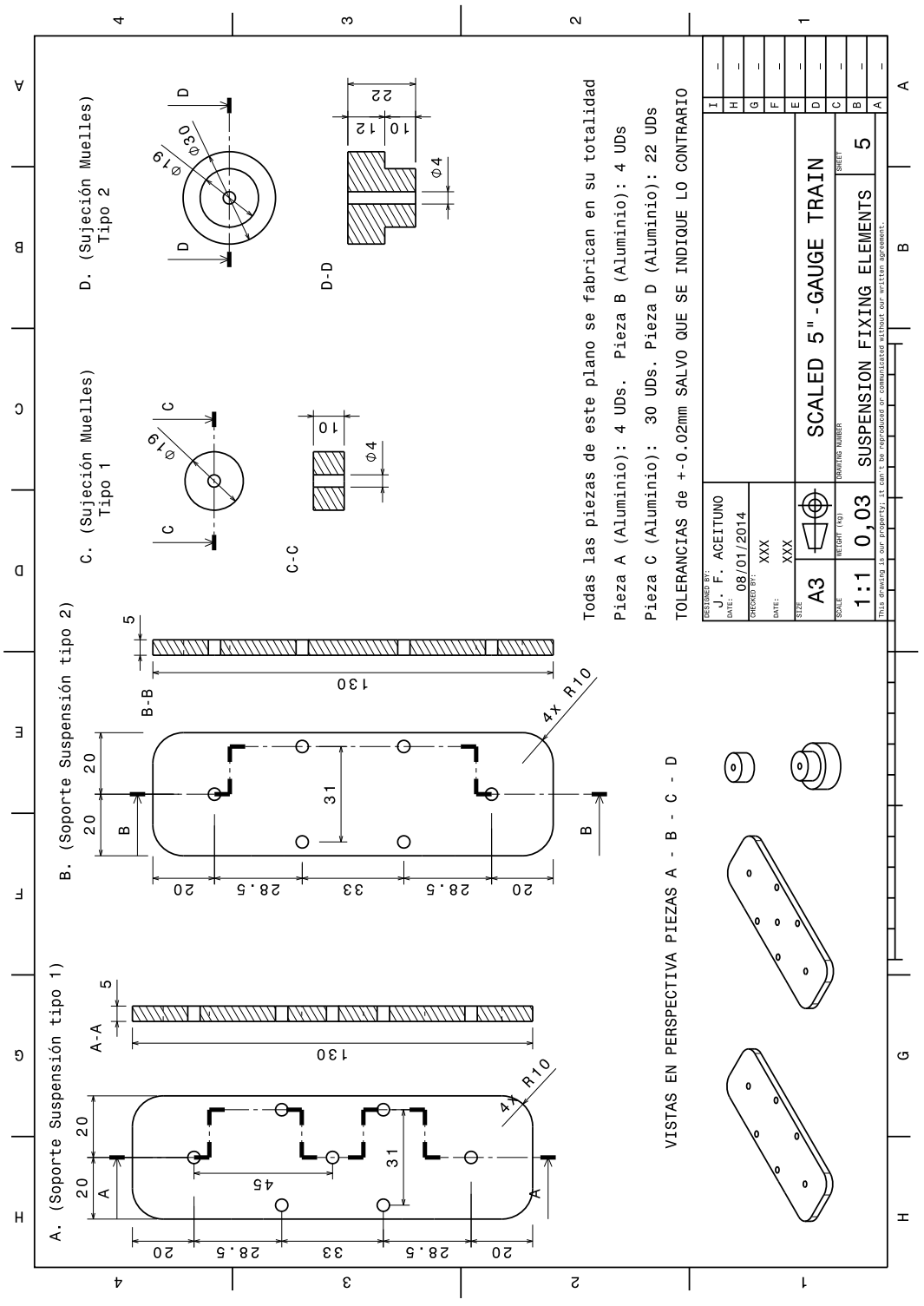

FIGURE A.7: Suspension fixing elements

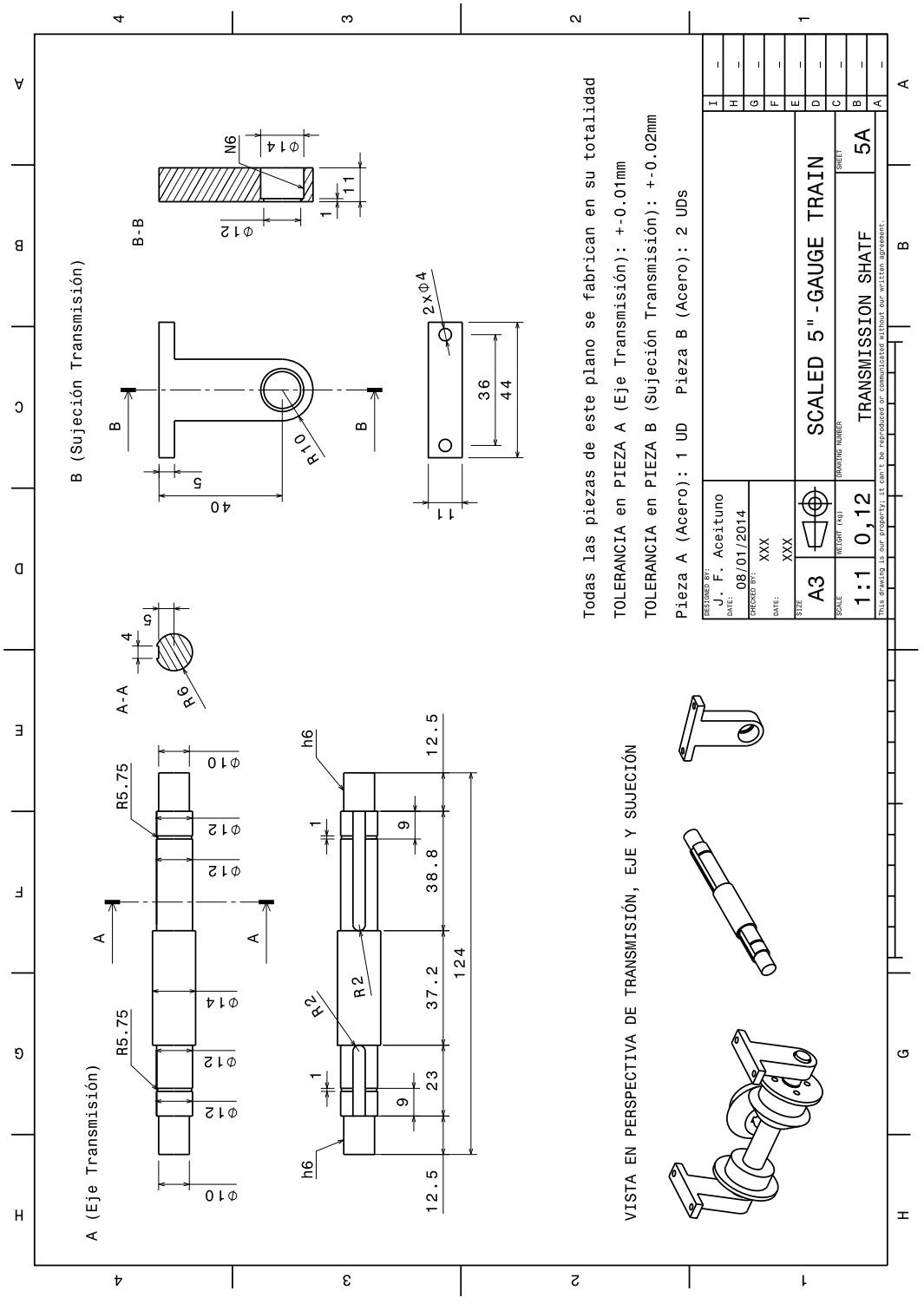

FIGURE A.8: Perspective drawing

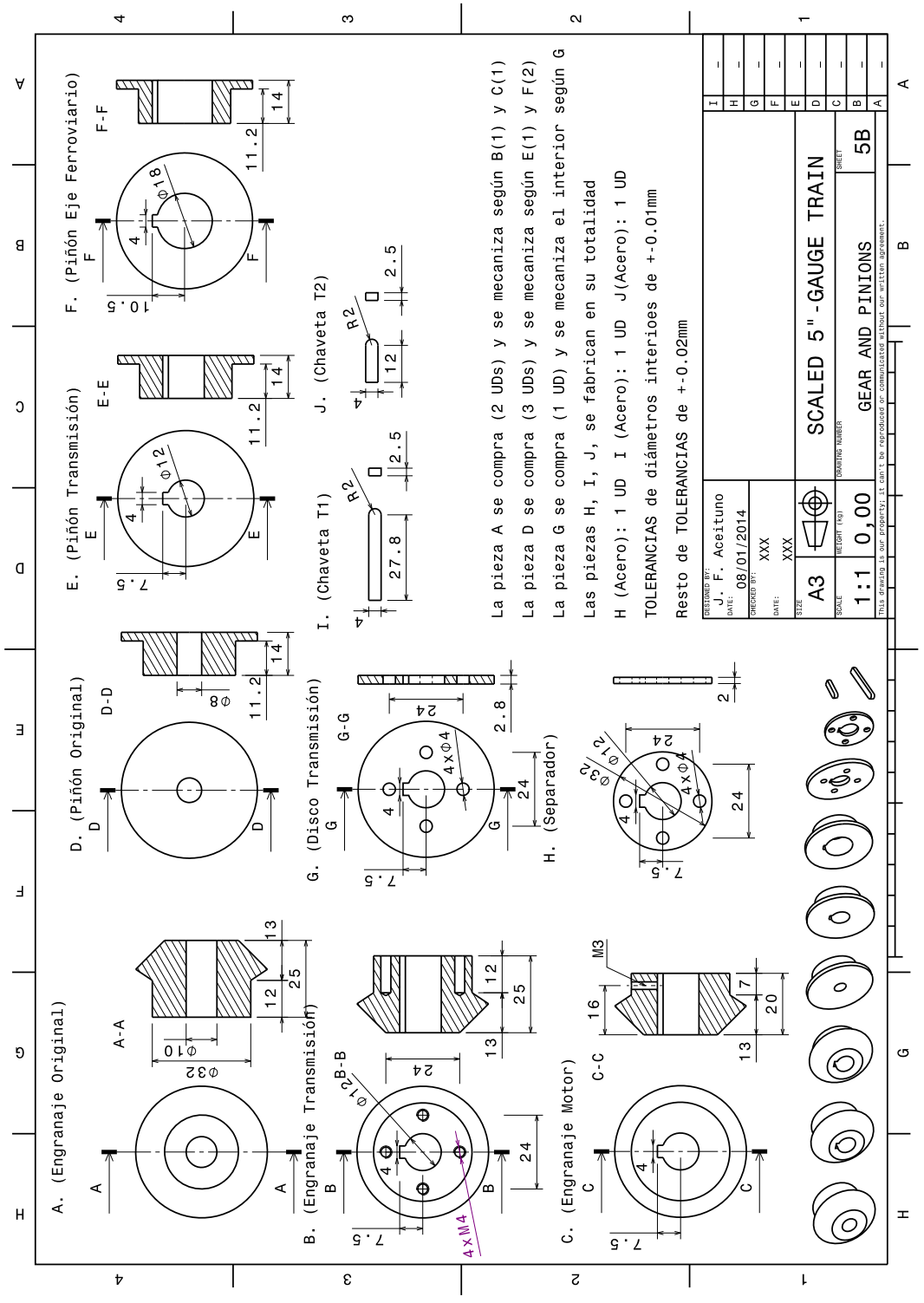

FIGURE A.9: Gear and pinions

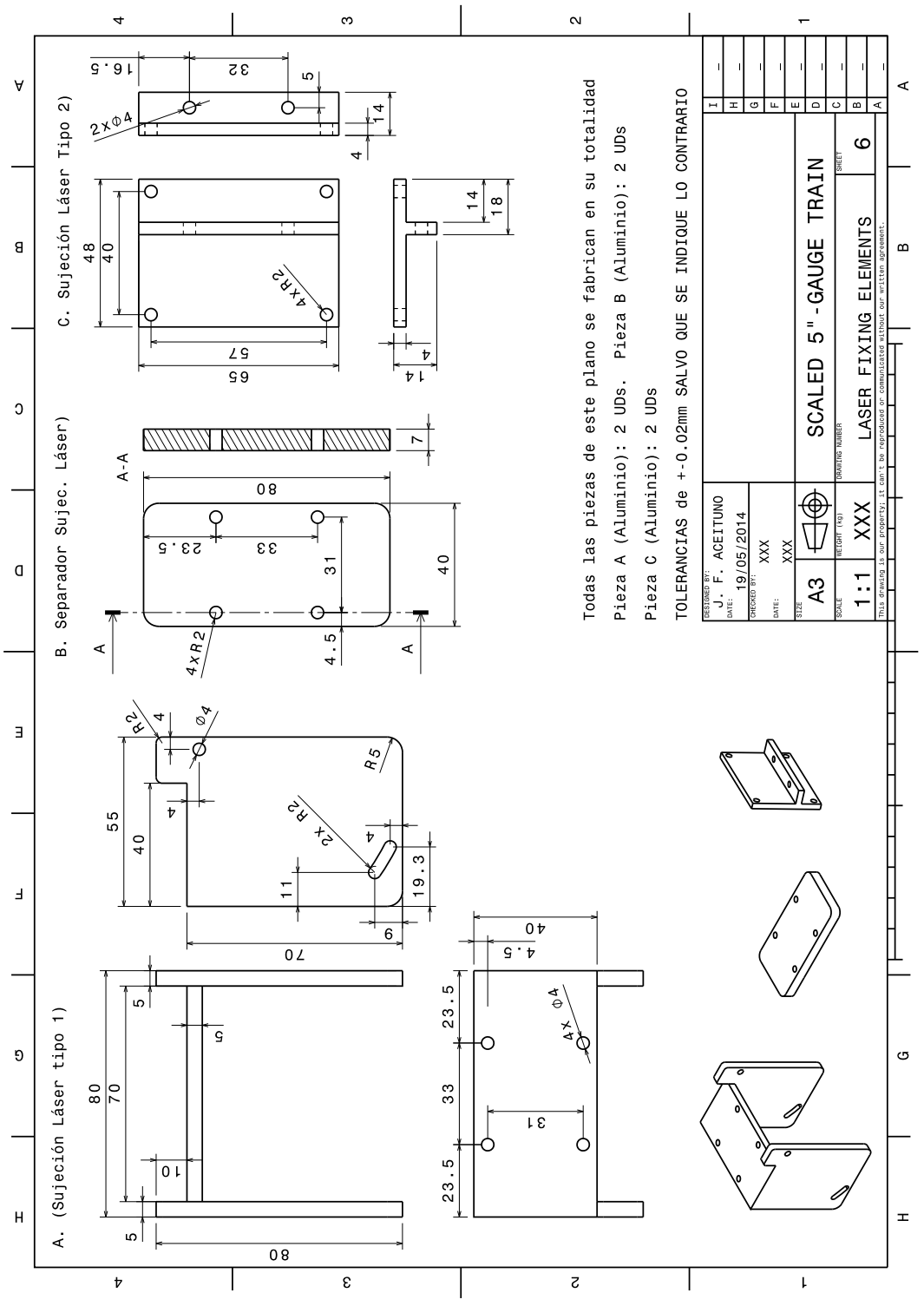

FIGURE A.10: Laser fixing elements

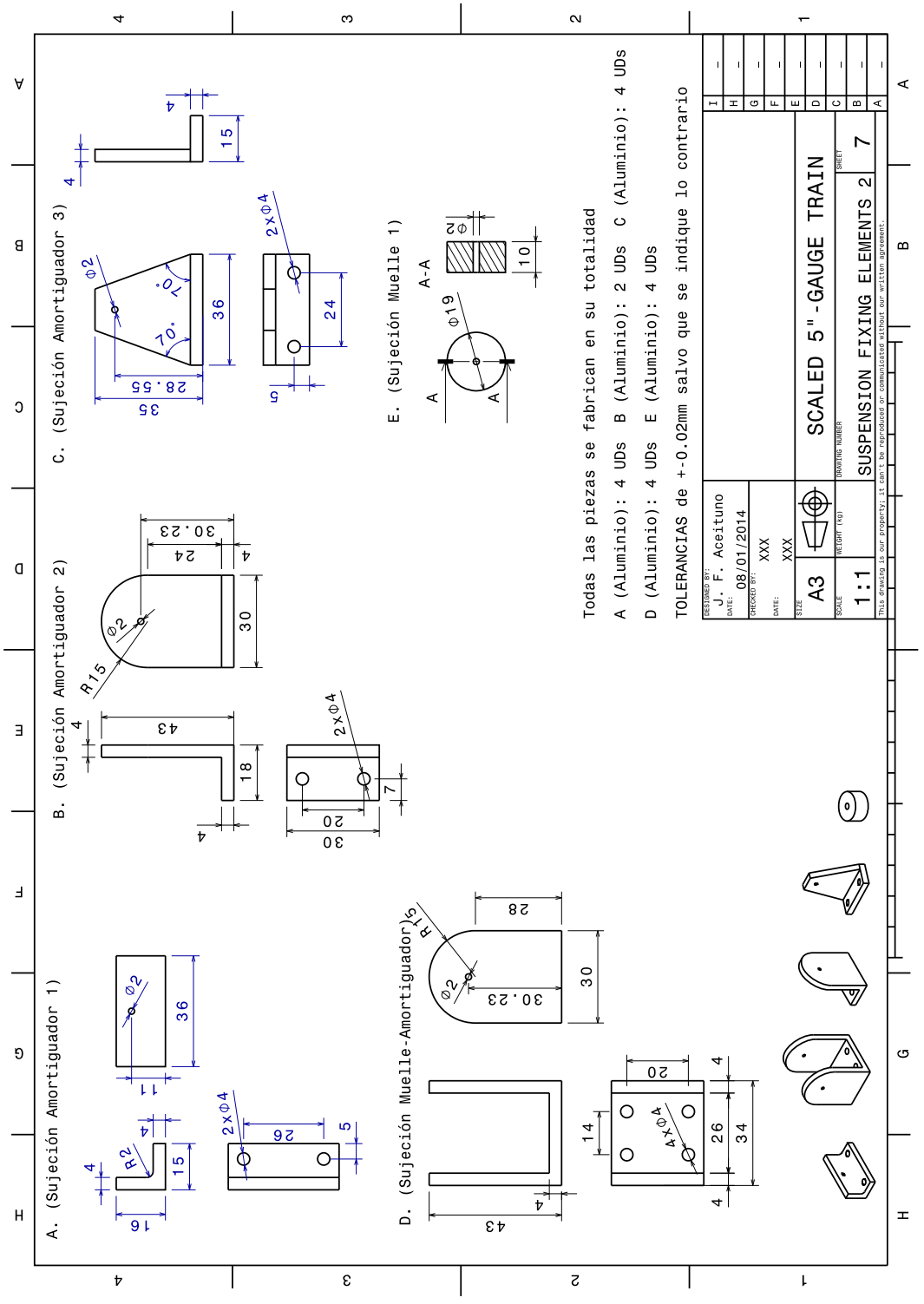

FIGURE A.11: Suspension fixing elements 2

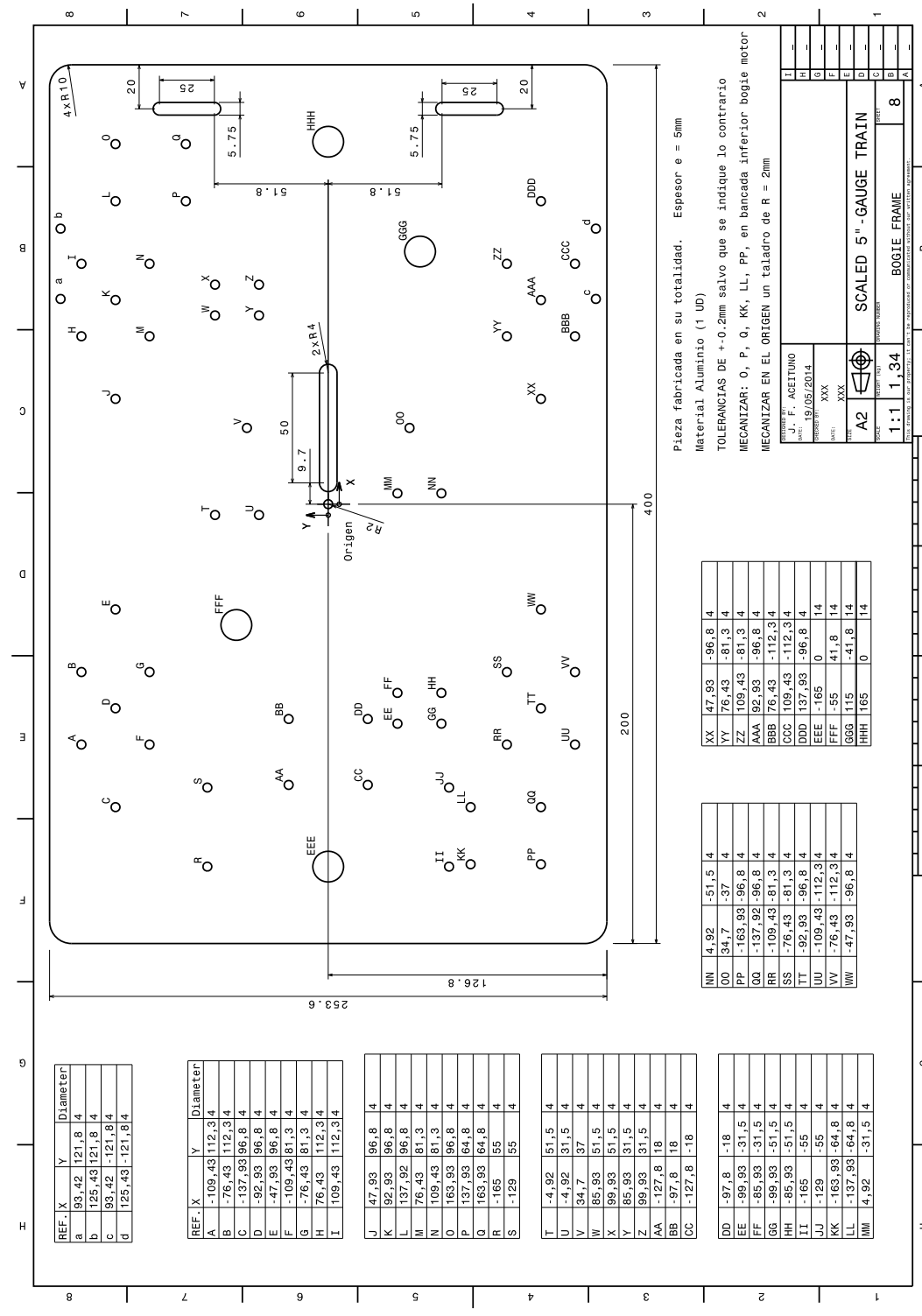

REF.	X	Y	Diameter
a	93,42	121,8	4
b	125,43	121,8	4
c	93,42	-121,8	4
d	125,43	-121,8	4

REF.	X	Y	Diameter
A	-109,43	112,3	4
B	-76,43	112,3	4
C	-137,93	96,8	4
D	-92,93	96,8	4
E	-47,93	96,8	4
F	-109,43	81,3	4
G	-76,43	81,3	4
H	76,43	112,3	4
I	109,43	112,3	4

J	47,93	96,8	4
K	92,93	96,8	4
L	137,92	96,8	4
M	76,43	81,3	4
N	109,43	81,3	4
O	163,93	96,8	4
P	137,93	64,8	4
Q	163,93	64,8	4
R	-165	55	4
S	-129	55	4

T	-4,92	51,5	4
U	-4,92	31,5	4
V	34,7	37	4
W	85,93	51,5	4
X	99,93	51,5	4
Y	85,93	31,5	4
Z	99,93	31,5	4
AA	-127,8	18	4
BB	-97,8	18	4
CC	-127,8	-18	4

DD	-97,8	-18	4
EE	-99,93	-31,5	4
FF	-85,93	-31,5	4
GG	-99,93	-51,5	4
HH	-85,93	-51,5	4
II	-165	-55	4
JJ	-129	-55	4
KK	-163,93	-64,8	4
LL	-137,93	-64,8	4
MM	4,92	-31,5	4

NN	4,92	-51,5	4
OO	34,7	-37	4
PP	-163,93	-96,8	4
QQ	-137,92	-96,8	4
RR	-109,43	-81,3	4
SS	-76,43	-81,3	4
TT	-92,93	-96,8	4
UU	-109,43	-112,3	4
VV	-76,43	-112,3	4
WW	-47,93	-96,8	4

XX	47,93	-96,8	4
YY	76,43	-81,3	4
ZZ	109,43	-81,3	4
AAA	92,93	-96,8	4
BBB	76,43	-112,3	4
CCC	109,43	-112,3	4
DDD	137,93	-96,8	4
EEE	-165	0	14
FFF	-55	41,8	14
GGG	115	-41,8	14
HHH	165	0	14

FIGURE A.12: Bogie frame

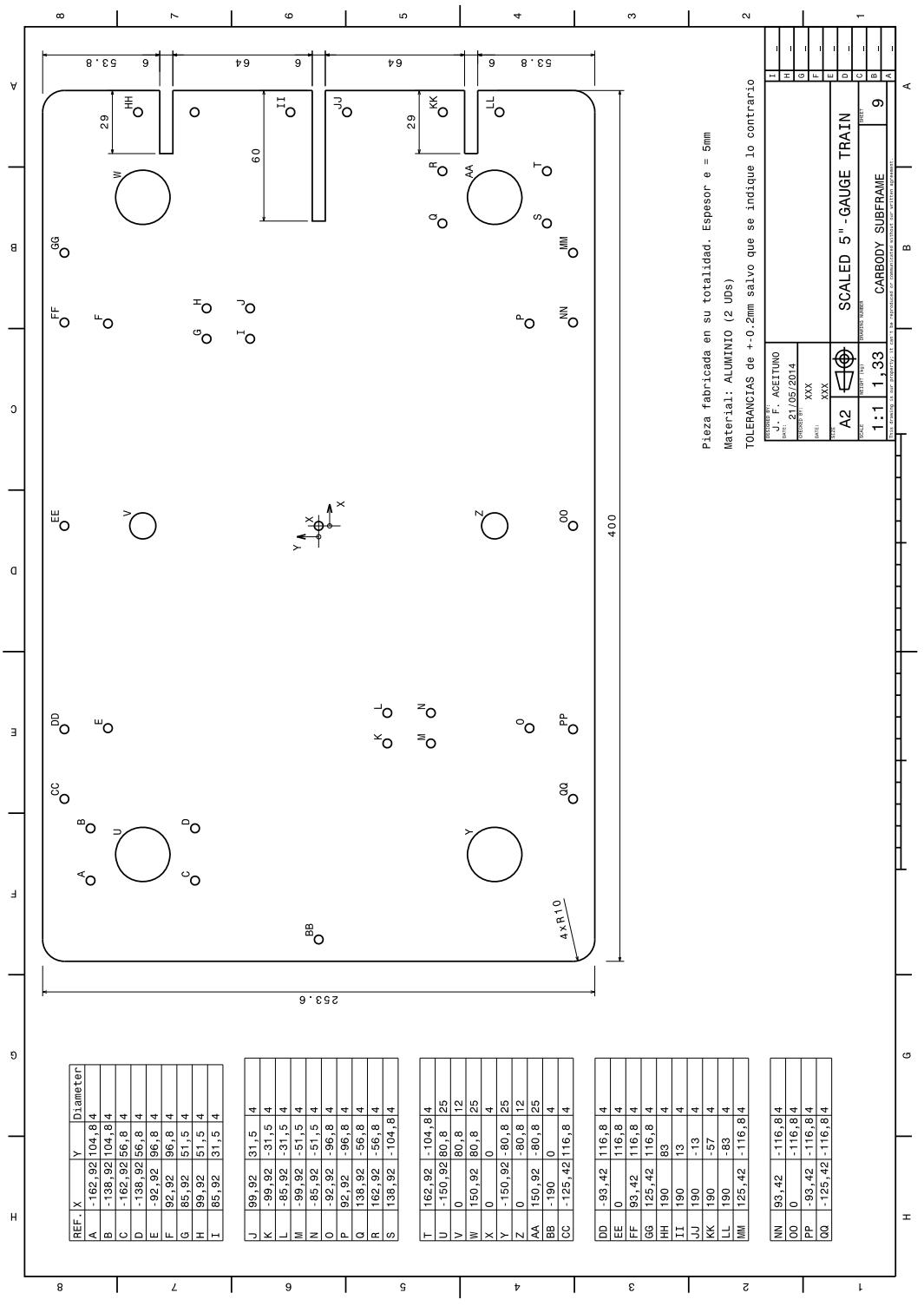

REF.	X	Y	Diameter
A	-162,92	104,8	4
B	-138,92	104,8	4
C	-162,92	56,8	4
D	-138,92	56,8	4
E	-92,92	96,8	4
F	92,92	96,8	4
G	85,92	51,5	4
H	99,92	51,5	4
I	85,92	31,5	4

J	99,92	31,5	4
K	-99,92	-31,5	4
L	-85,92	-31,5	4
M	-99,92	-51,5	4
N	-85,92	-51,5	4
O	-92,92	-96,8	4
P	92,92	-96,8	4
Q	138,92	-56,8	4
R	162,92	-56,8	4
S	138,92	-104,8	4

T	162,92	-104,8	4
U	-150,92	80,8	25
V	0	80,8	12
W	150,92	80,8	25
X	0	0	4
Y	-150,92	-80,8	25
Z	0	-80,8	12
AA	150,92	-80,8	25
BB	-190	0	4
CC	-125,42	116,8	4

DD	-93,42	116,8	4
EE	0	116,8	4
FF	93,42	116,8	4
GG	125,42	116,8	4
HH	190	83	4
II	190	13	4
JJ	190	-13	4
KK	190	-57	4
LL	190	-83	4
MM	125,42	-116,8	4

NN	93,42	-116,8	4
OO	0	-116,8	4
PP	-93,42	-116,8	4
QQ	-125,42	-116,8	4

FIGURE A.13: Carbody subframe

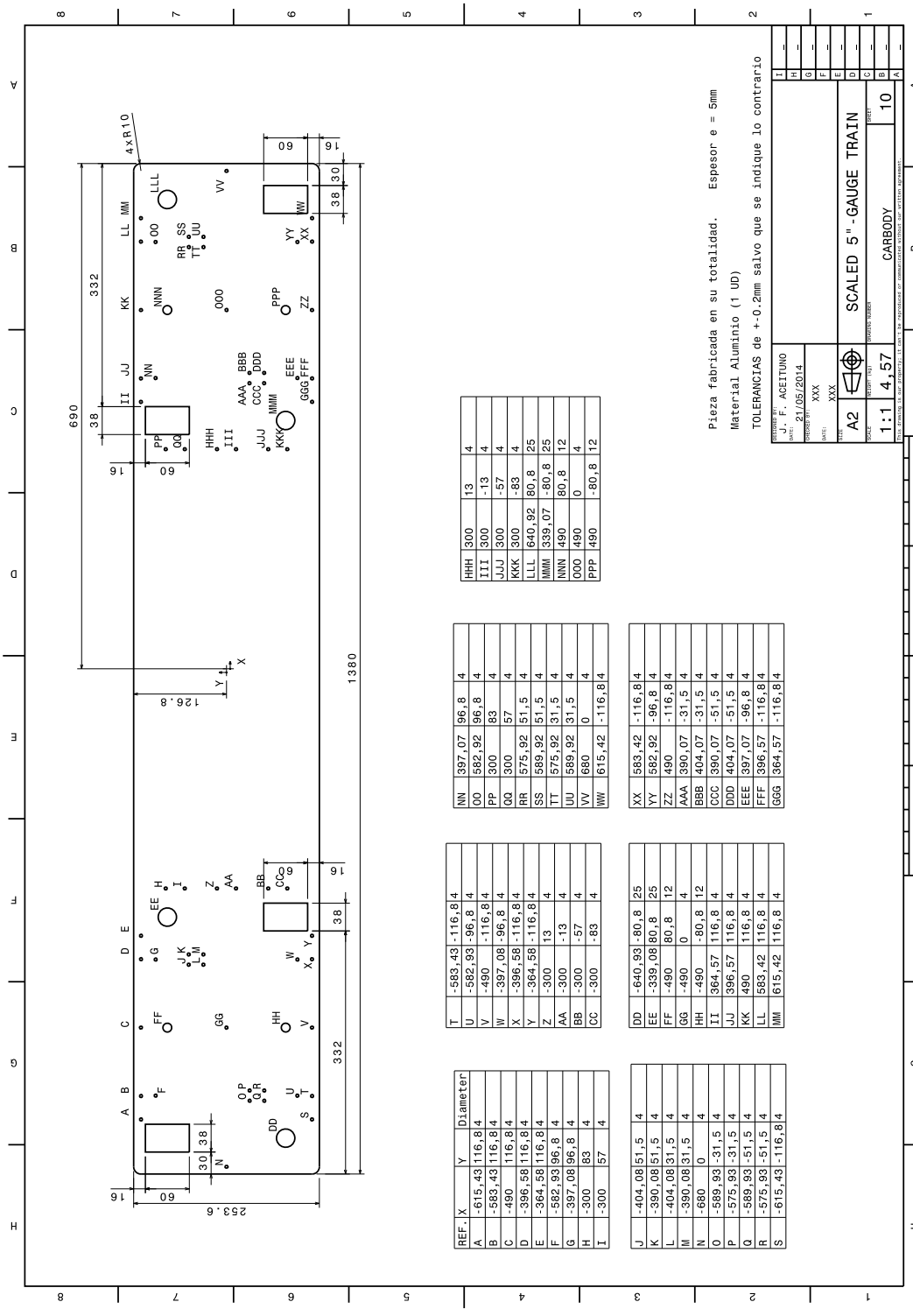

REF.	X	Y	Diameter
A	-615,43	116,8	4
B	-583,43	116,8	4
C	-490	116,8	4
D	-396,58	116,8	4
E	-364,58	116,8	4
F	-582,93	96,8	4
G	-397,08	96,8	4
H	-300	83	4
I	-300	57	4

J	-404,08	51,5	4
K	-390,08	51,5	4
L	-404,08	31,5	4
M	-390,08	31,5	4
N	-680	0	4
O	-589,93	-31,5	4
P	-575,93	-31,5	4
Q	-589,93	-51,5	4
R	-575,93	-51,5	4
S	-615,43	-116,8	4

T	-583,43	-116,8	4
U	-582,93	-96,8	4
V	-490	-116,8	4
W	-397,08	-96,8	4
X	-396,58	-116,8	4
Y	-364,58	-116,8	4
Z	-300	13	4
AA	-300	-13	4
BB	-300	-57	4
CC	-300	-83	4

DD	-640,93	-80,8	25
EE	-339,08	80,8	25
FF	-490	80,8	12
GG	-490	0	4
HH	-490	-80,8	12
II	364,57	116,8	4
JJ	396,57	116,8	4
KK	490	116,8	4
LL	583,42	116,8	4
MM	615,42	116,8	4

NN	397,07	96,8	4
OO	582,92	96,8	4
PP	300	83	4
QQ	300	57	4
RR	575,92	51,5	4
SS	589,92	51,5	4
TT	575,92	31,5	4
UU	589,92	31,5	4
VV	680	0	4
WW	615,42	-116,8	4

XX	583,42	-116,8	4
YY	582,92	-96,8	4
ZZ	490	-116,8	4
AAA	390,07	-31,5	4
BBB	404,07	-31,5	4
CCC	390,07	-51,5	4
DDD	404,07	-51,5	4
EEE	397,07	-96,8	4
FFF	396,57	-116,8	4
GGG	364,57	-116,8	4

HHH	300	13	4
III	300	-13	4
JJJ	300	-57	4
KKK	300	-83	4
LLL	640,92	80,8	25
MMM	339,07	-80,8	25
NNN	490	80,8	12
OOO	490	0	4
PPP	490	-80,8	12

FIGURE A.14: Carbody

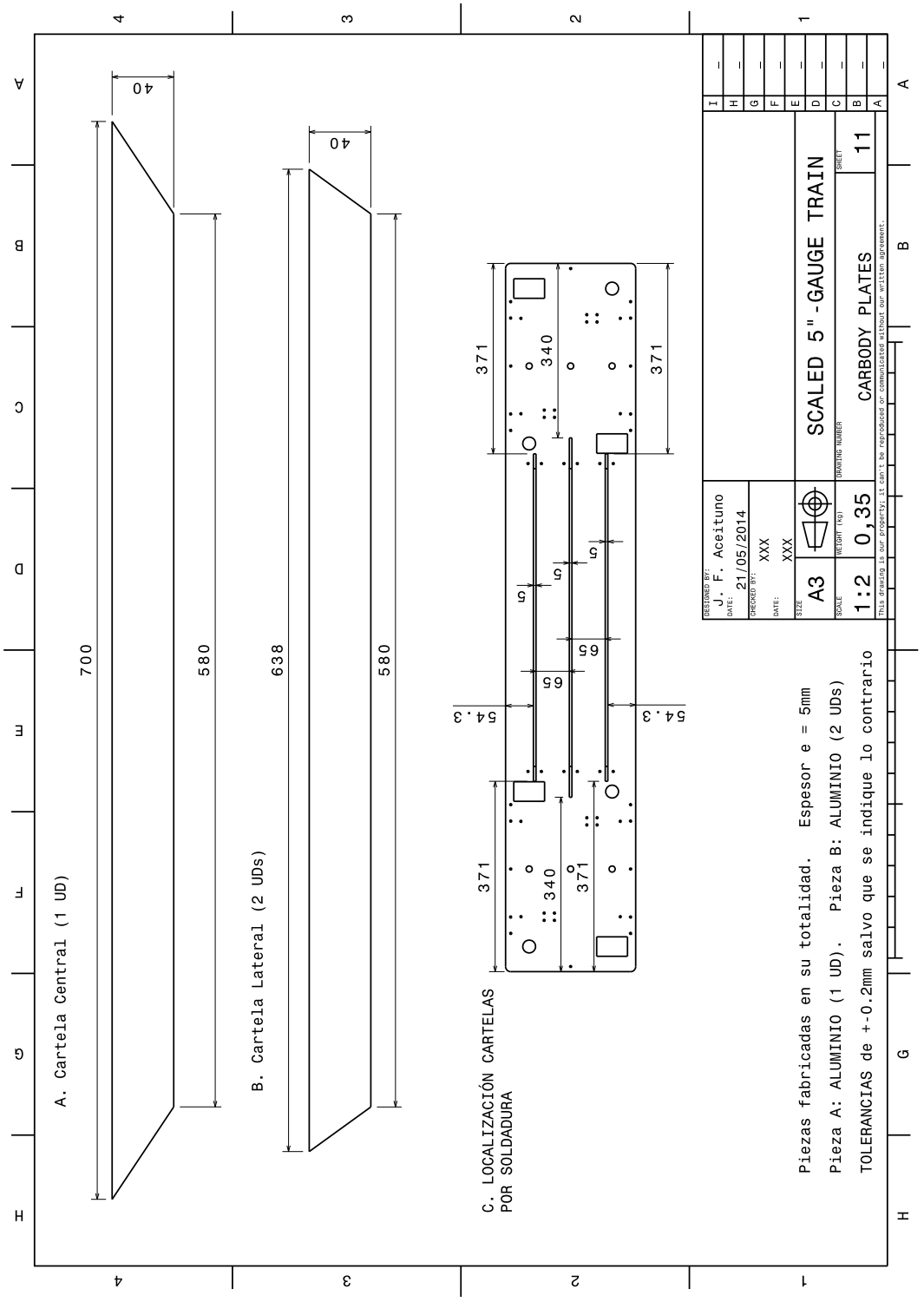

FIGURE A.15: Carbody plates

Bibliography

[1] European Standard EN 12299, *Railway applications - Ride comfort for passengers - Measurement and evaluation*, Submitted to CEN Members for Enquiry, 2009.

[2] J. Auciello, E. Meli, S. Falomi, and M. Malvezzi, *Dynamic simulation of railway vehicles: wheel/rail contact analysis*, Vehicle system dynamics **47** (2009), no. 7, 867–899.

[3] J. Baumgarte, *Stabilization of constraints and integrals of motion in dynamical systems*, Computer methods in applied mechanics and engineering **1** (1972), no. 1, 1–16.

[4] E.G. Berggren, M.X.D. Li, and J. Spännar, *A new approach to the analysis and presentation of vertical track geometry quality and rail roughness*, Wear **265** (2008), no. 9, 1488–1496.

[5] D.P. Bertsekas, *Constrained optimization and Lagrange multiplier methods*, Academic press, 2014.

[6] A. Bevan, P. Molyneux-Berry, B. Eickhoff, and M. Burstow, *Development and validation of a wheel wear and rolling contact fatigue damage model*, Wear **307** (2013), no. 1, 100–111.

[7] D. Boocock, *Steady-state motion of railway vehicles on curved track*, Journal of Mechanical Engineering Science **11** (1969), no. 6, 556–566.

[8] F.W. Carter, *The electric locomotive (Including Appendix and plate at back of volume)*, Minutes of the Proceedings, vol. 201, Thomas Telford, 1916, pp. 221–252.

[9] F.W. Carter, *On the stability of running of locomotives*, Proceedings of the Royal Society of London A: Mathematical, Physical and Engineering Sciences, vol. 121, The Royal Society, 1928, pp. 585–611.

[10] R.A. Clark, B.M. Eickhoff, and G.A. Hunt, *Prediction of the dynamic response of vehicles to lateral track irregularities*, Vehicle System Dynamics **10** (1981), no. 2-3, 106–109.

[11] J. Cuadrado, D. Dopico, M.A. Naya, and M. González, *Penalty, semi-recursive and hybrid methods for MBS real-time dynamics in the context of structural integrators*, Multibody System Dynamics **12** (2004), no. 2, 117–132.

[12] A.D. De Pater, *On the reciprocal pressure between two elastic bodies*, Proc. Symp. Rolling Contact Phenomena, Elsener Publishing Co., Amsterdam, 1962, pp. 24–75.

[13] A.D. De Pater, *The geometrical contact between track and wheelset*, Vehicle System Dynamics **17** (1988), no. 3, 127–140.

[14] R. de Possel and J. Beautefoy, *Papers awarded prizes in the competition sponsored by Office of Research and Experiment of the International Union of Railways*, 1960.

[15] A.B. DE-solver, *GENSYS User's Manual, release 0103*, Östersund, Sweden (2001).

[16] EN DIN, *13906-1*, Cylindrical helical spring made from round wire and bars-Calculation and design Part **1**.

[17] J.A. Elkins and R.J. Gostling, *A general quasi-static curving theory for railway vehicles*, Vehicle System Dynamics **6** (1977), no. 2-3, 100–106.

[18] R. Enblom, *Deterioration mechanisms in the wheel–rail interface with focus on wear prediction: a literature review*, Vehicle System Dynamics **47** (2009), no. 6, 661–700.

[19] J.L. Escalona and J.F. Aceituno, *Modeling of railway vehicles with symbolic computation and contact look-up tables for real-time simulations*, The 3rd International Conference on Multibody System Dynamics IMSD and The 7th Asian Conference on Multibody Dynamics ACMD (Busan, Korea 2014).

[20] J.L. Escalona and J.F. Aceituno, *Modeling wheel-rail contact with pre-calculated lookup tables in arbitrary-geometry tracks with irregularities*, Proceedings of the ASME 2015 International Design Engineering Technical Conferences & Computers and Information in Engineering Conference IDETC/CIE (Boston, USA, 2015).

[21] J.L. Escalona, T.-W. Park, and K.E. Zaazaa, *Railroad vehicle dynamics - A roadmap to high speed trains*, Journal of Computational and Nonlinear Dynamics **7** (2012), no. 4.

[22] D.J. Ewins, *Modal testing: theory and practice*, Letchworth: Research studies press LTD., 2000.

[23] P. Fisette, *Robotran Release 3.0–User Manual*, 1998.

[24] V. Garg, *Dynamics of railway vehicle systems*, Elsevier, 2012.

[25] A.O. Gilchrist, *Power Spectral Measurements by TMMl: Proving Trials and Three Site Measurements*, British Railway Research Department, 1967.

[26] A.O. Gilchrist, A.E.W. Hobbs, B.L. King, and V. Washby, *The riding of two particular designs of four-wheeled railway vehicle*, Proceedings of the Institution of Mechanical Engineers, Conference Proceedings, vol. 180, SAGE Publications, 1965, pp. 99–113.

[27] W. Goldsmith, *Impact: The theory and physical behavior of colliding solids*, E. Arnold, 1960.

[28] S.L. Grassie, *Rail corrugation: characteristics, causes, and treatments*, Proceedings of the Institution of Mechanical Engineers, Part F: Journal of Rail and Rapid Transit **223** (2009), no. 6, 581–596.

[29] S.L. Grassie and J. Kalousek, *Rail corrugation: characteristics, causes and treatments*, Proceedings of the Institution of Mechanical Engineers, Part F: Journal of Rail and Rapid Transit **207** (1993), no. 1, 57–68.

[30] M. Gretzschel and A. Jaschinski, *Design of an active wheelset on a scaled roller rig*, Vehicle System Dynamics **41** (2004), no. 5, 365–381.

[31] A. Hamid and T.L. Yang, *Analytical descriptions of track-geometry variations*, no. 838, 1982.

[32] R. Illingworth, *Railway wheelset lateral excitation by track irregularities*, Vehicle System Dynamics **6** (1977), no. 2-3, 144–147.

[33] Advanced Mechanical Technology Inc., *Force and Motion*, http://www.amti.biz/.

[34] S. Iwnicki, *Handbook of railway vehicle dynamics*, CRC press, 2006.

[35] S. Iwnicki and A.H. Wickens, *Validation of a MATLAB railway vehicle simulation using a scale roller rig*, Vehicle System Dynamics **30** (1998), no. 3-4, 257–270.

[36] A. Jaschinski, *On the application of similarity laws to a scaled railway bogie model*, Ph.D. thesis, TU Delft, Delft University of Technology, 1990.

[37] H.H. Jenkins, J.E. Stephenson, G.A. Clayton, G.W. Morland, and D. Lyon, *The effect of track and vehicle parameters on wheel/rail vertical dynamic forces*, Railway Engineering Journal **3** (1974), no. 1.

[38] J.J. Kalker, *The transmission of force and couple between two elastically similar rolling spheres*, Part I, II and III Proc K ned Akad **67** (1964), 150.

[39] J.J. Kalker, *On the rolling of two elastic bodies in the presence of dry friction*, Delft,, The Netherlands: Delft University of Technology. PhD Thesis (1967).

[40] J.J. Kalker, *Three-dimensional elastic bodies in rolling contact*, vol. 2, Springer Science & Business Media, 2013.

[41] J.J. Kalker, *A fast algorithm for the simplified theory of rolling contact*, Vehicle system dynamics **11** (1982), no. 1, 1–13.

[42] A.D. Kerr, *Fundamentals of railway track engineering*, Simmons Boardman Pub Co, 2003.

[43] W. Kik and H. Steinborn, *Wheel/rail connexion-element for use in a multi-body-algorithm*, Dynamics of Vehicles on Roads and Tracks, Proceedings of 8th IAVSD Symposium, Cambridge, MA, USA, 1984, pp. 303–316.

[44] S.-S. Kim and W. Jeong, *Subsystem synthesis method with approximate function approach for a real-time multibody vehicle model*, Multibody System Dynamics **17** (2007), no. 2-3, 141–156.

[45] P. Klauser, N. Wilson, S. Handal, and M. Dembosky, *Users Manual for NUCARS–Version 2.1*, SD-043-(rev 9/95) Association of American Railroads (1995).

[46] J. Klingel, *Ueber den Lauf der Eisenbahnwagen auf gerader Bahn*, Organ Fortschr. Eisenbahnwesen Neue Folge **20** (1883), no. 4, 113–123.

[47] W. Kortüm, *Analysis of railway vehicle system dynamics with the multibody program MEDYNA*, Railroad Conference, 1990., Technical Papers Presented at the 1990 ASME/IEEE Joint, IEEE, 1990, pp. 57–63.

[48] W. Kortüm, *Review of multibody computer, codes for vehicle system dynamics*, Vehicle System Dynamics **22** (1993), no. S1, 3–31.

[49] V.V. Krylov, *Generation of ground vibrations by superfast trains*, Applied Acoustics **44** (1995), no. 2, 149–164.

[50] V.V. Krylov and C. Ferguson, *Calculation of low-frequency ground vibrations from railway trains*, Applied Acoustics **42** (1994), no. 3, 199–213.

[51] M.X.D. Li, E.G. Berggren, M. Berg, and I. Persson, *Assessing track geometry quality based on wavelength spectra and track–vehicle dynamic interaction*, Vehicle System Dynamics **46** (2008), no. S1, 261–276.

[52] L. Ljung, *System Identification Toolbox for Use with MATLAB*, (2007).

[53] B. Luber, *Railway track quality assessment method based on vehicle system identification*, e & i Elektrotechnik und Informationstechnik **126** (2009), no. 5, 180–185.

[54] M. Malvezzi, E. Meli, S. Falomi, and A. Rindi, *Determination of wheel–rail contact points with semianalytic methods*, Multibody System Dynamics **20** (2008), no. 4, 327–358.

[55] M. Malvezzi, E. Meli, S. Papini, and L. Pugi, *Parametric models of railway systems for real-time applications*, Multibody dynamics, Milano, Italy (2007).

[56] MD MDI, *ADAMS/Rail 9.1–Technical Manual*, Ann Arbor, Michigan (1995).

[57] E. Meli, M. Malvezzi, S. Papini, L. Pugi, M. Rinchi, and A. Rindi, *A railway vehicle multibody model for real-time applications*, Vehicle System Dynamics **46** (2008), no. 12, 1083–1105.

[58] Micro-Epsilon, *Micro-Epsilon opto-NCDT*, http:www.micro-epsilon.com/.

[59] MicroStrain, *LORD MicroStrain Sensing Systems*, http://www.microstrain.com/.

[60] D.E. Newland, *Steering a flexible railway truck on curved track*, Journal of Manufacturing Science and Engineering **91** (1969), no. 3, 908–918.

[61] J.C.O. Nielsen, A. Ekberg, and R. Lundén, *Influence of short-pitch wheel/rail corrugation on rolling contact fatigue of railway wheels*, Proceedings of the Institution of Mechanical Engineers, Part F: Journal of Rail and Rapid Transit **219** (2005), no. 3, 177–187.

[62] J.C.O. Nielsen and A. Igeland, *Vertical dynamic interaction between train and track influence of wheel and track imperfections*, Journal of Sound and Vibration **187** (1995), no. 5, 825–839.

[63] J.C.O. Nielsen, *High-frequency vertical wheel–rail contact forces—validation of a prediction model by field testing*, Wear **265** (2008), no. 9, 1465–1471.

[64] Department of Transportation Federal Railroad Administration, *Track safety standards, Part 213, Subpart G, Class of Track 6 and Higher*, Simmons-Boardman Books, 1998.

[65] J.-P. Pascal, *About multi-hertzian-contact hypothesis and equivalent conicity in the case of S1002 and UIC60 analytical wheel/rail profiles*, Vehicle System Dynamics **22** (1993), no. 2, 57–78.

[66] J. Pombo and J. Ambrósio, *A multibody methodology for railway dynamics applications*, Technical Report IDMEC/CPM-2004/003, IDMEC-Institute of Mechanical Engineering, Instituto Superi-or Técnico, Lisbon, Portugal (2004).

[67] J. Pombo, J. Ambrósio, and M. Silva, *A new wheel–rail contact model for railway dynamics*, Vehicle System Dynamics **45** (2007), no. 2, 165–189.

[68] J. Pombo and J. Ambrósio, *A computational efficient general wheel-rail contact detection method*, Journal of mechanical science and technology **19** (2005), no. 1, 411–421.

[69] K. Popp, H. Kruse, and I. Kaiser, *Vehicle-track dynamics in the mid-frequency range*, Vehicle System Dynamics **31** (1999), no. 5-6, 423–464.

[70] K. Popp and W. Schiehlen, *Ground vehicle dynamics*, Springer Berlin Heidelberg, 2010.

[71] European Standard prEN 13848-5, *Railway Applications - Track - Track Geometry Quality - Part 5: Geometric Quality Assessment*, Submitted to CEN Members for Enquiry, 2005.

[72] V.A. Profillidis, *Railway engineering*, 2000.

[73] Delta Rail, *Vampire User Manual*.

[74] C. Rathod and A.A. Shabana, *Geometry and differentiability requirements in multibody railroad vehicle dynamic formulations*, Nonlinear Dynamics **47** (2007), no. 1-3, 249–261.

[75] A.M. Recuero, J.F. Aceituno, J.L. Escalona, and A.A. Shabana, *A nonlinear approach for modeling rail flexibility using the absolute nodal coordinate formulation*, Nonlinear Dynamics **83** (2016), no. 1-2, 463–481.

[76] A.M. Recuero, J.L. Escalona, and R. Chamorro, *A trajectory frame-based dynamic formulation for railroad vehicles simulation*, International Journal for Raiway Technology (2012).

[77] A.M. Recuero, J.L. Escalona, and A.A. Shabana, *Finite-element analysis of unsupported sleepers using three-dimensional wheel–rail contact formulation*, Proceedings of the Institution of Mechanical Engineers, Part K: Journal of Multibody Dynamics **225** (2011), no. 2, 153–165.

[78] A.M. Recuero and J.L. Escalona, *Application of the trajectory coordinate system and the moving modes method approach to railroad dynamics using Krylov subspaces*, Journal of Sound and Vibration **332** (2013), no. 20, 5177–5191.

[79] A.H. Register, *A guide to Matlab object-oriented programming*, CRC Press, 2007.

[80] O. Reynolds, *An experimental investigation of the circumstances which determine whether the motion of water shall be direct or sinuous, and of the law of resistance in parallel channels*, Proceedings of the royal society of London **35** (1883), no. 224-226, 84–99.

[81] W. Rulka and A. Eichberger, *Simpack an analysis and design tool for mechanical systems*, Vehicle system dynamics **22** (1993), no. S1, 122–126.

[82] W. Rulka and E. Pankiewicz, *MBS approach to generate equations of motions for HiL-simulations in vehicle dynamics*, Multibody system dynamics **14** (2005), no. 3-4, 367–386.

[83] R.R. Ryan, *ADAMS—Multibody system analysis software*, Multibody Systems Handbook, Springer, 1990, pp. 361–402.

[84] J.-C. Samin and P. Fisette, *Symbolic modeling of multibody systems*, vol. 112, Springer Science & Business Media, 2003.

[85] J. Santamaría, E.G. Vadillo, and J. Gómez, *A comprehensive method for the elastic calculation of the two-point wheel–rail contact*, Vehicle System Dynamics **44** (2006), no. sup1, 240–250.

[86] Y. Sato, A. Matsumoto, and K. Knothe, *Review on rail corrugation studies*, Wear **253** (2002), no. 1, 130–139.

[87] W.O. Schiehlen, *Multibody systems handbook*, vol. 6, Springer, 1990.

[88] G. Schupp, H. Netter, L. Mauer, and M. Gretzschel, *Multibody system simulation of railway vehicles with SIMPACK*, Vehicle system dynamics **31** (1999), 101–118.

[89] G. Schupp, C. Weidemann, and L. Mauer, *Modelling the contact between wheel and rail within multibody system simulation*, Vehicle System Dynamics **41** (2004), no. 5, 349–364.

[90] A.A. Shabana, *Computational dynamics*, John Wiley & Sons, 2009.

[91] A.A. Shabana, M. Berzeri, and J.R. Sany, *Numerical procedure for the simulation of wheel/rail contact dynamics*, Journal of Dynamic Systems, Measurement, and Control **123** (2001), no. 2, 168–178.

[92] A.A. Shabana and J.R. Sany, *An augmented formulation for mechanical systems with non-generalized coordinates: application to rigid body contact problems*, Nonlinear dynamics **24** (2001), no. 2, 183–204.

[93] A.A. Shabana, M. Tobaa, H. Sugiyama, and K.E. Zaazaa, *On the computer formulations of the wheel/rail contact problem*, Nonlinear dynamics **40** (2005), no. 2, 169–193.

[94] A.A. Shabana, K.E. Zaazaa, J.L. Escalona, and J.R. Sany, *Modeling two-point wheel/rail contacts using constraint and elastic-force approaches*, ASME 2002 International Mechanical Engineering Congress and Exposition, American Society of Mechanical Engineers, 2002, pp. 35–50.

[95] A.A. Shabana, K.E. Zaazaa, J.L. Escalona, and J.R. Sany, *Dynamics of the wheel/rail contact using a new elastic force model*, Chicago: University of Illinois. Technical Report No. MBS02-3-UIC, Department of Mechanical Engineering (2002).

[96] A.A. Shabana, K.E. Zaazaa, and H. Sugiyama, *Railroad vehicle dynamics: a computational approach*, CRC press, 2007.

[97] A.A. Shabana, *Dynamics of multibody systems*, Cambridge university press, 2013.

[98] L.F. Shampine and M.W. Reichelt, *The Matlab ODE suite*, SIAM journal on scientific computing **18** (1997), no. 1, 1–22.

[99] X. Sheng, C.J.C. Jones, and D.J. Thompson, *A theoretical model for ground vibration from trains generated by vertical track irregularities*, Journal of sound and vibration **272** (2004), no. 3, 937–965.

[100] H. Sugiyama, K. Araki, and Y. Suda, *On-line and off-line wheel/rail contact algorithm in the analysis of multibody railroad vehicle systems*, Journal of mechanical science and technology **23** (2009), no. 4, 991–996.

[101] H. Sugiyama and Y. Suda, *Wheel/rail two-point contact geometry with back-of-flange contact*, Journal of Computational and Nonlinear Dynamics **4** (2009), no. 1, 011010.

[102] W. Thomson, *Theory of vibration with applications*, CRC Press, 1996.

[103] J. Tunna, J. Sinclair, and J. Perez, *A review of wheel wear and rolling contact fatigue*, Proceedings of the Institution of Mechanical Engineers, Part F: Journal of Rail and Rapid Transit **221** (2007), no. 2, 271–289.

[104] Virtualmech, *Virtual engineering, real results*, http://www.virtualmech.com/.

[105] R.A. Wehage and E.J. Haug, *Generalized coordinate partitioning for dimension reduction in analysis of constrained dynamic systems*, Journal of mechanical design **104** (1982), no. 1, 247–255.

[106] A.H. Wickens, *The dynamic stability of railway vehicle wheelsets and bogies having profiled wheels*, International Journal of Solids and Structures **1** (1965), no. 3, 319–341.

[107] J. Williams, *Engineering tribology*, Cambridge University Press, 1994.

[108] W. Zhang, J. Chen, X. Wu, and X. Jin, *Wheel/rail adhesion and analysis by using full scale roller rig*, Wear **253** (2002), no. 1, 82–88.